DISSERTATION

ACCESSING A NEW MOLECULAR SCAFFOLD FOR FE(II) SPIN STATE SWITCHING THROUGH FIRST COORDINATION CHANGES

Submitted by

Brooke N. Livesay

Department of Chemistry

In partial fulfillment of the requirements

For the Degree of Doctor Philosophy

Colorado State University

Fort Collins, Colorado

Fall 2021

Doctoral Committee:

Advisor: Matthew P. Shores

Anthony K. Rappé
Alan Van Orden
Kathryn A. Ross

ABSTRACT

ACCESSING A NEW MOLECULAR SCAFFOLD FOR FE(II) SPIN STATE SWITCHING THROUGH FIRST COORDINATION CHANGES

Presented in this dissertation are the syntheses and characterizations of iron spin state switching complexes. The magnetic properties are extremely sensitive to environmental changes such as ligand field, coordination environment, and crystal packing. These studies focus on developing a better understanding of how the magnetic properties of iron complexes can be controlled by environmental modifications.

The first chapter provides a detailed introduction to spin state switching. The chapter includes the origins of the phenomenon and background into previous efforts to modify the spin switching event. This chapter highlights the challenges of designing a spin state switching complex and the different pathways used to induce spin switching events in the solid state and solution phase.

Chapter 2 describes the procedures used to collect solution magnetic data. This chapter details the advantages of collecting solution data using a MPMS instrument compared to the Evans' (^{1}H NMR) Method. The standard operating procedures for the method using a MPMS instrument are described for future researchers. Examples of solution magnetic data collected by both methods are described and compared.

Chapter 3 discusses the challenges that were encountered during the synthesis of an iron(II) complex. The synthesis stopped producing the desired product after it was successful for several months. Investigations into the reproducibility, synthetic methods, and purification steps were performed to understand why the original synthetic procedure stopped working. This chapter

describes how commercially-available starting materials can differ between lot numbers and manufacturers and how these small differences can lead to significant changes in the purity of the final product.

Chapter 4 discusses the impact of speciation on the spin state switching properties of the neutral iron(II) compound synthesized in Chapter 3. Analysis in the solid state indicates the iron(II) complex is in the high spin state at all temperatures. When this compound is dissolved in strongly coordinating solvents the bound anions are replaced by the solvent resulting in a high spin species when the solvent is oxygen-donating and low spin species when the solvent is nitrogen-donating. In non-coordinating solvents the iron(II) complex loses one of the bound anions but remains high spin. However, in moderately coordinating solvents like acetone, the iron(II) loses the bound anions upon decreasing the temperature, resulting in a coordination induced spin state switching event. These studies highlight the sensitivity of solvent choice on the solution magnetic properties of iron(II) compounds.

Chapter 5 discusses the thought process used to design the synthetic procedure for the post-synthetic modification of an iron(II) compound. The azide alkyne cycloaddition reaction was tested with several catalysts and deprotecting agents. Thoughtful consideration was taken to avoid the transmetallation reaction between the cycloaddition catalyst and the iron(II) compound. The successful reaction conditions for the post synthetic modification were found and resulted in the formation of the desired iron(II) triazole compound.

Additional iron(II) triazole complex salts synthesized following the method described in Chapter 5 are described and characterized in Chapter 6. Electron-donating, electron-withdrawing, and oxidation-sensitive substituents are included on the iron(II) triazole ligand to show the scope of the post synthetic modification reaction and allow for investigation into how substituents effect

the magnetic properties of the resulting compounds. Variable temperature solid state magnetic characterization indicates the resulting iron(II) compounds show a variety of magnetic behaviors. However, analysis of the crystallographic data and comparison to related previously published iron(II) triazole compounds indicate the differences in the magnetic properties are due to the solid state crystal packing effects.

In Chapter 7 the solution magnetic properties of the iron(II) triazole compounds described in Chapter 6 are discussed. Removing the crystal packing effects by characterizing the compounds in solution allows for discovery of a relationship between the substituent properties and the magnetic behavior of the resulting compounds. The compounds were characterized in d_4-CD_4OD by Evans' ^1H NMR method and show a thermal spin state switching event. However, no relationship between the Hammett parameter of the substituents and the spin state properties was observed.

Chapter 8 summarizes the investigation of solvent induced spin state switching and post-synthetic modification. Additionally, I discuss some future work that would expand on the studies presented in this dissertation.

DEDICATION

For Susan, Mike, and Ian

TABLE OF CONTENTS

LIST OF TABLES

LIST OF FIGURES

Chapter 1: Controlling Magnetic Properties of Iron(II) Complexes Through Chemical Modifications

1.1 Spin State Switching Background

Transition metal coordination complexes in an octahedral environment with a d^4-d^7 electron count can adopt a high spin (HS) or a low spin (LS) state. The spin state a complex adopts is directly related to which d orbitals the electrons occupy. In an octahedral environment, the five d orbitals split into two e_g and three t_{2g} subsets (Figure 1.1.1). When the energy gap between these subsets (ligand field splitting, Δ) is larger than the electron pairing energy (Π) the electrons fill the lower lying t_{2g} orbitals resulting in a LS complex. Alternatively, if Π is larger than Δ, Hund's first rule is obeyed and the electrons enter an empty orbital before pairing, resulting in a HS complex. When the magnitude of Δ and Π are comparable, then reversible switching between the LS and HS states can occur. This phenomenon, known as spin state switching, can be promoted by physical or chemical stimuli, the most common being temperature.

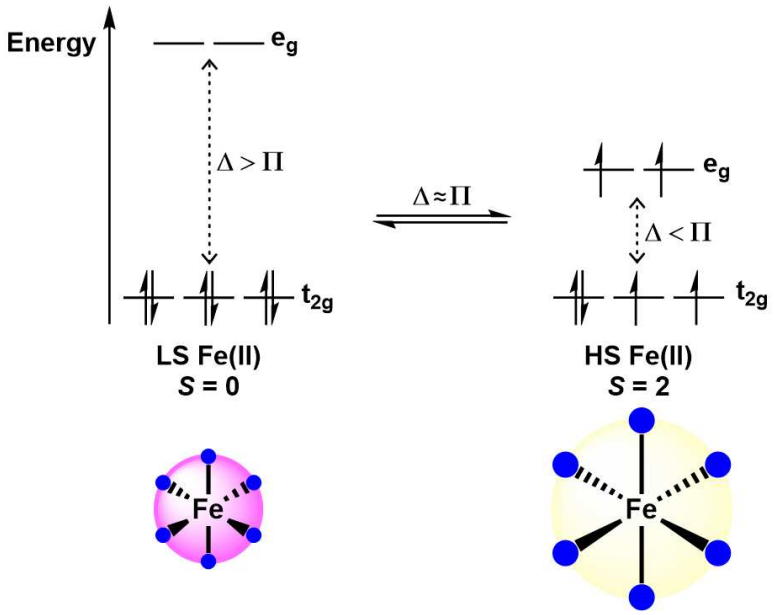

Figure 1.1.1. The electronic and physical structures of LS and HS Iron(II) ions.

1.1.1 Spin State Switching and Spin Crossover

Complexes that undergo spin state switching upon a temperature change are commonly referred to as spin crossover (SCO) complexes. Over time, this term has gained popularity and is now used to describe complexes that undergo the spin switching event promoted by stimuli other than temperature (i.e. pressure, light, chemical changes). However, this term does not justifiably describe all complexes that undergo LS to HS transitions. Spin crossover more specifically describes a spin switching event that is intrinsic to the metal complex. Meaning, there are no changes to the coordination environment and no breaking or formation of bonds during the LS to HS transition. For systems that undergo the LS to HS transition upon chemical modifications, the broader term spin state switching is used herein. For the remainder of this chapter and the following, the term spin crossover (SCO) will be used for complexes with an intrinsic LS to HS transitions and the term spin state switching will be used for LS to HS transitions that occur from a chemical modification of the metal complex or when mentioning the overall phenomenon.

1.1.2 Spin State Properties and Applications

Owing to the stark contrast in the properties between the LS and HS states, iron(II) (d^6) complexes, frequently with six nitrogen donor ligands, are the most commonly studied spin state switching complexes. The change in the spin multiplicity for a d^6 electron count is the largest possible for spin state switching complexes. All electrons are paired in the LS state resulting in a total spin of zero, whereas the four unpaired electrons in the HS state result in a total spin of two (Figure 1.1.1). This results in iron(II) having a diamagnetic LS state and a paramagnetic HS state. The magnetic change between the two spin states is also accompanied by dramatic physical and optical changes. The Fe-N bond lengths tend to be shorter in the LS state (1.80 Å - 2.00 Å) than in the HS state (2.00 Å - 2.20 Å).[1] Additionally, LS species are strongly colored resulting in high

molar absorptivity values and high intensity charge transfer bands, whereas HS species are dull in color resulting in low molar absorptivity values. The differences in the properties between the LS and HS states allow the spin state switching event to be monitored through several techniques (magnetometry, single-crystal X-ray diffraction, UV-Vis spectroscopy, NMR spectroscopy).[2]

Additionally, these unique properties lead to interest in using spin state switching complexes for a variety of applications.[3,4] Some iron(II) SCO complexes have been incorporated into prototypes of memory devices, optical devices, and molecular electronics.[5–8] To be included in these applications, SCO complexes must meet several conditions. The complex must have an abrupt LS to HS transition occurring within a very small temperature window and undergo thermal hysteresis.[9] Hysteresis occurs when the $T_{1/2}$, temperature at which half of the sample is LS and the other half HS, of the warming mode is higher than the $T_{1/2}$ of the cooling mode (Figure 1.1.2). Additionally, the hysteresis loop should be 30-50 K wide and centered around room temperature. This event should also be easily detectible by having a drastic color change between the LS and HS states.[4,9,10] Unfortunately, most SCO complexes do not meet all of these requirements.[11]

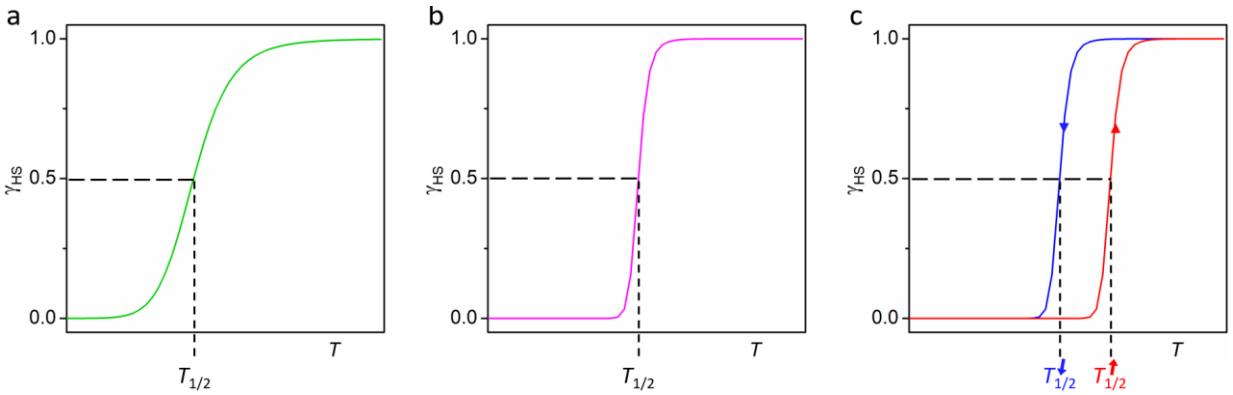

Figure 1.1.2. Illustration of various spin crossover events plotted as high spin fraction (γ_{HS}) versus temperature (T): gradual (a), abrupt (b), and spin crossover with thermal hysteresis (c). The temperature at which half the sample is HS, $T_{1/2}$, is highlighted in all plots.

While researchers are trying to design SCO complexes to meet all the requirements for solid state applications, others are investigating spin state switching complexes for solution base applications like contrast agents and sensors.[3,12,13] These applications do not require abrupt LS to HS transitions with hysteresis, as many rely on the interaction of the metal complex with the solvent or an analyte to induce the spin state switching event around room temperature.[14,15] For both solid state and solution phase applications the coordinated ligands need to be carefully chosen to ensure the metal complex will meet all the required conditions.

1.2 Efforts to Modify Thermal Spin Crossover

While many studies try to find trends between the coordinated ligand and the magnetic properties of a complex, there is no way to accurately predict which ligands will promote SCO.[16–24] The challenge in predicting the effect a ligand has on the magnetic properties of a complex is due to the extreme sensitivity of SCO to external perturbations. In the solid state, co-crystallized solvent, charge balancing anions, and crystal packing environment can overshadow the influence of the ligand field resulting in a single complex with vastly different magnetic properties.[25–27]

The crystal packing effects present in solid state samples are not present in solution samples. This can lead to complexes with contrasting magnetic properties in the solid state and solution phase.[28,29] In solution, ligand field effects dominate allowing for comparison of ligand substitution effects. Several reports show modifications to the ligand through addition of a substituent has an impact on solution SCO properties.[18,30] Additionally, the choice of solvent used can impact the magnetic properties, where the polarity and hydrogen bonding ability of a solvent can increase the $T_{1/2}$ of a SCO complex.[29,31–33]

1.3 Chemically Inducing Spin State Switching

Many researchers have had success tuning the thermal SCO properties by modifying the crystal packing effects or the ligand field, although, it is still challenging to purposely design a ligand that will promote this phenomenon. In recent years, researchers have focused on chemically inducing a spin switching event around room temperature. Some promote this event by retaining the molecular structure of the metal complex, while others modify the complex through chemical reactions and/or ligand exchange.

Our group has previously focused on using anion ligand binding to promote a spin switching event. Guest-dependent spin state switching of high spin $[Fe(H_2bip)_3](BPh_4)_2$ (H_2bip = 2,2′-bi-1,4,5,6-tetrahydropyrimidine) was shown through various anion titrations.[13] The anions bind to the ligand promoting a change in the ligand field strength while still retaining the molecular structure of the iron(II) complex. Similar non-covalent ligand interactions that promote spin state switching have been reported by other groups.[14]

The spin state switching event can also be promoted by post synthetic modifications. In most studies, the first coordination environment around the metal center is retained as the modification takes place on the ligand backbone. Khusniyarov and coworkers showed a LS to HS switching event at room temperature upon a photoisomerization of the bound diarylethene-derived ligand.[34,35] Additionally, the spin switching event can be promoted by increasing the electron-drawing ability of a ligand by protonation as shown by Oshio and coworkers.[36]

Alternatively, the ligand field around the metal ion can be altered through first coordination sphere modifications. The spin state of a metal is determined by the number and type of its donor atoms and can change significantly upon addition or removal of one donor atom. This is known as coordination induced spin state switching (CISSS) and is commonly used to induce spin state

changes of nickel(II) complexes.[14] There are no reports, to our knowledge, of CISSS in the solid state as it is more operative in the solution phase. New complexes form as the labile ligand dissociates, leaving an open coordination site or are replaced with the solvent or counter anions. This can occur immediately or upon a temperature change. It is often challenging to determine if the latter is operative due to its similarity to classical thermal dependent SCO. Identification between the two events can be achieved through several solution based analytical techniques, such as ^{1}H NMR and UV-Vis.

1.4 Outline of Chapters

The ability to predictably design a ligand that will promote a complex to undergo a spin switching event near room temperature is the goal of many studies. Few have reported the ability to tune the thermal SCO event of a complex by addition of electron donating or withdrawing group to the coordinated ligand.[18–20] Unfortunately, these studies focus on a particular family of complexes and do not show the same results when applied to other iron(II) systems.

To ensure a spin switching event would occur, we designed a ligand to promote a switching event when the resulting complex is subjected to several chemical influences. To induce CISSS in the presence of various solvents, the ligand was synthesized to contain only four nitrogen donor atoms. This allows the other two remaining coordination sites open for coordination of the counter anions and/or solvent molecules. Three alkyne functional groups were then affixed to support post synthetic modification reactions. The synthesis of the resulting iron(II) complex is described in Chapter 3 and the characterization in various solvents is summarized in Chapter 4. Additionally, Chapter 2 provides a detailed standard operating procedure for measuring solution samples on the MPMS instrument.

The alkyne groups of the iron(II) complex support various post-synthetic modification reactions. In Chapter 5, the conditions for the azide-alkyne cycloaddition post-synthetic reaction are described in detail. This reaction was chosen as the resulting triazole coordinates to the iron(II) center promoting a first coordination environment change, as well as providing the necessary ligand field to promote thermal SCO. The resulting iron(II) triazole complexes are characterized in the solid state (Chapter 6) and in solution (Chapter 7).

Chapter 8 summarizes the investigations into how first coordination modifications affect the magnetic properties of iron(II) complexes. The outlook and future directions of this work is also discussed.

References

(1) Olguín, J.; Brooker, S. Spin Crossover Active Iron(II) Complexes of Selected Pyrazole-Pyridine/Pyrazine Ligands. *Coordination Chemistry Reviews*. Elsevier January 1, 2011, pp 203–240.

(2) Gütlich, P.; Goodwin, H. A. Spin Crossover-An Overall Perspective. *Top. Curr. Chem.* **2004**, *233*, 1–47.

(3) Brooker, S. Spin Crossover with Thermal Hysteresis: Practicalities and Lessons Learnt. *Chem. Soc. Rev.* **2015**, *44* (10), 2880–2892.

(4) Halcrow, M. A. Structure:Function Relationships in Molecular Spin-Crossover Complexes. *Chem. Soc. Rev.* **2011**, *40* (7), 4119–4142.

(5) Muller, R. N.; Elst, L. Vander; Laurent, S. Spin Transition Molecular Materials: Intelligent Contrast Agents for Magnetic Resonance Imaging. *J. Am. Chem. Soc.* **2003**, *125* (27), 8405–8407.

(6) Matsuda, M.; Isozaki, H.; Tajima, H. Electroluminescence Quenching Caused by a Spin-Crossover Transition. *Chem. Lett.* **2008**, *37* (3), 374–375.

(7) Matsuda, M.; Isozaki, H.; Tajima, H. Reproducible On-off Switching of the Light Emission from the Electroluminescent Device Containing a Spin Crossover Complex. *Thin Solid Films* **2008**, *517* (4), 1465–1467.

(8) Kahn, O.; Martinez, C. J. Spin-Transition Polymers: From Molecular Materials toward Memory Devices. *Science (80-.).* **1998**, *279* (5347), 44–48.

(9) Jonas, K.; Jean-Paul, A.; Renée, C.; Epiphane, C.; Olivier, K.; Haasnoot, J. G.; Françoise, G.; Charlotte, J.; Bousseksou, A.; Jorge, L.; et al. Spin Transitions and Thermal Hysteresis in the Molecular-Based Materials [Fe(Htrz)2(Trz)](BF4) and [Fe(Htrz)3](BF4)2·H2O (Htrz = 1,2,4-4H-Triazole; Trz = 1,2,4-Triazolato). *Chem. Mater.* **1994**, *6* (8), 1404–1412.

(10) Kahn, O.; Kröber, J.; Jay, C. Spin Transition Molecular Materials for Displays and Data Recording. *Adv. Mater.* **1992**, *4* (11), 718–728.

(11) Létard, J.-F.; Guionneau, P.; Goux-Capes, L. Towards Spin Crossover Applications. In *Spin Crossover in Transition Metal Compounds III*; 2006; Vol. 235, pp 221–249.

(12) Jeon, I.-R.; Park, J. G.; Haney, C. R.; Harris, T. D. Spin Crossover Iron(Ii) Complexes as PARACEST MRI Thermometers. *Chem. Sci.* **2014**, *5* (6), 2461–2465.

(13) Ni, Z.; Shores, M. P. Magnetic Observation of Anion Binding in Iron Coordination Complexes: Toward Spin-Switching Chemosensors. *J. Am. Chem. Soc.* **2009**, *131* (1), 32–33.

(14) Khusniyarov, M. M. How to Switch Spin-Crossover Metal Complexes at Constant Room Temperature. *Chem. - A Eur. J.* **2016**, *22* (43), 15178–15191.

(15) Hasserodt, J.; Kolanowski, J. L.; Touti, F. Magnetogenesis in Water Induced by a Chemical Analyte. *Angew. Chemie Int. Ed.* **2014**, *53* (1), 60–73.

(16) Rodríguez-Jiménez, S.; Yang, M.; Stewart, I.; Garden, A. L.; Brooker, S. A Simple Method of Predicting Spin State in Solution. *J. Am. Chem. Soc.* **2017**, *139* (50), 18392–18396.

(17) Singh, S.; Brooker, S. Extension of Azine-Triazole Synthesis to Azole-Triazoles Reduces Ligand Field, Leading to Spin Crossover in Tris-L Fe(II). *Inorg. Chem.* **2020**, *59* (2), 1265–1273.

(18) Kershaw Cook, L. J.; Kulmaczewski, R.; Mohammed, R.; Dudley, S.; Barrett, S. A.; Little, M. A.; Deeth, R. J.; Halcrow, M. A. A Unified Treatment of the Relationship Between Ligand Substituents and Spin State in a Family of Iron(II) Complexes. *Angew. Chemie* **2016**, *55* (13), 4327–4331.

(19) Lin, H.-J.; Siretanu, D.; Dickie, D. A.; Subedi, D.; Scepaniak, J. J.; Mitcov, D.; Clérac, R.; Smith, J. M. Steric and Electronic Control of the Spin State in Three-Fold Symmetric, Four-Coordinate Iron(II) Complexes. *J. Am. Chem. Soc.* **2014**, *136* (38), 13326–13332.

(20) Prat, I.; Company, A.; Corona, T.; Parella, T.; Ribas, X.; Costas, M. Assessing the Impact of Electronic and Steric Tuning of the Ligand in the Spin State and Catalytic Oxidation Ability of the FeII(Pytacn) Family of Complexes. *Inorg. Chem.* **2013**, *52* (16), 9229–9244.

(21) Nakano, K.; Suemura, N.; Yoneda, K.; Kawata, S.; Kaizaki, S. Substituent Effect of the Coordinated Pyridine in a Series of Pyrazolato Bridged Dinuclear Diiron(II) Complexes on the Spin-Crossover Behavior. *Dalt. Trans.* **2005**, No. 4, 740–743.

(22) Hogue, R. W.; Feltham, H. L. C.; Miller, R. G.; Brooker, S. Spin Crossover in Dinuclear N4S2 Iron(II) Thioether-Triazole Complexes: Access to [HS-HS], [HS-LS], and [LS-LS] States. *Inorg. Chem.* **2016**, *55* (9), 4152–4165.

(23) Pan, Y.; Meng, Y. S.; Liu, Q.; Gao, W. Q.; Liu, C. H.; Liu, T.; Zhu, Y. Y. Construction of SCO-Active Fe(II) Mononuclear Complexes from the Thio-Pybox Ligand. *Inorg. Chem.* **2020**, *59* (11), 7398–7407.

(24) Capel Berdiell, I.; Kulmaczewski, R.; Halcrow, M. A. Iron(II) Complexes of 2,4-Dipyrazolyl-1,3,5-Triazine Derivatives - The Influence of Ligand Geometry on Metal Ion Spin State. *Inorg. Chem.* **2017**, *56* (15), 8817–8828.

(25) Sorai, M.; Ensling, J.; Hasselbach, K. M.; Gütlich, P. Mössbauer Effect Study on Low-Spin 1A1 ⇌ High Spin 5T2 Transition in [Fe(2-Pic)3]Cl2. II. Influence of Non-Coordinating Solvent Molecule in [Fe(2-Pic)3] Cl2 · X1 X = C2H5OH, CH3OH, H2O and 2H2O. *Chem. Phys.* **1977**, *20* (2), 197–208.

(26) Lemercier, G.; Bréfuel, N.; Shova, S.; Wolny, J. A.; Dahan, F.; Verelst, M.; Paulsen, H.;

Trautwein, A. X.; Tuchagues, J. P. A Range of Spin-Crossover Temperature T1/2 > 300 K Results from out-of-Sphere Anion Exchange in a Series of Ferrous Materials Based on the 4-(4-Imidazolylmethyl)-2-(2-Imidazolylmethyl)Imidazole (Trim) Ligand, [Fe(Trim)2]X2 (X = F, Cl, Br, I): Comparison O. *Chem. - A Eur. J.* **2006**, *12* (28), 7421–7432.

(27) Han, W. K.; Qin, L. F.; Pang, C. Y.; Cheng, C. K.; Zhu, W.; Li, Z. H.; Li, Z.; Ren, X.; Gu, Z. G. Polymorphism of a Chiral Iron(II) Complex: Spin-Crossover and Ferroelectric Properties. *Dalt. Trans.* **2017**, *46* (25), 8004–8008.

(28) Weber, B.; Walker, F. A. Solution NMR Studies of Iron(II) Spin-Crossover Complexes. *Inorg. Chem.* **2007**, *46* (16), 6794–6803.

(29) Rodríguez-Jiménez, S.; Barltrop, A. S.; White, N. G.; Feltham, H. L. C.; Brooker, S. Solvent Polarity Predictably Tunes Spin Crossover T1/2 in Isomeric Iron(II) Pyrimidine Triazoles. *Inorg. Chem.* **2018**, *57* (11), 6266–6282.

(30) Phonsri, W.; Macedo, D. S.; Vignesh, K. R.; Rajaraman, G.; Davies, C. G.; Jameson, G. N. L.; Moubaraki, B.; Ward, J. S.; Kruger, P. E.; Chastanet, G.; et al. Halogen Substitution Effects on N2O Schiff Base Ligands in Unprecedented Abrupt FeII Spin Crossover Complexes. *Chem. - A Eur. J.* **2017**, *23* (29), 7052–7065.

(31) Barrett, S. A.; Kilner, C. A.; Halcrow, M. A. Spin-Crossover in [Fe(3-Bpp)2][BF4]2 in Different Solvents - A Dramatic Stabilisation of the Low-Spin State in Water. *Dalt. Trans.* **2011**, *40* (45), 12021–12024.

(32) Kershaw Cook, L. J.; Mohammed, R.; Sherborne, G.; Roberts, T. D.; Alvarez, S.; Halcrow, M. A. Spin State Behavior of Iron(II)/Dipyrazolylpyridine Complexes. New Insights from Crystallographic and Solution Measurements. *Coord. Chem. Rev.* **2015**, *289–290* (1), 2–12.

(33) Strauß, B.; Gutmann, V.; Linert, W. Spin-Crossover Complexes in Solution, II Solvent Effects on the High Spin-Low Spin-Equilibrium of [Fe(Bzimpy)2](ClO4)2. *Monatshefte für Chemie Chem. Mon.* **1993**, *124* (5), 515–522.

(34) Milek, M.; Heinemann, F. W.; Khusniyarov, M. M. Spin Crossover Meets Diarylethenes: Efficient Photoswitching of Magnetic Properties in Solution at Room Temperature. *Inorg. Chem.* **2013**, *52* (19), 11585–11592.

(35) Mörtel, M.; Witt, A.; Heinemann, F. W.; Bochmann, S.; Bachmann, J.; Khusniyarov, M. M. Synthesis, Characterization, and Properties of Iron(II) Spin-Crossover Molecular Photoswitches Functioning at Room Temperature. *Inorg. Chem.* **2017**, *56* (21), 13174–13186.

(36) Luo, Y. H.; Nihei, M.; Wen, G. J.; Sun, B. W.; Oshio, H. Ambient-Temperature Spin-State Switching Achieved by Protonation of the Amino Group in [Fe(H2Bpz2)2(Bipy-NH2)]. *Inorg. Chem.* **2016**, *55* (16), 8147–8152.

Chapter 2: Beginner's Guide to Solution Magnetic Measurements with a MPMS Instrument

2.1 Introduction

Magnetic materials can be used in various solid state or solution phase applications. Therefore, it is vital for researchers to collect detailed magnetic susceptibility in both states. The methods and instrumentation to determine the magnetic susceptibility of complexes have been developed and improved over time. In the late 1880s, Louis-Georges Gouy derived equations with which scientists could calculate the magnetic susceptibility of solid or liquid samples using an analytical balance and a magnet; this setup was later named the Gouy balance.[1] Unfortunately, air sensitive samples were difficult to measure due to the way samples were suspended. Over the following years, scientists developed similar instruments that allowed for easier measurement of air free samples with overall increased sensitivity and accuracy.[2] In the 1950s nuclear magnetic resonance (NMR) instrumentation became available for researchers. Shortly after, Dennis F. Evans published his namesake method that used the NMR chemical shifts of an internal standard to determine the solution phase magnetic susceptibility.[3] Thirty years later, Quantum Design, Inc. commercialized the Magnetic Property Measurement System (MPMS) that provided automated temperature, magnetic field, and measurement control.[4] As the MPMS became more readily available, it replaced instruments like the Guoy balance, and is now one of the most common ways to measure the temperature dependence of magnetic susceptibility in the solid state. For solution magnetic susceptibility, Evans' method is currently still the most used method. Over the years other techniques have been used for susceptibility measurements, like XRD, DSC, UV-Vis, Mössbauer spectroscopy, but none have surpassed the popularity of the MPMS and Evans' method NMR.[5]

For solid state magnetic data, the MPMS is favored due to its reliable and precise data collection. Few researchers use this instrument to collect solution phase data, relying on the variable temperature Evans' method NMR technique. However, the NMR method relies on the use of an internal standard to calculate the magnetic susceptibility and this additional species can enable interaction and speciation issues that can lead to changes in the magnetic susceptibility. As well, the equation used for these susceptibility calculations requires knowledge of the exact concentration at all temperatures measured. Due to this, the density changes in a solvent need to be known and corrected for at each temperature to provide accurate magnetic values. If the change in solvent density is not corrected, the normal 5-10 % error from Evans' method can increase to 20-25 %.[6,7] The temperature range that can be used is also limited to the NMR instrument and the freezing point of the deuterated solvent. Due to this, temperature windows are very small in some solvents. All these complications can be avoided when a MPMS is used to collect solution magnetic data. Due to the way the MPMS instrument collects data no internal standard is needed, any solvent can be used, and temperatures below the freezing point can be measured. Additionally, collected data does not need to be corrected for solvent density changes and there are minimal margins of error compared to Evans' method. Unfortunately, the MPMS requires ~15 times larger sample concentrations than Evans' method to provide enough signal for accurate data collection. While each technique has its advantages for collecting magnetic susceptibility measurement, using an MPMS offers more freedom in data collection than Evans' method NMR.

This chapter will provide details into how to use a MPMS to collect solution magnetic data. The following sections will explain two methods of how to prepare samples depending on which solvent the measurements are in and how to collect solution data using the MPMS. Finally, a brief example of how to analyze and compare MPMS and Evans' method data will be described.

2.2 Division of Labor

The types of sample holders that can be used in the MPMS were determined with help from Brian Newell and Daniel Bates. Quartz tubes were sealed with help from Cassidy Jackson and Roxanna Martinez. All other work in this chapter was carried out by Brooke N. Livesay.

2.3 Magnetic Properties Measurement System (MPMS) Background

The magnetic properties measurement system (MPMS) by Quantum Design was introduced in 1982.[4] The MPMS is set apart from Quantum Design's original instrument, the physical properties measurement system (PPMS), by the inclusion of a superconducting quantum interference device (SQUID) that provides the instrument with extreme sensitivity (Figure 2.3.1). However, the SQUID doesn't directly measure the magnetic susceptibility of the sample.

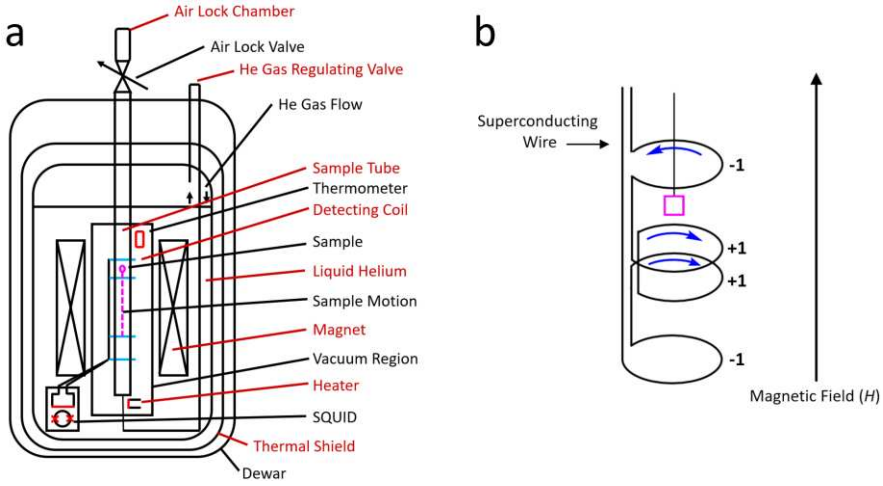

Figure 2.3.1. Diagram of a magnetic properties measurement system (MPMS) with the components labeled[8] (a) and a diagram of the sample moving through the detection coils[9] (b).

During a measurement, the sample moves through the superconducting detection coils, that are located on the outside of the sample chamber (Figure 2.3.1b). The detection coils are connected to the SQUID through superconducting wires, forming a closed superconducting loop.[9] The magnetic

moment of the sample induces changes in the electric current in the detection coils, which produces similar variation in the output voltage in the SQUID.[9] These changes in voltage are proportional to the sample's magnetic susceptibility.

Samples are mounted on a rigid sample rod that is inserted into the instrument through a double seal, allowing the sample rod to move up and down. During measurements, the sample is moved through the detection coils and is stopped at several positions to record multiple readings of the SQUID voltage.[9] These readings are then averaged to increase the signal to noise ratio. The MPMS has two different standard sample transport measurement techniques, DC and VSM. For the DC technique, the sample starts at the lowest point of the designated scan length, moves upward through the detection coils, and then returns to the lowest point at the end of the measurement. For this technique it is required to have at least 32 point scans (how many times the sample stops in the detection coils) to have better accuracy.[10] With the VSM technique, the sample is vibrated near the detection coils and provides increased sensitivity.[11] However, for liquid samples, the VSM technique is not recommended as it can lead to sloshing of the liquid during the measurement, resulting in less accurate results.

2.4 Materials

All manipulations should be performed under inert conditions with a nitrogen-filled glovebox or Schlenk line to avoid any oxygen contamination that can be observed in the final magnetic data. The quartz tube used should have a 3 mm inner diameter, 5 mm outer diameter, and a shelf 3 cm from the bottom and can be purchased from Galaxy Glass. Additional supplies that are required include a 4 inch or longer 21G needle affixed to a 1 mL syringe, the desired dry degassed solvent, a push pin, one 7 ¾ inch polypropylene drinking straw, a stopcock, electrical tape, parafilm,

hydrogen torch, scotch tape, and a 2-inch piece of tubing with a ½-inch outer diameter, ¼-inch inner diameter, and ⅛-inch wall.

2.5 Sample Preparation

Before preforming any solution magnetic measurements, several conditions must be met for sample preparation. To avoid inaccurate measurements when measuring a sample, Quantum Design recommends that when in the appropriate sample holder, the sample should be 4 mm in height.[12] This prevents any distortions in the MPMS signal by keeping the susceptibility consistent over the length of the sample. To ensure the needed 4 mm sample length given the constraints of the sample holders, the volume of the sample should be no larger than 0.05 mL. With this volume constraint, high concentrations are needed (ideally, between 0.05 M and 0.08 M) to ensure enough magnetic material is present in the sample to provide a signal between the recommended 10^{-4} and 10^{-3} emu range (Table 2.5.1). Therefore, solvent choice should be determined by whether these concentrations can be achieved with the desired complex. One advantage to using an MPMS over Evans' method is that the magnetic moment of the sample can be collected below the freezing point, therefore a solvent should be chosen to prevent precipitation from occurring at low temperatures. Upon precipitation, the MPMS instrument measures both the solid state and solution phase magnetic susceptibilities. Environmental factors can have a significant impact on the magnetic properties of a complex leading to dramatically different solid state and solution phase magnetic data.[6,13] To ensure any interesting results are related only to the properties of the sample, a solvent should be chosen where the desired complex is still soluble at low temperatures.

Table 2.5.1. Calculated concentration ranges for solution magnetometry samples with various total spin values that will provide a signal between the recommended 10^{-4} and 10^{-3} emu range at 25 K.

Total Spin (*S*)	Concentration Range (M)
0	--
0.5	0.20 – 1.35
1	0.10 – 0.51
1.5	0.07 – 0.27
2	0.05 – 0.17
2.5	0.04 – 0.12
3	0.03 – 0.08

2.5.1 Sample Preparation with Quartz Tubes

Sample preparation should be carried out under inert conditions to avoid any oxygen contamination. While only 0.05 mL of sample is needed for the measurement, a 0.5 mL or larger quantity should be prepared in a vial, which allows for easier transfer to the sample holder. To prepare the solution, a shell vial is pre-weighed on an analytical balance. Then the desired compound is added, and the vial is weighed again to obtain the mass of the compound. The appropriate volume of the choice solvent is added to the vial using a micropipetter to obtain a 0.05 M to 0.08 M sample solution. After all the compound has dissolved, the solution is then loaded into the sample holder, with the process described below. The use of heat to help the compound dissolve should be avoided as the solvent may evaporate and lead to a change in the sample concentration.

A quartz glass tube is pumped into the glovebox, along with a section of tubing and a stopcock attachment (Figure 2.5.1a). Electrical tape is wrapped on the outside of the top of the quartz tube so that the section of tubing can snuggly fit over the quartz tube. With the 1 mL plastic syringe fitted with a long metal needle, 0.05 mL of the sample solution is loaded into the long part of the quartz tube. The plastic tubing is then placed on the end fitted with electrical tape. The stopcock adaptor is attached to the other side of the tubing and sealed (Figure 2.5.1b). The whole setup is

then carefully removed from the glovebox and attached to a Schleck line in a hood with an available hydrogen torch. The tubing used to attach the quartz tube to the Schleck line is placed under vacuum and the stopcock for the quartz sample remains closed. The quartz tube is placed into a small liquid nitrogen dewar to freeze the sample. Once fully frozen, the stopcock is opened, exposing the headspace of the quartz tube to vacuum. With the help of a trained person, the quartz tube is sealed with the hydrogen torch. The total length of the quartz tube needs to be between 11 mm and 13 mm after it is sealed to ensure the sample is at the appropriate height for the MPMS. After the tube is sealed, a piece of straw is placed on the top of the quartz tube and secured with scotch tape. Four pin holes are poked evenly around the straw right above the quartz tube and tape (Figure 2.5.1d).

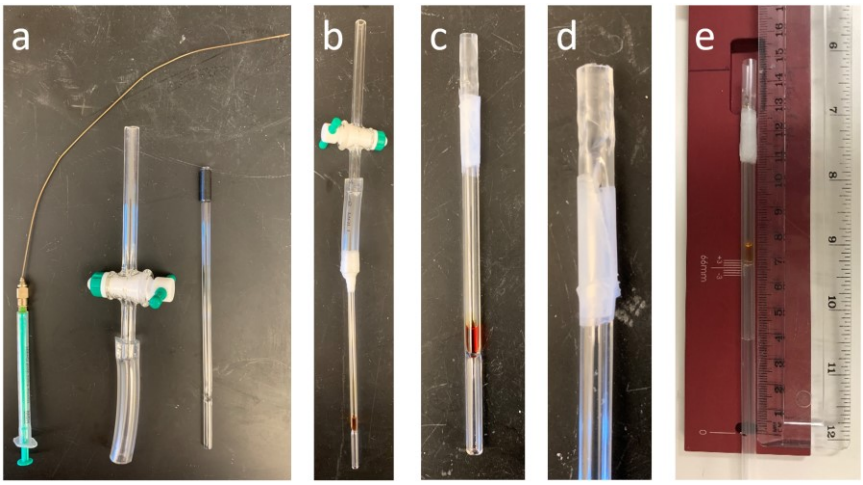

Figure 2.5.1. Supplies needed for quartz tube method (a), quartz setup before sealing tube (b), final quartz tube sample attached to straw (c), close up of straw with pin holes in final set up (d), addition of a straw sleeve to extend the end of the sample for easier centering (e).

After ensuring the quartz tube is securely taped to the straw, the sample is then ready to be loaded into the MPMS instrument. Once placed on the metal sample ruler and the top of the sample is aligned with the top line, the sample solvent should be close to the 66 mm mark. The bottom of

the quartz tube will not reach the 0 mm mark and may cause some centering issues when placed into the instrument. Minimal centering problems occur when an extra straw is placed over the quartz tube and trimmed so the overall sample reaches the 0 mm mark (Figure 2.5.1e)

2.6 Collecting Data

Samples are loaded into the MPMS in the same manner as a solid-state sample. With solution samples, a blank of pure solvent in the same type of sample holder needs to be collected with the exact same sequence as the desired solution sample. The solvent blank data only needs to be collected once and can be used for future samples if those sample are run with the same sequence. The solvent blank can be measured before or after the sample, although it is best to run the sample first to avoid collecting any unnecessary or insufficient data on the solvent blank. The same MPMS sequences used for solid state samples can be used for solution samples. The only parameter that might need to be changed is the temperature range. Solution samples can be brought down to 2 K, as long as the sample holder will not crack or break as the sample freezes. This can be checked before loading into the MPMS instrument by placing the sealed sample holder into a dewar filled with liquid nitrogen and freezing/thawing the sample multiple times. If the holder does not crack or break upon freezing the sample at least three times, then it will not likely break during MPMS measurements. As well, samples can be measured above room temperature as long as the sample holder will not crack or shatter. The polypropylene straws used to connect the solution sample to the MPMS sample rod have been measured up to 360 K for solid state samples with no problems. If these measurements need to be performed, a quartz tube sample holder should be used only after the integrity of the sealed quartz tube has been tested at these higher temperatures. Note that the integrity of the scotch tape, used to secure the quartz tube to the straw, above 360 K has not been

tested at the time of writing this chapter, and this should be investigated before high-temperature measurements are performed.

When loading the sample, it is best to compare the solvent placement with a previous sample to ensure the solution sample is as close to center as possible. This will help determine which signal in the centering scan is the sample signal. Unlike a solid-state sample, multiple diamagnetic peaks can be observed for solution samples in the large centering window that are attributed to the sample holder and tape. This will be more prevalent in the sample blank, as the solution sample will have a larger signal than what will be observed for the sample holder and tape. To ensure that the correct signal is used to center the blank, a previous paramagnetic sample can be used. The paramagnetic sample is loaded into the MPMS and a centering scan is performed. The location of the sample signal is recorded, and the sample is removed from the instrument. The paramagnetic sample holder is placed next to the blank sample matching up the samples, if needed, the blank sample straw should be trimmed so that the samples are even when placed on the rod (Figure 2.6.1). The blank solvent is loaded into the instrument and a centering scan is performed. The closest peak to where the paramagnetic sample was, is the solvent blank signal. Knowing the approximate location of solvent blank centering signal will be helpful if there are any future centering challenges when collecting data.

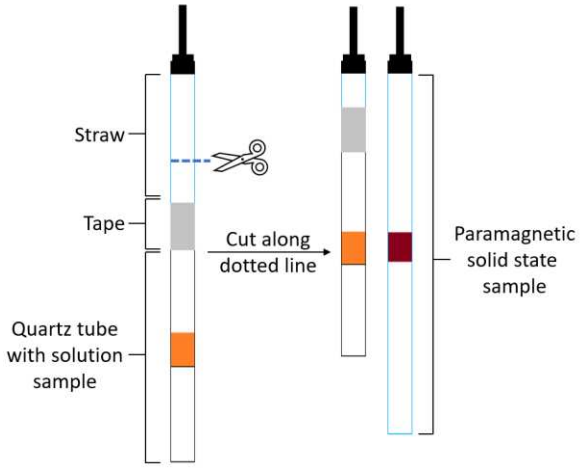

Figure 2.6.1. How to trim solution sample straw to ensure sample is at correct position before loading into the MPMS instrument.

After centering, few problems may arise during sample collection. Frequent monitoring of the data collection should help the user quickly identify any issues. The main problem that may occur is the loss of the sample centering. This is most common when the sample has a low magnetic moment, for example the blank sample holder or blank solvent. To help alleviate some of the problem, remove all automatic center commands in the data sequence. Removing this command may stop the problem in the solution sample, but the centering issue may still occur in the solvent blank due to its small magnetic moment. This issue can be recognized during data collecting as a dramatic increase or decrease in the raw magnetic data. Sometimes, this increase/decrease will only be observed at one temperature and the next data point returns to normal, this will not be an issue when working up the data, but it can be recollected if desired. If the data continues at the same magnitude as the increase/decrease point, then the sample centering needs to be examined. The data sequence should be stopped, and a centering scan should be performed. After the sample is re-centered, the data collection should be re-started three data points before the first increase/decrease of the centering issue. If the three data points are about the same as they were the first time, the centering issue has been corrected. If not, go further back in the sequence until

the data points overlay. Sometimes this unfortunately means restarting the susceptibility part of the sequence all over again.

2.7 Processing the Data

After the data collection on both the sample and blank solvent is complete, processing the data is similar to that of a solid-state sample. If there were any centering issues where data was collected multiple times, remove the problematic raw data before working up the remaining data. Besides the raw data for both the solution sample and the solvent blank, the only other information needed is the actual amount of compound in the solvent holder used and the compound's diamagnetic correction.

When processing the MPMS data it is important to know the diamagnetic correction of both the sample holder and solvent used. These corrections are the magnetic susceptibility of the solvent blank sample. The magnetic moment obtained from the solvent blank are used in place of the bucket/bag correction for solid state samples. If no solvent blank is used when working up solution samples, the resulting magnetic susceptibility will have a downwards slant (Figure 2.7.1). This slant might also be observed when using solvent blanks that were collected in different sample holders, i.e. straw vs quartz tubes. Ideally, the solvent blank will have the same magnetic moment at all temperatures in a magnetic susceptibility measurement. In some solvents the magnetic moment varies slightly around room temperature. Therefore, an average of the solvent blank's long moment between the high and low temperatures can be used for all the magnetic susceptibility solvent correction values (Figure 2.7.1).

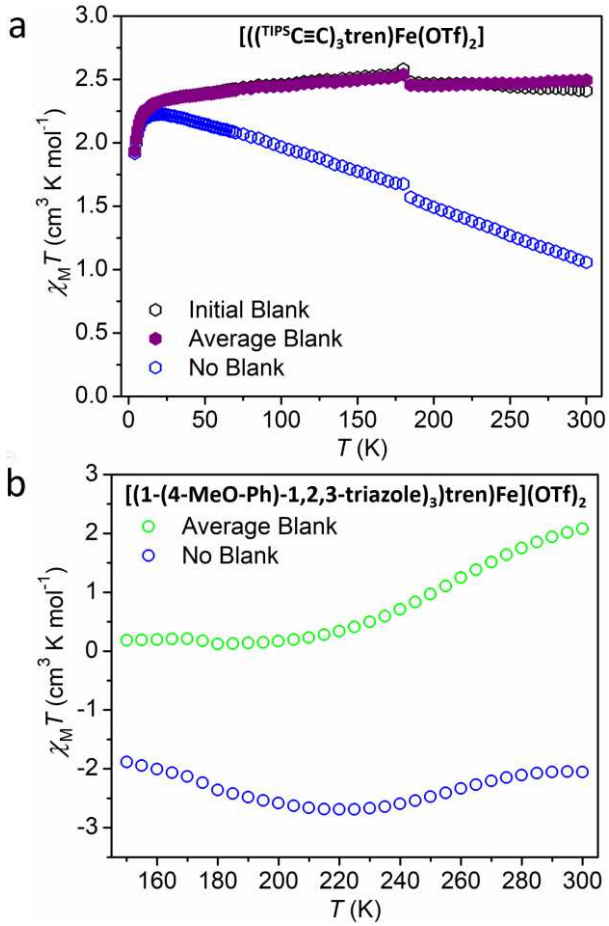

Figure 2.7.1. Variable temperature magnetic susceptibility of [((^{TIPS}C≡C)$_3$tren)Fe(OTf)$_2$] (a) and [(1-(4-MeO-Ph)-1,2,3-triazole)$_3$)tren)Fe](OTf)$_2$ (b) in CH_3OH corrected with no blank (blue open hexagons (a) and circles (b)), initial blank (open black hexagons (a)), and average blank (filled purple hexagons (a) and open green circles (b)).

2.8 MPMS Analysis

The magnetic data should look relatively similar to a typical solid-state measurement after including the correct solvent blanks. Data analyses will be described briefly for [((^{TIPS}C≡C)$_3$tren)Fe(OTf)$_2$] and [(1-(4-MeO-Ph)-1,2,3-triazole)$_3$)tren)Fe](OTf)$_2$, both collected in CH_3OH (Figure 2.7.1 and 2.10.1); a more in-depth analysis of the [((^{TIPS}C≡C)$_3$tren)Fe(OTf)$_2$] data can be found in Chapter 4 . The magnetic susceptibility for both compounds was measured between 2 K and 300 K and the average CH_3OH blank was used. At 300 K, the $\chi_M T$ value of [((^{TIPS}C≡C)$_3$tren)Fe(OTf)$_2$] is 2.49 cm^3 K mol^{-1}, consistent with the presence of a high spin iron(II)

complex. As the temperature decreases a small discontinuity is observed right before the freezing point of CH_3OH. This discontinuity can be observed in high spin complexes but will be obscured if a spin crossover event occurs around the freezing point of the solvent. This discontinuity is observed when the sample is warmed but not when it is cooled. A potential cause for this may be due to the sample not thawing uniformly, thus parts of the sample are liquid, allowing the portions that are frozen to torque. Below the freezing point, the complex is frozen in the solvent matrix, resulting in solid-state like sample with no random motion. Below the freezing point, the $\chi_M T$ value of $[((^{TIPS}C{\equiv}C)_3tren)Fe(OTf)_2]$ decreases gradually but steadily until it reaches 2.24 cm^3 K mol^{-1} at 10 K. With continued cooling a pronounced downturn is observed around 4 K.

At 300 K, the $\chi_M T$ value of [(1-(4-MeO-Ph)-1,2,3-triazole)$_3$)tren)Fe](OTf)$_2$ is 2.07 cm^3 K mol^{-1}, lower than the expected value for a high spin iron(II) complex (S = 2, $\chi_M T$ = 3). As the temperature decreases a spin switching event occurs and the $\chi_M T$ value decreases dramatically until it reaches 0.15 cm^3 K mol^{-1} at 200 K. Upon further cooling a small discontinuity in the data is observed around the freezing point of CH_3OH. Below the freezing point the $\chi_M T$ value stays consistently around 0.13 cm^3 K mol^{-1}, consistent with a low spin iron(II) complex.

2.9 Variable Temperature Evans' Method

2.9.1 Temperature Limitations

Unlike the MPMS, the temperature range used in the Evans' method NMR technique is limited to the temperature range of the NMR probe and of solvent used for the experiment. At CSU, the 500 MHz NMR instrument is commonly used for variable temperature NMR experiments. This instrument has several probes, with each probe having its own temperature window. Additionally, the temperature range that can be used will depend on the sample solvent. It is suggested that

temperature range should be 10 °C above the freezing point of the solvent and 10 °C below the boiling point of the solvent, to ensure the NMR tube used will not break and damage the NMR instrument.

2.9.2 Solvent Preparation

Evans' method requires a deuterated solvent and an internal standard. The internal standard should be diamagnetic, have a singlet ^{1}H NMR signal, not overlap with any ^{1}H NMR signals of the sample complex, and should not react with the sample complex. The most common internal standard used is tetramethylsilane (TMS) as its ^{1}H NMR signal, 0 ppm, is relatively inert and located far away from the signals observed for most metal complexes.

In the presence of a paramagnetic complex, the internal standard ^{1}H NMR signal moves due to a pseudocontact shift. The difference between the unaffected and the new signal of the internal standard is used to calculate the magnetic susceptibility of a complex. To accurately measure the difference between the two internal standard signals, a capillary containing pure deuterated solvent and the internal standard should be added to the NMR sample. The volume percentage of internal standard in the capillary and sample solution should be consistent. Therefore, to ensure enough internal standard is present in the capillary to provide sufficient signal in the final ^{1}H NMR spectra, between 0.2 % and 2 % by volume of internal standard in the deuterated solvent should provide a good signal in the final ^{1}H NMR spectra without suppressing the solvent and/or complex signals.

2.9.3 Sample Preparation

The magnitude of the internal standard shift depends on the magnetic susceptibility and the concentration of the sample used. The larger the two, the larger the internal standard shift will be. Additionally, larger concentrations (~0.08 M and above) can result in broad sample signals that are hard to distinguish and/or characterize. These concentrations can also prevent the instrument

from measuring the samples as it will have a hard time locking on the solvent and shimming. Samples set at concentrations around 5 mM provide acceptable intensities of the complex and do not cause any locking or shimming issues.

The NMR instrument only heats/cools the part of the NMR tube that sits within the magnet. This section is typically the size of the window that is used to center the sample (Figure 2.9.1). To ensure that the whole sample used for variable temperature Evans' method is heated/cooled equally, the sample solution volume should be around 0.3 mL. While only 0.3 mL of sample is needed, preparing a slightly larger quantity will allow for easier transfer to the NMR tube. The desired complex is added to a pre-weighed shell vial and weighed on an analytical balance. Then the desired deuterated solvent spiked with internal standard is added with a micropipette to obtain the desired sample concentration. The solution sample is then transferred to an NMR tube and a capillary containing pure deuterated solvent spiked with internal standard is added. Once the NMR tube is capped the sample is ready for variable temperature Evans' method measurements; if needed, J-young tubes or NMR tubes with parafilm wrapped around the top of the tube and cap can be used to ensure the sample stays air-free.

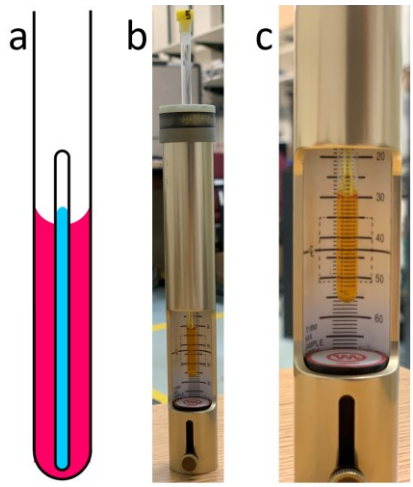

Figure 2.9.1 Diagram of Evans' Method sample where pink represents the NMR solvent, internal standard, and sample and the blue represents the NMR solvent with internal standard (A), NMR tube with Evans' Method sample (B), and close up of solvent level in the NMR tube compared to the centering window (C).

2.9.4 Data Processing and Analysis

After measuring the sample, the NMR spectra should be referenced to the deuterated solvent used. The chemical shifts of the two internal standard peaks are marked and recorded. The temperature, T, molarity, M, and the difference between the internal standard peaks in ppm, $\Delta\delta$, are used to calculate the magnetic susceptibility, $\chi_M T$, following equation 2.1. This equation is derived from Evans' original formula by converting to common units and combining the constants.[14]

$$\chi_M T = \frac{477\Delta\delta}{2\times10^6 M} \times T \qquad (2.1)$$

2.9.5 Potential Errors During Evans' Method Procedures and Analysis

The error for Evans' method can range from 5 – 25 % depending on how the sample is prepared, measured, and analysized.[6,7] To minimize any errors during sample preparation, care should be taken when weighing and dissolving the sample. Obtaining accurate weights using a analytical balance can prove difficult, especially for an air-sensitive compound, which increases the error of the measurement.[15] In addition, some low boiling solvents, i.e. CH_2Cl_2, may be difficult

to accurately measure the desired volume. For these solvents, it would be best to make the sample solution with the desired solvent and then weigh the sample solution and use the density of the solvent to determine the concentration of the resulting sample solution.

During sample measurement, error can come from changing the temperature of the sample. The NMR instrument only cools the portion of the sample that is sitting in the coils. To avoid any thermogradients throughout the sample, the amount of sample solvent should be located at approximately the same height as the centering window. When performing the measurement, the temperature of instrument and length of time during which the sample is equilibrated can lead to increased error. The temperature of the sample may not match the nominal setting for the NMR instrument. The temperature can be calibrated by using the NMR methanol thermometer.[16] This technique is useful for temperature between 180 K and 300 K. A 100% methanol NMR standard sample is loaded into the instrument and the temperature is decreased to the desired temperature and equilibrated for at least 15 minutes. After running a standard proton experiment, the differences in the two methanol proton signals can be related to the temperature of the sample by equation 2.2; where T is the calculated temperature and Δ is the shift difference in ppm between the CH_3 and OH signals.

$$T = -23.832\Delta^2 - 29.46\Delta + 403.0 \qquad (2.2)$$

This calibration should be done at several temperatures to get a calibration curve that can be used for future samples. In addition to performing the temperature calibration, a sample should be equilibrated at a temperature for a minimum of 15 minutes before the desired NMR experiment is performed. This will ensure that the sample is at the desired temperature and the spectrum shows the correct reference shifts for that temperature.

After all the desired spectra are collected, errors can occur from data analysis. As an insidious example, sometimes the internal standard can interact with the sample, resulting in unintended reference shift changes. To avoid this error, the reference signal chemical shift should be compared to the solvent signals from the sample and capillary: if the reference does not interact with the sample, the differences in the solvent signals should be approximately the same as the reference signals.

The addition of a solvent density and diamagnetic correction during analysis will help provide more accurate magnetic susceptibility values. The inclusions of these corrections during analysis were not mentioned in Evans' original paper and their inclusion has been debated in several communications.[3,14,17–19] Out of all of the references found in this dissertation, only 3% correct for solvent density as the temperature changes during their Evans' method studies. The density of a solvent is dependent on the temperature, and for most organic solvents, the density decreases as temperature decreases. This results in different sample concentrations at different temperatures. For accurate magnetic susceptibility and thermodynamic values from Evans' method, the exact concentration of the sample should be used during data analysis at each temperature. If not corrected, a solvent with a 10% density change over 75 K difference would result in about 20-25% error.[18] The solvent density correction involves finding the densities of the solvent used at each temperature and using equation 2.3:

$$M_T = M_0 \times \frac{\rho_T}{\rho_0} \tag{2.3}$$

where M_T is the concentration at the desired temperature, M_0 is the concentration at room temperature, ρ_T is the density at the desired temperature, and ρ_0 is the density at room temperature. The variable temperature density values can be found through various industrial chemical websites.

In recent years, the inclusion of a diamagnetic correction is more common, however only about 40% of the references used in this dissertation include a diamagnetic correction. In 1997, a paper published by Claude Piguet argued that accurate magnetic susceptibility values from Evans' method require diamagnetic corrections only for large molecules.[17] The paper considers large molecules as supramolecular assemblies and biomolecules, however there is no designation as to when a molecule is considered large enough to start including the diamagnetic correction.[17] On the other hand, there is a report that indicates the presence of excess diamagnetic species do not impart a significant effect on the magnetic susceptibility values, suggesting there is no need to include a diamagnetic correction.[20] The formula originally reported by Evans calculates the molar susceptibility, χ_M; therefore, if the paramagnetic susceptibility is desired, then the diamagnetic contribution should be subtracted during analysis. However, there is no definitive answer as to if the inclusion of this diamagnetic correction is needed to minimize error. This uncertainty and lack of inclusion of the diamagnetic and solvent correction may partially account for the large error for Evans' method NMR compared to other methods.

2.10 Comparison of MPMS and Evans' Method

The solution magnetic susceptibility obtained from the MPMS can be compared to the values obtained from variable temperature Evans' method NMR. Unfortunately, due to the limitations of variable temperature Evans' method, only susceptibility values collected at temperatures above the freezing point can be compared. Normally, the values obtained from Evans' method will be close to those obtained from solution MPMS measurements as is observed for [(1-(4-MeO-Ph)-1,2,3-triazole)$_3$)tren)Fe](OTf)$_2$ (Figure 2.10.1b).[21,22] However, differences can be observed with certain compounds. Due to the unique properties of [((^{TIPS}C≡C)$_3$tren)Fe(OTf)$_2$] in solution, see

Chapter 4, the magnetic susceptibility obtained from the two methods are not similar. The temperature dependence of the magnetic susceptibility of [((^{TIPS}C≡C)$_3$tren)Fe(OTf)$_2$] collected by Evans' method (CD_3OD) and solution MPMS (CH_3OH) are shown in Figure 2.10.1a. The magnetic susceptibility collected *via* Evans' method was measured between 298 K and 188 K. At 298 K, the $\chi_M T$ value is 3.01 cm^3 K mol^{-1}, indicative of a high spin iron(II) complex. As the temperature decreases, the magnetic susceptibility does not significantly change and reaches 2.98 cm^3 K mol^{-1} at 188 K. These values are larger than the ones collected at the same temperatures from the solution MPMS measurement. The difference in these values can be attributed to how [((^{TIPS}C≡C)$_3$tren)Fe(OTf)$_2$] behaves in the two different concentrations used for each method; samples for Evans' method are run at 0.005 M and for solution MPMS at 0.08 M (see Chapter 4 for more information). In samples without concentration dependent speciation, the MPMS and Evans' method susceptibilities should be similar but not exact due to the large error that can occur with Evans' method measurements (Figure 2.10.1b).

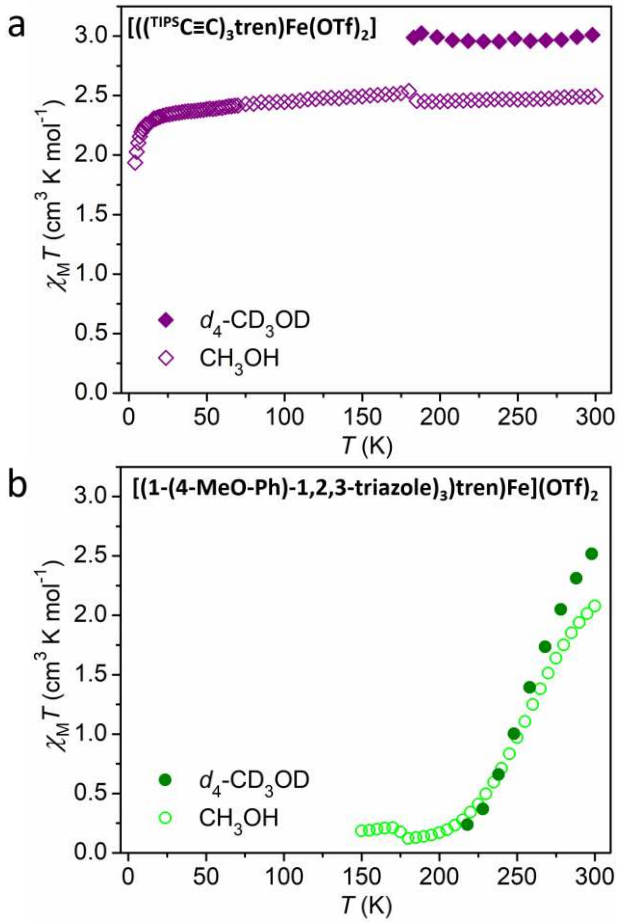

Figure 2.10.1. Comparison of magnetic susceptibility of [((^{TIPS}C≡C)$_3$tren)Fe(OTf)$_2$] (a) and [(1-(4-MeO-Ph)-1,2,3-triazole)$_3$)tren)Fe](OTf)$_2$ (b) collected by Evans' method in d$_3$-CD$_3$OD (closed hexagons (a) and circles (b)) and solution MPMS in CH$_3$OH (open hexagons (a) and circles (b)).

2.11 Conclusion

Magnetic complexes have the potential to be used in a variety of solid-state and solution-based applications. Understanding how these complexes behave under various conditions is vital for providing insight into how these can be designed for use in specific applications. Many researchers rely on the MPMS instrument for solid-state magnetic susceptibility measurements, and use Evans' method for solution measurements. While Evans' method has its advantages, the use of a MPMS instrument for solution phase magnetic data allows for more solvent options and data to be collected. Two sample methods, practical experimental details, and data analysis described here

provide researchers with the current practices to start using the MPMS instrument for their solution phase magnetic measurements.

References

(1) Mulay, L. N. Techniques for Measuring Magnetic Susceptibility. In *Physical Methods of Chemistry*; Weissberger, A., Rossiter, B. W., Eds.; Wiley: New York, NY, 1972; p 431.

(2) Evans, D. F. A New Type of Magnetic Balance. *J. Phys. E.* **1974**, *7* (4), 247–249.

(3) Evans, D. F. The Determination of the Paramagnetic Susceptibility of Substances in Solution by Nuclear Magnetic Resonance. *J. Chem. Soc.* **1959**, 2003–2005.

(4) Sager, R. E. Quantum Design-a Brief History of a Company Successful in Superconductivity. *IEEE/CSC ESAS Eur. Supercond. News Forum* **2010**, *11*.

(5) Gütlich, P.; Goodwin, H. A. Spin Crossover-An Overall Perspective. *Top. Curr. Chem.* **2004**, *233*, 1–47.

(6) Weber, B.; Walker, F. A. Solution NMR Studies of Iron(II) Spin-Crossover Complexes. *Inorg. Chem.* **2007**, *46* (16), 6794–6803.

(7) Ostfeld, D.; Cohen, I. A. A Cautionary Note on the Use of the Evans Method for Magnetic Measurements. *J. Chem. Educ.* **1972**, *49* (12), 829.

(8) Maguire-Boyle, S.; Barron, A. R. *Practical Guide to Using a Superconducting Quantum Interference Device*; Raja, P. M. V., Barron, A. R., Eds.; 2019.

(9) McElfresh, M. Fundamentals of Magnetism and Magnetic Measurements; Quantum Design, 1994.

(10) Measuring Large Moment Samples in the Magnetic Property Measurement System (MPMS).

(11) Product Description Magnetic Property Measurement System.

(12) Sample Mounting Considerations. Quantum Design November 1, 2000, pp 1–9.

(13) Rodríguez-Jiménez, S.; Barltrop, A. S.; White, N. G.; Feltham, H. L. C.; Brooker, S. Solvent Polarity Predictably Tunes Spin Crossover T1/2 in Isomeric Iron(II) Pyrimidine Triazoles. *Inorg. Chem.* **2018**, *57* (11), 6266–6282.

(14) Shores, M. P.; Klug, C. M.; Fiedler, S. R. Spin-State Switching in Solution. In *Spin-Crossover Materials: Properties and Applications*; Halcrow, M. A., Ed.; John Wiley & Sons Ltd: Oxford, UK, 2013; pp 281–301.

(15) Halcrow, M. A. *Spin-Crossover Materials*; HALCROW, M. A., Ed.; John Wiley & Sons Ltd: Oxford, UK, 2013.

(16) VT-Calibration Manual. *Bruker Instruments Inc.*

(17) Piguet, C. Paramagnetic Susceptibility by NMR: The "Solvent Correction" Removed for Large Paramagnetic Molecules. *J. Chem. Educ.* **1997**, *74* (7).

(18) Ostfeld, D.; Cohen, I. A. A Great Advantage of the Evans A Cautionary Note on the Use of

the Evans Method for Magnetic Measurements.

(19) Grant, D. H. Paramagnetic Susceptibility by NMR The "Solvent Correction" Reexamined. **1995**, *72*, 11.

(20) Ni, Z.; McDaniel, A. M.; Shores, M. P. Ambient Temperature Anion-Dependent Spin State Switching Observed in "Mostly Low Spin" Heteroleptic Iron(II) Diimine Complexes. *Chem. Sci.* **2010**, *1* (5), 615–621.

(21) Keisers, K.; Hüppe, H. M.; Iffland-Mühlhaus, L.; Hoffmann, A.; Göbel, C.; Apfel, U. P.; Weber, B.; Herres-Pawlis, S. Interplay of Spin Crossover and Coordination-Induced Spin State Switch for Iron Bis(Pyrazolyl)Methanes in Solution. *Inorg. Chem.* **2020**, *59* (20), 15343–15354.

(22) Schober, A.; Demeshko, S.; Meyer, F. Spin State Variations and Spin-Crossover in Diiron(II) Complexes of Bis(Pentadentate) Pyrazolate-Based Ligands. *Zeitschrift fur Anorg. und Allg. Chemie* **2018**, *644* (14), 719–728.

Chapter 3: Conditions and Challenges of the [((^{TIPS}C≡C)$_3$tren)Fe(OTf)$_2$] Synthesis

3.1 Introduction

The first synthesis of [((^{TIPS}C≡C)$_3$tren)Fe(OTf)$_2$] differs from the final and reported procedure, as described in Chapter 4. The initial synthesis, detailed below, was successful and reproducible for several months, but became problematic over time. The investigation into the reproducibility of this reaction is recorded here in hopes that it will be useful for future syntheses involving related compounds. The following chapter will discuss the synthetic issues that occurred and how the reaction procedure was modified to synthesize pure [((^{TIPS}C≡C)$_3$tren)Fe(OTf)$_2$].

3.2 Division of Labor

All work in this chapter was carried out by Brooke N Livesay.

3.3 Results and Discussion

3.3.1 Original [((^{TIPS}C≡C)$_3$tren)Fe(OTf)$_2$] synthesis

Initially, the starting aldehyde, 3-(triisopropylsilyl)propiolaldehyde (^{TIPS}C≡CCOH), prepared following a literature preparation[1], was isolated and condensed with tris(2-aminoethyl)amine (tren) under ambient air conditions. This preparation successfully produced the desired pale yellow (^{TIPS}C≡C)$_3$tren ligand. Under a dinitrogen atmosphere, a one to one mixture of (^{TIPS}C≡C)$_3$tren and iron(II) triflate, Fe(OTf)$_2$, in dichloromethane, CH_2Cl_2, produced the desired [((^{TIPS}C≡C)$_3$tren)Fe(OTf)$_2$] complex after one hour (Figure 3.3.1). This synthesis was used for many months and resulted in some of the results found in Chapter 4. However, after a new bottle

of iron(II) triflate was purchased, this reaction procedure no longer produced clean [((^{TIPS}C≡C)$_3$tren)Fe(OTf)$_2$].

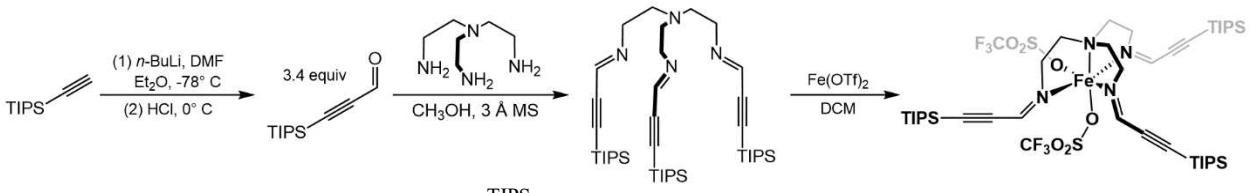

Figure 3.3.1. Original synthesis of [((^{TIPS}C≡C)$_3$tren)Fe(OTf)$_2$].

3.3.2 Complications with Ligand Synthesis

Over time, the synthesis of ^{TIPS}C≡CCHO resulted in a neon yellow oil instead of a pale-yellow oil. A silica column was performed to remove any impurities that were causing this color, but the color remained. Purity tests *via* ^{1}H NMR spectroscopy were performed on all starting materials for the ^{TIPS}C≡CCHO reaction. These tests indicated that the new bottle of (triisopropylsilyl)acetylene purchased from Frontier Scientific was not pure. A new bottle was purchased from Oakwood Chemical and the neon yellow color was no longer observed after the ^{TIPS}C≡CCHO reaction. Overtime, the pure isolated ^{TIPS}C≡CCHO started to turn orange even when stored at -40 ˚C in a dinitrogen atmosphere. The ^{1}H NMR of the orange oil is not significantly different to the pale-yellow oil, suggesting this color change is due to an inorganic impurity from the *n*-butyllithium. The orange ^{TIPS}C≡CCHO can be purified by a silica plug to reestablish the pale-yellow color and no discoloration occurs when this isolated product is stored at -40 ˚C under a dinitrogen atmosphere after several days. However, to avoid this additional purification step, the quality of the ^{n}Butyl lithium reagent was investigated. Bottles of ^{n}Butyl lithium purchased from Sigma Aldrich result in formation of the orange oil, but when changing the manufacturer to Acros Chemicals, only pale yellow ^{TIPS}C≡CCHO is isolated.

The Schiff base condensation between $^{TIPS}C{\equiv}CCHO$ and tren in CH_2Cl_2 normally results in the formation of $(^{TIPS}C{\equiv}C)_3$tren as a yellow oil (Figure 3.3.1, step 2). However, after many syntheses using the original procedure, the condensation reaction started producing yellow and red-orange oils. The ^{1}H NMR spectra of the red-orange oils do not differ from the original yellow $(^{TIPS}C{\equiv}C)_3$tren spectrum (Figure 3.3.2). The $(^{TIPS}C{\equiv}C)_3$tren synthesis was run in several solvents (methanol, acetonitrile, and diethyl ether) to help understand the color change. Directly after the syntheses in these solvents, the reaction mixture was concentrated *in vacuo* and a pale-yellow product was isolated, but when left under vacuum the product started to darken and after 24 hours the oil was orange in color (Figure 3.3.3). The UV-Vis spectra of the products formed from these solvents have more pronounced peaks at 275 nm and 287 nm when compared to the original yellow $(^{TIPS}C{\equiv}C)_3$tren product (Figure 3.3.3). It is unclear what is causing these impurities, but they increase in intensity when isolated $(^{TIPS}C{\equiv}C)_3$tren stands for long periods of time. To prevent these impurities from forming, I began to perform the $(^{TIPS}C{\equiv}C)_3$tren synthesis step in tandem with the $[(^{TIPS}C{\equiv}C)_3\text{tren})Fe(OTf)_2]$ synthesis, removing the need for the ligand isolation step.

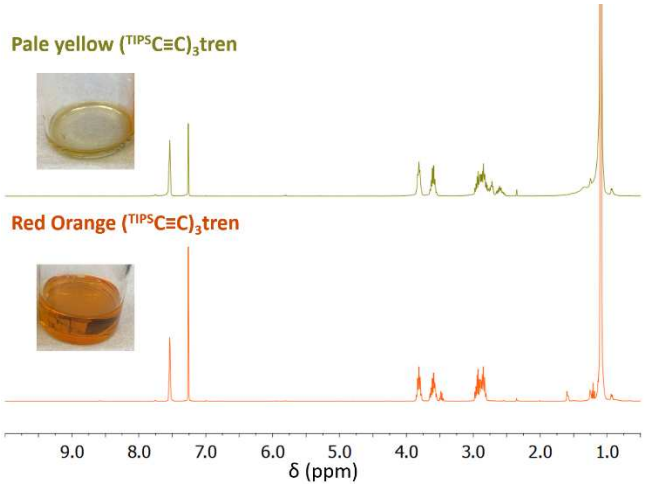

Figure 3.3.2. The ^{1}H NMR spectra of pale yellow and red orange $(^{TIPS}C{\equiv}C)_3$tren in d_1-$CDCl_3$.

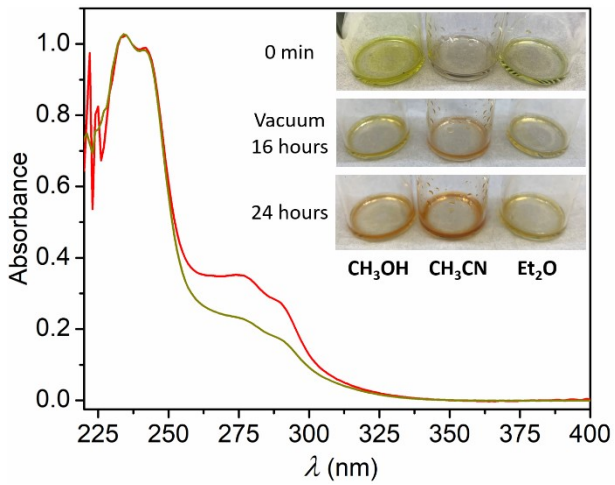

Figure 3.3.3. Electronic absorption spectra in dichloromethane (CH_2Cl_2) of ($^{TIPS}C{\equiv}C)_3$tren as a yellow oil (yellow) and red orange oil (red). The inset shows the color change of isolated ($^{TIPS}C{\equiv}C)_3$tren synthesized from methanol (CH_3OH), acetonitrile (CH_3CN) and diethyl ether (Et_2O) upon sitting for 0 hours to 24 hours.

3.3.3 Complications with [(($^{TIPS}C{\equiv}C)_3$tren)Fe(OTf)$_2$] Synthesis

Initially, pure ($^{TIPS}C{\equiv}C)_3$tren was combined with $Fe(OTf)_2$ in a one to one ratio in CH_2Cl_2, and the desired orange powder of [(($^{TIPS}C{\equiv}C)_3$tren)$Fe(OTf)_2$] was isolated after 1 hour. After numerous syntheses following this procedure, a new bottle of $Fe(OTf)_2$ starting material was purchased. Both the bottles purchased from Strem Chemicals were labeled as anhydrous 98% iron(II) triflate. When the new bottle is used following the original synthesis procedure a brick red powder is isolated. A paramagnetic ^{1}H NMR experiment shows that this brick red powder does not match the spectrum for [(($^{TIPS}C{\equiv}C)_3$tren)$Fe(OTf)_2$], the desired orange powder. The two distinct paramagnetic chemical shifts observed for [(($^{TIPS}C{\equiv}C)_3$tren)$Fe(OTf)_2$] were no longer present, and additional signals were observed between 105 ppm and 30 ppm (Figure 3.3.4).

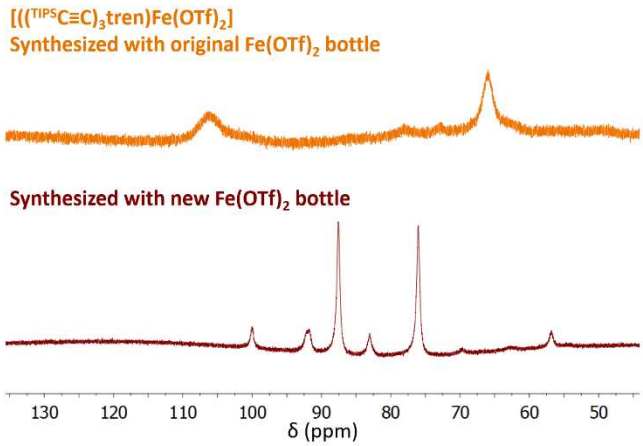

Figure 3.3.4. Paramagnetic ^{1}H NMR spectra of pure [((^{TIPS}C≡C)$_3$tren)Fe(OTf)$_2$] synthesized with original bottle of Fe(OTf)$_2$ (orange, top) and product produced following original synthesis with new bottle of Fe(OTf)$_2$ (red, bottle), obtained in d$_4$-CD$_3$OD.

As the bottle of Fe(OTf)$_2$ used was the only difference between the orange and brick red powders, the properties of both Fe(OTf)$_2$ starting materials were compared to help understand why the same reaction produced vastly different products. The quality analyses from Strem Chemicals for both the original and new bottles of Fe(OTf)$_2$ showed no obvious differences between the two batches. Infrared spectroscopy performed on samples from both bottles revealed two extra peaks around 3250 cm^{-1} in the original bottle compared to the new bottle (Figure 3.3.5a). Thermogravimetric analyses carried out on both bottles indicate that the original bottle contains one more equivalent of water than the new bottle (Figure 3.3.5b).

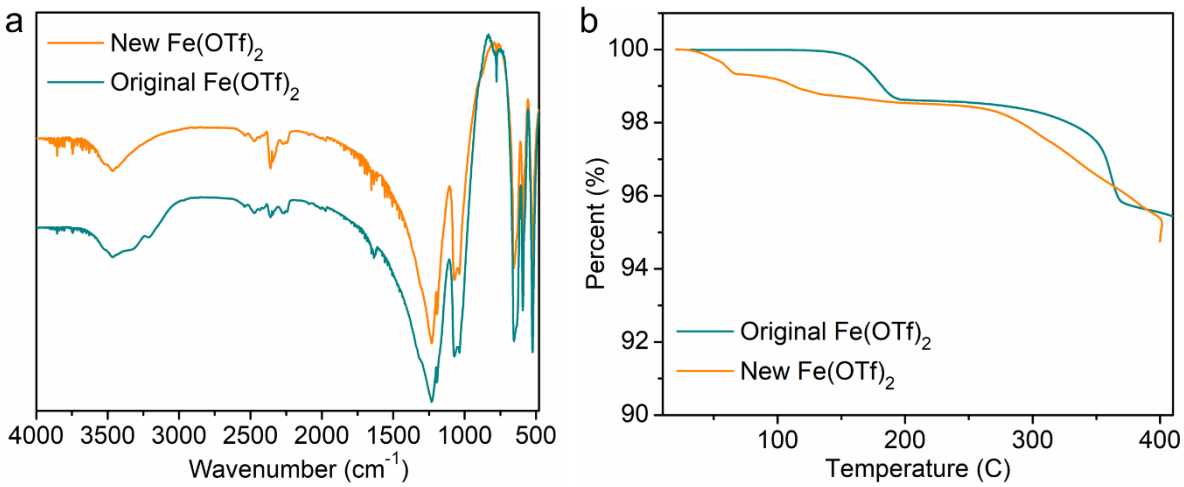

Figure 3.3.5. The IR spectra (a) and TGA analysis (b) of the original and new bottle of $Fe(OTf)_2$.

To replicate the original bottle, subsequent reactions with the new bottle of $Fe(OTf)_2$ were performed with the addition of varying amounts of water (Figure 3.3.6). When 1.5 equivalents of water are added to the reaction, the paramagnetic ^1H NMR of the final product closely resembles that of $[(({}^{TIPS}C{\equiv}C)_3tren)Fe(OTf)_2]$ made with the original bottle of $Fe(OTf)_2$. Although, a few extra peaks are observed at 82 ppm and 53 ppm. Ideally, upon crystallization of the product, these peaks would be removed; unfortunately, only a sticky solid was isolated after crystallization. While addition of the water produced the desired $[(({}^{TIPS}C{\equiv}C)_3tren)Fe(OTf)_2]$ complex, the purification to obtain clean product was unsuccessful.

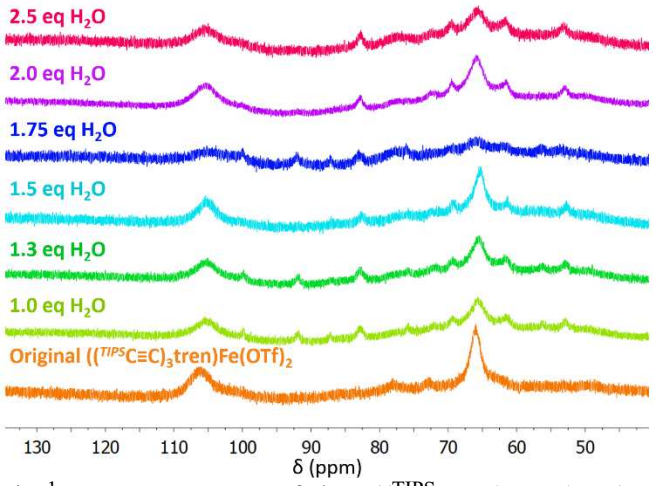

Figure 3.3.6. Paramagnetic ^{1}H NMR spectra of the [((^{TIPS}C≡C)$_3$tren)Fe(OTf)$_2$] synthesis after 1 hour with the new bottle of Fe(OTf)$_2$ and additional equivalents of water relative to Fe(OTf)$_2$ compared to pure [((^{TIPS}C≡C)$_3$tren)Fe(OTf)$_2$] (bottom, orange).

Time dependent UV-Vis spectroscopy was used to analyze the [((^{TIPS}C≡C)$_3$tren)Fe(OTf)$_2$] synthesis when the original and new bottle of Fe(OTf)$_2$ were used (Figure 3.3.7). Forty minutes after the addition of (^{TIPS}C≡C)$_3$tren to the original bottle of Fe(OTf)$_2$ a transition starts to appear around 450 nm. This transition is attributed to the formation of [((^{TIPS}C≡C)$_3$tren)Fe(OTf)$_2$], suggesting that the main species in solution at this time is the desired complex. The transition at 450 nm continues to increase in intensity until no more changes are observed after seventeen hours, indicating that the synthesis is complete. When the new bottle of Fe(OTf)$_2$ is used, the transition at 450 nm slowly increases in intensity until no more changes are observed at twenty hours. At this time, the spectrum is similar to what is observe after a 2 hour reaction time with the original bottle of Fe(OTf)$_2$, suggesting that [((^{TIPS}C≡C)$_3$tren)Fe(OTf)$_2$] can be synthesized with the new bottle of Fe(OTf)$_2$ without any additional reactants.

Both time dependent UV-vis experiments were run with similar reagent concentrations, but the lower absorbance values observed with the new bottle of Fe(OTf)$_2$ indicate a smaller amount of [((^{TIPS}C≡C)$_3$tren)Fe(OTf)$_2$] is formed during these experiments compared to when the original

bottle is used. These two time dependent UV-Vis experiments suggest that when using the new bottle of $Fe(OTf)_2$ a longer reaction time is needed and a slightly lower yield is obtained than if using the original bottle.

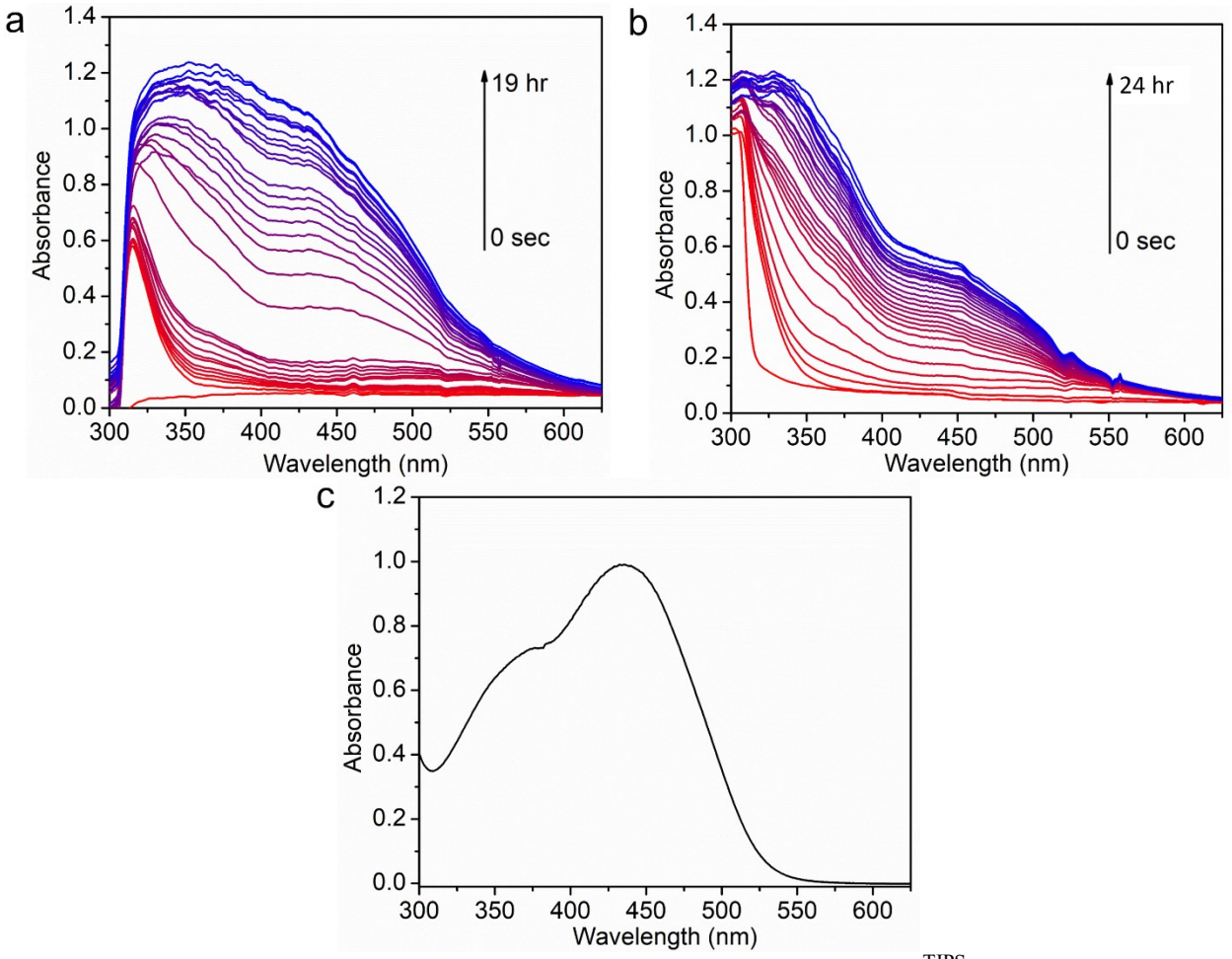

Figure 3.3.7. Time dependent UV-Vis spectra in CH_2Cl_2 of the [(($^{TIPS}C\equiv C)_3$tren)$Fe(OTf)_2$] reaction mixture when the original bottle (a) or the new bottle of $Fe(OTf)_2$ (b) is used and of pure [(($^{TIPS}C\equiv C)_3$tren)$Fe(OTf)_2$].

The results from the time dependent UV-Vis and ligand impurity experiments were used to modify the original [(($^{TIPS}C\equiv C)_3$tren)$Fe(OTf)_2$] synthesis. A one pot synthesis was performed using three equivalents of $^{TIPS}C\equiv CCOH$, one equivalent of tren, and one equivalent of the new $Fe(OTf)_2$ (Figure 3.3.8). Aliquots of the reaction were removed and analyzed using paramagnetic

^{1}H NMR spectroscopy over the course of 1 week. The ^{1}H NMR spectra of the reaction after 24 hours shows the two distinct paramagnetically shifted peaks of [((^{TIPS}C≡C)$_3$tren)Fe(OTf)$_2$] at 105 ppm and 65 ppm (Figure 3.3.9). The spectra of aliquots taken between 2 days and 6 days do not differ from the 24-hour spectrum, suggesting the reaction is complete after 24 hours. By increasing the original reaction time from 1 hour to 24 hours, I found that pure [((^{TIPS}C≡C)$_3$tren)Fe(OTf)$_2$] can be isolated reproducibly when the new bottle of Fe(OTf)$_2$ is used.

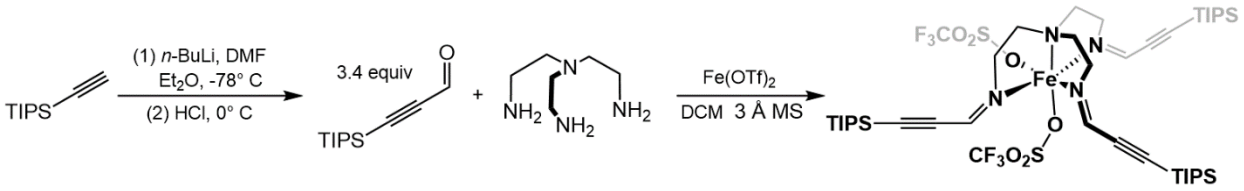

Figure 3.3.8. Modified synthesis of [((^{TIPS}C≡C)$_3$tren)Fe(OTf)$_2$].

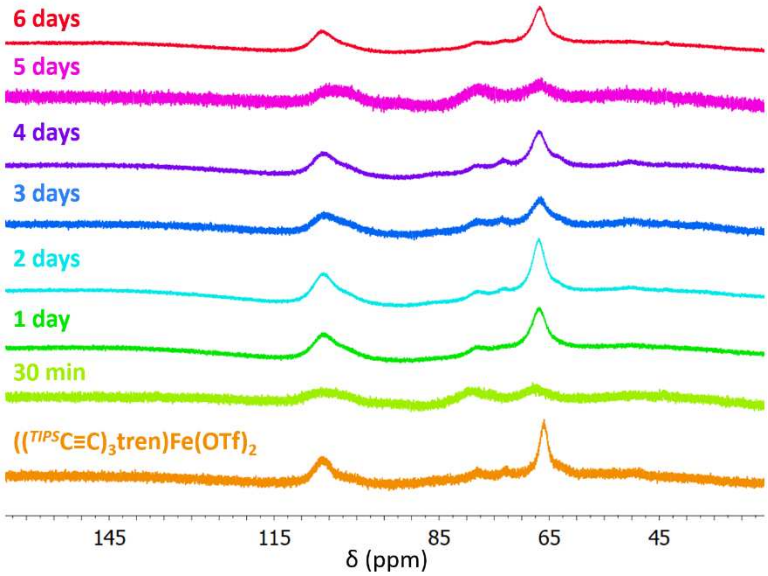

Figure 3.3.9. Paramagnetic ^{1}H NMR spectra in d$_4$-CD$_3$OD of aliquots of [((^{TIPS}C≡C)$_3$tren)Fe(OTf)$_2$] synthesis with new Fe(OTf)$_2$, 3 equivalents of ^{TIPS}C≡CCHO and 1 equivalent of tren.

The modified one pot reaction procedure successfully produces pure [((^{TIPS}C≡C)$_3$tren)Fe(OTf)$_2$] when bottles of Fe(OTf)$_2$ from different manufacturers are used.

However, additional studies on the synthetic conditions indicate that the order addition and glovebox atmosphere are important for isolating pure product. When a solution of $^{TIPS}C{\equiv}CCOH$ is added to a solution of tren and $Fe(OTf)_2$ and reacted overnight, the ^1H NMR indicates formation of $[((^{TIPS}C{\equiv}C)_3tren)Fe(OTf)_2]$ and $[(tren)Fe(OTf)_2]$ (Figure 3.3.10). This suggests that once $[(tren)Fe(OTf)_2]$ is formed, the condensation reaction between tren and $^{TIPS}C{\equiv}CCOH$ is more challenging than if iron(II) was not present. Additionally, the glovebox atmosphere contributes to the formation of $[((^{TIPS}C{\equiv}C)_3tren)Fe(OTf)_2]$. When the reaction is performed before a regeneration of the glovebox catalyst, more impurities are observed than if the reaction was run directly after a catalyst regeneration (Figure 3.3.10).

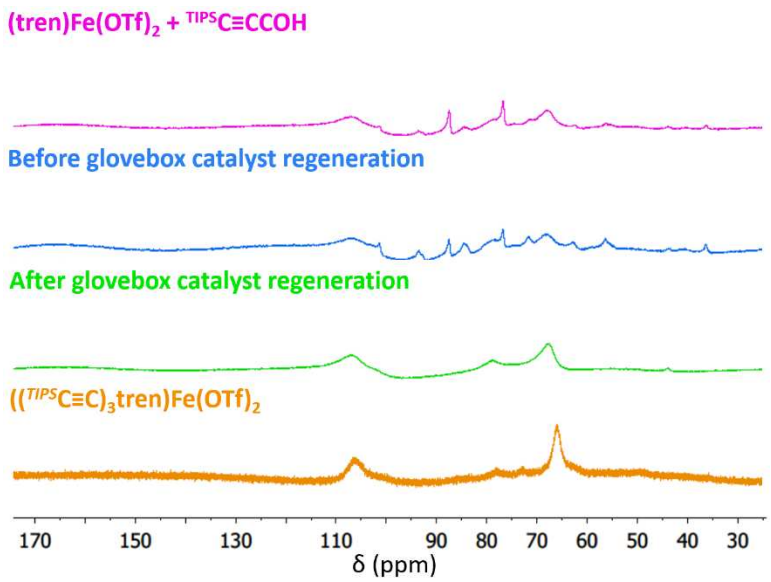

Figure 3.3.10. Paramagnetic ^1H NMR spectra in d_4-CD_3OD of the $[((^{TIPS}C{\equiv}C)_3tren)Fe(OTf)_2]$ synthesis with new $Fe(OTf)_2$, $^{TIPS}C{\equiv}CCHO$, and tren; where tren and $Fe(OTf)_2$ were reacted before addition of $^{TIPS}C{\equiv}CCHO$ (pink), the one pot reaction was performed before a glovebox catalyst regeneration (blue) and after a glovebox catalyst regeneration (green), compared to pure $[((^{TIPS}C{\equiv}C)_3tren)Fe(OTf)_2]$ (orange).

3.4 Conclusion

The initial synthetic procedure for [((^{TIPS}C≡C)$_3$tren)Fe(OTf)$_2$] resulted in clean product with minimal to no complications. Over time, the (^{TIPS}C≡C)$_3$tren ligand synthesis produced a red-orange oil instead of the desired pale-yellow product. Characterization of this red-orange oil by UV-vis spectroscopy showed more intense transitions around 275 nm and 287 nm. Removing the ligand isolation step and performing the ligand synthesis in tandem with the [((^{TIPS}C≡C)$_3$tren)Fe(OTf)$_2$] synthesis prevents this impurity from causing any problems during the complexation reaction. When a new bottle of Fe(OTf)$_2$, purchased from the same manufacturer, was used to synthesize [((^{TIPS}C≡C)$_3$tren)Fe(OTf)$_2$] no desired product was formed. Characterization of both Fe(OTf)$_2$ starting materials by TGA and IR suggests that the original bottle of Fe(OTf)$_2$ contains an equivalent of water whereas the new bottle does not. Addition of water to the [((^{TIPS}C≡C)$_3$tren)Fe(OTf)$_2$] synthesis with the new bottle of Fe(OTf)$_2$ produces the desired product, bulk purification was unsuccessful. Through use of time dependent UV-Vis and ^{1}H NMR spectroscopic experiments to monitor the [((^{TIPS}C≡C)$_3$tren)Fe(OTf)$_2$] synthesis, I found that an overnight reaction time is required when the new anhydrous bottle of Fe(OTf)$_2$ is used. Pure [((^{TIPS}C≡C)$_3$tren)Fe(OTf)$_2$] can be isolated after 24 hours when the modified one pot reaction with three equivalents of ^{TIPS}C≡CCOH, one equivalent of tren, and one equivalent of the new Fe(OTf)$_2$ is used. Unfortunately, only bottles of Fe(OTf)$_2$ from Strem Chemicals were used during this investigation. However, I believe that the new reaction procedure will be successful with bottles from other reputable manufacturers, as this updated procedure has been successful with multiple new Fe(OTf)$_2$ bottles from Strem Chemicals.

This investigation into the reproducibility of the synthetic procedures of [((^{TIPS}C≡C)$_3$tren)Fe(OTf)$_2$] shows how sensitive some reaction conditions are to fresh starting

materials. The quality of purchased materials can differ between manufacturers as found during the investigation into the $^{TIPS}C{\equiv}CCHO$ synthesis. Additionally, new bottles of a material from the same company can have different impurities or solvent contents. For most reactions, these differences do not affect the synthetic procedures, but they should be considered when synthetic problems arise from reactions that have been previously shown to be successful.

3.5 Experimental

3.5.1 General Considerations.

All reactions were performed under inert conditions carried out on a dinitrogen Schlenk line or in a dinitrogen-filled Vigor glovebox. Dichloromethane (CH_2Cl_2) was dried over calcium chloride, then distilled and degassed prior to use. Diethyl ether (Et_2O) and acetonitrile (CH_3CN) were sparged with nitrogen, passed through an alumina column and degassed prior to use. Anhydrous methanol (CH_3OH) was purchased from Sigma-Aldrich. Anhydrous iron(II) trifluoromethanesulfonate ($Fe(OTf)_2$) was purchased from Strem Chemicals (LOT 29571600 and 33220300). The starting material 3-(triisopropylsilyl)propioladldehyde was prepared according to literature.[1] All other chemicals were purchased from commercial vendors and used as received.

3.5.2 Physical Methods.

All methods were performed at room temperature unless otherwise noted. Absorption spectra were obtained with a Hewlett-Packard 8453 spectrometer in quartz cuvettes with a 1 cm path length. Room temperature ^1H NMR spectra were gathered on an Agilent 400 MHz spectrometer. For paramagnetic spectra, changes to standard ^1H NMR acquisition were as follows: relaxation delay (1 ms), pulse angle (90°) and acquisition time (1 s). IR spectra were measured with a Nicolet 380 FT-IR spectrophotometer using a Smart Performer ZnSe attenuated total reflectance (ATR)

accessory. TGA measurements were collected on a TA instrument Q500. Mass spectrometry measurements were performed in the positive ion mode on a Thermo LTQ mass spectrometer equipped with an analytical electrospray ion source and a quadrupole ion trap mass analyzer at 175 °C.

3.5.3 Synthesis of (^{TIPS}C≡C)$_3$tren.

In air, a solution of tren (92.8 mg, 0.63 mmol) in CH_2Cl_2 (6 mL) was added to a solution of 3-(triisopropylsilyl)propiolaldehyde (427.0 mg, 2.03 mmol) in CH_2Cl_2 (2 mL) and the resulting mixture was stirred in the presences of 3 Å molecular sieves for 1 hour at 23 °C. The solution was then filtered, and the filtrate was concentrated *in vacuo*, giving (^{TIPS}C≡C)$_3$tren as a yellow oil (446.8 mg, 97.4% yield).

(^{TIPS}C≡C)$_3$tren: ^{1}H NMR (400 MHz, $CDCl_3$): δ 7.5 (s, 1H), 3.8 (m, 1H), 3.6 (m, 1H), 2.9 (m, 2H), 1.1 (s, 20H) ppm; ^{13}C NMR (100 MHz, $CDCl_3$): δ 146.1, 143.7, 103.7, 101.7, 98.6, 94.6, 60.9, 55.4, 55.7, 18.7, 11.3 ppm; IR (KBr): 2945, 2866, 1612, 1463, 1019, 883, 678 cm^{-1}; HRMS (ESI+): *m/z* calc'd for $(M+H)^+$ $[C_{42}H_{79}N_4Si_3]^+$: 723.5613, found 723.5607.

3.5.4 Synthesis of [((^{TIPS}C≡C)$_3$tren)Fe(OTf)$_2$]

Procedure A. A solution of $Fe(OTf)_2$ (200 mg, 0.565 mmol) in CH_2Cl_2 (4 mL) was added to (^{TIPS}C≡C)$_3$tren (408 mg, 0.565 mmol) in CH_2Cl_2 (1 mL), and the resulting dark orange mixture was stirred for 1 hour. The reaction mixture was passed through a syringe filter and concentrated *in vacuo*. The resulting light orange powder was dissolved in 2 mL of Et_2O and the desired Fe complex was precipitated by addition of hexanes (20 mL), and the resulting mixture was stirred overnight. The suspension was then filtered and washed with hexanes (3 × 2 mL) and the resulting orange powder was crystallized via hexanes diffusion into a concentrated toluene solution, giving dark orange crystals of ((^{TIPS}C≡C)$_3$tren)$Fe(OTf)_2$ (112 mg, 18.4% yield).

Procedure B. To a solution of 3-(triisopropylsilyl)propiolaldehyde (323.5 mg, 1.54 mmol) in CH_2Cl_2 (3 mL) was added a solution of tris(2-aminoethyl)amine (67.6 mg, 0.46 mmol) in CH_2Cl_2 (2 mL), and the resulting mixture was stirred in the presence of 3 Å molecular sieves for 5 minutes at 23 °C. Then a solution of $Fe(OTf)_2$ (131.4 mg, 0.37 mmol) in CH_2Cl_2 (5 mL) was added, and the resulting dark orange mixture was stirred for 19 hours. The dark orange reaction mixture was then passed through a syringe filter and concentrated *in vacuo*. The resulting orange oil was dissolved in Et_2O (2 mL) and the desired Fe complex was precipitated by addition of hexanes (20 mL), and the resulting mixture was stirred overnight. The suspension was filtered and washed with hexanes (3 × 5 mL), providing $(({}^{TIPS}C{\equiv}C)_3tren)Fe(OTf)_2$ as an orange powder (176.0 mg, 44% yield). This powder was recrystallized *via* diffusion of hexanes into a concentrated toluene solution, giving dark orange block crystals of **1** (107.0 mg, 27% yield).

[((^{TIPS}C≡C)$_3$tren)Fe(OTf)$_2$]: ^{1}H NMR (CD_3OD, 400 MHz): δ 101.3, 77.4, 1.0, 0.87 ppm. Absorption spectrum: CH_3OH, λ (ε_M): 251 nm (9750 $M^{-1}cm^{-1}$), 358 nm (623 $M^{-1}cm^{-1}$), 447 nm (1120 $M^{-1}cm^{-1}$); CH_3CN, λ (ε_M): 247 nm (42809 $M^{-1}cm^{-1}$), 447 nm (21720 $M^{-1}cm^{-1}$). MS (ESI^+): *m/z* calcd for $(M - OTf)^+$ $[C_{43}H_{78}F_3FeN_4O_3SSi_3]^+$: 927.44, found 927.58; *m/z* calcd for $(M - 2OTf)^{2+}$ $[C_{42}H_{78}FeN_4Si_3]^{2+}$: 389.25, found 389.42. Anal. calcd for $C_{44}H_{78}N_4O_6F_6S_2Si_3Fe$: C 49.05 %, H 7.30 %, N 5.20 %, found C 48.82 %, H 7.36 %, N 5.19 %.

References

(1) Gómez-Bengoa, E.; García, J. M.; Jiménez, S.; Lapuerta, I.; Mielgo, A.; Odriozola, J. M.; Otazo, I.; Razkin, J.; Urruzuno, I.; Vera, S.; et al. Asymmetric Synthesis of Propargylic Alcoholsviaaldol Reaction of Aldehydes with Ynals Promoted by Prolinol Ether–Transition Metal–Brønsted Acid Cooperative Catalysis. *Chem. Sci.* **2013**, *4* (8), 3198–3204.

Chapter 4: Influence of coordinated triflate anions on the solution magnetic properties of a neutral iron(II) complex*

4.1 Synopsis

In an effort to probe the impacts of speciation on spin-state switching, the synthesis and unique solution phase magnetic properties of [((^{TIPS}C≡C)$_3$tren)Fe(OTf)$_2$] (**4-1**) are described. Analysis of the single-crystal X-ray diffraction data shows that the tris(iminoalkyne) ligand coordinates to the iron(II) center through all four nitrogen atoms, while the other two coordination sites are filled by the oxygen atoms from triflate anions. Solid state variable temperature (VT) magnetic studies show that **4-1** remains high spin (HS) at all temperatures. In the presence of moderately strong coordinating solvents, solvent replaces the two bound triflate counteranions, as observed by ^{19}F NMR spectroscopy and supported by conductivity measurements. VT solution measurements show **4-1** to be in the HS state when this solvent is oxygen donating, but low spin (LS) with a nitrogen donating solvent. In the noncoordinating solvent dichloromethane, both triflates are bound to the iron(II) center at room temperature, but upon cooling **4-1** undergoes a coordination change, resulting in the loss of one triflate, as shown by ^{19}F NMR. With the moderately coordinating solvent acetone, triflate dissociation upon cooling results in a spin switching species with a $T_{1/2}$ value of 171 K, characterized *via* ^{19}F NMR, Evans' method, and solution magnetometry measurements. Solution magnetic measurements collected in structurally similar cyclopentanone suggest that the spin-state switching event is exclusive to the acetone environment, suggesting the influence of both the local coordination environment and aggregation. Additionally, a comparison

* "Influence of Coordinated Triflate Anions on the Solution Magnetic Properties of a Neutral Iron(II) Complex." Livesay, B. N.; Shores, M. P. *Inorg. Chem.* **2021**, *60*, 15445-15455 – Reproduced in part by permission of the American Chemical Society. https://pubs.acs.org/doi/10.1021/acs.inorgchem.1c02112

of the solvodoynamic diameters *via* dynamic light scattering suggests that aggregation of **4-1** is significantly different in $(CH_3)_2CO$ and $(CD_3)_2CO$, leading to the observation of spin-switching behavior in the former and fully HS behavior in the latter. This study highlights the sensitivity of solution magnetic properties to solvent choice.

4.2 Introduction

Octahedral first row transition metal complexes with electron counts between d^4 and d^7 can exist in a high spin (HS) or a low spin (LS) state. When the metal ion experiences a strong field ligand it, occupies the LS state, and with a weak field ligand, it occupies a HS state. In the presence of a medium ligand field, reversible switching between the HS and LS state can occur. This spin state switching event can be stimulated by physical (e.g. temperature, light, magnetic field) or chemical (e.g. solvent, hydrogen bonding) stimuli.[1,2] The most studied spin switching complexes contain iron(II) because of the vast differences in properties between the HS (S = 2) and LS (S = 0) states.[3] These unique properties allow spin-state switching complexes to be used in a variety of practical applications, like optical devices, information storage, molecular electronics, sensing, and magnetic contrast agents.[2,4–9]

While most research into using spin state switching for these types of application focuses on tuning the ligand field strength, there are many other factors that influence spin state switching events.[10–18] In the solid state, crystal packing, intermolecular interactions, and cocrystallized solvents promote the spin switching event. In the solution phase, ligand field and solvent polarity have been found to influence the classic switching event.[19] These different environmental factors can lead to a single complex with contrasting magnetic data between the solid state and solution phases.[20,21]

In addition, ligand exchange in solution can impact the spin state properties of a complex. Labile ligands can be replaced by solvent, counter anions, or leave open coordination sites when dissolved, resulting in the formation of new species.[22–29] Such ligand exchanges can generate the conditions under which coordination-induced spin-state switching (CISSS) can occur.[24,28,29] It is often difficult to differentiate CISSS from classical spin-state switching in solution, but the simultaneous analysis of several solution-based analytical techniques can help with this determination.

Both classical and CISSS mechanisms are very sensitive to solvent identity. There are many solution phase studies targeting ligand field and/or analyte effects on the spin switching properties, but there are few reports on the differential impacts of a variety of solvents on the magnetic properties.[9,11–16,21,24] Some literature precedent on iron(II) complexes show that the spin-switching event shifts to higher temperature with increasing solvent polarity or hydrogen bond acceptor ability.[10,20,30–33] A better understanding of how a variety of solvents affect the spin-switching properties of a single complex can provide greater insight into the use of these complexes for more solution-based applications. Herein, we report the synthesis of a neutral iron(II) complex and its characterization in both the solid state and a variety of solvents. Magnetic studies in solution show this complex can be HS, LS, or undergo CISSS depending on the dissolving solvent.

4.3 Division of Labor

Quartz tubes were sealed with help from Cassidy Jackson and Roxanna Martinez. All other work in this chapter was carried out by Brooke N. Livesay. This work is supported by National Science Foundation (Grants CHE-1363274, CHE-1800554, and CHE-1956399) and Colorado State University. We thank Dr. Chris Rithner for assistance with VT NMR experiments and

analyses. We also thank Dr. Indrani Bhowmick for assistance with solution magnetometry measurements. We thank the Analytical Resources Core, Center for Materials and Molecular Analysis at Colorado State University for instrument access, training and assistance with sample analysis.

4.4 Experimental Section

4.4.1 Preparation of Compounds.

Unless otherwise mentioned, reactions were performed under inert conditions carried out in a dinitrogen-filled Vigor glovebox. Syringe filters were purchased from VWR International and fitted with 0.2 μm poly(tetrafluoroethylene) membranes. Diethyl ether (Et_2O), toluene (MePh), hexanes, tetrahydrofuran (THF), and acetonitrile (CH_3CN) were sparged with nitrogen, passed through an alumina column and degassed prior to use. Acetone ($(CH_3)_2CO$) and dichloromethane (CH_2Cl_2) were dried over potassium carbonate or calcium chloride, respectively, then distilled and degassed prior to use. Cyclopentanone and 3-pentanone were distilled and degassed prior to use. Anhydrous methanol (CH_3OH), ethanol (CH_3CH_2OH), and nitromethane (CH_3NO_2) were purchased from Sigma-Aldrich. The starting material 3-(triisopropylsilyl)propiolaldehyde was prepared according to the literature.[34] Anhydrous iron(II) trifluoromethanesulfonate [$Fe(OTf)_2$] was purchased from Strem Chemicals. All other chemicals were purchased from commercial vendors and used as received.

*4.4.2 Synthesis of [(($^{TIPS}C\equiv C)_3$tren)$Fe(OTf)_2$] (**4-1**).*

To a solution of 3-(triisopropylsilyl)propiolaldehyde (323.5 mg, 1.54 mmol) in CH_2Cl_2 (3 mL) was added a solution of tris(2-aminoethyl)amine (67.6 mg, 0.46 mmol) in CH_2Cl_2 (2 mL), and the resulting mixture was stirred in the presence of 3 Å molecular sieves for 5 min at 23 °C. Then a

solution of $Fe(OTf)_2$ (131.4 mg, 0.37 mmol) in CH_2Cl_2 (5 mL) was added, and the resulting dark orange mixture was stirred for 19 h. The dark orange reaction mixture was then passed through a syringe filter and concentrated *in vacuo*. The resulting orange oil was dissolved in Et_2O (2 mL), and the desired iron complex was precipitated by the addition of hexanes (20 mL), and the resulting mixture was stirred overnight. The suspension was filtered and washed with hexanes (3 × 5 mL), providing **4-1** as an orange powder (176.0 mg, 44% yield). This powder was recrystallized *via* the diffusion of hexanes into a concentrated MePh solution, giving dark orange block crystals of **4-1** (107.0 mg, 27% crystal yield overall). ^{1}H NMR (CD_3OD, 400 MHz): δ 107.30, 67.09, 1.25, 0.99 ppm. Absorption spectrum: CH_3OH, λ_{max}, nm (ε_M, M^{-1} cm^{-1}): 250 (29500), 360 (2310), 447 (3670); CH_2Cl_2, λ_{max}, nm (ε_M, M^{-1} cm^{-1}): 358 (2790), 440 (3950); $(CH_3)_2CO$, λ_{max}, nm (ε_M, M^{-1} cm^{-1}): 442 (3990); cyclopentanone, λ_{max}, nm (ε_M, M^{-1} cm^{-1}): 444 (4890); CH_3CN, λ_{max}, nm (ε_M, M^{-1} cm^{-1}): 247 (42809), 447 (21720). MS (ESI^+): *m/z* calcd for $(M - OTf)^+$ $[C_{43}H_{78}F_3FeN_4O_3SSi_3]^+$: 927.44, found 927.58; *m/z* calcd for $(M - 2OTf)^{2+}$ $[C_{42}H_{78}FeN_4Si_3]^{2+}$: 389.25, found 389.42. Anal. calcd for $C_{44}H_{78}N_4O_6F_6S_2Si_3Fe$: C 49.05 %, H 7.30 %, N 5.20 %, found C 48.82 %, H 7.36 %, N 5.19 %.

4.4.3 Physical Methods.

All methods were performed at room temperature unless otherwise noted. Absorption spectra were obtained with a Hewlett-Packard 8453 spectrometer in quartz cuvettes with a 1 cm path length. Mass spectrometry measurements were performed in the positive ion mode on a Thermo LTQ mass spectrometer equipped with an analytical electrospray ion source and a quadrupole ion trap mass analyzer at 175 °C. Room temperature ^{1}H and ^{19}F spectra were gathered on an Agilent 400 MHz spectrometer and variable temperature (VT) spectra were collected on a Varian Inova 500 MHz spectrometer. For paramagnetic samples, changes to standard ^{1}H NMR acquisition were

as follows: relaxation delay, 1 ms; pulse angle, 90°; acquisition time, 1 s. For Evans' method measurements of the magnetic susceptibility, samples were measured at a concentration of 5 mM and collected 1 – 24 h after the sample was made. Conductivity measurements were carried out using a Yellow Springs model 31 conductivity bridge and a glass conductivity cell with platinum plates. Cell constants were determined by calibrating with an aqueous 1 mM potassium chloride solution. All measurements were performed multiple times on 1 mM solutions of **4-1** under an inert atmosphere. The conductivity values reported herein are the averages of all trials. The solvodynamic diameters were measured by dynamic light scattering using a Malvern Zetasizer ZS in 1 cm glass cuvettes. Each sample was measured nine times and the sizes reported herein are the averages of the measurements. Elemental analyses were performed by Midwest Microlab, Indianapolis, IN.

4.4.4 Crystallographic Measurements.

Crystallographic parameters for **4-1** are listed in Table A1.1. For data collection, the crystal was coated in Paratone oil, supported on a Cryoloop, and then mounted on a Bruker D8 Advance Quest diffractometer under a stream of dinitrogen. Mo Kα radiation and a graphite monochromator were used for data collection. The initial lattice parameters were determined from reflections found in eight frames. Data sets were collected targeting complete coverage and 4-fold redundancy. Data were integrated and corrected for absorption effects with APEX software.[35] Structures were solved and refined with the SHELXTL software package.[36] Unless noted otherwise, thermal parameters for all fully occupied, non-hydrogen atoms were refined anisotropically. Hydrogen atoms were inserted at calculated positions and refined isotropically, using a riding model where the thermal parameters were set at 1.2 times those of the attached carbon or nitrogen atom and 1.5 times those for methyl groups.

4.4.5 Magnetic Measurements using a Magnetic Property Measuring System (MPMS).

Data were collected using a Quantum Design MPMS XL SQUID magnetometer. All sample preparations were performed in a dinitrogen filled Vigor glovebox. For solid state samples, powdered microcrystalline samples were loaded into polyethylene bags, sealed, and inserted into drinking straws for measurements. For solution phase samples, powdered microcrystalline samples were dissolved in the appropriate solvent at an 80 mM concentration and placed into straws or quartz tubes, whereupon the straw or tube was sealed. Samples were collected 1 – 48 h after **4-1** was dissolved in solution. Ferromagnetic impurities were checked through a variable field measurement (0 – 10 kOe) of the magnetization at 100 K; linear fits of the *M* versus *H* data between 0 and 10 kOe (Figure A1.1, A1.7 – A1.12) indicated the absence of ferromagnetic impurities. Magnetization measurements were collected at 2 K at applied fields ranging from 0 to 50 kOe (Figure A1.2). Magnetic susceptibility data were collected between 2 K and 300 K. The solution phase samples were inserted into the magnetometer at ~50 – 100 K. After the *M* versus *H* scan, the samples were then cooled to 2 K to begin the susceptibility sequence. Data were corrected for the diamagnetic contributions of the sample holder and solvent by subtracting empty containers; corrections for the sample were calculated from Pascal's constants.[37] Fits of magnetic susceptibility data and reduced magnetization were performed using *PHI*[38] according to the following general spin Hamiltonian:

$$\widehat{\mathrm{H}} = \mathrm{D}\widehat{\mathrm{S}_\mathrm{z}^2} + \mathrm{E}\left(\widehat{\mathrm{S}_\mathrm{x}^2} + \widehat{\mathrm{S}_\mathrm{y}^2}\right) + \mathrm{g_{iso}}\beta\vec{\mathrm{S}} \cdot \vec{\mathrm{B}}$$

4.5 Results

4.5.1 Synthesis and Crystal Structure.

Compound **4-1** is synthesized via an in situ Schiff-base condensation in CH_2Cl_2 between 3-(triisopropylsilyl)propiolaldehyde and tris(2-aminoethyl)amine, followed by addition of

anhydrous iron(II) triflate. Diffusion of hexanes into a concentrated solution of **4-1** in MePh affords diffraction-quality dark orange crystals. The structure, collected via single-crystal X-ray diffraction at 100 K, shows that **4-1** is neutral with the ligand, $(^{TIPS}C{\equiv}C)_3$tren, bound to iron through all four nitrogen atoms and the other two coordination sites occupied by the triflate counter anions in a cis fashion (Figure 4.5.1). A continuous shape analysis indicates the first coordination sphere is best described as a distorted octahedron.[39] The average Fe-N_{imine} bond distance is 2.141(3) Å and the Fe-$N_{bridgehead}$ distance is 2.196(3) Å. The two triflate bond distances differ: the Fe-O bond trans to N_{imine} has a distance of 2.178(3) Å, while the Fe-O bond trans to the $N_{bridgehead}$ is 2.053(3) Å. The resulting asymmetry of these Fe-O bonds is due to a weaker *trans*-influence of a $N_{bridgehead}$ than an N_{imine} and has been observed in similar compounds bound by the tetradentate ligand tris(2-pyridylmethyl)amine and two monodentate oxygen donor ligands.[23,40,41] Overall, the metal-ligand distances in **4-1** are characteristic of a HS iron(II) center.

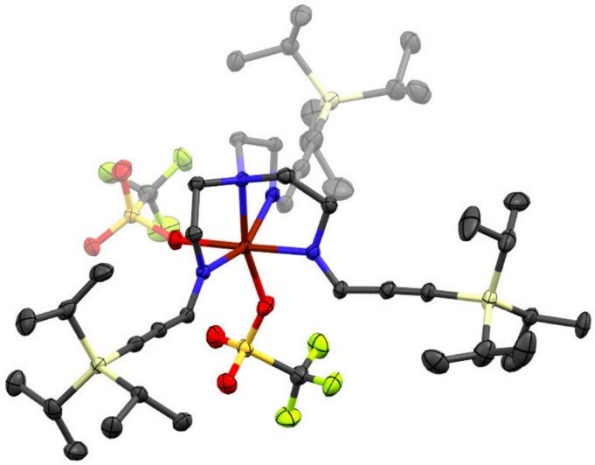

Figure 3.5.1. Crystal structure of **1**, depicted with 40% thermal ellipsoids, hydrogens have been omitted for clarity. Dark red, blue, gray, red, yellow, lime green, and pale-yellow ellipsoids represent Fe, N, C, O, S, F, and Si atoms, respectively.

4.5.2 Solid state magnetic behavior.

The solid-state temperature dependence of the magnetic susceptibility temperature product ($\chi_M T$; Figure 4.5.2) is consistent with HS iron(II) at all temperatures probed. At 300 K, the $\chi_M T$ value is 3.54 cm^3 K mol^{-1}, higher than the expected spin only value ($g = 2$, $\chi_M T = 3.00$ cm^3 K mol^{-1}) but consistent with the solid state $\chi_M T$ products reported for other reported HS iron(II) compounds. Upon a decrease in the temperature, the $\chi_M T$ value decreases monotonically until ~10 K, whereupon the decrease becomes more dramatic: at 2 K, $\chi_M T$ is 2.43 cm^3 K mol^{-1}. This downturn in the magnetic susceptibility at low temperatures is due to magnetic anisotropy or intermolecular antiferromagnetic coupling. The magnetic susceptibility data, fit in tandem with reduced magnetization data (Figure A1.2, Table A1.2) using PHI,[38] give best-fit parameters for an $S = 2$ species with $g_{iso} = 2.08$, $|D| = 3.58$ cm^{-1}, and $|E| = 0.656$ cm^{-1}.

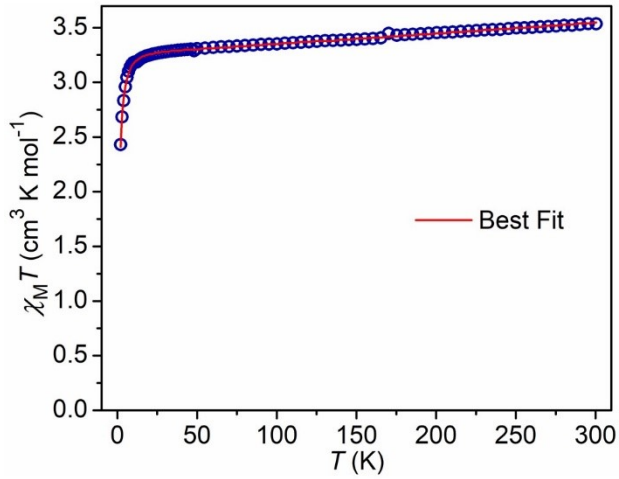

Figure 3.5.2. Temperature dependence of magnetic susceptibility for a solid-state sample of **4-1**, collected between 2 K and 300 K at 1000 Oe. The best fit determined using PHI[38] is shown by the red line.

4.5.3 Solution-Phase Experiments.

A variety of solvents ranging in coordination ability (a^{TM}) were used for solution phase experiments to understand the behavior of the triflate counteranions. The coordination ability of a solvent to a transition metal (a^{TM}) was determined by Díaz-Torres and Alvarez[42,43] by the following equation, which uses the number of transition-metal crystal structures with the solvent coordinated (c), semicoordinated (s), and uncoordinated (u): a^{TM} = log(c+s)/u. Table 4.5.1 compiles information for all of the solvents that were used, what experiments were performed, and where the resulting data are reported. The following sections will focus on the experiments performed in strongly coordinating (CH_3CN, -0.2 a^{TM}, and CH_3OH, -0.3 a^{TM}), weakly coordinating ($(CH_3)_2CO$, -1 a^{TM}, and cyclopentanone) and noncoordinating (CH_2Cl_2, -1.8 a^{TM}) solvents as well as their deuterated analogs.[42,43]

Table 3.5.1. Solution phase experimental data available for **4-1**.

Solvent	Electronic Absorption	Solution MPMS	^{19}F NMR	VT ^{19}F NMR	VT ^{1}H NMR	Conductivity	DLS
CH_3CN	Main Text		Main Text			Main Text	
THF	Appendix 1		Main Text			Main Text	
CH_3OH	Main Text						
CH_3CH_2OH	Appendix 1		Main Text			Main Text	
$(CH_3)_2CO$	Main Text						
Cyclopentanone	Main Text		Main Text	Appendix 1		Main Text	
3-pentanone	Appendix 1		Main Text			Main Text	
CH_3NO_2	Appendix 1		Main Text			Main Text	
CH_2Cl_2	Main Text						

4.5.4 Electronic Absorption.

The UV–visible spectra of **4-1** collected in several solvents are shown in Figure 4.5.3, and the molar absorptivity values were calculated by analyzing several samples ranging in concentration (5.7×10^{-4} M – 1.7×10^{-5} M). In CH_3CN and CH_3OH, a transition is observed at ~250 nm that is expected to be ligand-based. Moving into the visible region, all solvents show a metal-to-ligand charge transfer band at ~445 nm; in CH_2Cl_2 and CH_3OH a higher energy transition is also seen at 360 nm. The molar absorptivity for the 445 nm transition is vastly different for CH_3CN compared to the other solvents: 21796 M^{-1} cm^{-1} (CH_3CN) and ~4000 M^{-1} cm^{-1} (other solvents). The larger molar absorptivity in CH_3CN indicates that **4-1** is in the LS state at room temperature, while in other solvents **4-1** is primarily in the HS state. The VT UV–visible spectra of **4-1** in CH_2Cl_2, CH_3OH, and $(CH_3)_2CO$, collected between 298 K and 195 K (Figures A1.4 – A1.6), show no significant increases in the molar absorptivity of the 445 nm transition, suggesting that **4-1** remains dominantly HS throughout this temperature range for these solvents, and certainly does not change spin state in that temperature range.

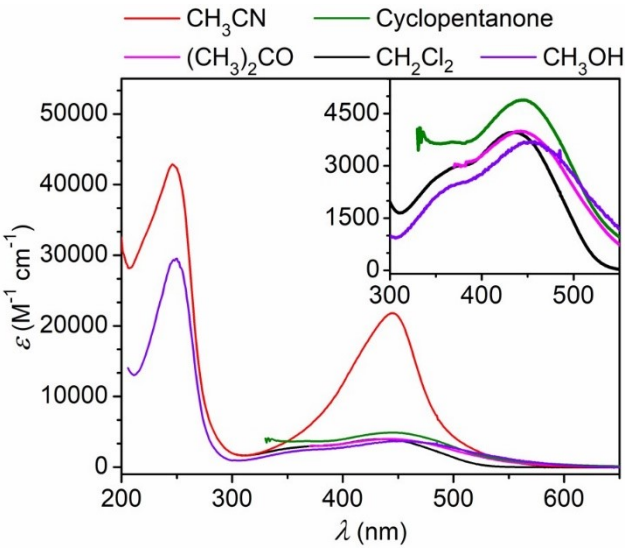

Figure 3.5.3. Electronic absorption spectra of **4-1** in various solvents. The inset focuses on the visible region (300-670 nm).

4.5.5 Solution Magnetic Data.

The temperature dependence of the magnetic susceptibility for **4-1** is measured in several solvents at an 80 mM concentration between 2 and 300 K (Figures 4.5.4, 4.5.8, and A1.14). Because of the similarity between the magnetic behavior of **4-1** in cyclopentanone, CH_2Cl_2, CH_3OH, and $(CD_3)_2CO$, the measurement performed in CH_3OH will be used to describe the magnetic behavior in these four solvents. At 300 K, the $\chi_M T$ value in CH_3OH is 2.49 cm^3 K mol^{-1}, and upon a decrease in the temperature, a small discontinuity is observed in the $\chi_M T$ value around the freezing point of the solvent. Upon further cooling, the $\chi_M T$ value steadily decreases until ~10 K; below this, the decrease becomes more dramatic, and at 4 K the $\chi_M T$ value is 1.94 cm^3 K mol^{-1}. This behavior is similar to the solid state data; suggesting that when **4-1** is dissolved in these solvents, the first coordination environment around the iron(II) center is N_4O_2, similar to the solid state.

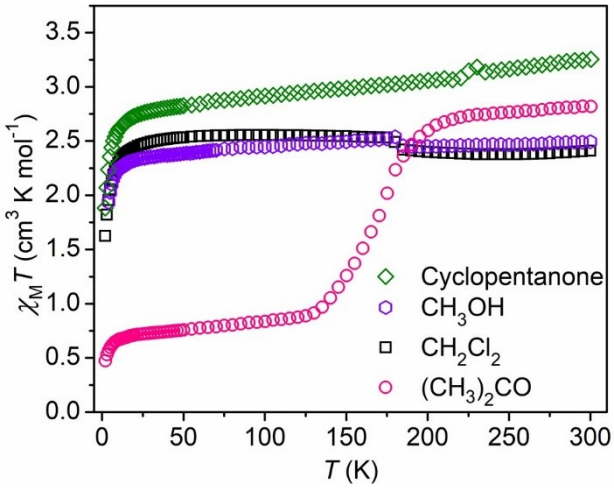

Figure 3.5.4. Temperature dependence of magnetic susceptibility for an 80 mM solution of **4-1** in cyclopentanone (green diamonds), $(CH_3)_2CO$ (pink circles), CH_3OH (purple hexagons), and CH_2Cl_2 (black squares) collected between 2 K and 300 K at 1000 Oe.

The behavior of **4-1** dissolved in $(CH_3)_2CO$ differs significantly from the other solvents. The $\chi_M T$ value at 300 K is 2.75 cm^3 K mol^{-1} and decreases monotonically upon cooling to ~200 K, at which point a dramatic decrease in the susceptibility is observed, indicative of a spin-state switching event. The sharp decrease continues until 130 K, whereupon the $\chi_M T$ value decreases more gradually until ~10 K, where the $\chi_M T$ value is 0.67 cm^3 K mol^{-1} (HS fraction $\gamma_{HS} \approx 0.22$, Figure A1.16). Upon further cooling the decrease in $\chi_M T$ becomes more dramatic; at 2 K the $\chi_M T$ value is 0.47 cm^3 K mol^{-1}. This final downturn at lower temperatures is most likely due to anisotropy and/or antiferromagnetic coupling of the remaining HS species. In $(CH_3)_2CO$, **4-1** never reaches a fully LS state, resulting in an incomplete spin state switching event with a $T_{1/2}$ value of 171 K. The thermodynamic values for this spin-switching event were calculated by fitting the data to the ideal solution model; see Appendix 1 for more information.[44,45] Assuming 80% of the sample undergoes the spin-switching event and the other 20% remains HS at all temperatures the best fit gives the following spin-state-switching enthalpy and entropy values, 19 kJ mol^{-1} and 112 J mol^{-1} K^{-1}, respectively. These values agree with previously reported values for solution spin-switching compounds.[11,16,19,46]

The significant differences in the magnetic data collected in $(CH_3)_2CO$ compared to the other solvents and the solid state lead us to hypothesize that one or both triflates are no longer coordinated to the iron(II) center and/or that interaction with $(CH_3)_2CO$ freezes the compound into a conformation that favors a LS species. Regarding the second possibility, we first measured the susceptibility in the warming cycle and then the cooling cycle and found that both cycles overlay (Figure A1.15), suggesting that the spin-state switching event is not due to the freezing event, but this does not rule out the possibility of a spin-change-enabling aggregation step while **4-1** is still in the solution phase.

4.5.6 ^{19}F NMR.

The room temperature ^{19}F NMR spectra of concentrated samples of **4-1** in a variety of solvents are shown in Figure 4.5.5. In CD_2Cl_2, cyclopentanone, and $(CD_3)_2CO$ a single broad signal can be observed between -18 and -26 ppm. In CD_3OD, a broad signal is found more upfield at -69 ppm. Further upfield at -77 ppm, a sharp signal is observed in CD_3CN. The broadness of the signals in CD_2Cl_2, cyclopentanone, $(CD_3)_2CO$, and CD_3OD, indicates the presence of a paramagnetic species in solution; whereas in CD_3CN, the sharp signal indicates a diamagnetic species. To determine whether a solvent is displacing triflate counteranions and therefore causing changes in the magnetic properties and chemical shifts of **1**, metal-bound and unbound triflate standards were also characterized (Figure 4.5.5). The paramagnetic complex, (1,4-bis(*N,N*-dimethylpropan-1-amine)-2,3-dimethyl-1,4-diazabutadiene)$Fe(OTf)_2$, ($[N_4Fe(OTf)_2]$),[47] is reported to contain bound triflate anions that result in one broad signal at -8 ppm ($CDCl_3$). The metal complex salts $Fe(OTf)_2$ and $Zn(OTf)_2$ serve as unbound triflate standards, as the triflate anions dissociate in the presence of coordinating solvents. In addition, the paramagnetic iron(II) and diamagnetic zinc(II) ions illustrate the effect that a HS or a LS species, respectively, will have on the triflate anion ^{19}F signal. The unbound triflates have a broad signal at -69 ppm in a paramagnetic environment [$Fe(OTf)_2$ and CD_3CN] and a sharp signal at -77 ppm in a diamagnetic environment [$Zn(OTf)_2$ and CD_3CN]. The bound triflate standard suggests that the downfield shifting of the resonances for **4-1** in CD_2Cl_2, cyclopentanone, and $(CD_3)_2CO$ is the result of one or both triflate anions still bound to the iron(II) center. The assignment of the coordination of the triflate anions cannot be determined by the number of ^{19}F NMR signals observed. Rapid exchange between bound and unbound triflate anions can result in a single resonance that is the average of the coordination modes present in solution. The unbound triflate standards indicate that the signal observed when **4-1** is dissolved in

CD_3CN is due to both triflates being replaced by CD_3CN solvent, resulting in an iron(II) compound that is diamagnetic. Similarly, the broad upfield resonance observed for **4-1** in CD_3OD indicates that the triflates are no longer bound, but the resulting iron(II) species is paramagnetic.

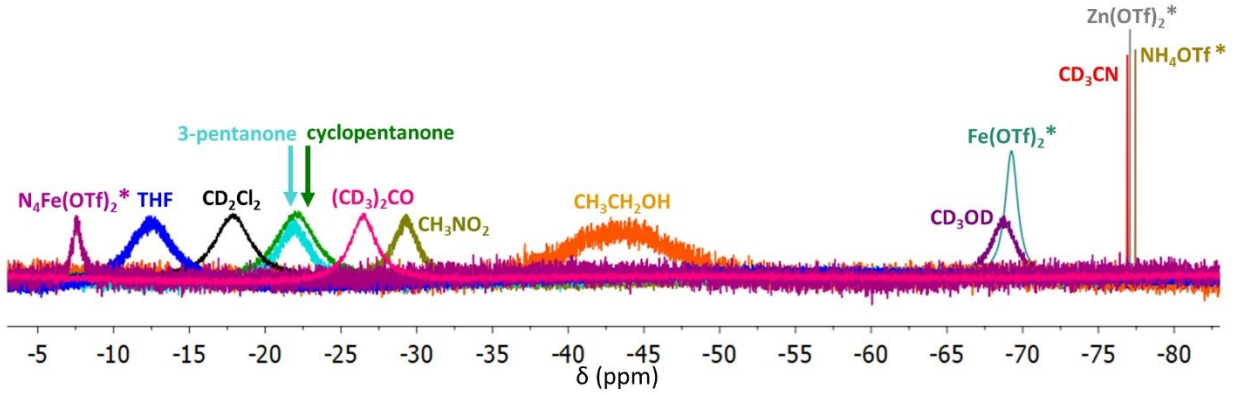

Figure 3.5.5. Overlay of ^{19}F NMR spectra of **4-1** in various deuterated and nondeuterated solvents compared to several standards. The spectra of **4-1** are labeled with the solvent; the triflate-containing standards (*) are labeled with the name of the standard and were collected in d_1-$CDCl_3$ or d_3-CD_3CN (see text).

4.5.7 VT ^{19}Fluorine NMR.

The ^{19}F NMR response of a 5 mM solution of **4-1** was measured between 188 and 298 K in CD_3OD, $(CD_3)_2CO$, and CD_2Cl_2 (Figure 4.5.6). At 298 K in CD_2Cl_2 (Figure 4.5.6a), a broad signal is observed at -19 ppm. As the temperature decreases this signal broadens further until it is no longer observed at 268 K. No precipitate was observed at this temperature, indicating that this signal loss is due to the fast exchange occurring between triflate anions in solution that results in the signal broadening into the baseline. No signals are observed until 218 K, where a very broad signal at -27 ppm grows in. Upon further cooling, this signal starts to sharpen and moves downfield to -24 ppm at 188 K. Along with this, two peaks appear between 193 K and 188 K: a sharp peak at -65 ppm and broad signal at -73 ppm. The downfield resonances are within the region where a triflate anion bound to a paramagnetic iron(II) center is expected, and the two upfield resonances

are where free triflate anions are observed. The data suggest that at room temperature, both triflates are bound, and upon decreasing the temperature one triflate stays bound while the other is unbound; the emergence of a third peak at -65 ppm suggests the formation of an additional species at low temperatures, or possibly a change in the aggregation of iron complexes and triflate anions.

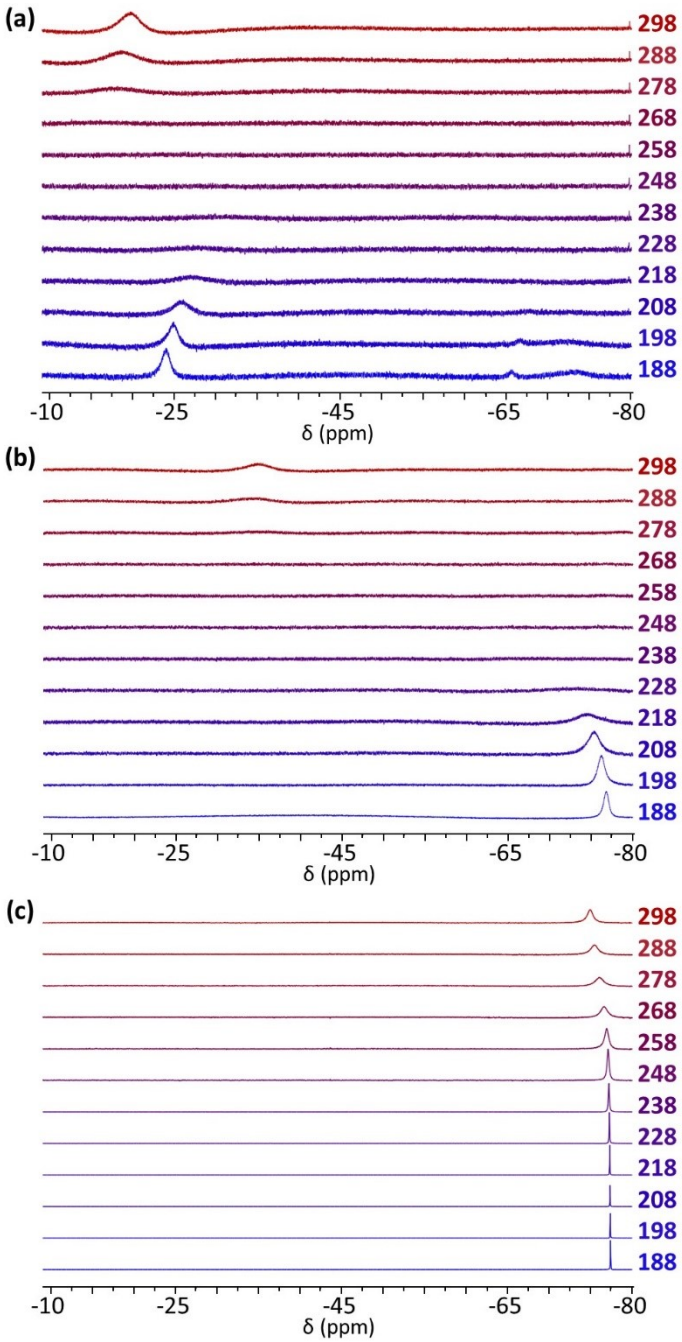

Figure 3.5.6. Variable temperature ^{19}F NMR of **4-1** in a 5 mM solution in d_2-CD_2Cl_2 (a), d_6-$(CD_3)_2CO$ (b), and d_4-CD_3OD (c), collected between 298 K and 188 K in 10 K increments.

When **4-1** is dissolved in $(CD_3)_2CO$, a broad signal is observed at -35 ppm at 298 K (Figure 4.5.6b). This chemical shift indicates the presence of a triflate bound to a paramagnetic iron(II) center. As the temperature decreases, the signal starts to broaden further until it is no longer observed at 268 K. At 228 K and below, a very broad signal appears at -73 ppm. As the temperature decreases further, this peak continues to sharpen and move further upfield, where at 188 K the signal is observed at -77 ppm. Similar to the CD_2Cl_2 sample, these data indicate the triflates are both bound to the iron(II) center at 298 K, but upon lowering of the temperature both anions are no longer bound.

Finally, in d_4-CD_3OD at 298 K, a broad signal at -75 ppm is observed (Figure 4.5.6c). As the temperature is decreased, the signal sharpens and shifts upfield until 238 K, where the peak is observed at -77 ppm and remains at this chemical shift until 188 K. Throughout this temperature range, the chemical shift is similar to what is observed for the unbound triflate standards, indicating that the triflates remain separated from the iron(II) center at all temperature measured.

4.5.8 Evans' Method (^{1}H NMR) Magnetic Susceptibility Measurements.

Evans' method was performed at 298 K on a 5 mM CD_3CN solution of **4-1** (Figure A1.21). At this temperature, only one tetramethylsilane (TMS) signal is observed, indicating a $\chi_M T$ value of 0.00 cm^3 K mol^{-1}, suggesting a LS species. VT Evans' method data were collected in CD_3OD, $(CD_3)_2CO$, and CD_2Cl_2 and run in tandem with the VT ^{19}F NMR experiments (Figures A1.23 – A1.25). Because of the similarity of the magnetic data in all solvents, CD_3OD will be used as a representative example to describe the magnetic behavior. At 298 K, the $\chi_M T$ value is 3.01 cm^3 K mol^{-1}, what is expected for a spin only value for HS iron(II) (g = 2, $\chi_M T$ = 3.00 cm^3 K mol^{-1}). As the temperature decreases, the magnetic susceptibility does not change significantly and reaches 2.98 cm^3 K mol^{-1} at 188 K (Figure A1.33). Two paramagnetic peaks can be observed at 298 K at

101 and 77 ppm. As the temperature decreases the peaks broaden and shift further downfield until they disappear at 258 and 218 K, for the 101 ppm and 77 ppm signals, respectively. A third broad paramagnetic signal is observed, only in CD_3OD, at 288 K. As the temperature decreases the peak sharpens at 258 K, then broadens again until it is no longer observed at 228 K.

4.5.9 Conductivity Measurements.

To further probe the extent of solvent displacement of bound triflate anions, the conductivity of a 1 mM solution of **4-1** was measured in a variety of solvents at room temperature (Table 4.5.2). In CH_2Cl_2 the conductivity of **4-1** is 4.8 μS cm^{-1}, this low value indicates that the triflates are most likely still bound to the iron(II) center. When **4-1** is dissolved in CH_3CN the conductivity is 253 μS cm^{-1}; this large value indicates that both triflates are no longer bound to the iron(II) center, whereas in cyclopentanone, $(CH_3)_2CO$, and CH_3OH the conductivity values are between those observed for CH_2Cl_2 and CH_3CN, suggesting the possibility of one bound triflate.

Table 3.5.2. Conductivity values for 1 mM solutions of **4-1** collected at 298 K in various solvents and listed in order of the solvent coordination ability index (a^{TM}).

Solvent	a^{TM}	Conductivity (μS cm^{-1})
CH_3CN	-0.2	252.9 ± 20
CH_3OH	-0.3	139.9 ± 11
THF	-0.3	1.9 ± 0.02
CH_3CH_2OH	-0.5	37.7 ± 0.6
$(CH_3)_2CO$	-1.0	117.8 ± 8
CH_3NO_2	-1.4	134 ± 0.9
CH_2Cl_2	-1.8	4.8 ± 0.03
3-pentanone		51.5 ± 0.5
Cyclopentanone		22.1 ± 0.4

4.5.10 Dynamic Light Scattering.

Previous reports have indicated aggregation and concentration can affect the magnetic properties.[48,49] To explore the extent to which aggregation plays a role in the magnetic properties

of **1**, dynamic light scattering experiments were performed at various temperatures (Table 4.5.3). Measurements were collected at the concentrations used for Evans' method NMR and solution MPMS magnetic susceptibility measurements, 5 and 80 mM, respectively. Studies performed in CH_3OH indicate minimal to no aggregation occurs at 5 and 80 mM. Meanwhile, the solvodynamic diameter is 2 orders magnitude larger in $(CD_3)_2CO$, $(CH_3)_2CO$, and CH_2Cl_2, suggesting some degree of aggregation of the iron-containing species. Interestingly, in $(CH_3)_2CO$, the two concentrations give significantly different solvodynamic diameter sizes, with smaller diameters found at lower concentrations at all temperatures measured. In addition, at 80 mM, the solovodynamic diameter appears to increase as the temperature is lowered: although this may be within the uncertainty of the measurement, it is the only such temperature-related change noted in the different measurements. The limited but combined studies suggest that $(CH_3)_2CO$ is uniquely showing concentration-dependent complex aggregation.

Table 3.5.3. Solvodynamic diameter of **4-1** in various solvents.

Solvent	Concentration (mM)	Diameter (nm) 298 K	Diameter (nm) 288 K	Diameter (nm) 278 K
CH_3OH	5	1.5 ± 0.6	1.0 ± 0.1	1.1 ± 0.3
	80	1.7 ± 0.3	1.6 ± 0.2	1.5 ± 0.1
$(CH_3)_2CO$	5	86 ± 8	83 ± 2	82 ± 2
	80	160 ± 40	180 ± 40	190 ± 50
$(CD_3)_2CO$	5	130 ± 30	130 ± 30	120 ± 40
	80	140 ± 50	140 ± 20	140 ± 40
CH_2Cl_2	5	120 ± 20	150 ± 60	110 ± 20
	80	170 ± 50	270 ± 80	230 ± 90

4.6 Discussion

The correlation of physical and electronic structures, key to developing an understanding in coordination chemistry, is intimately related to speciation. The iron(II)-containing compound **4-1** appears to offer many different species depending on the environmental conditions (Figure 4.6.1),

and while the spin-state changes observed may be attributed to traditional thermal spin-crossover (SCO) behavior, they may also arise from CISSS. In the solid state, the iron(II) center in **4-1** is bound by the ligand, (^{TIPS}C≡C)$_3$tren, and two triflate anions, resulting in a *cis*-N_4O_2 coordination environment. The Fe-N bond distances at 100 K suggest that the complex is in the HS state; solid state magnetic data support this assignment and show that this spin state is retained between 2 and 300 K. Because of the weakly-coordinated triflate counter anions, the coordination environment around the iron(II) center can change in the presence of solvents. Given the differences in the solid-state Fe-O bond distances, we might expect that the triflate trans to the imine will be the first to dissociate in the presence of a coordinating solvent; notwithstanding, we recognize that in solution the two triflates could have similar properties and dissociate equally. Remarkably, the solubility of **4-1** allows for a variety of coordinating and noncoordinating solvents to be examined to probe the extent to which they promote SCO and/or CISSS. The following discussion will focus on CH_3CN, CH_3OH, $(CH_3)_2CO$, cyclopentanone, CH_2Cl_2, and their deuterated analogs; the results for all other solvents tested can be found in Appendix 1.

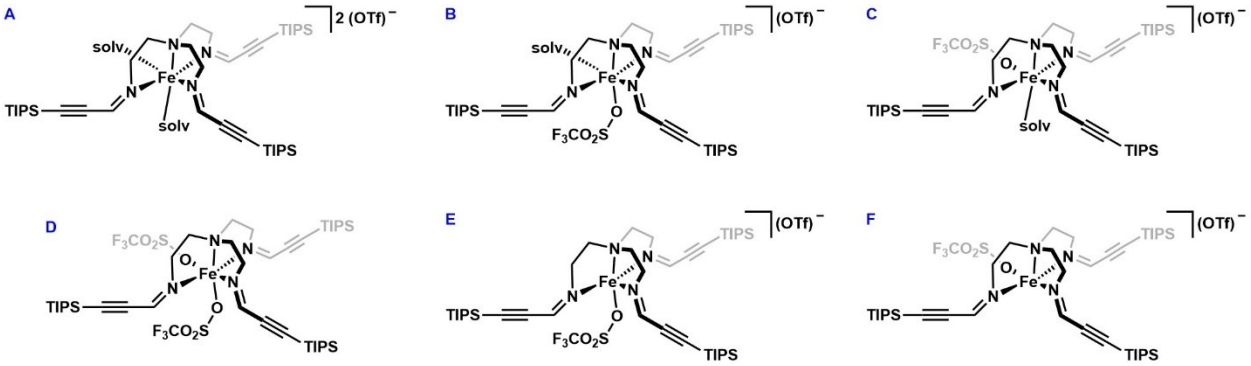

Figure 3.5.7. Overview of coordination environment of **4-1** in various media: replacement of both triflate anions by solvent (A), replacement of one triflate with solvent (B or C), two bound triflate anions (D), pentacoordination via dissociation of one triflate (E or F).

4.6.1 Speciation and Spin in Coordinating Environments.

When **4-1** is dissolved in the two moderately strong coordinating solvents, CH_3CN and CH_3OH, it exhibits different magnetic properties compared to the solid state. Spectroscopic results tell us that these differences are due to the change in the coordination environment around the iron center upon interaction with these solvents. The chemical shift of the ^{19}F NMR signal in CD_3CN (-77 ppm) is found where an unbound triflate in a diamagnetic environment [$Zn(OTf)_2$] signal is observed. Similarly, in d_4-CD_3OD, the signal is observed at -69 ppm near where an unbound triflate in a paramagnetic environment ($Fe(OTf)_2$) is found. Upon a decrease in the temperature to 188 K for the CD_3OD sample, the ^{19}F chemical shift shifts slightly to -77 ppm. This upfield shift is due to the temperature dependence of the paramagnetic signal of **4-1** and indicates that even at low temperatures the triflates are unbound in CD_3OD. For CH_3CN and CH_3OH solvent environments, structure A is most likely (Figure 4.6.1). While it is possible that more than two CH_3OH molecules are bound to the iron(II) center, via displacement of the bridgehead nitrogen and both triflates, the similarity of the room temperature ^1H NMR spectra in multiple solvents indicate that the local geometry for **4-1** is similar in $(CD_3)_2CO$ and CD_2Cl_2, suggesting that the bridgehead nitrogen is still bound to the iron(II) center.

While both solvents displace the triflate counteranions in **1**, the magnetic properties are vastly different, as found by a comparison of the electronic absorption and solution magnetic susceptibility data. The large molar absorptivity in CH_3CN (21796 M^{-1} cm^{-1}) is typical for a LS iron(II) species; whereas, in CH_3OH the molar absorptivity (3670 M^{-1} cm^{-1}) indicates a HS species. These magnetic assignments are supported by the room temperature Evans' method. As well, the solution magnetometry data for **4-1** in CH_3OH indicate that a HS species is present in the full temperature range measured, 300 K to 2 K. The differences in the magnetic data between these

two moderately strong coordinating solvents are due to the differences in the coordination environment around the iron(II) center. When dissolved in CH_3CN, the solvent molecules displace the triflates and cause **4-1** to change from a N_4O_2 to a N_6 first coordination sphere, leading to a LS state, whereas in CH_3OH, the solvent still displaces the triflates, but results in the first coordination sphere staying as N_4O_2 to retain the HS state.

The contrasting magnetic susceptibility data between the two moderately strong coordinating solvents also lead to differences in the conductivity measurements. The conductivity values in these solvents indicate the presence of two unbound triflate counteranions, consistent with structure A. In addition, conductivity can be connected to spin state properties. The room temperature conductivity value for CH_3CN (253 $\mu S\ cm^{-1}$) is larger than the value for CH_3OH (140 $\mu S\ cm^{-1}$). Upon changing the spin state, the size of the metal center also changes, leading to smaller LS iron(II) and larger HS iron(II) ions. The larger HS iron(II) might be expected to lead to a smaller conductivity value due to the higher viscosity from the stronger Van der Waals interactions between the cationic and anionic species.[50,51] Because of this, we correlate the higher conductivity observed in CH_3CN to **4-1** being in the LS state, whereas the lower value in CH_3OH is consistent with **4-1** in the HS state. This change in conductivity values due to the spin state has been observed previously for bis(pyrazolyl)methane iron(II) complexes in solution.[25]

4.6.2 Spin and Speciation in Noncoordinating Environments.

When **4-1** is dissolved in the noncoordinating solvent CH_2Cl_2, the magnetic properties are similar to what is observed in the solid-state, but the speciation is more complicated. The room temperature ^{19}F NMR chemical shift is close to where the bound triflate standard in a paramagnetic environment is observed, indicating that both triflates are most likely bound to the iron(II) center to give structure D (Figure 4.6.1). This assignment is supported by the small room temperature

conductivity value, 4.8 μS cm^{-1}. Dynamic light scattering experiments indicate that temperature independent aggregation of **4-1** occurs at 5 and 80 mM concentrations in CH_2Cl_2. VT magnetic measurements of **4-1** in an 80 mM solution in CH_2Cl_2 (magnetometry) and a 5 mM solution in CD_2Cl_2 (Evans' method) samples indicate that **4-1** stays HS at all temperatures measured, suggesting that aggregation in noncoordinating solvents does not significantly impact the magnetic properties of **1**. However, at lower temperatures, the ^{19}F NMR data are consistent with one bound triflate and one unbound triflate, and the presence of an additional unbound triflate species, suggesting a change from structure D at 300 K to structure B/C or E/F upon a lowering of the temperature of the sample, likely involving the conversion between mono-vacant octahedral geometries given the poor coordinating ability of CH_2Cl_2 and the similarity of the ^1H NMR spectra with other octahedral versions of **4-1** in other solvents. This increased anion-cation dissociation upon *lowering* of the temperature is reversed from typical ligand/anion dissociations for transition metal complexes. Notwithstanding, a similar low temperature dissociation process has been observed before in a diiron(II) complex.[52] In that case, the dissociation of all of the bound triflate anions at low temperatures results in a the formation of a LS species for the diiron species.

4.6.3 Speciation and Spin in Ketones.

Dissolved in ketones, **4-1** exhibits interesting and diverse behaviors. The room temperature ^{19}F NMR signal for **4-1** in $(CD_3)_2CO$ is found between where bound and free triflate shifts are observed. The observation of one downfield signal is consistent with an average environment where one triflate is bound to the iron(II) center, but exchanging rapidly with the unbound triflate. The room temperature conductivity is lower than what is observed for **4-1** in the moderately strong coordinating solvents, when both triflates are free, but much higher than near-zero, as is observed

in a noncoordinating solvent. Therefore, both the ^{19}F NMR spectrum and the conductivity value suggest that **4-1** exists as structure B/C at room temperature.

VT magnetic measurements via magnetometry of **4-1** in $(CH_3)_2CO$, at an 80 mM concentration, indicate that the iron(II) center undergoes an incomplete spin-state switching event, with a $T_{1/2}$ value of 171 K (Figures 4.5.4 and 4.6.2). The warming and cooling curves for this spin switching event overlay, indicating that the species formed upon freezing of the sample at low temperatures can be reproduced, so we surmise that the spin switching event is due to the species present in solution as it freezes, and not from a change in packing upon freezing. To determine if this partial spin switching is intrinsic to **4-1** with one triflate bound (SCO) or due to the loss of a second triflate from the coordination sphere (CISSS), VT ^{19}F NMR was used in tandem with Evans' method. As the temperature is decreased the ^{19}F NMR signal of **4-1** in $(CD_3)_2CO$ shifts upfield to a range consistent with two unbound triflates (structure A).

To this point, we have assumed that solution structures of **4-1** do not depend on the hydrogen isotopes involved, and that the structural data from NMR spectroscopy can map onto spin changes probed by magnetometry. However, while ligand exchange occurs in $(CD_3)_2CO$ as the temperature is decreased, similar to what is observed in CD_2Cl_2, this anion dissociation event does not lead to a spin state change as is evidenced by VT magnetometry measurements, both at low (5 mM via Evans' method; Figure A1.33) and higher (80 mM via magnetometry; Figure 4.6.2) concentrations.

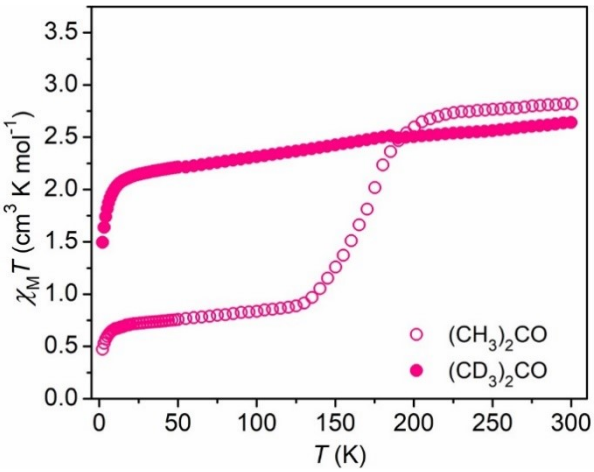

Figure 3.5.8. Comparison of solution magnetic data of and 80 mM solution of **4-1** in non-deuterated acetone (open pink circles) and deuterated acetone (closed pink circles) collected via magnetometry.

We are not able to quantify the magnetic susceptibility via Evans' method in an 80 mM $(CD_3)_2CO$ sample, because the high concentration obscures the solvent signals, but we note that the ^{19}F NMR signals give a qualitatively similar trend to the 5 mM sample (Figures A1.25 – A1.26), suggesting that triflates continue to dissociate at higher concentrations. Importantly, dissociation of the triflates is *not* dependent on the isotope identity, because the VT ^{19}F NMR spectra of **4-1** in $(CH_3)_2CO$ show ligand dissociation behavior similar to $(CD_3)_2CO$ for both 5 and 80 mM concentrations (Figure A1.28 – A1.29). The loss of the remaining bound triflate in the 80 mM samples occurs right at the onset of the spin state switching event in the magnetometry experiment, suggesting that this event is due to $(CH_3)_2CO$ fully displacing both triflates to produce structure A (Figure 4.6.1), resulting in a coordination environment that supports spin state switching in $(CH_3)_2CO$. The speciation result is unusual in that structure A implies a N_4O_2 coordination environment, very similar to that found for **4-1** in CH_3OH, and yet for $(CH_3)_2CO$ spin state switching is operative.

Dynamic light scattering experiments performed on **4-1** in $(CD_3)_2CO$ and $(CH_3)_2CO$ reveal significant differences in the effective particle sizes for the two solvents. In $(CD_3)_2CO$, the

solvodynamic diameter is invariant to the concentration and temperature, at least in the range of the Evans' method and MPMS magnetometry measurements, and suggests some aggregation between complexes, relative to the measurements carried out in CH_3OH. However, in the $(CH_3)_2CO$ environment, the solvodynamic diameter changes significantly between 5 and 80 mM, becomes larger than what is seen in the deuterated solvent, and increases as the temperature is lowered. These results suggest that aggregation plays a role in the spin switching event that is observed in the solution MPMS measurements.

Our provisional interpretation of the available data suggests that concentration-dependent aggregation of the $[((^{TIPS}C{\equiv}C)_3tren)Fe(OC(CH_3)_2)_2]^{2+}$ complex is important to the observation of spin-state switching. Attempts to measure magnetic susceptibility via MPMS for more dilute samples (< 80 mM) in $(CH_3)_2CO$ is complicated by the large background signal of the solvent, but preliminary measurements suggest fully HS behavior at 20 mM concentrations of **1**. We note that second-coordination-sphere interactions between a 1D Fe(II) coordination polymer and $(CH_3)_2CO$ lead to a spin switching event without the need for direct replacement of anion by solvent,[53] but there is evidence *via* ^{19}F NMR experiments for ligand exchange preceding the spin-state switching event of **1**. We also note that concentration dependence of SCO properties have been reported for iron(III) salen complexes,[48,49,54] but we are not aware of studies probing differences between protonated and deuterated solvents. Perhaps the 10% difference in density between $(CH_3)_2CO$ and $(CD_3)_2CO$ is sufficient to perturb spin-state switching properties for a precariously balanced ligand field, as **4-1** seems to have. Further studies of concentration and aggregation effects on the magnetic properties of **4-1** are planned for a future report.

The relative proximity of the $T_{1/2}$ value of the spin switching event of **4-1** in $(CH_3)_2CO$, 171 K, to the freezing point of the solvent, 178 K, led us to investigate the magnetic properties of

another moderately coordinating solvent to elucidate spin and potential aggregation behaviors. We chose cyclopentanone because of its higher freezing point, but otherwise near structural and chemical homology with $(CH_3)_2CO$. The room temperature ^{19}F NMR signal is slightly more downfield than what is observed in $(CD_3)_2CO$, but not where a fully bound triflate is observed, suggesting that one triflate is bound while the other is undergoing fast exchange, preventing two ^{19}F NMR signals from being observed. Meanwhile, the conductivity value at room temperature is 22.1 μS cm^{-1}, significantly lower than what is observed in $(CH_3)_2CO$. The combined data suggest that while in both solvents one triflate stays bound, in cyclopentanone the anion exchange equilibrium favors the second triflate also remaining bound, whereas in $(CH_3)_2CO$ the equilibrium favors the second triflate being free. Solution magnetometry data indicate that **4-1** dissolved in cyclopentanone remains HS at all temperatures measured, similar to the data obtained in CH_3OH. VT ^{19}F NMR experiments performed in cyclopentanone show no change in the chemical shift between 298 and 278 K (Figure A1.27), consistent with no significant change in speciation as the temperature is decreased and suggesting an equilibrium between structures B/C and D with D preferred (Figure 4.6.1). Similar to d_6-$(CD_3)_2CO$, the signal broadens out and is no longer observed below 278 K. Unfortunately, because of the freezing point of cyclopentanone, the study could not go below 218 K, and at this temperature the ^{19}F signal is too broad to be observed. Thus, while a temperature-dependent speciation change in cyclopentanone cannot be definitively determined, the solution magnetic data show that even if a speciation change did occur, the resulting species does not support a spin switching event but instead favors the HS state.

4.7 Conclusion

Herein we present the synthesis and characterization of the novel complex **4-1** in the solid state and several solution environments. The solid-state structure shows a N_4O_2 first coordination sphere and metal–ligand distances suggesting a HS species. The magnetic measurements in the solid state show that **4-1** remains HS at all temperatures, but once in solution a variety of magnetic properties are observed. Strongly coordinating solvents replace both triflate counter anions as seen in the ^{19}F NMR spectra. The change from a N_4O_2 coordination environment to a N_6 environment in CH_3CN results in a LS species, but in CH_3OH the N_4O_2 environment as well as the high spin state at all temperatures is retained. In the noncoordinating solvent CH_2Cl_2, **4-1** has both triflates bound and remains HS at room temperature, but upon cooling, one triflate dissociates from the HS iron(II) center. Finally, when placed in weakly coordinating solvents, the ^{19}F NMR data indicate that only one triflate remains bound to the iron(II) center. This results in HS species at room temperature, but upon cooling **4-1** remains HS in cyclopentanone and undergoes spin switching in $(CH_3)_2CO$ with a $T_{1/2}$ value of 171 K. VT ^{19}F NMR in $(CH_3)_2CO$ suggests that both triflates are no longer bound to the iron(II) center *before* the spin switching event occurs. Therefore, the observed spin switching event is due to the species formed by a temperature-dependent coordination change, rather than intrinsic SCO of $[((^{TIPS}C{\equiv}C)_3tren)Fe(OTf)(OC(CH_3)_2)]^+$. Intriguingly, magnetic susceptibility data collected at different concentrations suggest additional impacts of aggregation on the iron(II) spin state, and in a comparison of the behaviors in $(CH_3)_2CO$ and $(CD_3)_2CO$, it can be seen that deuteration/protonation of the $(CH_3)_2CO$ can have a large impact on the magnetic properties of **1**. The relationship between the spin state, aggregation, and deuteration will be further examined in a future report. The studies presented here indicate the importance of the solvent

choice on speciation and magnetic properties of a neutral complex and highlight the need for multiple physicochemical probes to identify complex species in solution.

References

(1) Gütlich, P.; Goodwin, H. A. Spin Crossover-An Overall Perspective. *Top. Curr. Chem.* **2004**, *233*, 1–47.

(2) Khusniyarov, M. M. How to Switch Spin-Crossover Metal Complexes at Constant Room Temperature. *Chem. - A Eur. J.* **2016**, *22* (43), 15178–15191.

(3) Brooker, S. Spin Crossover with Thermal Hysteresis: Practicalities and Lessons Learnt. *Chem. Soc. Rev.* **2015**, *44* (10), 2880–2892.

(4) Senthil Kumar, K.; Ruben, M. Emerging Trends in Spin Crossover (SCO) Based Functional Materials and Devices. *Coord. Chem. Rev.* **2017**, *346*, 176–205.

(5) Kahn, O.; Martinez, C. J. Spin-Transition Polymers: From Molecular Materials toward Memory Devices. *Science (80-.).* **1998**, *279* (5347), 44–48.

(6) Halcrow, M. A. Structure:Function Relationships in Molecular Spin-Crossover Complexes. *Chem. Soc. Rev.* **2011**, *40* (7), 4119–4142.

(7) Jeon, I.-R.; Park, J. G.; Haney, C. R.; Harris, T. D. Spin Crossover Iron(Ii) Complexes as PARACEST MRI Thermometers. *Chem. Sci.* **2014**, *5* (6), 2461–2465.

(8) Molnár, G.; Salmon, L.; Nicolazzi, W.; Terki, F.; Bousseksou, A. Emerging Properties and Applications of Spin Crossover Nanomaterials. *J. Mater. Chem. C* **2014**, *2* (8), 1360–1366.

(9) Ni, Z.; Shores, M. P. Magnetic Observation of Anion Binding in Iron Coordination Complexes: Toward Spin-Switching Chemosensors. *J. Am. Chem. Soc.* **2009**, *131* (1), 32–33.

(10) Singh, S.; Brooker, S. Extension of Azine-Triazole Synthesis to Azole-Triazoles Reduces Ligand Field, Leading to Spin Crossover in Tris-L Fe(II). *Inorg. Chem.* **2020**, *59* (2), 1265–1273.

(11) Kershaw Cook, L. J.; Kulmaczewski, R.; Mohammed, R.; Dudley, S.; Barrett, S. A.; Little, M. A.; Deeth, R. J.; Halcrow, M. A. A Unified Treatment of the Relationship Between Ligand Substituents and Spin State in a Family of Iron(II) Complexes. *Angew. Chemie* **2016**, *55* (13), 4327–4331.

(12) Lin, H.-J.; Siretanu, D.; Dickie, D. A.; Subedi, D.; Scepaniak, J. J.; Mitcov, D.; Clérac, R.; Smith, J. M. Steric and Electronic Control of the Spin State in Three-Fold Symmetric, Four-Coordinate Iron(II) Complexes. *J. Am. Chem. Soc.* **2014**, *136* (38), 13326–13332.

(13) Prat, I.; Company, A.; Corona, T.; Parella, T.; Ribas, X.; Costas, M. Assessing the Impact of Electronic and Steric Tuning of the Ligand in the Spin State and Catalytic Oxidation Ability of the FeII(Pytacn) Family of Complexes. *Inorg. Chem.* **2013**, *52* (16), 9229–9244.

(14) Nakano, K.; Suemura, N.; Yoneda, K.; Kawata, S.; Kaizaki, S. Substituent Effect of the Coordinated Pyridine in a Series of Pyrazolato Bridged Dinuclear Diiron(II) Complexes on the Spin-Crossover Behavior. *Dalt. Trans.* **2005**, No. 4, 740–743.

(15) Hogue, R. W.; Feltham, H. L. C.; Miller, R. G.; Brooker, S. Spin Crossover in Dinuclear N4S2 Iron(II) Thioether-Triazole Complexes: Access to [HS-HS], [HS-LS], and [LS-LS] States. *Inorg. Chem.* **2016**, *55* (9), 4152–4165.

(16) Rodríguez-Jiménez, S.; Yang, M.; Stewart, I.; Garden, A. L.; Brooker, S. A Simple Method of Predicting Spin State in Solution. *J. Am. Chem. Soc.* **2017**, *139* (50), 18392–18396.

(17) Pan, Y.; Meng, Y. S.; Liu, Q.; Gao, W. Q.; Liu, C. H.; Liu, T.; Zhu, Y. Y. Construction of SCO-Active Fe(II) Mononuclear Complexes from the Thio-Pybox Ligand. *Inorg. Chem.* **2020**, *59* (11), 7398–7407.

(18) Capel Berdiell, I.; Kulmaczewski, R.; Halcrow, M. A. Iron(II) Complexes of 2,4-Dipyrazolyl-1,3,5-Triazine Derivatives - The Influence of Ligand Geometry on Metal Ion Spin State. *Inorg. Chem.* **2017**, *56* (15), 8817–8828.

(19) Shores, M. P.; Klug, C. M.; Fiedler, S. R. Spin-State Switching in Solution. In *Spin-Crossover Materials: Properties and Applications*; Halcrow, M. A., Ed.; John Wiley & Sons Ltd: Oxford, UK, 2013; pp 281–301.

(20) Rodríguez-Jiménez, S.; Barltrop, A. S.; White, N. G.; Feltham, H. L. C.; Brooker, S. Solvent Polarity Predictably Tunes Spin Crossover T1/2 in Isomeric Iron(II) Pyrimidine Triazoles. *Inorg. Chem.* **2018**, *57* (11), 6266–6282.

(21) Weber, B.; Walker, F. A. Solution NMR Studies of Iron(II) Spin-Crossover Complexes. *Inorg. Chem.* **2007**, *46* (16), 6794–6803.

(22) Bryliakov, K. P.; Duban, E. A.; Talsi, E. P. The Nature of the Spin-State Variation of [FeII(BPMEN)(CH3CN)2](ClO4)2 in Solution. *Eur. J. Inorg. Chem.* **2005**, *2005* (1), 72–76.

(23) Diebold, A.; Hagen, K. S. Iron(II) Polyamine Chemistry: Variation of Spin State and Coordination Number in Solid State and Solution with Iron(II) Tris(2-Pyridylmethyl)Amine Complexes. *Inorg. Chem.* **1998**, *37* (2), 215–223.

(24) Nowak, R.; Adi Prasetyanto, E.; De Cola, L.; Bojer, B.; Siegel, R.; Senker, J.; Rössler, E.; Weber, B. Proton-Driven Coordination-Induced Spin State Switch (PD-CISSS) of Iron(II) Complex. *Chem. Commun* **2017**, *53* (5), 971–974.

(25) Keisers, K.; Hüppe, H. M.; Iffland-Mühlhaus, L.; Hoffmann, A.; Göbel, C.; Apfel, U. P.; Weber, B.; Herres-Pawlis, S. Interplay of Spin Crossover and Coordination-Induced Spin State Switch for Iron Bis(Pyrazolyl)Methanes in Solution. *Inorg. Chem.* **2020**, *59* (20), 15343–15354.

(26) Thies, S.; Sell, H.; Schutt, C.; Bornholdt, C.; Nather, C.; Tuczek, F.; Herges, R. Light-Induced Spin Change by Photodissociable External Ligands: A New Principle for Magnetic

Switching of Molecules. *J. Am. Chem. Soc.* **2011**, *133* (40), 16243–16250.

(27) Kroll, N.; Theilacker, K.; Schoknecht, M.; Baabe, D.; Wiedemann, D.; Kaupp, M.; Grohmann, A.; Hörner, G. Controlled Ligand Distortion and Its Consequences for Structure, Symmetry, Conformation and Spin-State Preferences of Iron(II) Complexes. *Dalt. Trans.* **2015**, *44*, 19232–19247.

(28) Blakesley, D. W.; Payne, S. C.; Hagen, K. S. Spin-State Variation in Solid State and Solution of Mononuclear Iron(II) 1,4,7-Trimethyl-1,4,7-Triazacyclonane Complexes. *Inorg. Chem.* **2000**, *39* (9), 1979–1989.

(29) Goldsmith, C. R.; Jonas, R. T.; Cole, A. P.; Stack, T. D. P. A Spectrochemical Walk: Single-Site Perturbation within a Series of Six-Coordinate Ferrous Complexes. *Inorg. Chem.* **2002**, *41*, 4642–4652.

(30) Barrett, S. A.; Kilner, C. A.; Halcrow, M. A. Spin-Crossover in [Fe(3-Bpp)2][BF4]2 in Different Solvents - A Dramatic Stabilisation of the Low-Spin State in Water. *Dalt. Trans.* **2011**, *40* (45), 12021–12024.

(31) Kershaw Cook, L. J.; Mohammed, R.; Sherborne, G.; Roberts, T. D.; Alvarez, S.; Halcrow, M. A. Spin State Behavior of Iron(II)/Dipyrazolylpyridine Complexes. New Insights from Crystallographic and Solution Measurements. *Coord. Chem. Rev.* **2015**, *289–290* (1), 2–12.

(32) Turner, J. W.; Schultz, F. A. Solution Characterization of the Iron(II) Bis(1,4,7-Triazacyclononane) Spin-Equilibrium Reaction. *Inorg. Chem.* **2001**, *40* (20), 5296–5298.

(33) Strauß, B.; Gutmann, V.; Linert, W. Spin-Crossover Complexes in Solution, II Solvent Effects on the High Spin-Low Spin-Equilibrium of [Fe(Bzimpy)2](ClO4)2. *Monatshefte für Chemie Chem. Mon.* **1993**, *124* (5), 515–522.

(34) Gómez-Bengoa, E.; García, J. M.; Jiménez, S.; Lapuerta, I.; Mielgo, A.; Odriozola, J. M.; Otazo, I.; Razkin, J.; Urruzuno, I.; Vera, S.; et al. Asymmetric Synthesis of Propargylic Alcoholsviaaldol Reaction of Aldehydes with Ynals Promoted by Prolinol Ether–Transition Metal–Brønsted Acid Cooperative Catalysis. *Chem. Sci.* **2013**, *4* (8), 3198–3204.

(35) APEX3. Bruker Analytical X-Ray Systems, Inc.: Madison, WI. 2016.

(36) Sheldrick, G. M. SHELXTL. *SHELXTL*. Version 6. Analytical X-Ray Systems: Madison, WI. 1999.

(37) Bain, G. A.; Berry, J. F. Diamagnetic Corrections and Pascal's Constants. *J. Chem. Educ.* **2008**, *85* (4), 532–536.

(38) Chilton, N. F.; Anderson, R. P.; Turner, L. D.; Soncini, A.; Murray, K. S. PHI: A Powerful New Program for the Analysis of Anisotropic Monomeric and Exchange-Coupled Polynuclear d- and f-Block Complexes. *J. Comput. Chem.* **2013**, *34* (13), 1164–1175.

(39) Alvarez, S.; Alemany, P.; Casanova, D.; Cirera, J.; Llunell, M.; Avnir, D. Shape Maps and

Polyhedral Interconversion Paths in Transition Metal Chemistry. *Coord. Chem. Rev.* **2005**, *249* (17–18), 1693–1708.

(40) Chiou, Y.-M.; Que Jr., L. Models for Alpha-Keto Acid-Dependent Non-Heme Iron Enzymes: Structures and Reactivity of [FeII(L)(O2CCOPh)](ClO4) Complexes. *J. Am. Chem. Soc.* **1995**, *117* (14), 3999–4013.

(41) Jang, H. G.; Cox, D. D.; Que Jr., L. A Highly Reactive Functional Model for the Catechol Dioxygenases. Structure and Properties of [Fe(TPA)DBC]BPh4. *J. Am. Chem. Soc.* **1991**, *113* (24), 9200–9204.

(42) Díaz-Torres, R.; Alvarez, S. Coordinating Ability of Anions and Solvents towards Transition Metals and Lanthanides. *Dalt. Trans.* **2011**, *40* (40), 10742–10750.

(43) Alvarez, S. Coordinating Ability of Anions, Solvents, Amino Acids, and Gases towards Alkaline and Alkaline-Earth Elements, Transition Metals, and Lanthanides. *Chem. – A Eur. J.* **2020**, *26* (19), 4350–4377.

(44) Kahn, O. *Molecular Magnetism*; VCH: New York, NY, 1993.

(45) Ni, Z.; Shores, M. P. Supramolecular Effects on Anion-Dependent Spin-State Switching Properties in Heteroleptic Iron(II) Complexes. *Inorg. Chem.* **2010**, *49* (22), 10727–10735.

(46) Toftlund, H. Spin Equilibrium in Solution. *Monatshefte Fur Chemie* **2001**, *132*, 1269–1277.

(47) Hardman, N. J.; Fang, X.; Scott, B. L.; Wright, R. J.; Martin, R. L.; Kubas, G. J. High-Spin Diimine Complexes of Iron(II) Reject Binding of Carbon Monoxide: Theoretical Analysis of Thermodynamic Factors Inhibiting or Favoring Spin-Crossover. *Inorg. Chem.* **2005**, *44* (23), 8306–8316.

(48) Vicente, A. I.; Wu, X.; Ortin, Y.; Ferreira, L. P.; Carvalho, M. D. D.; Realista, S.; Barker, A.; Morgan, G. G.; Galamba, N.; Costa, P. J.; et al. Directing Self-Assembly in Solution towards Improved Cooperativity in Fe(Iii) Complexes with Amphiphilic Tridentate Ligands. *Dalt. Trans.* **2019**, *48* (13), 4239–4247.

(49) Johnson, C. J.; Morgan, G. G.; Albrecht, M. Predictable Adjustment of Spin Crossover Temperature in Solutions of Iron(III) Complexes Functionalized with Alkyl-Urea Tails. *J. Mater. Chem. C* **2015**, *3*, 7883–7889.

(50) Makhlooghiazad, F.; Guazzagaloppa, J.; O'Dell, L. A.; Yunis, R.; Basile, A.; Howlett, P. C.; Forsyth, M. The Influence of the Size and Symmetry of Cations and Anions on the Physicochemical Behavior of Organic Ionic Plastic Crystal Electrolytes Mixed with Sodium Salts. *Phys. Chem. Chem. Phys.* **2018**, *20* (7), 4721–4731.

(51) Arkhipova, E. A.; Ivanov, A. S.; Maslakov, K. I.; Savilov, S. V.; Lunin, V. V. Effect of Cation Structure of Tetraalkylammonium- and Imidazolium-Based Ionic Liquids on Their Conductivity. *Electrochim. Acta* **2019**, *297*, 842–849.

(52) Samanta, S.; Demesko, S.; Dechert, S.; Meyer, F. A Two-in-One Pincer Ligand and Its Diiron(II) Complex Showing Spin State Switching in Solution through Reversible Ligand Exchange. *Angew. Chemie - Int. Ed.* **2015**, *54* (2), 583–587.

(53) Lennartson, A.; Southon, P.; Sciortino, N. F.; Kepert, C. J.; Frandsen, C.; Mørup, S.; Piligkos, S.; McKenzie, C. J. Reversible Guest Binding in a Non-Porous FeII Coordination Polymer Host Toggles Spin Crossover. *Chem. – A Eur. J.* **2015**, *21* (45), 16066–16072.

(54) Gandolfi, C.; Morgan, G. G.; Albrecht, M. A Magnetic Iron(III) Switch with Controlled and Adjustable Thermal Response for Solution Processing. *Dalt. Trans.* **2012**, *41*, 3726–3730.

Chapter 5: Synthetic Efforts Towards the Post-Synthetic Azide-Alkyne Cycloaddition Reaction on [((^{TIPS}C≡C)$_3$tren)Fe(OTf)$_2$]

5.1 Introduction

Post-synthetic modifications have been widely used for supramolecular architectures to add new functionalities to a complex after it has formed.[1,2] Successful post-synthetic reactions have mild reaction conditions, high yields, and minimal side products. This allows sensitive substituents to be added to the already formed complex, prevents decomposition of the complex, and ensures all reactive sites are fully converted to the desired product. Additionally, post-synthetic modifications can be paired with compounds that can undergo spin state switching. The moderate ligand field changes from the post synthetic modifications influence the magnetic properties of the resulting complexes providing a new pathway to induce the spin state switching event.[3–16] However, previously reported modifications have focused on modifying the ligand backbone and few have used these modifications to induce a spin state switching event by changing the first coordination sphere around the metal center.[11]

Pairing post synthetic modifications with changes to the first coordination sphere provides a targeted approach to modify the coordination environment around a metal center. This intentional coordination change by post synthetic modifications allows for synthetically challenging ligands to be bound to a metal center to form unique spin state switching complexes. Of the previously reported post-synthetic modification reactions, the azide-alkyne cycloaddition 1,2,3-triazole product is an ideal ligand for these studies. It has been shown that, when bound to an iron(II) center, the 1,2,3-triazole ring provides the appropriate ligand field for a thermal spin switching event.[17–20]

Additionally, the azide alkyne cycloaddition is an efficient reaction that has been reported to work under a variety of conditions.[21–24] When the reaction is performed without a catalyst, a mixture of 1,4 and 1,5 isomers can be obtained (Figure 5.1.1). However, regiospecificity can be achieved with the addition of a catalyst: the 1,4-isomer is explicitly synthesized with copper-based catalysts and the 1,5-isomer by ruthenium-based catalysts. The most common catalysts used for azide-alkyne cycloadditions are copper(I) salts, although terminal alkynes are needed for this type of catalyst (Figure 5.1.1).[23,24] Whereas, copper n-heterocyclic carbene (Cu(NHC)) and ruthenium based catalysts can transform both terminal and internal alkynes into fully substituted 1,2,3-triazoles.[21,22]

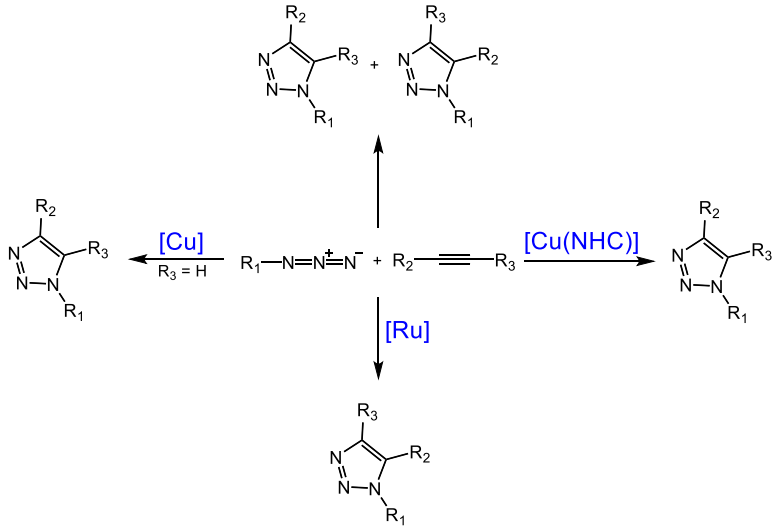

Figure 5.1.1. Cycloaddition of azides and alkynes results in mixtures of 1,4- and 1,5-isomers (top). When copper n-heterocyclic carbene catalysts are used the reaction proceeds with both terminal and internal alkynes and gives the 1,4-isomer (right). The cycloaddition on terminal and internal alkynes also proceeds with ruthenium catalyst but produces the 1,5-isomer (bottom). The cycloaddition with copper(I) catalysts only proceeds with terminal alkynes and produces the 1,4-isomer (left).

The alkyne containing compound [((^{TIPS}C≡C)$_3$tren)Fe(OTf)$_2$] (**5-1**) described in Chapter 4 is ideal for a post-synthetic modification using the azide-alkyne cycloaddition reaction. Efforts to

develop the rational synthetic procedure to promote the successful post-synthetic modification on **5-1** with minimal transmetallation are described in detail below.

5.2 Division of Labor

All work in this chapter has been carried out by Brooke N Livesay.

5.3 Results and Discussion

Each of the three arms of the ($^{TIPS}C\equiv C)_3$tren ligand in [(($^{TIPS}C\equiv C)_3$tren)Fe$(OTf)_2$] (**5-1**) contains an internal alkyne that is bound to the imine carbon and protected by triisopropylsilyl (TIPS) groups. In the presence of an organic azide, these internal alkyne groups should undergo the cycloaddition reaction to produce a 1,2,3-triazole ring. For the newly formed 1,2,3-triazoles to displace the weakly coordinated triflate anions of **5-1** and lead to a first coordination sphere change, the 1,4-isomer should be synthesized. Although, it is hypothesized that the 1,5-isomer will not form as to alleviate the steric strain that would occur when the organic groups from the azide point towards the center of the complex (Figure 5.3.1).

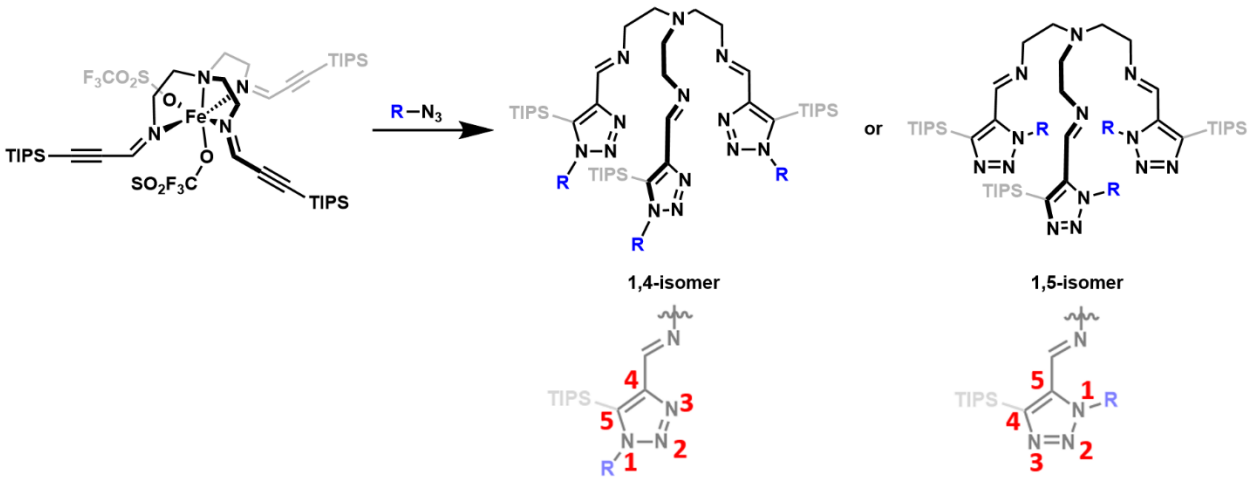

Figure 5.3.1. The cycloaddition reaction of [((^{TIPS}C≡C)$_3$tren)Fe(OTf)$_2$] (**5-1**) and an organic azide without a catalyst present results in the formation of 1,4- and 1,5- isomer 1,2,3-triazole products. The products are shown without the iron(II) center for clarity and the numbering of the 1,2,3-triazole is shown below each product.

Considering this hypothesis, mixture of 1,4- and 1,5-isomers should not form when no catalyst is used. This is ideal considering **5-1** is likely to undergo transmetallation, unintentional swapping of metals, in the presence of a catalyst. The uncatalyzed post synthetic azide-alkyne cycloaddition reaction of **5-1** was tested with phenyl azide. After reacting for two days the ^{1}H NMR spectrum of the concentrated reaction mixture did not show the desired four triazole iron(II) complex signals between 20 ppm and 8 ppm (Figure 5.3.2). The lack of product formation from these conditions indicates the need for a cycloaddition catalyst.

5.3.1 Internal Azide-Alkyne Cycloaddition Catalysts.

The alkyne of **5-1** is fully substituted requiring the use of a catalyst that can promote the cycloaddition reaction on an internal alkyne. Both ruthenium and Cu(NHC) catalysts have been shown to successfully promote the cycloaddition reaction with internal alkynes.[21,22] The ruthenium catalyst, Cp*RuCl(COD), was chosen to test whether the 1,5-isomer forms preferentially, or if steric hinderance from the substituent on the azide forces the formation of the 1,4-isomer. Unfortunately, no peaks related to the 1,4- or 1,5-isomer are observed in the ^{1}H NMR spectrum

after reacting **5-1** and phenyl azide in the presence of Cp*RuCl(COD) for several days, as seen in Figure 5.3.2.

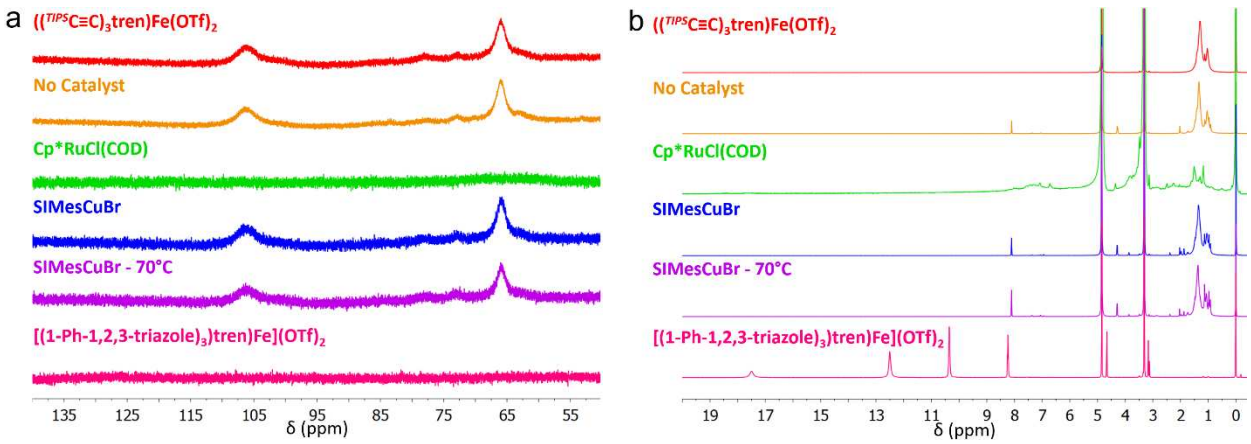

Figure 5.3.2. The d_4-CD_3OD paramagnetic ^{1}H NMR spectra between 140 ppm - 50 ppm (a) and 20 ppm – 0 ppm (b) of the cycloaddition reactions of [((^{TIPS}C≡C)$_3$tren)Fe(OTf)$_2$] (**5-1**) and phenyl azide with no catalyst (orange), Cp*RuCl(COD) (green), SIMesCuBr (at room temperature (blue) and at 70°C (purple) compared to pure [(1-Ph-1,2,3-triazole)$_3$)tren)Fe(OTf)$_2$ (pink).

The Cu(NHC) catalyst, SIMesCuBr (SIMes = N,N′-bis(2,4,6-trimethylphenyl)-4,5-dihydro-imidazol-2-ylidene)) was tested. The cycloaddition was performed at room temperature and at 70 °C in benzene and toluene. The ^{1}H NMR spectra of the reaction mixture after two days showed the distinctive paramagnetic signals of **5-1** at 105 ppm and 65 ppm, indicating no cycloaddition reaction occurred (Figure 5.3.2). It has been shown that the addition of an amine to the reaction helps the copper catalyst facilitate the cycloaddition.[25] Upon addition of several amines to the reaction conditions, resulting paramagnetic ^{1}H NMR spectra show the formation of three new peaks between 105 ppm and 70 ppm (Figure 5.3.3). When compared to the paramagnetic ^{1}H NMR spectrum of the desired product, [(1-(Ph)-1,2,3-triazole)$_3$)tren)Fe](OTf)$_2$ (**5-2**) synthesized *via* the traditional method (reacting the pre-made triazole ligand with Fe(OTf)$_2$, Figure 5.3.3), the new paramagnetic signals observed after these cycloadditions do not match with the desired triazole

product signals. The paramagnetic signals of **1** are still observed when triethylamine and *N*,*N*-diisopropylethylamine are used, but are no longer observed after the cycloaddition with 1,4-Diazabicyclo[2.2.2]octane, suggesting that amines react with **5-1** rather than helping to promote the cycloaddition reaction. The lack of triazole product from the reactions with the Cp*Ru(COD)Cl and SIMesCuBr catalysts suggest that the cycloaddition reaction will not occur when **5-1** contains an internal alkyne.

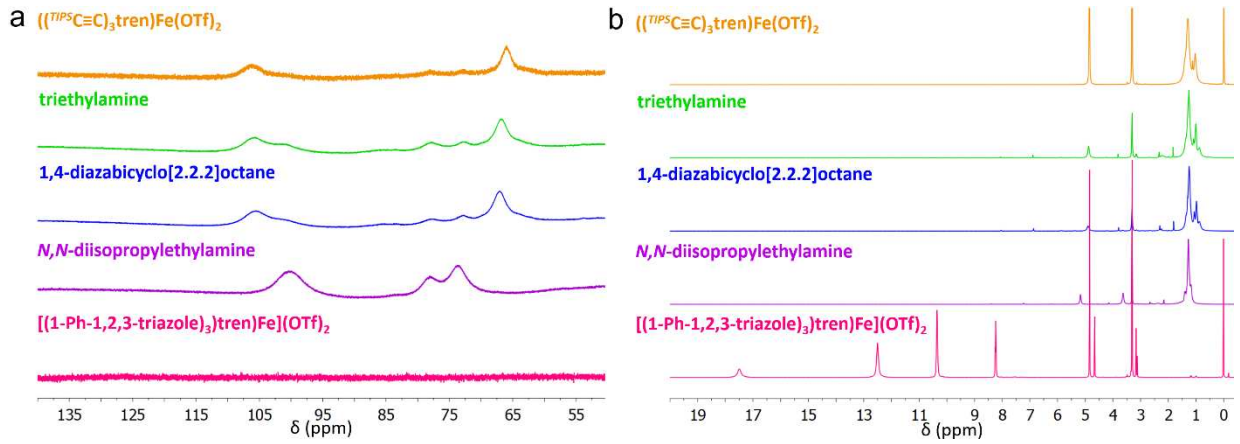

Figure 5.3.3. The d_4-CD_3OD paramagnetic ^{1}H NMR spectra between 140 ppm - 50 ppm (a) and 20 ppm – 0 ppm (b) of the cycloaddition reactions of [((^{TIPS}C≡C)$_3$tren)Fe(OTf)$_2$] (**5-1**) and phenyl azide with SIMesCuBr and triethyl amine (green), 1,4-diazabicyclo[2.2.2]octane (blue), and *N*,*N*-diisopropylethylamine (purple) compared to pure [(1-Ph-1,2,3-triazole)$_3$)tren)Fe(OTf)$_2$ (pink).

5.3.2 First Deprotection Agent Compatibility Test.

To use other common cycloaddition catalysts, for example Cu(I)-based catalysts, a terminal alkyne is needed. The internal alkyne of **5-1** can be easily transformed into a terminal alkyne by removing the TIPS groups by reaction with a fluoride source. A compatibility test of **5-1** with several fluoride sources was performed to find a source that would remove the TIPS groups and not result in decomposition. The fluoride sources were added to **5-1** in methanol and stirred for three hours. After this time, the colors of the resulting solutions were compared to unreacted **5-1**

to assess stability (Figure 5.3.4). In the presence of silver fluoride (AgF), **5-1** formed a black precipitate, suggestive of the decomposition of **5-1**. When tetrabutylammonium fluoride (TBAF), tetrabutylammonium difluorotriphenylsilicate (TBAT), and cesium fluoride (CsF) were used, the solution turned a dark orange. This color change upon addition of these fluoride sources, excluding AgF, is due to the change in the physical properties of **5-1** upon removal of the TIPS group. Attempts to characterize the resulting compounds were unsuccessful, as removal of the solvent produces an insoluble purple product. The dark orange color and the lack of a precipitate when TBAF, TBAT, and CsF are used as the fluoride source suggest the successful removal of the TIPS groups without decomposition of **5-1** or the resulting deprotected iron(II) complex.

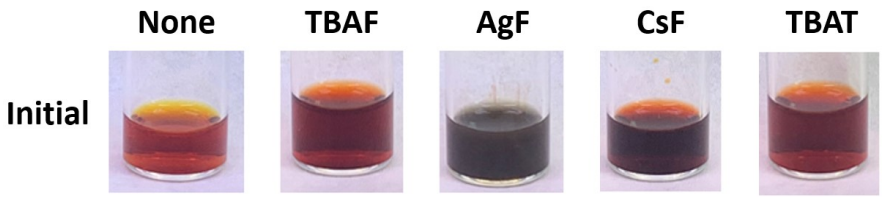

Figure 5.3.4. Stability test of [((^{TIPS}C≡C)$_3$tren)Fe(OTf)$_2$] (**5-1**) in the presence of several fluoride sources after three hours.

5.3.3 Terminal Azide-Alkyne Cycloaddition Catalysts with CsF.

Due to successes reported by past group members when using CsF, it was the first fluoride source tested in this study.[14] Initial cycloaddition reactions of **5-1** and phenyl azide with Cp*RuCl(COD) or SIMesCuBr and CsF did not produce the desired triazole product. Due to this, other common cycloaddition catalysts were then tested. I investigated copper sulfate ($CuSO_4$) with sodium ascorbate, copper iodine (CuI), and copper trifluoromethanesulfonate benzene complex (CuOTf benzene) as potential catalysts. However, no desired triazole products were observed in the ^{1}H NMR spectra (Figure 5.3.5). Notwithstanding, when triethylamine was included in the

reaction mixtures with CsF and a CuI or CuOTf benzene catalyst, the desired triazole compound **5-2** was synthesized, as seen by the ^{1}H NMR spectra (Figure 5.3.5). However, the ^{1}H NMR spectra of both reactions indicate the formation of the transmetallated product [(1-(Ph)-1,2,3-triazole)$_3$)tren)Cu](OTf) **5-3**.

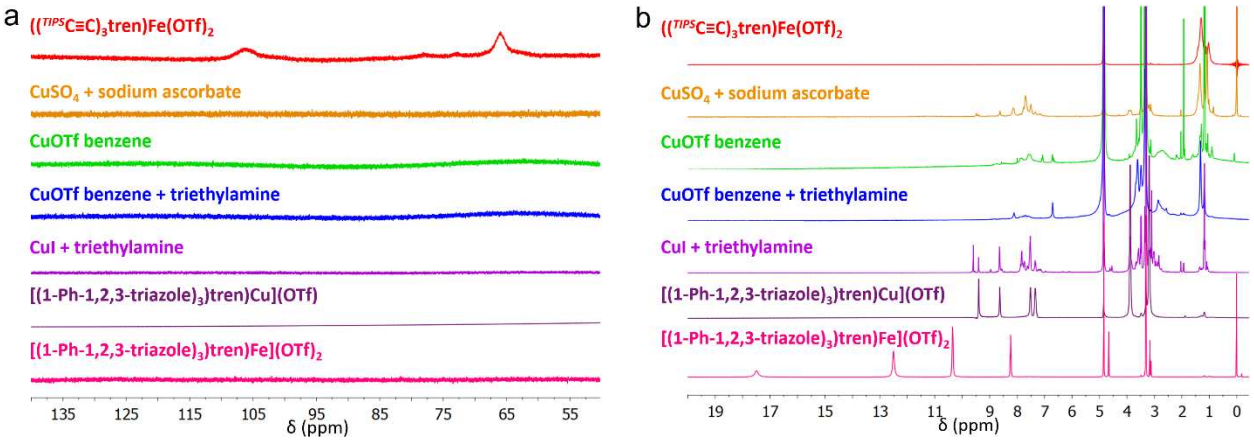

Figure 5.3.5. The d_4-CD_3OD paramagnetic ^{1}H NMR spectra between 140 ppm - 50 ppm (a) and 20 ppm – 0 ppm (b) of the cycloaddition reactions of [((^{TIPS}C≡C)$_3$tren)Fe(OTf)$_2$] (**5-1**), cesium fluoride, and phenyl azide with copper sulfate and sodium ascorbate (orange), copper triflate benzene complex (green), copper triflate benzene complex and triethylamine (blue), copper iodide and triethyl amine (light purple) compared to pure [(1-Ph-1,2,3-triazole)$_3$)tren)Cu(OTf) (dark purple) and [(1-Ph-1,2,3-triazole)$_3$)tren)Fe(OTf)$_2$ (pink).

A color change is also observed during the cycloaddition reaction with CsF and CuOTf benzene. The orange red solution of **5-1** changes color to dark red upon addition of CsF. This color change is attributed to the removal of the TIPS groups. Upon addition of CuOTf benzene and phenyl azide the reaction mixture starts lightening in color. After 16 hours, the reaction mixture is light orange. This color change was initially thought to be due to the production of the desired triazole product, **5-2**. However, the reaction was run several times and **5-2** was not observed by ^{1}H NMR spectroscopy again.

The compatibility of **5-1** with CuOTf benzene and CsF was tested due to the inability to reproduce the initial results. Compound **5-1** showed no change in color after stirring with CuOTf-benzene for several days. However, when **5-1** is reacted with only CsF for several days the solution turns from a dark orange color after 3 hours to yellow after 2 days. This is color change is similar to what was observed during the cycloaddition reaction, indicating that the CsF is reacting with **5-1**.

Electrochemistry was used to determine if the color change that occurs after **5-1** reacts with CsF is due to decomposition of iron(II) complex (Figure 5.3.6). The square wave voltammogram of pure **1** shows an iron II/III couple at 0.5 V and a ligand-based event at 0.1 V, referenced to ferrocene. Upon addition of CsF, the iron II/III couple shifts to 0.55 V and decreases in intensity. Two days after addition of CsF the iron II/III couple decreases in intensity even more suggesting the decomposition of **5-1** decomposes is occurring after prolonged exposure to CsF.

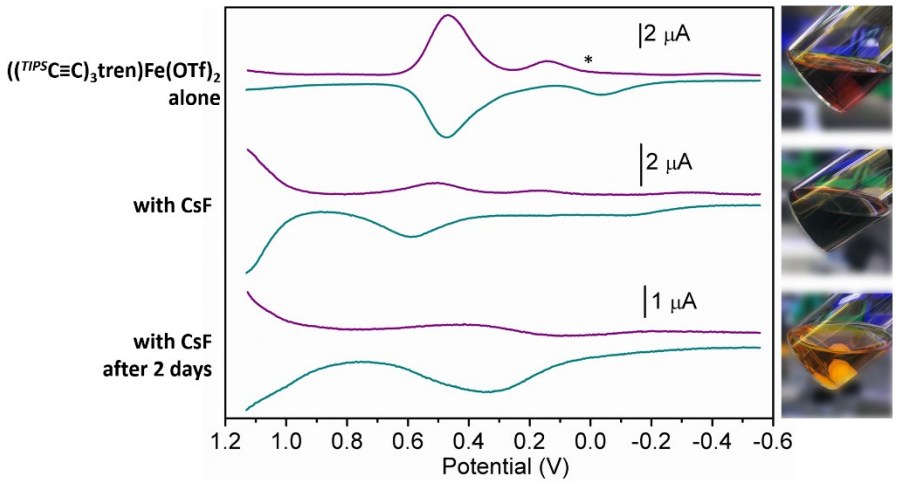

Figure 5.3.6. The square wave voltammogram and images of pure [((^{TIPS}C≡C)$_3$tren)Fe(OTf)$_2$] (top), after addition of cesium fluoride (middle), and after two days with cesium fluoride (bottom). The open circuit potential is marked with an asterisk (*), reduction scan is shown in purple and the oxidative scan shown in teal.

5.3.4 Second Deprotecting Agent Compatibility Test

The initial compatibility test indicated all tested fluoride sources, except for AgF, were compatible with **5-1**. However, it was discovered CsF results in decomposition of **5-1** after several days. The compatibility of **5-1** with the fluoride sources was run again with longer reaction times in an effort to find at least one source that does not cause decomposition during the time it takes to run the post-synthetic cycloaddition reaction. After 16 hours, all the test solutions turned to a lighter color than what was originally observed after 3 hours (Figure 5.3.7). Use of CsF results in the formation of a yellow solution after 16 hours. While TBAF and TBAT were initially the same color, after 16 hours the TBAF solution turned a pale orange while the TBAT solution only lightened slightly in color. The initial change in the solution of **5-1** with TBAT and the minimal color change after 16 hours suggest that TBAT can remove the TIPS groups from **1** without causing decomposition.

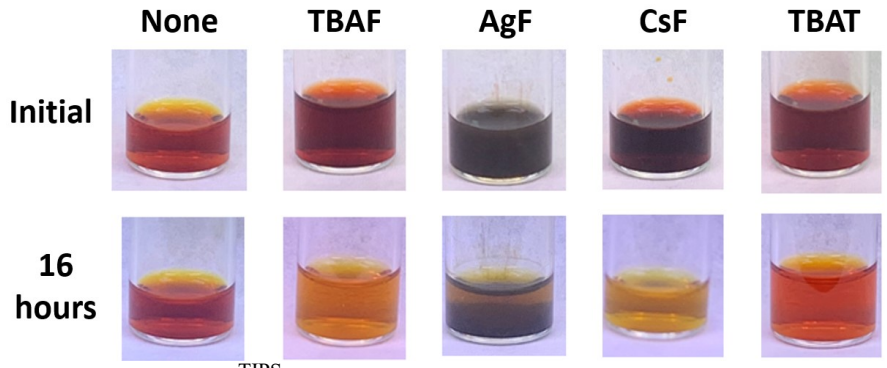

Figure 5.3.7. Stability test of [((^{TIPS}C≡C)$_3$tren)Fe(OTf)$_2$] (**5-1**) in the presence of several fluoride sources after three hours (top) and sixteen hours (bottom).

5.3.5 Terminal Azide-Alkyne Cycloaddition Catalyst with TBAT

The post-synthetic cycloaddition reaction on **5-1** with CuOTf-benzene and CsF resulted in some formation of **5-2**. Due to this, the same conditions were tested using TBAT as the fluoride source. The ^{1}H NMR spectra show the formation of the desired iron(II) triazole (**5-2)** and the

transmetalated copper triazole analogue (**5-3**) (Figure 5.3.8). Hoping to prevent the formation of **5-3**, the catalyst was changed to SIMesCuBr. While the desired iron(II) triazole complex (**5-2**) was formed, the observed yield was lower than when CuOTf benzene was used as the catalyst and the copper triazole product (**5-3**) was still observed in the ^{1}H NMR spectrum (Figure 5.3.8). Other copper catalysts were then investigated to minimize the formation of **5-3**. A review written by Hein and Fokin indicates when the copper oxides and carbonates on the surface of the elemental copper are used as the cycloaddition catalyst, lower level of copper contamination is observed compared to other copper catalysts.[25] Due to this, the cycloaddition of **5-1** was tested using small amounts of elemental copper powder. This reproducibly formed the desired iron(II) triazole product (**5-2**) and no copper triazole product (**5-3**) was observed in the ^{1}H NMR spectrum (Figure 5.3.8). However, if larger amounts of copper powder are added to the cycloaddition reaction, I found that the copper triazole product (**5-3**) will form. The small amounts of elemental copper needed for the successful cycloaddition of **5-1** with no transmetalated product are challenging to accurately measure when performing the reaction inside of the glovebox. Due to this, CuOTf benzene was returned to for the cycloaddition catalyst as it is easy to measure. This procedure was successful in producing the desired iron(II) triazole product **5-2**.

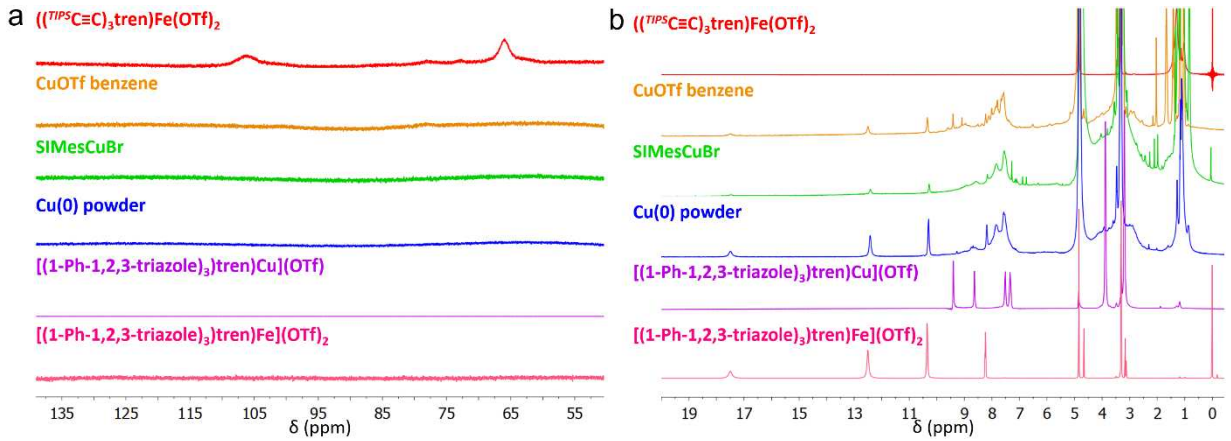

Figure 5.3.8. The d_4-CD_3OD paramagnetic ^1H NMR spectra between 140 ppm - 50 ppm (a) and 20 ppm – 0 ppm (b) of the cycloaddition reactions of [((^{TIPS}C≡C)$_3$tren)Fe(OTf)$_2$] (red), TBAT, and phenyl azide with copper triflate benzene complex (orange), SIMesCuBr (green), elemental copper powder (blue), compared to pure [(1-Ph-1,2,3-triazole)$_3$)tren)Cu(OTf) (purple) and [(1-Ph-1,2,3-triazole)$_3$)tren)Fe(OTf)$_2$ (pink).

5.3.6 Reaction Workup Conditions

To obtain pure iron(II) triazole (**5-2**), the byproducts from the deprotection and cycloaddition reactions, as well as any unreacted starting material need to be removed. Before purification conditions were tested, the byproducts were identified, and solubility tests were performed (Figure 5.3.9). The deprotection reaction produces fluorotriisopropylsilane and fluorotriphenylsilane that can be easily removed through diethylether washes. The tetrabutylammonium (TBA) cation remains to charge balance the freshly deprotected alkyne as no base was added to protonate this group. It is possible that the reaction solvent, methanol, protonates the alkyne; in this case the TBA would charge balance the resulting methoxy anion. The proposed reaction mechanisms of the copper catalyzed cycloaddition suggest the copper(I) ion remains bound to the newly formed 1,2,3-triazole until it is replaced by a proton.[25] The free copper can then promote another cycloaddition or undergo transmetallation to form the transmetalated copper triazole complex (**5-3**).

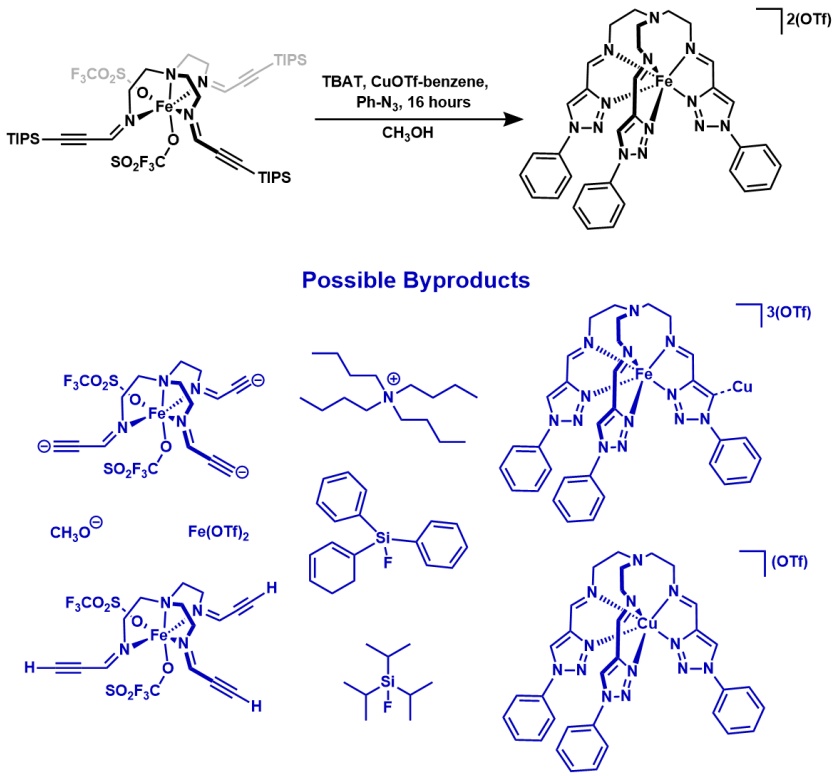

Figure 5.3.9. The post-synthetic azide-alkyne cycloaddition on [((^{TIPS}C≡C)$_3$tren)Fe(OTf)$_2$] (black) and the possible reaction byproducts (blue).

The crude ^{1}H NMR spectrum of the post-synthetic cycloaddition with TBAT and CuOTf benzene indicates all the above-mentioned byproducts are present. To ensure no copper remains bound to the 1,2,3-triazole rings, ammonium trifluoromethanesulfonate (NH_4OTf) was added to the reaction mixture after the cycloaddition was run for 16 hours. Upon addition of NH_4OTf the ^{1}H NMR signals sharpen (Figure 5.3.10). Removal of the byproducts formed from the deprotection reaction can be done through several washes of the crude reaction mixture with diethyl ether. The removal of the transmetallated copper triazole product (**5-3**) was more challenging. Pure **5-3** was made by reacting the synthesized ligand, (1-(Ph)-1,2,3-triazole)$_3$)tren, with CuOTf benzene. Solubility tests of **5-3** indicate the same solubility as **5-2** in all solvents except toluene. Compound **5-2** is insoluble in toluene while **5-3** is soluble, allowing for successful removal **5-3** after several

toluene washes. Following these reaction purification steps, addition of NH_4OTf and several diethyl ether and toluene washes, pure **5-2** can be isolated.

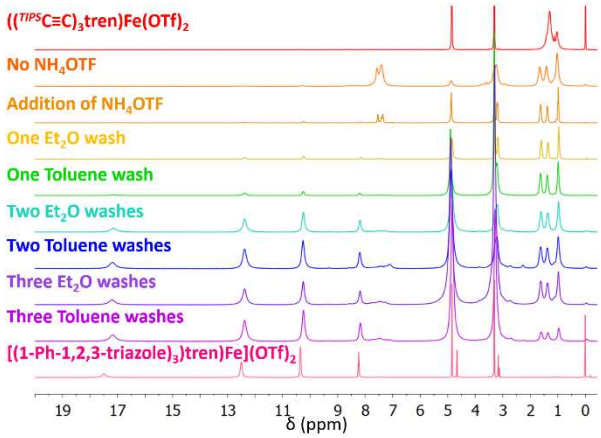

Figure 5.3.10. The d_4-CD_3OD paramagnetic ^1H NMR spectra between 20 ppm – 0 ppm of purification steps for the cycloaddition reaction of $[((^{TIPS}C{\equiv}C)_3tren)Fe(OTf)_2]$ (**5-1**, red), TBAT, phenyl azide, and copper triflate benzene complex compared to pure $[(1\text{-Ph-}1,2,3\text{-triazole})_3)tren)Fe(OTf)_2$ (pink).

5.3.7 Reaction Conditions

After successfully synthesizing and isolating pure **5-2** *via* a post-synthetic azide-alkyne cycloaddition, the reactant amounts were adjusted to improve the yield. To ensure the TIPS groups from each alkyne on **5-1** were removed, 1.1 equivalents of TBAT per alkyne were used: resulting in 3.3 equivalents of TBAT per 1 equivalent of **5-1**. Similarly, the amount of phenyl azide per alkyne was increased to 3 equivalents to ensure full conversion of the alkynes to 1,2,3-triazoles. The catalyst loading was ranged between 0.5% and 3% to produce **5-2** while also trying to minimize the amount of copper added to the system. While each loading produced **5-2**, the ratio of byproducts to the desired triazole product **5-2** was reduced when a 3% catalyst loading was used (Figure 5.3.11).

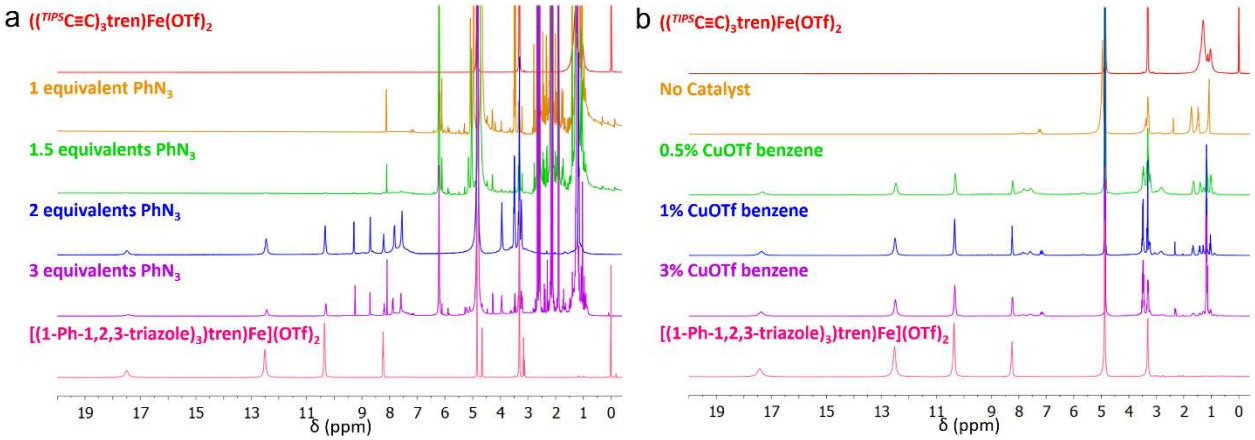

Figure 5.3.11 The d_4-CD_3OD paramagnetic ^1H NMR spectra between 20 ppm – 0 ppm of the cycloaddition reactions of [((^{TIPS}C≡C)$_3$tren)Fe(OTf)$_2$] (**5-1**, red), TBAT, varying amounts of phenyl azide (a, relative to **5-1**), and varying amounts of copper triflate benzene complex (b, relative to **5-1**) compared to pure [(1-Ph-1,2,3-triazole)$_3$)tren)Fe(OTf)$_2$ (pink).

5.3.8 Final Reaction Conditions

After much trial and error, conditions to achieve a successful post-synthetic azide-alkyne cycloaddition reaction on **5-1** were found. The triisopropylsilyl alkyne protecting groups in **5-1** are removed by addition of 3.3 equivalents of TBAT. After removal of these protecting groups, the azide-alkyne cycloaddition proceeded with a 3% CuOTf benzene catalyst loading and 9 equivalents of phenyl azide relative to **5-1** to produce the desired iron(II) triazole (**5-2**) after 16 hours. The impurities produced during cycloaddition reaction were removed after addition of NH_4OTf and several diethyl ether and toluene washes to isolate pure **5-2**.

5.4 Conclusion

The studies present here show the synthetic challenges that were overcome to perform the successful azide alkyne cycloaddition post synthetic modification of an iron(II) compound. The final reaction conditions provide full conversion of the alkyne containing iron(II) compound, [((^{TIPS}C≡C)$_3$tren)Fe(OTf)$_2$] (**5-1**), to the triazole containing iron(II) compound, [(1-Ph-1,2,3-triazole)$_3$)tren)Fe(OTf)$_2$ (**5-2**). The post synthetic modification required the use of a copper

catalyst; however some formation of the transmetallated product [(1-Ph-1,2,3-triazole)$_3$)tren)Cu(OTf) (**5-3**) occurred. This product as well as additional impurities can be easily removed to afford pure **5-2**. The reaction works with several organic azides to form iron(II) triazole products, as will be discussed in Chapters 6 and 7. Performing the azide alkyne cycloaddition post synthetically should enable the formation of novel iron(II) triazole compounds that could not be formed through traditional synthetic conditions; one example will be described in Chapter 6.

5.5 Experimental

5.5.1 Preparation of Compounds.

Unless otherwise mentioned, reactions were performed under inert conditions carried out in a dinitrogen-filled Vigor glovebox. Syringe filters were purchased from VWR International and were fitted with 0.2 μm PTFE membranes. Diethyl ether (Et_2O), toluene (MePh), and acetonitrile (CH_3CN) were sparged with nitrogen, passed through an alumina column and degassed prior to use. Dichloromethane (CH_2Cl_2) was dried over calcium chloride then distilled and degassed prior to use. Anhydrous methanol (CH_3OH) was purchased from Sigma-Aldrich. The starting materials SIMesCuBr,[21] Cp*Ru(COD)Cl,[22] phenyl azide,[26] and (1-Ph-1,2,3-triazole)$_3$tren[18] were prepared according to literature. Anhydrous iron(II) trifluoromethanesulfonate ($Fe(OTf)_2$) was purchased from Strem Chemicals. All other chemicals were purchased from commercial vendors and used as received. [((^{TIPS}C≡C)$_3$tren)Fe(OTf)$_2$]. (**5-1**) was prepared following the synthesis outlined in Chapter 4.

5.5.2 Physical Methods.

All methods were performed at room temperature unless otherwise noted. Mass spectrometry measurements were performed in the positive ion mode on a Thermo LTQ mass spectrometer

equipped with an analytical electrospray ion source and a quadrupole ion trap mass analyzer at 175 °C. Room temperature ^{1}H spectra were gathered on an Agilent 400 MHz spectrometer. For paramagnetic samples, changes to standard ^{1}H NMR acquisition were as follows: relaxation delay (1 ms), pulse angle (90°) and acquisition time (1 s).

*5.5.3 [(1-Ph-1,2,3-triazole)$_3$)tren)Cu(OTf) (**5-3**)*

To a solution of (1-Ph-1,2,3-triazole)$_3$tren (219 mg, 0.36 mmol) in 2 mL dry methanol was added a solution of (CuOTf)$_2$ benzene (198.7 mg, 0.39 mmol) in 1 mL dry methanol and stirred for 3 hours. The light orange reaction mixture was passed through a syringe filter and concentrated *in vacuo.* The resulting yellow sloid was purified by precipitation out of a concentrated methanol solution with diethylether to obtain the desired compound, [(1-Ph-1,2,3-triazole)$_3$)tren)Cu(OTf) (**5-3**), as a yellow powder. ^{1}H NMR (CD_3OD, 400 MHz): δ 9.40, 8.63, 7.51, 7.34, 3.88, 3.30 ppm.

References

(1) Chakrabarty, R.; Mukherjee, P. S.; Stang, P. J. Supramolecular Coordination: Self-Assembly of Finite Two- and Three-Dimensional Ensembles. *Chem. Rev.* **2011**, *111* (11), 6810–6918.

(2) Zeng, H.; Stewart-Yates, L.; Casey, L. M.; Bampos, N.; Roberts, D. A. Covalent Post-Assembly Modification: A Synthetic Multipurpose Tool in Supramolecular Chemistry. *Chempluschem* **2020**, *85* (6), 1249–1269.

(3) Clements, J. E.; Price, J. R.; Neville, S. M.; Kepert, C. J. Perturbation of Spin Crossover Behavior by Covalent Post-Synthetic Modification of a Porous Metal-Organic Framework. *Angew. Chemie - Int. Ed.* **2014**, *53* (38), 10164–10168.

(4) Nowak, R.; Adi Prasetyanto, E.; De Cola, L.; Bojer, B.; Siegel, R.; Senker, J.; Rössler, E.; Weber, B. Proton-Driven Coordination-Induced Spin State Switch (PD-CISSS) of Iron(II) Complex. *Chem. Commun* **2017**, *53* (5), 971–974.

(5) Touti, F.; Maurin, P.; Hasserodt, J. Magnetogenesis under Physiological Conditions with Probes That Report on (Bio-)Chemical Stimuli. *Angew. Chemie - Int. Ed.* **2013**, *52* (17), 4654–4658.

(6) Gondrand, C.; Touti, F.; Godart, E.; Berezhanskyy, Y.; Jeanneau, E.; Maurin, P.; Hasserodt, J. Spring-Loaded Iron(II) Complexes as Magnetogenic Probes Reporting on a Chemical Analyte in Water. *Eur. J. Inorg. Chem.* **2015**, *2015* (8), 1376–1382.

(7) Martin, L. L.; Hagen, K. S.; Hauser, A.; Martin, R. L.; Sargeson, A. M. Spin Equilibria in Iron(II) Hexa-Amine Cages. *J. Chem. Soc. Chem. Commun.* **1988**, No. 19, 1313–1315.

(8) Rösner, B.; Milek, M.; Witt, A.; Gobaut, B.; Torelli, P.; Fink, R. H.; Khusniyarov, M. M. Reversible Photoswitching of a Spin-Crossover Molecular Complex in the Solid State at Room Temperature. *Angew. Chemie* **2015**, *127* (44), 13168–13172.

(9) Hasserodt, J.; Kolanowski, J. L.; Touti, F. Magnetogenesis in Water Induced by a Chemical Analyte. *Angew. Chemie Int. Ed.* **2014**, *53* (1), 60–73.

(10) Milek, M.; Heinemann, F. W.; Khusniyarov, M. M. Spin Crossover Meets Diarylethenes: Efficient Photoswitching of Magnetic Properties in Solution at Room Temperature. *Inorg. Chem.* **2013**, *52* (19), 11585–11592.

(11) McConnell, A. J.; Aitchison, C. M.; Grommet, A. B.; Nitschke, J. R. Subcomponent Exchange Transforms an FeII4L4 Cage from High- to Low-Spin, Switching Guest Release in a Two-Cage System. *J. Am. Chem. Soc.* **2017**, *139* (18), 6294–6297.

(12) Luo, Y. H.; Nihei, M.; Wen, G. J.; Sun, B. W.; Oshio, H. Ambient-Temperature Spin-State Switching Achieved by Protonation of the Amino Group in [Fe(H2Bpz2)2(Bipy-NH2)]. *Inorg. Chem.* **2016**, *55* (16), 8147–8152.

(13) Nihei, M.; Suzuki, Y.; Kimura, N.; Kera, Y.; Oshio, H. Bidirectional Photomagnetic Conversions in a Spin-Crossover Complex with a Diarylethene Moiety. *Chem. - A Eur. J.* **2013**, *19* (22), 6946–6949.

(14) Ozumerzifon, T. J.; Higgins, R. F.; Joyce, J. P.; Kolanowski, J. L.; Rappé, A. K.; Shores, M. P. Evidence for Reagent-Induced Spin-State Switching in Tripodal Fe(II) Iminopyridine Complexes. *Inorg. Chem.* **2019**, *58* (12), 7785–7793.

(15) Shiga, T.; Saiki, R.; Akiyama, L.; Kumai, R.; Natke, D.; Renz, F.; Cameron, J. M.; Newton, G. N.; Oshio, H. A Brønsted-Ligand-Based Iron Complex as a Molecular Switch with Five Accessible States. *Angew. Chemie - Int. Ed.* **2019**, *58* (17), 5658–5662.

(16) Gaudette, A. I.; Thorarinsdottir, A. E.; Harris, T. D. PH-Dependent Spin State Population and 19F NMR Chemical Shift: Via Remote Ligand Protonation in an Iron(Ii) Complex. *Chem. Commun.* **2017**, *53* (96), 12962–12965.

(17) Hagiwara, H.; Minoura, R.; Udagawa, T.; Mibu, K.; Okabayashi, J. Alternative Route Triggering Multistep Spin Crossover with Hysteresis in an Iron(II) Family Mediated by Flexible Anion Ordering. *Inorg. Chem.* **2020**, *59* (14), 9866–9880.

(18) Hagiwara, H.; Minoura, R.; Okada, S.; Sunatsuki, Y. Synthesis, Structure, and Magnetic Property of a New Mononuclear Iron(II) Spin Crossover Complex with a Tripodal Ligand Containing Three 1,2,3-Triazole Groups. *Chem. Lett.* **2014**, *43* (6), 950–952.

(19) Hagiwara, H.; Tanaka, T.; Hora, S. Synthesis, Structure, and Spin Crossover above Room Temperature of a Mononuclear and Related Dinuclear Double Helicate Iron(II) Complexes. *Dalt. Trans.* **2016**, *45* (43), 17132–17140.

(20) Schweinfurth, D.; Demeshko, S.; Hohloch, S.; Steinmetz, M.; Brandenburg, J. G.; Dechert, S.; Meyer, F.; Grimme, S.; Sarkar, B. Spin Crossover in Fe(II) and Co(II) Complexes with the Same Click-Derived Tripodal Ligand. *Inorg. Chem.* **2014**, *53* (16), 8203–8212.

(21) Díez-González, S.; Correa, A.; Cavallo, L.; Nolan, S. P. (NHC)Copper(I)-Catalyzed [3+2] Cycloaddition of Azides and Mono- or Disubstituted Alkynes. *Chem. - A Eur. J.* **2006**, *12* (29), 7558–7564.

(22) Boren, B. C.; Narayan, S.; Rasmussen, L. K.; Zhang, L.; Zhao, H.; Lin, Z.; Jia, G.; Fokin, V. V. Ruthenium-Catalyzed Azide−Alkyne Cycloaddition: Scope and Mechanism. *J. Am. Chem. Soc.* **2008**, *130* (28), 8923–8930.

(23) Himo, F.; Lovell, T.; Hilgraf, R.; Rostovtsev, V. V; Noodleman, L.; Sharpless, K. B.; Fokin, V. V. Copper(I)-Catalyzed Synthesis of Azoles. DFT Study Predicts Unprecedented Reactivity and Intermediates. *J. Am. Chem. Soc.* **2005**, *127* (1), 210–216.

(24) Worrell, B. T.; Malik, J. A.; Fokin, V. V. Direct Evidence of a Dinuclear Copper Intermediate in Cu(I)-Catalyzed Azide-Alkyne Cycloadditions. *Science (80-.).* **2013**, *340* (6131), 457–460.

(25) Hein, J. E.; Fokin, V. V. Copper-Catalyzed Azide-Alkyne Cycloaddition (CuAAC) and beyond: New Reactivity of Copper(i) Acetylides. *Chem. Soc. Rev.* **2010**, *39* (4), 1302–1315.

(26) Nallapati, S. B.; Sreenivas, B. Y.; Bankala, R.; Parsa, K. V. L.; Sripelly, S.; Mukkanti, K.; Pal, M. 1,2,3-Triazoles Derived from Olanzapine: Their Synthesis via an Ultrasound Assisted CuAAC Method and Evaluation as Inhibitors of PDE4B. *RSC Adv.* **2015**, *5* (115), 94623–94628.

Chapter 6: Post-synthetic Modification of a High Spin Iron(II) Complex to Promote Spin State Changes

6.1 Overview

We report the complete post-synthetic modification of our previously reported high spin iron(II) complex, [((^{TIPS}C≡C)$_3$tren)Fe(OTf)$_2$] (**6-1**), by azide-alkyne cycloaddition. The reaction proceeds via in-situ deprotection of the TIPS groups, followed by addition of azide species in the presence of a copper(I) catalyst. Several *para*-substituted phenyl azides are tested and result in full conversion of **6-1** into [(1-(4-X-Ph)-1,2,3-triazole)$_3$tren)Fe](OTf)$_2$ (X = H- (**6-2**), MeO- (**6-3**), F_3C- (**6-4**), and $HOCH_2$- (**6-5**)) as characterized by ^{1}H NMR spectroscopy and single-crystal X-ray diffraction. Compounds **6-2 - 6-4** show different solid state magnetic behavior between 2 K and 360 K: **6-2** stays high spin, **6-3** undergoes a one-step spin switching event, and **6-4** starts a spin switching event above room temperature. Comparison of **6-2** and **6-3** with the previously reported triflimide salts indicate that the anion and substituents have a large impact on the crystal packing environment, leading to differences in the magnetic data. This study highlights the successful first-coordination sphere change upon post-synthetic modification of a high spin iron(II) complex to afford spin switching complexes.

6.2 Introduction

Post-synthetic modification protocols provide access to unique compounds that could not be formed through traditional synthetic methods. This concept has been used in a variety of fields, including biological systems, self-organization, and sensing.[1,2] However, few studies pair post-synthetic modifications with transition metal complexes that can undergo a spin state switching

event.[3–7] While the building blocks of many systems can be designed and synthesized before formation of the final compound, some reaction conditions limit the range of substituents that can be included. Avoiding harsh reaction conditions, post-synthetic modifications provide a way to include sensitive substituents in the final compound. Since substituent changes have been shown in some cases to alter spin-state switching energetics considerably (e.g. $\Delta T_{1/2}$ > 100 K), incorporating post-synthetic modifications into metal complex synthesis can open the way toward new and improved classes of spin-crossover materials.[8–15]

For a post-synthetic modification reaction to be successful, it needs to employ mild and efficient reaction conditions. This prevents decomposition, allows sensitive groups to be added, and ensures all reactive sites are fully converted to the desired product. Previously reported post-synthetic modifications use the azide-alkyne cycloaddition,[16–18] condensation,[6,19] and inverse electron demand Diels-Alder reactions.[20–23] However, studies that perform post-synthetic modifications on spin state switching complexes tend to use milder reactions, such as ligand isomerization,[24,25] protonation,[26–29] and subcomponent exchange.[30]

Reversible switching between the high spin (HS) and low spin (LS) states of octahedral d^4-d^7 first row transition metals is incredibly sensitive to ligand field, external perturbations, and environmental changes (e.g. intermolecular interactions, coordination number). Due to this, post-synthetic modifications can be used to promote the spin switching event. Many reports focus on modifying iron(II) compounds due to the vast differences in the physical properties between the paramagnetic HS and diamagnetic LS states. In these studies the spin switching event is promoted by changing the ligand field strength through post-synthetic modifications on the ligand backbone.[3,4,31]

However, there are reports of post-synthetic modifications that cause a spin switching event by inducing a change to the first coordination sphere through the reduction of the ligand or a subcomponent exchange.[7,30] We have recently reported a high spin iron(II) complex with alkyne groups on the ligand and two weakly bound triflate anions.[32] The complete post-synthetic modification of this compound by the azide-alkyne cycloaddition reaction results in changes of the first coordination sphere, and the reaction is described in detail with a variety of azides. Additionally, magnetic studies performed on the resulting triazole-containing complexes in the solid state show they exhibit a variety of spin state behaviors.

6.3 Division of Labor

All work in this chapter has been carried out by Brooke N. Livesay. This work is supported by NSF (CHE-1363274, CHE-1800554, and CHE-1956399) and Colorado State University.

6.4 Results and Discussion

6.4.1 Synthesis.

The previously reported high spin iron(II) complex, $[((^{TIPS}C{\equiv}C)_3tren)Fe(OTf)_2]$ (**6-1**), is ideal for post-synthetic modifications using the azide-alkyne cycloaddition reaction (Figure 6.4.1). The three alkynes present on the ligand permit the complex to undergo cycloaddition reactions with organic azides. As well, the weakly coordinated triflates of **6-1** can be displaced upon formation of the resulting triazole, leading to a significant change in the first coordination sphere of the iron(II) center.

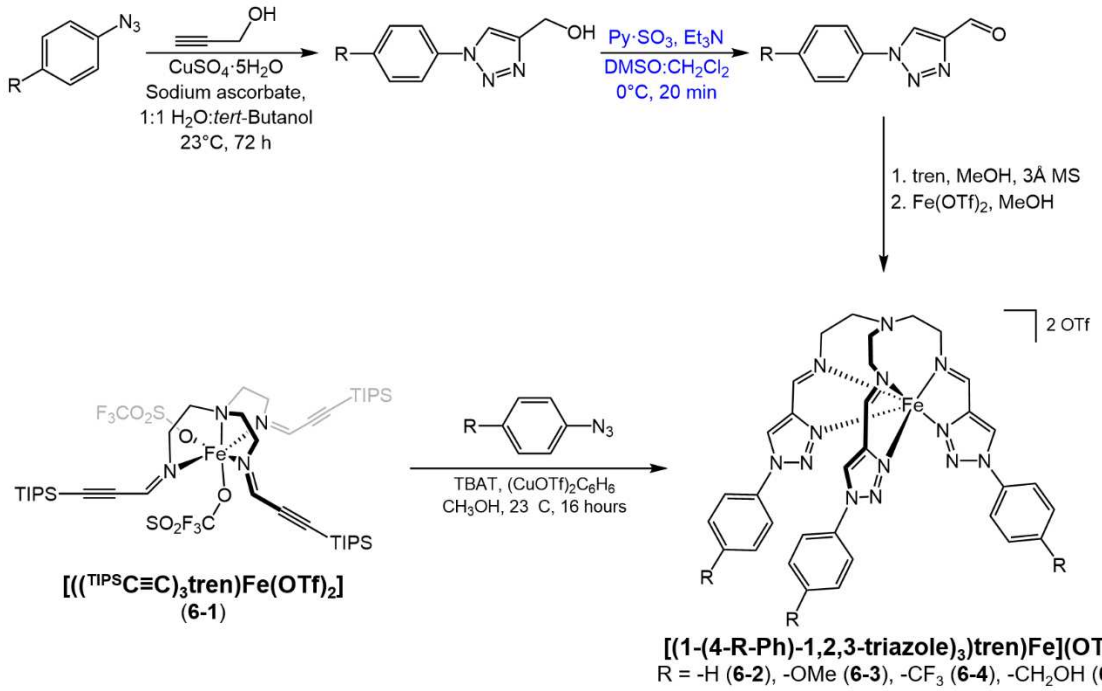

Figure 5.5.1. The post synthetic modification of [((^{TIPS}C≡C)$_3$tren)Fe(OTf)$_2$] (**6-1**) to form [(1-(4-R-Ph)-1,2,3-triazole)$_3$)tren)Fe](OTf)$_2$ (**6-2 – 6-5**) avoids the oxidation step required to synthesize the 1-(4-R-Ph)-1,2,3-triazole)$_3$)tren ligand (shown in blue). TBAT = tetrabutylammonium difluorotriphenylsilicate, (CuOTf)$_2$C$_6$H$_6$ = copper(I) trifluoromethanesulfonate benzene complex, CH$_3$OH = methanol.

We find that use of a cycloaddition catalyst is needed to perform this post-synthetic modification on **6-1**. Ideally, the azide-alkyne cycloaddition should proceed in the absence of catalysts, relying on the presence of the iron(II) complex to provide a template and sufficient steric bulk to favor the formation of the desired 1,4-1,2,3-triazole isomer. To avoid the possibility of transmetallation during the modification, the cycloaddition was attempted without a catalyst present, but formation of the desired triazole complex was not observed. Modification attempts using catalysts that promote cycloaddition reactions with internal alkynes, such as Cp*Ru(COD)Cl and SIMesCuBr, were not successful in forming the desired compound; for more information see Chapter 5. Ultimately, we found that Cu(I) enables the cycloaddition reaction to proceed, but even this requires prior in-situ removal of the alkyne-protecting triisopropylsilyl groups from **6-1**, using tetrabutylammonium difluorotriphenylsilicate (TBAT) in dry methanol (CH$_3$OH). The resulting

species is treated with the phenyl azide and a catalytic amount of copper(I) triflate under inert conditions to afford the triazole containing iron(II) complex, [(1-Ph-1,2,3-triazole)$_3$)tren)Fe](OTf)$_2$ (**6-2**). Not surprisingly, the ^{1}H NMR spectrum of the reaction mixture shows the desired triazole iron(II) complex with a small amount of the copper(I) transmetallation product (Figure A2.1). The Cu(I) product and other impurities are easily removed by addition of diethyl ether (Et_2O) and toluene to the concentrated reaction mixture in CH_3OH, thus selectively precipitating the iron(II) complex.

The cycloaddition reaction was performed with several *para*-substituted phenyl azides to form a family of [(1-(4-X-Ph)-1,2,3-triazole)$_3$)tren)Fe](OTf)$_2$ (X = H- (**6-2**), MeO- (**6-3**), F_3C- (**6-4**), and $HOCH_2$- (**6-5**)) complex salts. The unsubstituted, electron donating (methoxy), electron withdrawing (trifluoromethyl), and oxidation sensitive (hydroxymethyl) azides were chosen to show the scope and advantages of performing the alkyne-azide reaction post-synthetically. Compound **6-5** was targeted specifically to avoid the oxidation step that would be required to form the precursor aldehyde during the traditional triazole ligand synthesis (Figure 6.4.1). We note that the bis(trifluoromethanesulfonyl)imide (NTf_2) salts of complexes **6-2** and **6-3** have been reported previously: those salts were formed by synthesizing the ligand before coordination to the iron(II) center.[33,34] The properties of triflate-containing **6-2** and **6-3** will be compared to their analogous NTf_2 salts below.

6.4.2 ^{1}H NMR

Tracking the assembly reactions by ^{1}H NMR spectroscopy, the characteristic paramagnetic signals of **6-1** are no longer observed in the spectra of the purified post-synthetic reaction mixtures. Instead, six signals are observed for **6-2**, **6-3**, and **6-5** between 4 ppm and 30 ppm, while three signals are observed for **6-4** (Figure 6.4.2). The four protons of the tren ligand backbone are

observed as two broad peaks around 30 ppm and 22 ppm, as observed in **6-2**, **6-3**, and **6-5**. These signals are most likely too broad to be observed in **6-4**. The signals observed around 17 ppm are related to the imine proton, while the two resonances observed around 12 ppm and 10 ppm are assigned to meta and ortho protons of the phenyl ring for **6-2** - **6-5**. The signals assigned to the substituent groups of **6-2**, **6-3**, and **6-5** are found at 8.2 ppm, 5.0 ppm, and 6.6 ppm, respectively. These signals observed for **6-2** - **6-5** indicate full conversion of **6-1** to the triazole containing complexes occurred.

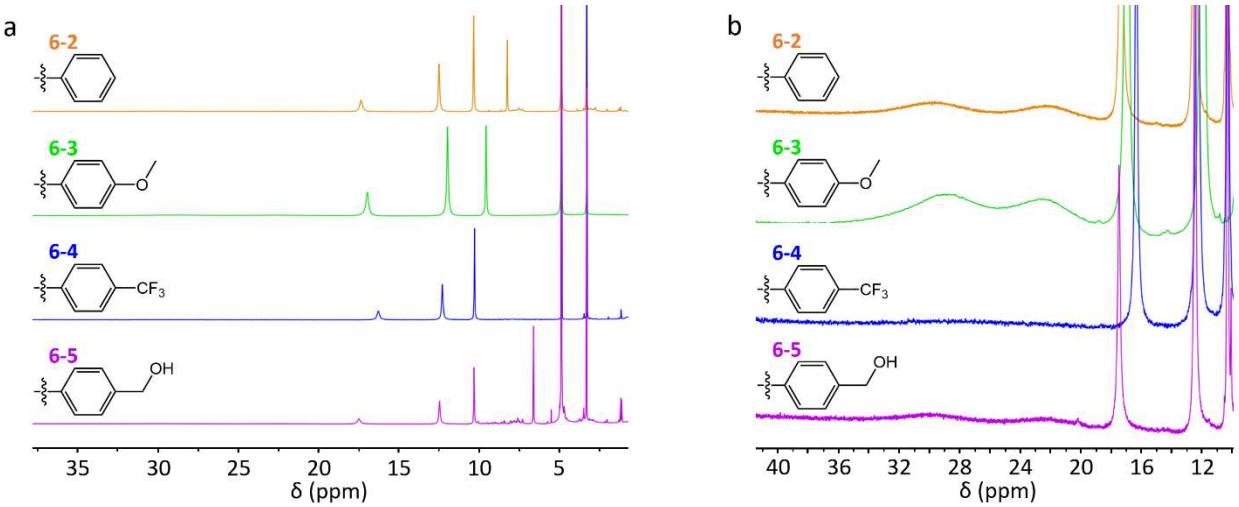

Figure 5.5.2. Room temperature paramagnetic ^{1}H NMR spectra of **6-2** - **6-5** in d_4-CD_3OD between 35 ppm and 0 ppm (a) and between 41 ppm and 10 ppm (b).

6.4.3 Crystal Structures

Full conversion to the tris(triazole) species is also supported by X-ray diffraction studies. Crystals of **6-2** and **6-3** are obtained from slow diffusion of Et_2O into CH_3OH solutions of the compounds; crystals of **6-4** are made by layering of Et_2O onto a CH_3OH solution. Several attempts were made to crystalize **6-5**, but none resulted in diffraction quality crystals. Single crystal X-ray diffraction data were collected on **6-2** - **6-4** at 100 K (Figure 6.4.3). The crystal structures show that all of the alkynes of **6-1** undergo full cycloaddition conversion to the appropriate triazole after

the post-synthetic modification. All three newly-formed triazoles bind to the iron(II) metal center resulting in a N_6 first coordination sphere. Crystallographic details for the compounds are provided below.

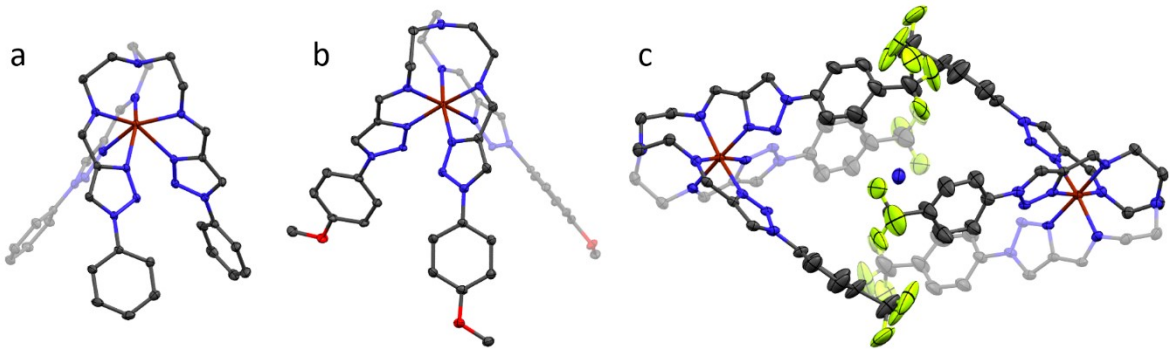

Figure 5.5.3. Crystal structures of ***6*-2** (a), ***6*-3** (b), and ***6*-4** (c) depicted with 40% thermal ellipsoids; hydrogen and counter anion atoms have been omitted for clarity. Dark red, blue, gray, red, and lime-green ellipsoids represent Fe, N, C, O, and F, respectively.

The structure of **6-2**, collected at 100 K, shows that the neutral (1-Ph-1,2,3-triazole)$_3$tren ligand binds to the iron(II) center through the imine and triazole nitrogen atoms, resulting in a doubly charged cationic unit that is charged balanced by two unbound triflate (OTf) anions (Figure 6.4.3a). The bridgehead nitrogen from the tren backbone is located 2.571(1) Å away from the iron(II) center, providing a pseudo-heptacoordinate environment around the iron(II) center. The continuous shape measurement (CShM) for **6-2** indicates a distorted capped octahedron first coordination geometry (Table 6.4.1).[35] The average Fe-N_{imine} bond distance of 2.148(1) Å is shorter than the average Fe-$N_{triazole}$ distance (2.250(1) Å). Overall, the Fe-N bond distances are characteristic of a high spin (HS) iron(II) center, contrasting what has been observed for the NTf_2 salt of the same cationic unit, which is low spin (LS) at 135 K.[33] For **6-2**, the intermolecular interactions between the cationic unit and triflate anions, as well as the complex stacking, are similar to what are observed for the NTf_2 salt. The cation stacking **6-2** results in intermolecular

Fe···Fe distances of 10.057(9) Å, whereas it is 9.074(9) Å for the NTf_2 salt. However, the space between the cation stacking channels occupied by the anion are closer and less stagged due to packing of the smaller OTf cation in **6-2**, leading to intermolecular Fe···Fe distances of 10.378(1) Å and 11.540(1) Å, compared to 12.118(9) Å and 12.334(9) Å for the NTf_2 salt (Figure A2.3). These closer cationic stacking channels in **6-2** provide more rigidity to the structure, preventing the flexibility needed for the transition to a low spin species. This is likely the cause of the observed spin state difference between the two salts.

Table 5.5.1. Selected crystallographic parameters.

	6-2		**6-3**		**6-4**
Temperature (K)	100	100	265	298	100
Fe-$N_{bridgehead}$ (Å)	2.571(1)	3.452(3)	3.066(7)	2.883(6)	3.282(5)
Average Fe-N_{imine} (Å)	2.148(1)	1.989(2)	2.060(5)	2.106(5)	1.986(6)
Average Fe-$N_{triazole}$ (Å)	2.250(1)	1.942(2)	2.086(4)	2.159(4)	1.918(5)
SHAPE value[a]	1.411[a] 2.907[b]	0.7961[b]	2.716[a] 1.508[b]	2.152[a] 1.998[b]	0.874[b]

[a] Continuous shape measurement (CShM) values were calculated for capped octahedron. [b]CShM values were calculated for octahedron.

The crystal structure of **6-3**, collected at 100 K, reveals one hexacoordinate iron(II) with two triflate counter anions and a cocrystallized methanol solvate molecule in the asymmetric unit. The fully converted (1-(4-MeO)-Ph)-1,2,3-triazole)$_3$tren ligand binds to the iron(II) ion through the imine and triazole nitrogen atoms (Figure 6.4.3b). Unlike **6-2**, the average Fe-N_{imine} distances (1.989(2) Å) in **6-3** are longer than the Fe-$N_{triazole}$ distances (1.942(2) Å). As well, the bridgehead nitrogen of the tren ligand backbone is further way (3.452(3) Å) in **6-3** than what is observed in **6-2**, providing a close to ideal octahedral coordination geometry around the iron(II) center (Table 6.4.1). The minimal distortion along with the short Fe-N bond distances are characteristic of a LS iron(II) center. The spin state assignment of **6-3** agrees with one of the two cationic units present

in the previously published related NTf_2 salt.[34] Both salts form 1D chains through π-π stacking between ligands. In **6-3**, the 5.643 Å π-π interaction leads to intermolecular Fe···Fe distances of 9.704 Å, shorter than what is observed for the NTf_2 salt.[34]

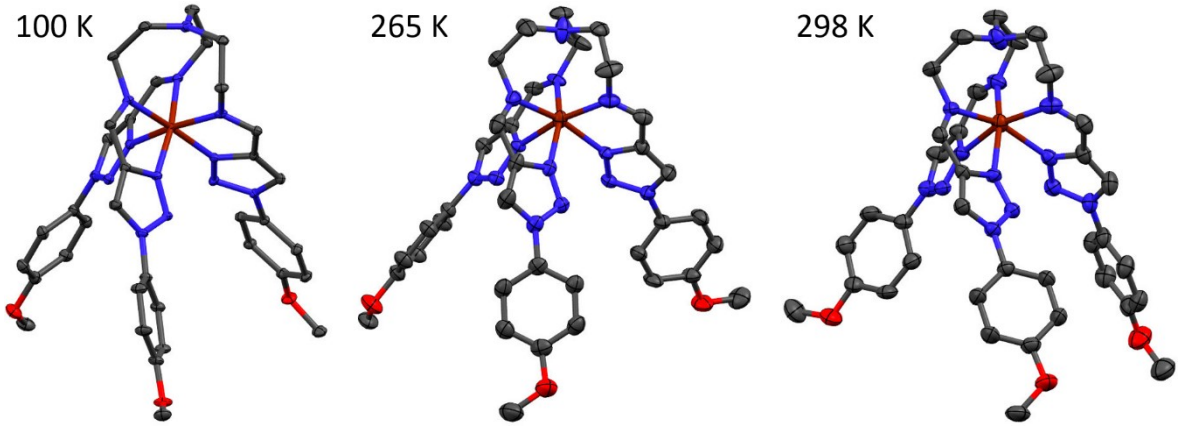

Figure 5.5.4. Crystal structures **6-3** at 100 K, 265 K, and 298 K depicted with 40% thermal ellipsoids; hydrogen and counter anion atoms have been omitted for clarity. Dark red, blue, gray, and red ellipsoids represent Fe, N, C, and O, respectively.

The crystal structure of **6-3** was also collected at 265 K and 298 K (Figure 6.4.4). The unit cell contents do not change between 100 and 298 K, and one hexacoordinate iron(II) with two triflate counter anions and a cocrystallized methanol solvate molecule are observed at all three temperatures. However, the average bond distance change as the temperature increases (Table 6.3.1). At 265 K, the average Fe-N_{imine} bond distances are 2.060(5) Å and the average Fe-$N_{triazole}$ bond distances are 2.086(4) Å. Whereas at 298 K, the average Fe-N_{imine} bond distances are 2.106(5) Å and the average Fe-$N_{triazole}$ bond distances are 2.159(4) Å. These increases in the average Fe-N bond distances indicate a spin state switching event is occurring, and the bond distances at 298 K are consistent with a high spin iron(II) center. In addition, the Fe-$N_{bridgehead}$ distance starts to decrease as the temperature increases, resulting in a pseudo-capped octahedron coordination geometry at 298 K. This contraction of the Fe-$N_{bridgehead}$ distance causes the distance between the

three 4-methoxy-phenyl groups on the ligand to increase, resulting in closer intermolecular π-π interaction (4.182(1) Å) but still maintains a similar intermolecular Fe···Fe distances (9.701(1) Å) to the structure collected at 100 K.

Similar to **6-2** and **6-3**, the fully converted (1-(4-CF_3)-Ph)-1,2,3-triazole)$_3$tren ligand binds to the iron(II) through the imine and triazole nitrogen atoms, resulting in a hexacoordinate geometry for **6-4**, for diffraction data collected at 100 K. The average Fe-N_{imine} distance of 1.986(6) Å and an average Fe-$N_{triazole}$ distance of 1.918(5) Å are characteristic of a LS iron(II) center. Additionally, the bridgehead nitrogen of the tren backbone is 3.282(5) Å away from the iron(II) center, resulting in a close to ideal octahedral coordination geometry. The trifluoromethyl (CF_3) groups on one complex interact with the phenyl rings on an adjacent complex through hydrogen bonds, resulting in the formation of a cavity between the two iron(II) centers (Figure 6.4.3c). The middle of the cavity is occupied by a single ammonium cation that interacts with the phenyl rings of the ligands that form the cavity through six cation-π interactions (Figure A2.6). An additional ammonium ion is found interacting with oxygen atoms from six triflate anions through hydrogen bonds. These six triflate anions charge balance the two iron(II) cationic units and the two ammonium ions found in the structure and are observed in a cluster between adjacent iron(II) complexes (Figure A2.7). Additionally, the oxygen atoms of the triflate anions hydrogen bond with the imine and triazole protons, while the triflate CF_3 groups interact with the CF_3 groups on the iron(II) complex. Attempts to remove the co-crystallized ammonium triflate were unsuccessful, leading us to believe that it is important for the isolation of **6-4**. While ammonium triflate is needed for the post-synthetic reaction, it is not used during the traditional synthetic route. Therefore, the comparison of the traditionally and post-synthetically made **6-4** will be investigated in a future report to

determine whether the ammonium triflate is needed to isolate **6-4** and what impacts it has on the solid-state magnetic properties.

6.4.4 Solid State Magnetic Data.

The N_4O_2 first coordination sphere around the iron(II) center in **6-1** results in a high spin complex at all temperatures in the solid state.[32] Upon the post-synthetic modification by the azide alkyne cycloaddition, the bridgehead nitrogen and the two bound triflate anions of **6-1** are replaced by three 1-X-1,2,3-triazole rings, leading to an N_6 coordination environment for **6-2** – **6-4**. Previous reports indicate bound triazole rings provide the appropriate ligand field for iron(II) complexes to undergo thermal spin state switching.[33,34,36,37] Additionally, Hagiwara and coworkers have shown the magnetic properties of the related iron(II) triazole compounds are sensitive to subtle modifications to the NTf_2 anion conformation.[34] Magnetic properties for **6-2** - **6-4** were measured to probe substituent and anion impacts on the spin state of the complexes with newly bound 1-X-1,2,3-triazole rings.

The temperature dependence of the magnetic susceptibility of crystalline samples of **6-2 - 6-4** were collected under an applied field of 1000 Oe between 2 K and 300 K (**6-2**) or 360 K (**6-3** and **6-4**) (Figure 6.4.5). All three complexes exhibit different magnetic behaviors: the parent compound **6-2** remains HS, methoxy-containing **6-3** undergoes one step spin state switching event, and trifluoromethyl-substituted **6-4** starts a spin state switching event above room temperature.

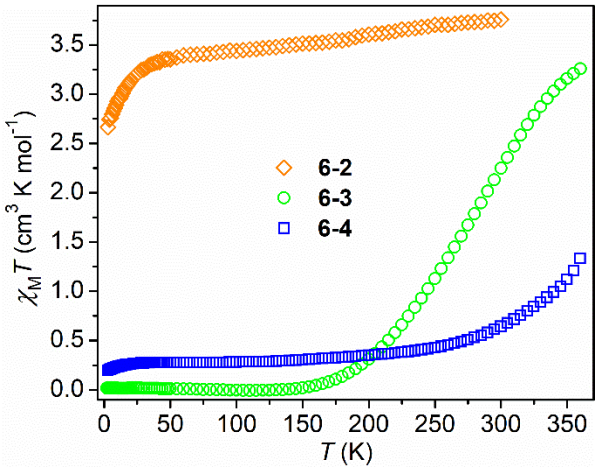

Figure 5.5.5. Temperature dependence of the magnetic susceptibility for powder samples of **6-2** - **6-4**, collected between 2 K and 300 K (**6-2**) or 360 K (**6-3** and **6-4**).

The magnetic susceptibility temperature product ($\chi_M T$) value for **6-2** at 300 K is 3.76 cm^3 K mol^{-1}, higher than the expected spin only value (g = 2, S = 2, $\chi_M T$ = 3.00 cm^3 K mol^{-1}), but consistent with other reported high spin iron(II) complexes. The $\chi_M T$ product decreases linearly until 40 K, whereupon the decrease becomes more dramatic: at 2 K, the $\chi_M T$ value is 2.66 cm^3 K mol^{-1}. The susceptibility data were fit to a $S = 2$ model using PHI;[38] magnetic parameters are shown in Table A2.1. Inclusion of a mean field approximation for intermolecular exchange (Θ) improved the fit; the positive value indicates ferromagnetic coupling of individual high-spin Fe(II) complexes that possibly arises from the short intermolecular contacts as noted in the structural analysis.

As indicated in the comparison of the structures, the magnetic properties of **6-2** and the related NTf_2 salt reported by Hagiwara and co-workers are vastly different.[33] While **6-2** remains high spin between 2 K and 300 K, the NTf_2 salt undergoes a thermal spin state switching event with a $T_{1/2}$ of 280 K.[33] The molecular assembly in the NTf_2 salt helps promote the spin state switching event, but the closer cationic channels in **6-2**, due to the smaller triflate anion, restrict the structural changes needed for the spin switching event to occur, resulting in a HS species at all temperatures.

These complexes demonstrate just how sensitive the solid-state magnetic properties of a cation are on anion choice and intermolecular interactions.

Complex **6-3** was measured upon warming from 2 K to 360 K at a sweep rate of 2 K per minute under a 1000 Oe applied field (Figure 6.4.5). The $\chi_M T$ value for **6-3** stays constant at 0.01 cm^3 K mol^{-1} between 2 K and 150 K, indicating the presence of a low spin iron(II) complex. Upon heating a spin switching event occurs ($T_{1/2}$ = 277 K) resulting in a $\chi_M T$ value of 2.25 cm^3 K mol^{-1} at 300 K. The susceptibility values continue to increase upon further heating, but the increase is less dramatic suggesting the end of the spin crossover event. At 360 K, the susceptibility value is 3.26 cm^3 K mol^{-1}, higher than the expected spin only value (g = 2, S = 2, $\chi_M T$ = 3.00 cm^3 K mol^{-1}), but consistent with other high spin iron(II) samples. The cooling curve of the spin crossover event shows the decrease in the magnetic susceptibility between 360 K and 150 K is slightly more dramatic resulting in a higher $T_{1/2}$ (Figure A2.11). This difference in the behavior is due to the loss of the co-crystallized CH_3OH after heating the sample to 360 K. The related NTf_2 salt also displays a spin crossover event ($T_{1/2}$ = 273 K (cooling mode) and 285 K (warming mode)).[34] However, only one of the two cation units in the crystal structure changes spin state upon increasing temperature, resulting in a ½ (HS + LS) to HS event.[34] The cation in the NTf_2 salt with similar intermolecular interactions as **6-3** undergoes the spin crossover event, suggesting the π-π interactions between the ligands help promote the spin state change for these complexes.

Compound **6-4** was measured upon warming from 2 K to 360 K with a 2 K per minute sweep rate. At 2 K, the magnetic susceptibility is 0.19 cm^3 K mol^{-1} and increases to 0.27 cm^3 K mol^{-1} at 20 K. Upon warming the $\chi_M T$ value stays consistent around 0.3 cm^3 K mol^{-1} between 20 K and 200 K, indicating the majority of the sample is in the low spin state (HS fraction $\gamma_{HS} \approx 0.1$). The $\chi_M T$ value dramatically increases upon further heating, suggesting the start of a spin crossover

event. At 360 K, the susceptibility value is 1.34 cm^3 K mol^{-1}, approximately half of what is expected for a HS iron(II) sample. The magnetic data was fit to the regular solution model to estimate the spin state switching temperature, $T_{1/2}$, of 534 K (Table A2.2).[13,39] Due to the temperature limitations of our MPMS instrument and the large $T_{1/2}$ value, the susceptibility of **6-4** was not collected at temperatures above 360 K. The large $T_{1/2}$ value is likely due to the intermolecular interaction of the trifluoromethyl groups stabilizing **6-4** in a conformation that favors the low spin state below room temperature.

Many studies show the electronic properties of ligand substituents affect the magnetic properties of the resulting complex.[9–12] Several reports suggest electron donating substituents result in lower $T_{1/2}$ values and electron withdrawing with higher $T_{1/2}$ values.[9,11,12] The spin-state properties of compounds **6-3** and **6-4** are consistent with this trend as the electron donating methoxy group of **6-3** lends a $T_{1/2}$ value of 289 K and the electron withdrawing trifluoromethyl group of **6-4** leads to a $T_{1/2}$ above room temperature. Unfortunately, **6-2** remains high spin at all temperatures measured so a trend cannot be established between the Hammett parameters of the substituents to the $T_{1/2}$ values for these three complexes. However, it is known that the ligand set found around **6-2** does provide the appropriate ligand field for a thermal spin switching event as such event is observed for the previously reported NTf_2 salt.[33] The differences between the magnetic properties of the OTf salts reported here and the NTf_2 salts reported by Hagiwara and coworkers of the cationic Fe(II) complexes in **6-2** - **6-3** lead us to believe that crystal packing has a significant, possibly dominant impact on the spin state properties, relative to electronic contributions of ligand substituents, at least for this family of complexes.[33,34]

Table 5.5.2. Comparison of the $T_{1/2}$ values for the OTf salts (this work) and NTf_2 salts[33,34] of [(1-(4-R-Ph)-1,2,3-triazole)$_3$)tren)Fe]$^{2+}$.

R	X = OTf salt (this work)	X = NTf_2 (ref 25 and 26)
-H	HS	280 K
-OMe	277 K	273 K ↓ and 285 K ↑
-CF_3	534 K*	--

*$T_{1/2}$ value was calculated by fitting the magnetic susceptibility data, collected between 2 K and 360 K, to the regular solution model.[13,39]

6.5 Conclusion

Successful post-synthetic modification of the high spin iron(II) complex, [((^{TIPS}C≡C)$_3$tren)Fe(OTf)$_2$] (**6-1**), has been demonstrated. The azide-alkyne cycloaddition reaction proceeds after removal of the triisopropylsilyl groups and in the presence of a catalytic amount of copper(I) triflate. Minimal transmetallation occurs and the desired pure triazole-containing iron(II) complex can be isolated through precipitation from the reaction mixture. The unsubstituted, electron donating (methoxy), electron withdrawing (trifluoromethyl), and oxidation sensitive (hydroxymethyl) *para*-substituted azides tested result in the formation of complexes **6-2** - **6-5**, respectively. Confirmation of triazole formation was followed by ^{1}H NMR (**6-2** - **6-5**) and single crystal X-ray diffraction (**6-2** - **6-4**). The solid-state structures show changes from the N_4O_2 first coordination sphere of **6-1** to N_6 first coordination spheres around the iron(II) centers in **6-2** - **6-4**. The crystal structures of **6-2** and **6-3** show shorter intermolecular interactions than what were observed for the related previously reported bis(trifluoromethanesulfonyl)imide (NTf_2) salts, synthesized by coordination of the fully formed triazole ligand to the iron(II) center.[33,34] These interactions lead to contrasting magnetic behavior between the OTf and NTf_2 salts. Compound **6-2** remains high spin at all temperatures measured and **6-3** undergoes a spin crossover event with a $T_{1/2}$ of 289 K; while the related NTf_2 salts undergo full and partial spin crossovers, respectively.[33,34] The crystal structure of **6-4** shows an ammonium ion inside of a supramolecular cavity of CF_3

groups. The solid-state magnetic susceptibility measurements of **6-4** show the start of a spin crossover event above room temperature.

The presence of the co-crystallized ammonium triflate may be important for isolating **6-4** and contribute to the stabilization of the low spin state below room temperature. The post-synthetic reaction conditions require the use of ammonium triflate to isolate clean product, but the traditional synthetic route does not. Comparison of **6-4** synthesized post-synthetically and traditionally will be examined in a future report to determine what impacts the ammonium triflate has on the isolation as well as the magnetic properties of **6-4**.

The studies presented here show successful azide-alkyne cycloaddition post-synthetic modification of an iron(II) complex with a variety of azides can be performed with minimal transmetallation. The cycloaddition results provide a way to incorporate synthetically-challenging substituents on a complex that could not be achieved through traditional synthetic methods. Given the sensitivity of spin state properties of the tren-capped iminotriazole complexes on ligand and anion choices, synthetic elaboration in this area may be expected to yield unique and/or enhanced spin state control.[34,36]

6.6 Experimental

6.6.1 Preparation of Compounds.

All reactions were performed at 23 °C in a dinitrogen filled Vigor glovebox. Syringe filters were purchased from VWR International and were fitted with 0.2 μm PTFE membranes. Diethyl ether (Et_2O) and toluene (MePh) were sparged with nitrogen, passed through an alumina column and degassed prior to use. Anhydrous methanol (CH_3OH) was purchased from Sigma-Aldrich. The starting complex [(($^{TIPS}C{\equiv}C)_3$tren)$Fe(OTf)_2$] (**6-1**) was prepared as described in our previous

report.[32] The azide-containing compounds phenyl azide (PhN_3), 4-methoxyphenyl azide (MeO-PhN_3), 4-trifluoromethylphenyl azide (F_3C-PhN_3), and 4-hydroxymethylphenyl azide ($HOCH_2$-PhN_3) were prepared according to literature.[40,41] All other chemicals were purchased from commercial vendors and used as received.

6.6.2 General Procedure for [(1-(4-R-Ph)-1,2,3-triazole)$_3$)tren)Fe](OTf)$_2$ complex salts.

To a solution of *[((^{TIPS}C≡C)$_3$tren)Fe(OTf)$_2$]* (0.50 mmol) in CH_3OH (1 mL) was added a solution of tetrabutylammonium difluorotriphenylsilicate (TBAT) (1.65 mmol) in CH_3OH (1 mL) and the resulting dark red-purple solution was stirred for 5 minutes. A solution of copper(I) trifluoromethanesulfonate benzene complex (0.015 mmol) in 1 mL of CH_3OH was then added to the reaction mixture. A solution of the corresponding azide (4.5 mmol) in 2 mL of CH_3OH was subsequently added, and the reaction mixture was stirred for 16 hours. A solution of NH_4OTf (4.65 mmol) in CH_3OH (2 mL) was then added to the reaction mixture and stirred for 30 min. The dark red reaction mixture was then passed through a syringe filter and concentrated *in vacuo*. The resulting red-orange solid was purified by alternating precipitations of a concentrated CH_3OH solution with Et_2O (3 × 18 mL) and MePh (3 × 18 mL). After the precipitation process, the resulting red-orange powder was recrystallized, via slow diffusion or layering of Et_2O on methanolic solutions, to obtain the desired [(1-(4-R-Ph)-1,2,3-triazole)$_3$)tren)Fe](OTf)$_2$ complex salts as single crystals.

[(1-(Ph)-1,2,3-triazole)$_3$)tren)Fe](OTf)$_2$, 6-2. ^{1}H NMR (CD_3OD, 400 MHz): δ 29.90, 22.70, 17.37, 12.49, 10.33, 8.25 ppm. Absorption spectrum: CH_3OH, λ_{max}, nm (ε_M, M^{-1} cm^{-1}): 243 (54400), 352 (2510), 447 (2570); MS (ESI^+): *m/z* calcd for $(M - OTf)^+$ $[C_{34}H_{33}F_3FeN_{13}O_3S]^+$: 816.19, found 816.17, *m/z* calcd for $(M - 2OTf)^{2+}$ $[C_{33}H_{33}FeN_{13}]^{2+}$: 333.62, found 333.76; Anal.

calcd for $C_{35}H_{33}F_6FeN_{13}O_6S_2$: C 43.53 %, H 3.44 %, N 18.86 %, found C 43.72 %, H 3.72 %, N 18.38 %.

[(1-(4-MeO-Ph)-1,2,3-triazole)$_3$)tren)Fe](OTf)$_2$, 6-3. ^{1}H NMR (CD_3OD, 400 MHz): δ 29.27, 22.47, 16.95, 11.96, 9.56, 5.03 ppm. Absorption spectrum: CH_3OH, λ_{max}, nm (ε_M, M^{-1} cm^{-1}): 253 (23100), 353 (1590), 448 (1340); MS (ESI^+): *m/z* calcd for $(M - OTf)^+$ $[C_{37}H_{39}F_3FeN_{13}O_6S]^+$: 906.22, found 906.20, *m/z* calcd for $(M - 2OTf)^{2+}$ $[C_{36}H_{39}FeN_{13}O_3]^{2+}$: 378.63, found 378.76. Anal. calcd for $C_{39}H_{43}N_{13}O_{10}F_6S_2Fe$: C 43.06 %, H 3.98 %, N 16.74 %, found C 42.97 %, H 3.89 %, N 17.00 %.

2([(1-(4-F$_3$C-Ph)-1,2,3-triazole)$_3$)tren)Fe](OTf)$_2$)·2NH$_4$OTf, 6-4. ^{1}H NMR (CD_3OD, 400 MHz): δ 28.03, 16.33, 12.29, 10.30 ppm. Absorption spectrum: CH_3OH, λ_{max}, nm (ε_M, M^{-1} cm^{-1}): 237 (26600), 365 (1540), 440 (1480); MS (ESI^+): *m/z* calcd for $(M - OTf)^+$ $[C_{37}H_{30}F_{12}FeN_{13}O_3S]^+$: 1020.15, found 1020.11, *m/z* calcd for $(M - 2OTf)^{2+}$ $[C_{36}H_{30}F_9FeN_{13}]^{2+}$: 435.6, found 435.75; Anal. calcd for $C_{81}H_{74}N_{27}O_{16}F_{33}S_5Fe_2$: C 37.70 %, H 2.89 %, N 14.66 %, found C 37.87%, H 3.06 % N 14.47 %.

[(1-(4-HOCH$_2$-Ph)-1,2,3-triazole)$_3$)tren)Fe](OTf)$_2$, 6-5. ^{1}H NMR (CD_3OD, 400 MHz): δ 29.90, 22.34, 17.47, 12.46, 10.31, 6.61 ppm. Several attempts were made to crystalize **6-5**, but all resulted in the formation of an oil. An anion exchange with $NaBPh_4$ was performed to help isolate diffraction quality crystals but only an oil was isolated after several crystallization conditions were tested. Due to this, all characterizations of **6-5** in this chapter use the powder that is isolate after several precipitation of the post-synthetic reaction mixture with Et_2O and MePh.

6.6.3 Physical Methods.

All methods were performed at room temperature unless otherwise noted. Absorption spectra were obtained with a Hewlett-Packard 8453 spectrometer in quartz cuvettes with a 1 cm path

length. Mass spectrometry measurements were performed in the positive ion mode on a Thermo LTQ mass spectrometer equipped with an analytical electrospray ion source and a quadrupole ion trap mass analyzer at 175 °C. Room temperature ^{1}H NMR spectra were gathered on an Agilent 400 MHz spectrometer. For paramagnetic spectra, changes to standard ^{1}H NMR acquisition were as follows: relaxation delay (1 ms), pulse angle (90°) and acquisition time (1 s). Elemental analyses were performed by Midwest Microlab in Indianapolis, IN.

6.6.4 Crystallographic Structure Determination and Refinement.

Crystallographic parameters for **6-2 - 6-4** are listed in Table 6.6.1. For data collection, crystals were coated in Paratone oil, supported on Cryoloops, and then mounted on a Bruker D8 Advance Quest diffractometer under a stream of dinitrogen. Mo Kα radiation and a graphite monochromator were used for data collection. Initial lattice parameters were determined from reflections found in 8 frames. Data sets were collected targeting complete coverage and fourfold redundancy. Data were integrated and corrected for absorption effects with APEX 3 software.[42] Structures were solved and refined with the SHELXTL software package.[43] Unless noted otherwise, thermal parameters for all fully occupied, nonhydrogen atoms were refined anisotropically. Hydrogen atoms were inserted at calculated positions and refined isotropically, using a riding model where the thermal parameters were set at 1.2 times those of the attached carbon or nitrogen atom and 1.5 times for methyl groups.

Table 5.5.3. Compiled crystallographic information for **6-2 – 6-4.**

	6-2	**6-3**	**6-4**
Formula	$C_{35}H_{33}F_6FeN_{13}O_6S_2$	$C_{78}H_{78}F_{12}Fe_2N_{26}O_{19}S_4$	$C_{39}H_{30}F_{18}FeN_{14}O_9S_3$
Formula weight	965.71	2151.60	1332.80
Color, habit	Orange, Block	Red, Block	Red, Block
T (K)	100	100	100
Space Group	$P2_1/c$	$P\bar{1}$	$R\bar{3}$
Z	4	1	6

a (Å)	17.6196(17)	12.2594(10)	14.050(2)
b (Å)	10.0566(10)	13.3785(10)	14.050(2)
c (Å)	23.031(2)	14.3654(12)	49.803(8)
α (°)	90	81.675(4)	90
β (°)	99.039(3)	77.418(4)	90
γ (°)	90	76.717(3)	120
V (Å^3)	4030.2(7)	2226.8(3)	8343(3)
d_{calc} (g cm^{-3})	1.592	1.605	1.592
GOF	0.996	0.983	0.987
R_1, wR_2[a] (%)	4.98, 15.55	8.00, 22.22	10.34, 28.98

[a] $R_1 = \sum\big||F_o| - |F_c|\big| / \sum |F_o|$, $wR_2 = \{\sum[w(F_o^2 - F_c^2)^2] / \sum[w(F_o^2)^2]\}^{1/2}$ for $F_o > 4\sigma(F_o)$.

6.6.5 Magnetic Measurements.

Data were collected using Quantum Design MPMS XL or MPMS3 SQUID magnetometers. All sample preparations were performed in a dinitrogen filled Vigor glovebox. For solid state samples, powdered microcrystalline samples were loaded into polyethylene bags, sealed, and inserted into drinking straws for measurements. Ferromagnetic impurities were checked through a variable field measurement (0 to 10 kOe) of the magnetization at 100 K; linear fits of the *M* versus *H* data between 0 and 10 kOe (Figure A2.8 – A2.10) indicates the absence of significant ferromagnetic impurities. Magnetic susceptibility data were collected between 2 K to 360 K. Data were corrected for the diamagnetic corrections for the sample calculated from Pascal's constants.[44]

References

(1) Zeng, H.; Stewart-Yates, L.; Casey, L. M.; Bampos, N.; Roberts, D. A. Covalent Post-Assembly Modification: A Synthetic Multipurpose Tool in Supramolecular Chemistry. *Chempluschem* **2020**, *85* (6), 1249–1269.

(2) Chakrabarty, R.; Mukherjee, P. S.; Stang, P. J. Supramolecular Coordination: Self-Assembly of Finite Two- and Three-Dimensional Ensembles. *Chem. Rev.* **2011**, *111* (11), 6810–6918.

(3) Milek, M.; Heinemann, F. W.; Khusniyarov, M. M. Spin Crossover Meets Diarylethenes: Efficient Photoswitching of Magnetic Properties in Solution at Room Temperature. *Inorg. Chem.* **2013**, *52* (19), 11585–11592.

(4) Luo, Y. H.; Nihei, M.; Wen, G. J.; Sun, B. W.; Oshio, H. Ambient-Temperature Spin-State Switching Achieved by Protonation of the Amino Group in [Fe(H2Bpz2)2(Bipy-NH2)]. *Inorg. Chem.* **2016**, *55* (16), 8147–8152.

(5) Komatsumaru, Y.; Nakaya, M.; Kobayashi, F.; Ohtani, R.; Nakamura, M.; Lindoy, L. F.; Hayami, S. Post-Synthetic Modification of a Dinuclear Spin Crossover Iron(III) Complex. *Zeitschrift fur Anorg. und Allg. Chemie* **2018**, *644* (14), 729–734.

(6) Enríquez-Cabrera, A.; Routaboul, L.; Salmon, L.; Bousseksou, A. Complete Post-Synthetic Modification of a Spin Crossover Complex. *Dalt. Trans.* **2019**, *48* (45), 16853–16856.

(7) Gondrand, C.; Touti, F.; Godart, E.; Berezhanskyy, Y.; Jeanneau, E.; Maurin, P.; Hasserodt, J. Spring-Loaded Iron(II) Complexes as Magnetogenic Probes Reporting on a Chemical Analyte in Water. *Eur. J. Inorg. Chem.* **2015**, *2015* (8), 1376–1382.

(8) Rodríguez-Jiménez, S.; Yang, M.; Stewart, I.; Garden, A. L.; Brooker, S. A Simple Method of Predicting Spin State in Solution. *J. Am. Chem. Soc.* **2017**, *139* (50), 18392–18396.

(9) Kershaw Cook, L. J.; Kulmaczewski, R.; Mohammed, R.; Dudley, S.; Barrett, S. A.; Little, M. A.; Deeth, R. J.; Halcrow, M. A. A Unified Treatment of the Relationship Between Ligand Substituents and Spin State in a Family of Iron(II) Complexes. *Angew. Chemie* **2016**, *55* (13), 4327–4331.

(10) Lin, H.-J.; Siretanu, D.; Dickie, D. A.; Subedi, D.; Scepaniak, J. J.; Mitcov, D.; Clérac, R.; Smith, J. M. Steric and Electronic Control of the Spin State in Three-Fold Symmetric, Four-Coordinate Iron(II) Complexes. *J. Am. Chem. Soc.* **2014**, *136* (38), 13326–13332.

(11) Prat, I.; Company, A.; Corona, T.; Parella, T.; Ribas, X.; Costas, M. Assessing the Impact of Electronic and Steric Tuning of the Ligand in the Spin State and Catalytic Oxidation Ability of the FeII(Pytacn) Family of Complexes. *Inorg. Chem.* **2013**, *52* (16), 9229–9244.

(12) Nakano, K.; Suemura, N.; Yoneda, K.; Kawata, S.; Kaizaki, S. Substituent Effect of the Coordinated Pyridine in a Series of Pyrazolato Bridged Dinuclear Diiron(II) Complexes on the Spin-Crossover Behavior. *Dalt. Trans.* **2005**, No. 4, 740–743.

(13) Hogue, R. W.; Feltham, H. L. C.; Miller, R. G.; Brooker, S. Spin Crossover in Dinuclear

N4S2 Iron(II) Thioether-Triazole Complexes: Access to [HS-HS], [HS-LS], and [LS-LS] States. *Inorg. Chem.* **2016**, *55* (9), 4152–4165.

(14) Pan, Y.; Meng, Y. S.; Liu, Q.; Gao, W. Q.; Liu, C. H.; Liu, T.; Zhu, Y. Y. Construction of SCO-Active Fe(II) Mononuclear Complexes from the Thio-Pybox Ligand. *Inorg. Chem.* **2020**, *59* (11), 7398–7407.

(15) Capel Berdiell, I.; Kulmaczewski, R.; Halcrow, M. A. Iron(II) Complexes of 2,4-Dipyrazolyl-1,3,5-Triazine Derivatives - The Influence of Ligand Geometry on Metal Ion Spin State. *Inorg. Chem.* **2017**, *56* (15), 8817–8828.

(16) Chakrabarty, R.; Stang, P. J. Post-Assembly Functionalization of Organoplatinum(II) Metallacycles via Copper-Free Click Chemistry. *J. Am. Chem. Soc.* **2012**, *134* (36), 14738–14741.

(17) Constable, E. C.; Housecroft, C. E.; Price, J. R.; Schweighauser, L.; Zampese, J. A. First Example of a CLICK Reaction of a Coordinated 4′-Azido-2,2′:6′,2″-Terpyridine Ligand. *Inorg. Chem. Commun.* **2010**, *13* (4), 495–497.

(18) Howson, S. E.; Clarkson, G. J.; Faulkner, A. D.; Kaner, R. A.; Whitmore, M. J.; Scott, P. Optically Pure Heterobimetallic Helicates from Self-Assembly and Click Strategies. *Dalt. Trans.* **2013**, *42*, 14967–14981.

(19) Wang, C. F.; Yang, G. Y.; Yao, Z. S.; Tao, J. Monitoring the Spin States of Ferrous Ions by Fluorescence Spectroscopy in Spin-Crossover–Fluorescent Hybrid Materials. *Chem. - A Eur. J.* **2018**, *24* (13), 3218–3224.

(20) Vinu, M.; Sivasankar, K.; Prabu, S.; Han, J. L.; Lin, C. H.; Yang, C. C.; Demel, J. Tetrazine-Based Metal-Organic Frameworks as Scaffolds for Post-Synthetic Modification by the Click Reaction. *Eur. J. Inorg. Chem.* **2020**, *2020* (5), 461–466.

(21) Pilgrim, B. S.; Roberts, D. A.; Lohr, T. G.; Ronson, T. K.; Nitschke, J. R. Signal Transduction in a Covalent Post-Assembly Modification Cascade. *Nat. Chem.* **2017**, *9* (12), 1276–1281.

(22) Roberts, D. A.; Pilgrim, B. S.; Cooper, J. D.; Ronson, T. K.; Zarra, S.; Nitschke, J. R. Post-Assembly Modification of Tetrazine-Edged FeII4L6 Tetrahedra. *J. Am. Chem. Soc.* **2015**, *137* (32), 10068–10071.

(23) Clements, J. E.; Price, J. R.; Neville, S. M.; Kepert, C. J. Perturbation of Spin Crossover Behavior by Covalent Post-Synthetic Modification of a Porous Metal-Organic Framework. *Angew. Chemie - Int. Ed.* **2014**, *53* (38), 10164–10168.

(24) Milek, M.; Heinemann, F. W.; Khusniyarov, M. M. Spin Crossover Meets Diarylethenes: Efficient Photoswitching of Magnetic Properties in Solution at Room Temperature. *Inorg. Chem.* **2013**, *52* (19), 11585–11592.

(25) Nihei, M.; Suzuki, Y.; Kimura, N.; Kera, Y.; Oshio, H. Bidirectional Photomagnetic Conversions in a Spin-Crossover Complex with a Diarylethene Moiety. *Chem. - A Eur. J.* **2013**, *19* (22), 6946–6949.

(26) Nowak, R.; Adi Prasetyanto, E.; De Cola, L.; Bojer, B.; Siegel, R.; Senker, J.; Rössler, E.; Weber, B. Proton-Driven Coordination-Induced Spin State Switch (PD-CISSS) of Iron(II)

Complex. *Chem. Commun* **2017**, *53* (5), 971–974.

(27) Gaudette, A. I.; Thorarinsdottir, A. E.; Harris, T. D. PH-Dependent Spin State Population and 19F NMR Chemical Shift: Via Remote Ligand Protonation in an Iron(Ii) Complex. *Chem. Commun.* **2017**, *53* (96), 12962–12965.

(28) Shiga, T.; Saiki, R.; Akiyama, L.; Kumai, R.; Natke, D.; Renz, F.; Cameron, J. M.; Newton, G. N.; Oshio, H. A Brønsted-Ligand-Based Iron Complex as a Molecular Switch with Five Accessible States. *Angew. Chemie - Int. Ed.* **2019**, *58* (17), 5658–5662.

(29) Martin, L. L.; Hagen, K. S.; Hauser, A.; Martin, R. L.; Sargeson, A. M. Spin Equilibria in Iron(II) Hexa-Amine Cages. *J. Chem. Soc. Chem. Commun.* **1988**, No. 19, 1313–1315.

(30) McConnell, A. J.; Aitchison, C. M.; Grommet, A. B.; Nitschke, J. R. Subcomponent Exchange Transforms an FeII4L4 Cage from High- to Low-Spin, Switching Guest Release in a Two-Cage System. *J. Am. Chem. Soc.* **2017**, *139* (18), 6294–6297.

(31) Ozumerzifon, T. J.; Higgins, R. F.; Joyce, J. P.; Kolanowski, J. L.; Rappé, A. K.; Shores, M. P. Evidence for Reagent-Induced Spin-State Switching in Tripodal Fe(II) Iminopyridine Complexes. *Inorg. Chem.* **2019**, *58* (12), 7785–7793.

(32) Livesay, B. N.; Shores, M. P. Influence of Coordinated Triflate Anions on the Solution Magnetic Properties of a Neutral Iron(II) Complex. *Inorg. Chem.* **2021**, *60* (20), 15445–15455.

(33) Hagiwara, H.; Minoura, R.; Okada, S.; Sunatsuki, Y. Synthesis, Structure, and Magnetic Property of a New Mononuclear Iron(II) Spin Crossover Complex with a Tripodal Ligand Containing Three 1,2,3-Triazole Groups. *Chem. Lett.* **2014**, *43* (6), 950–952.

(34) Hagiwara, H.; Minoura, R.; Udagawa, T.; Mibu, K.; Okabayashi, J. Alternative Route Triggering Multistep Spin Crossover with Hysteresis in an Iron(II) Family Mediated by Flexible Anion Ordering. *Inorg. Chem.* **2020**, *59* (14), 9866–9880.

(35) Alvarez, S.; Alemany, P.; Casanova, D.; Cirera, J.; Llunell, M.; Avnir, D. Shape Maps and Polyhedral Interconversion Paths in Transition Metal Chemistry. *Coord. Chem. Rev.* **2005**, *249* (17–18), 1693–1708.

(36) Hagiwara, H.; Tanaka, T.; Hora, S. Synthesis, Structure, and Spin Crossover above Room Temperature of a Mononuclear and Related Dinuclear Double Helicate Iron(II) Complexes. *Dalt. Trans.* **2016**, *45* (43), 17132–17140.

(37) Schweinfurth, D.; Demeshko, S.; Hohloch, S.; Steinmetz, M.; Brandenburg, J. G.; Dechert, S.; Meyer, F.; Grimme, S.; Sarkar, B. Spin Crossover in Fe(II) and Co(II) Complexes with the Same Click-Derived Tripodal Ligand. *Inorg. Chem.* **2014**, *53* (16), 8203–8212.

(38) Chilton, N. F.; Anderson, R. P.; Turner, L. D.; Soncini, A.; Murray, K. S. PHI: A Powerful New Program for the Analysis of Anisotropic Monomeric and Exchange-Coupled Polynuclear d- and f-Block Complexes. *J. Comput. Chem.* **2013**, *34* (13), 1164–1175.

(39) Kahn, O. *Molecular Magnetism*; VCH: New York, NY, 1993.

(40) Nallapati, S. B.; Sreenivas, B. Y.; Bankala, R.; Parsa, K. V. L.; Sripelly, S.; Mukkanti, K.;

Pal, M. 1,2,3-Triazoles Derived from Olanzapine: Their Synthesis via an Ultrasound Assisted CuAAC Method and Evaluation as Inhibitors of PDE4B. *RSC Adv.* **2015**, *5* (115), 94623–94628.

(41) Matikonda, S. S.; Orsi, D. L.; Staudacher, V.; Jenkins, I. A.; Fiedler, F.; Chen, J.; Gamble, A. B. Bioorthogonal Prodrug Activation Driven by a Strain-Promoted 1,3-Dipolar Cycloaddition. *Chem. Sci.* **2015**, *6* (2), 1212–1218.

(42) APEX3. Bruker Analytical X-Ray Systems, Inc.: Madison, WI. 2016.

(43) Sheldrick, G. M. SHELXTL. *SHELXTL*. Version 6. Analytical X-Ray Systems: Madison, WI. 1999.

(44) Bain, G. A.; Berry, J. F. Diamagnetic Corrections and Pascal's Constants. *J. Chem. Educ.* **2008**, *85* (4), 532–536.

Chapter 7: Investigation of Substituent Effects of 1,2,3-Triazole Containing Iron(II) Compounds

7.1 Introduction

Compounds that can reversibly undergo spin state switching have great potential in a variety of applications.[1,2] Octahedral iron(II)-based compounds are widely studied for these types of applications due to the vast differences in the physical properties of the paramagnetic high spin state and the diamagnetic low spin state. However, the spin state switching event is extremely sensitive to ligand choice. Weak field ligands lead to high spin complexes and strong field ligands result in low spin complexes. However, in the presence of a moderate ligand field reversible spin state switching can occur.

The ability to accurately control the ligand field strength around iron(II) has been explored by several groups.[3–6] In those studies, the field strength is modified by adding electron-donating and -withdrawing substituents to the ligand, and the relationship between the Hammett constant[7] of the substituents with the solution phase spin switching temperature, $T_{1/2}$, is then described. Unfortunately, these studies do not all agree on the effects a ligand has on the spin state switching properties of iron(II) complexes. For example, a report by Deeth and Halcrow on $[Fe(bpp^X)_2][BF_4]_2$ (bpp^X = 2,6-bis(pyrazolyl)-4-X-pyridine)) indicates electron withdrawing groups at the *para*-position stabilize the low spin state, resulting in higher $T_{1/2}$ values.[4] Whereas, a report by Clérac and Smith on $PhB(MesIm)_3Fe{-}N{=}P(p\text{-}XC_6H_4)_3$ indicate electron withdrawing groups at the para-position stabilize the high spin state, leading to lower $T_{1/2}$ values.[5] While these studies show there is a relationship between the Hammett constant and the solution magnetic

properties, the relationship is dependent on the ligand family used and does not always translate well to other systems.

This inability to expand to other systems is due to the many other influences that can overshadow the ligand field effects. In the solid state, ligand field effects can be overshadowed by crystal packing effects.[8] Whereas in solution, the solvent choice can move the spin state switching event to different temperatures.[9,10] These additional factors can lead to a single complex with different magnetic data in the solid state and in different solvents.[10,11]

With this in mind, we want to further investigate the magnetic behavior of the family of 1,2,3-triazoles iron(II) complexes from Chapter 6. The *para*-substituted phenyl 1,2,3-triazole complexes, $[(1\text{-}(4\text{-R-Ph})\text{-}1,2,3\text{-triazole})_3)\text{tren})\text{Fe}](\text{OTf})_2$ (R = H- (**7-1**), MeO- (**7-2**), F_3C- (**7-3**) exhibit different solid state magnetic behaviors depending on the substituent. The electron donating and withdrawing substituents lead to a spin switching event with $T_{1/2}$ values of 277 K and 534 K, respectively. However, the unsubstituted complex (**7-1**) remains high spin at all temperatures, which is not what is expected for these types of 1,2,3-triazole iron(II) complexes.[12,13] As solid state magnetic behavior can be affected by crystal packing, it is believed that the packing environment of **7-1** is overshadowing the ligand field effects. We expect when these crystal packing effects are removed, the solution magnetic data will reveal a relationship between the Hammett parameter of the substituent and the spin state switching temperature, $T_{1/2}$. In addition to the *para*-substituent effects on the phenyl ring, we have synthesized the unsubstituted 1-benzyl-1,2,3-triazole iron(II) complex. This will allow us to investigate the *meta*-substituent effect of the triazole ring. We hope this study will provide additional insight into the thought full design of new spin state switching compounds.

7.2 Division of Labor

All work in this chapter has been carried out by Brooke N. Livesay. This work is supported by Colorado State University and the NSF (CHE-1363274, CHE-1800554, and CHE-1956399).

7.3 Results and Discussion

7.3.1 Synthesis and Crystal Structure

All complexes are prepared following the azide-alkyne cycloaddition post synthetic modification of the high spin iron(II) compound, [((^{TIPS}C≡C)$_3$tren)Fe(OTf)$_2$], as previously described in Chapter 6. We also described the crystal structures of the phenyl triazole compounds, [(1-(4-R-Ph)-1,2,3-triazole)$_3$)tren)Fe](OTf)$_2$ (R = H- (**7-1**), MeO- (**7-2**), F_3C- (**7-3**)) in Chapter 6. The synthesis and structural analysis of the benzyl triazole compound [(1-(benzyl)-1,2,3-triazole)$_3$)tren)Fe](OTf)$_2$ (**7-4**) are presented in this chapter. Single crystals of (**7-4**) are obtained from a diffusion of diethyl ether into a concentrated acetonitrile solution, and the diffraction data were collected at 120 K. The neutral 1-benzyl-1,2,3-triazole)$_3$)tren ligand binds to the iron(II) center through the imine and triazole nitrogen atoms, resulting in a N_6 coordination environment for **7-4** (Figure 7.3.1). Two iron(II) cationic complexes are observed in the unit cell. One of the iron(II) centers in **7-4** is stabilized in the high spin state with an average Fe1-N_{imine} bond distance of 2.163(3) Å and average Fe1-$N_{triazole}$ distance equal to 2.358(3) Å. The bridgehead nitrogen on the ligand backbone is 2.678(3) Å away from the iron(II) center, providing a pseudo-heptacoordinate environment around Fe1. The value obtained from continuous shape measurements (CShM) indicates a close to ideal capped octahedron coordination geometry around Fe1 (CShM value of 1.856).[14] In contrast, the second iron(II) center in **7-4** crystallizes in a low spin state with average bond distances of 2.03(3) Å (Fe2-N_{imine}) and 2.01(3) Å (Fe2-$N_{triazole}$). A

close to ideal octahedron coordination geometry (CShM value 1.182) is obtained as the bridgehead nitrogen atom is 2.678(3) Å away from Fe2.

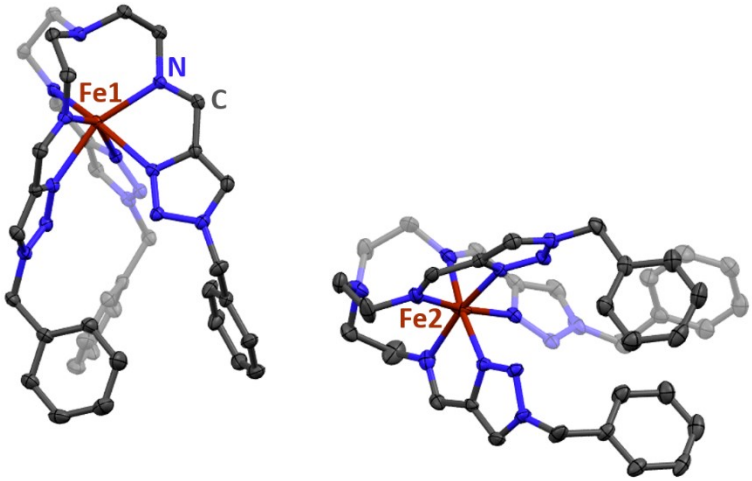

Figure 7.3.1. Crystal Structure of **7-4** depicted with 40% thermal ellipsoids, hydrogen and counter anions have been omitted for clarity. Dark red, blue, and gray ellipsoids represent Fe, N, and C, respectively.

7.3.2 Solid State MPMS

The solid-state magnetic behavior of **7-1** - **7-3** can be found in Chapter 6. The temperature dependence of the magnetic susceptibility in the solid state of crystalline **7-4** was measured at 1000 Oe between 4 K and 300 K (Figure 7.3.2). At 300 K, the $\chi_M T$ value is 3.31 cm^3 K mol^{-1}, higher than the spin only value ($S = 2$, $g = 2$, $\chi_M T = 3$ cm^3 K mol^{-1}) but consistent with previously reported HS iron(II) complexes. Upon decreasing the temperature, the $\chi_M T$ value slowly drops until it reaches 2.94 cm^3 K mol^{-1} at 25 K, consistent with the sample remaining high spin. A dramatic decrease is observed below 25 K; at 4 K the $\chi_M T$ value is 2.5 cm^3 K mol^{-1}. This data is inconsistent with the crystal structures of **7-4** collected at 120 K which would predict one HS and one LS species. This may be due to the different batches of **7-4** used to collect the crystallographic and the magnetic data. It is possible the two samples crystallized in different packing environments or with additional co-crystallized solvents. Small differences in the crystal packing environment have been

shown to affect the magnetic properties of previously reported compounds and is likely the cause to the inconsistency observed here.[8,15,16] Another possibility is that there are two HS species present in the crystal structure, but the low bond precision of Fe2 may suggest some disorder such that a HS species masquerades as a LS complex. Further characterization of a new single batch of **7-4** by single crystal X-ray diffraction and magnetometry will be necessary to help determine what is leading to the inconsistency between the structural and magnetic data, if there is any.

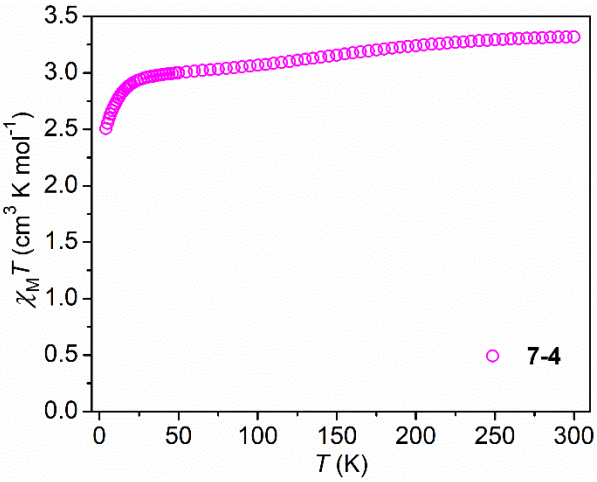

Figure 7.3.2. The solid-state temperature dependence of the magnetic susceptibility for **7-4**, collected between 4 K and 300 K with a measuring field of 1000 Oe.

7.3.3 Solution Magnetic Measurements

In contrast to the solid state, the tris(triazole) complexes show similar magnetic behavior in solution. When **7-1** – **7-4** are dissolved in d_4-CD_3OD, a yellow to dark orange color change is observed upon decreasing the temperature, indicative of a thermal spin state change in solution. This event was examined through the Evans' ^{1}H NMR Method between 198 K and 298 K (Figure 7.3.3). The solution magnetic data in d_4-CD_3OD are similar for all complexes. As a representative example, the data for **7-1** will be described. At 298 K, the $\chi_M T$ value is 2.71 cm^3 K mol^{-1} (high spin molar fraction, γ_{HS} = 0.90, assuming a γ_{HS} = 1 when $\chi_M T$ = 3 cm^3 K mol^{-1}). Upon decreasing the

temperature, the $\chi_M T$ abruptly decreases, indicating a spin state switching event. This event continues until 198 K, where the $\chi_M T$ value reaches 0.00 cm^3 K mol^{-1} (γ_{HS} = 0.00). The spin state switching events observed for **7-1 - 7-4** were fit with the regular solution model[17,18] to obtain the thermodynamic parameters and the transition temperature, $T_{1/2}$ (Table 7.3.1). The change in enthalpy (ΔH) and entropy (ΔS) values calculated for all four compounds agree with previously reported solution phase spin state switching compounds (ΔH = 4 – 41 kJ mol^{-1} and ΔS = 22 – 146 J mol^{-1} K^{-1}).[4,19–21] The spin state switching temperature, $T_{1/2}$, was calculated by dividing the enthalpy by the entropy ($\Delta H/\Delta S$). The $T_{1/2}$ values are compared to the Hammett constant of the *para*- and *meta*- ligand substituent to explore the extent of a relationship between the ligand substituents and the magnetic properties.

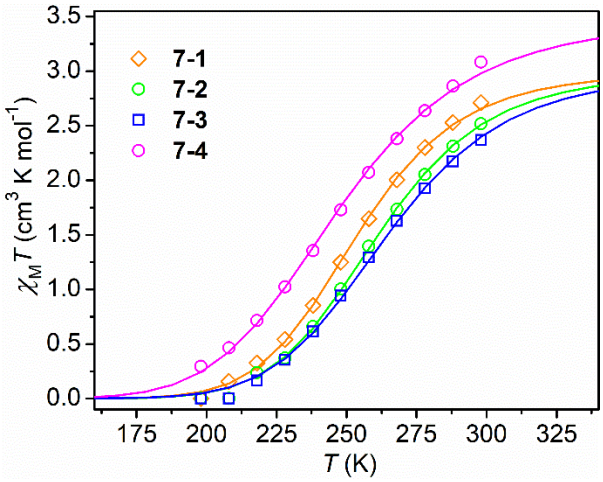

Figure 7.3.3. Solution phase temperature dependence of the magnetic susceptibility for **7-1** (open orange diamonds), **7-2** (open green circles), **7-3** (open blue squares), and **7-4** (open magenta circles) in d_4-CD_3OD collected from 198 K to 298 K. Solid lines represent the fits obtained from the regular solution model.

Table 7.3.1. Thermodynamic parameters and $T_{1/2}$ values obtained from fitting the solution magnetic data with the regular solution model.

Compound	$3\sigma_{para}$	$3\sigma_{meta}$	ΔH (kJ mol^{-1})	ΔS (J mol^{-1} K^{-1})	$\chi_M T$ max (cm^3 K mol^{-1})	$T_{1/2}$ (K)	R^2

7-1 H-Ph	0.00	0.54	29.13	114.75	3.0	253.8	0.99947
7-2 MeO-Ph	-0.81	--	28.74	110.01	3.0	261.2	0.99920
7-3 CF_3-Ph	1.62	--	27.17	102.68	3.0	264.6	0.99892
7-4 $PhCH_2$	--	-0.72	21.30	85.98	3.5	247.7	0.99896

7.3.4 Para substituent effects

The *para* effects of the substituents on the phenyl ring are determined by comparing the *para* Hammett parameter (σ_{para}) to the $T_{1/2}$ values of the related compounds (**7-1** – **7-3**). There is a small linear relationship between these quantities that suggests electron-withdrawing groups will stabilize the low spin state (Figure 7.3.4). However, the correlation between these values is negligible and is within error of the calculated $T_{1/2}$ values. While it is noted that the sample size is low, the electron donating (-OMe) and withdrawing (-CF_3) groups chosen here have the largest Hammett parameter values of the electron donating and withdrawing substituents we can include on the phenyl ring while still maintaining safe handling of the related organic azides. Due to this, we anticipate that including other substituents with Hammett values between the -OMe and -CF_3 values would not lead to a stronger correlation between the *para* Hammett parameters and the $T_{1/2}$.

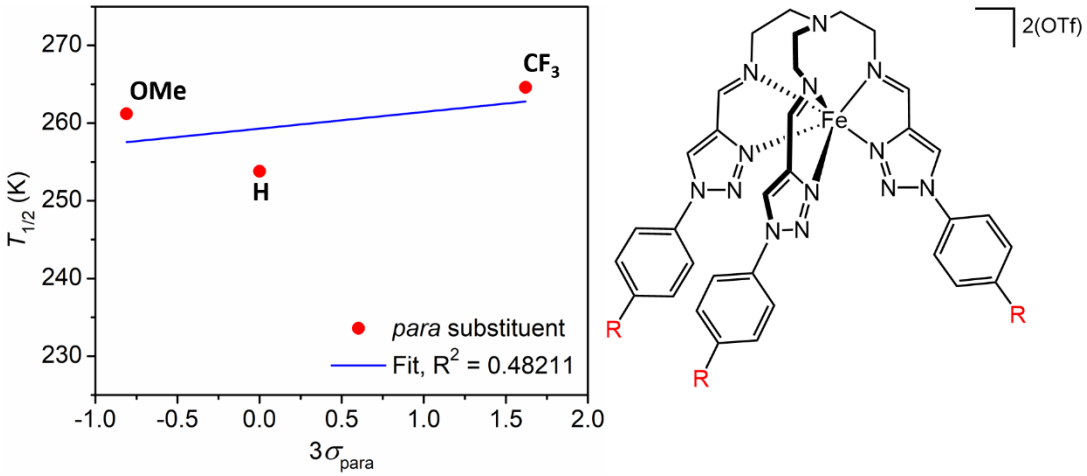

Figure 7.3.4. Plot of the $T_{1/2}$ as a function of the para Hammett parameter for **7-1** – **7-3**. The data was fit to a linear regression ($T_{1/2} = 2.15 \times 3\sigma_{para} + 259.29$), shown in blue.

7.3.5 Meta substituent effects

To investigate the *meta* effects on the magnetic properties of the resulting iron(II) compounds, the group bound directly to the nitrogen of the triazole ring is the substituent. Due to this, the substituents that can be included are limited due to the requirements for safe handling of organic azides. For this, the substituent needs to have a total carbon and oxygen count of six or more.[22] We found several substituent groups that fulfill this requirement, unfortunately only the phenyl and benzyl substituents afforded iron(II) triazole complexes that could be purified and isolated at this time. The relationship between the *meta* Hammett parameter and the $T_{1/2}$ of the related compounds **7-1** and **7-4** shows a strong response, especially relative to the *para* parameter, suggesting electron donating groups will stabilize the high spin state (Figure 7.3.5). However, this is correlation is only based on two data points and cannot be used to predicatively choose a *meta* substituent that would provide a desired $T_{1/2}$ value. Future studies should focus on isolating additional iron(II) triazole complexes with *meta* substituents. Ideal substituents to investigate that will provide a range of *meta* Hammett parameters may include 1-adamantyl (σ_{meta} = -0.12), 1-cyclohexenynl (σ_{meta} = -0.10), cyclohexyl (σ_{meta} = -0.05), CH_2SO_2R (σ_{meta} = 0.15), $COOCH(C_6H_5)_2$ (σ_{meta} = 0.36), 3-1H-naphtho[2,1-b]pyran-1-one (σ_{meta} = 0.38), and 2-(benzothiopyronyl) (σ_{meta} = 0.48).

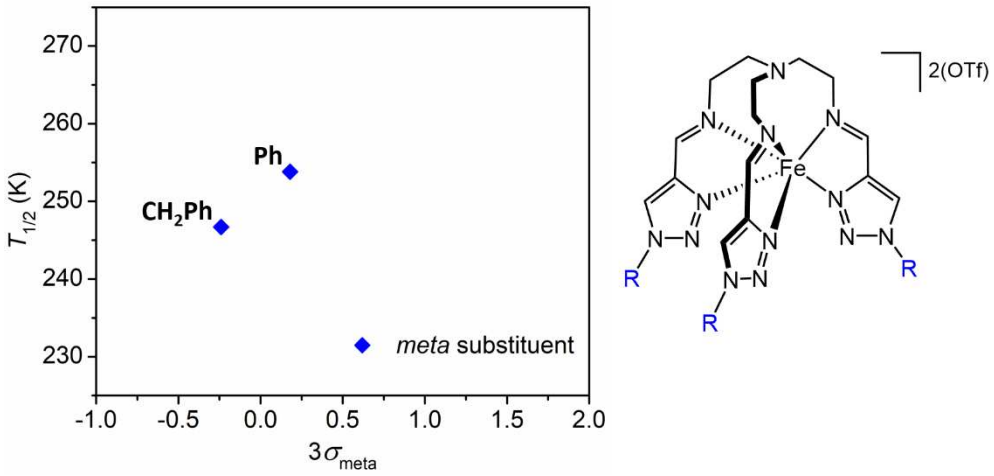

Figure 7.3.5. Plot of the $T_{1/2}$ as a function of the meta Hammett parameter for **7-1** and **7-4**.

7.4 Conclusion

We report the solution magnetic behavior of four iron(II) triazole compounds in d_4-CD_3OD. All compounds undergo thermal spin state switching with a transition temperature, $T_{1/2}$, between 247.7 K and 264.6 K. The *para* substituent effect for the phenyl substituted iron(II) triazole compounds **7-1** – **7-3** were evaluated. A small correlation between the *para* Hammett parameter and the $T_{1/2}$ was observed, indicating electron withdrawing groups stabilize the low spin state and lead to higher $T_{1/2}$ values. This lack of a strong correlations between the *para* effects is due to the distance between the substituent and the iron(II) center. When the substituent is closer to the iron(II) center, the electron donating and withdrawing substituent effects have a greater impact on the magnetic properties. This can be seen by the *meta* substituent effects on the triazole nitrogen. A strong correlation between the *meta* Hammett parameter and the $T_{1/2}$ for **7-1** and **7-4** indicates electron donating groups stabilize the high spin state and lead to lower $T_{1/2}$ values. However, this correlation is determined from two compounds and may change upon further investigation of additional *meta* substituents. This study suggests that the distance a substituent is from the metal center is just as impactful as the putative electron donating and withdrawing character.

7.5 Experimental

7.5.1 Preparation of Compounds.

All reactions were performed at 23 °C in a dinitrogen-filled Vigor glovebox. Syringe filters were purchased from VWR International and were fitted with 0.2 μm PTFE membranes. Diethyl ether (Et_2O) and toluene (MePh) were sparged with nitrogen, passed through an alumina column and degassed prior to use. Anhydrous methanol (CH_3OH) was purchased from Sigma-Aldrich. Preparation of the starting complex *[(($^{TIPS}C{\equiv}C)_3$tren)Fe(OTf)$_2$]* was previously described in Chapter 4. Benzyl azide was prepared according to literature procedures.[23] The triazole iron(II) complexes **7-1 - 7-4** were synthesized following our previously reported post synthetic reaction described in Chapter 6. All other chemicals were purchased from commercial vendors and used as received.

*7.5.2 [(1-(benzyl)-1,2,3-triazole)$_3$)tren)Fe](OTf)$_2$ (**7-4**)*

To a solution of *[(($^{TIPS}C{\equiv}C)_3$tren)Fe(OTf)$_2$]* (0.50 mmol) in CH_3OH (1 mL) was added a solution of tetrabutylammonium difluorotriphenylsilicate (TBAT) (1.65 mmol) in CH_3OH (1 mL), and the resulting dark red-purple solution was stirred for 5 minutes. A solution of copper(I) trifluoromethanesulfonate benzene complex (0.015 mmol) in 1 mL of CH_3OH was then added to the reaction mixture. A solution of benzyl azide (4.5 mmol) in 2 mL of CH_3OH was subsequently added, and the reaction mixture was stirred for 16 to 24 hours. A solution of NH_4OTf (4.65 mmol) in CH_3OH (2 mL) was then added to the reaction mixture and stirred for 30 mins. The dark red reaction mixture was then passed through a syringe filter and concentrated *in vacuo*. The resulting red-orange solid was purified by alternating precipitations of a concentrated CH_3OH solution with Et_2O (3 × 18 mL) and MePh (3 × 18 mL). After the precipitation process, a concentrated solution

of the red-orange powder in acetonitrile was crystallized by slow diffusion of diethyl ether to obtain [(1-(benzyl)-1,2,3-triazole)$_3$)tren)Fe](OTf)$_2$ as single crystals.

[(1-(benzyl)-1,2,3-triazole)$_3$)tren)Fe](OTf)$_2$ (7-4). Yield: 68%; ^{1}H NMR (CD_3OD, 400 MHz): δ 30.84, 24.40, 16.90, 16.36, 14.64, 11.38, 9.18, 8.22 ppm. Absorption spectrum: CH_3OH, λ_{max}, nm (ε_M, M^{-1} cm^{-1}): 205 (52100), 249 (19700), 327 (2160), 448 (2230); Anal. calcd for $C_{38}H_{39}F_6FeN_{13}O_6S_2$: C 45.29 %, H 3.90 %, N 18.07 %, found C 44.92 %, H 4.02 %, N 17.85 %.

7.5.3 Physical Methods.

All methods were performed at room temperature unless otherwise noted. Absorption spectra were obtained with a Hewlett-Packard 8453 spectrometer in quartz cuvettes with a 1 cm path length. Mass spectrometry measurements were performed in the positive ion mode on a Thermo LTQ mass spectrometer equipped with an analytical electrospray ion source and a quadrupole ion trap mass analyzer at 175 °C. Room temperature ^{1}H spectra were gathered on an Agilent 400 MHz spectrometer. For paramagnetic spectra, changes to standard ^{1}H NMR acquisition were as follows: relaxation delay (1 ms), pulse angle (90°) and acquisition time (1 s). For Evans' method measurements of magnetic susceptibility, the paramagnetic iron(II) species were measured at 5 mM. Elemental analyses were performed by Midwest Microlab in Indianapolis, IN.

7.5.4 Crystallographic Measurements.

Crystallographic parameters for **7-4** are listed in Table 7.6.1. For data collection, the crystal was coated in Paratone oil, supported on Cryoloops, and then mounted on a Bruker D8 Advance Quest diffractometer under a stream of dinitrogen. Mo Kα radiation and a graphite monochromator were used for data collection. Initial lattice parameters were determined from reflections found in 8 frames. Data sets were collected targeting complete coverage and fourfold redundancy. Data were integrated and corrected for absorption effects with APEX 3 software.[24] Structures were

solved and refined with the SHELXTL software package.[25] Unless noted otherwise, thermal parameters for all fully occupied, nonhydrogen atoms were refined anisotropically. Hydrogen atoms were inserted at calculated positions and refined isotropically, using a riding model where the thermal parameters were set at 1.2 times those of the attached carbon or nitrogen atom.

Table 7.5.1. Compiled crystallographic information for 7-4.

	7-4
Formula	$C_{78}H_{78}F_{12}Fe_2N_{26}O_{14}S_4$
Formula weight	2066.5
Color, habit	Red, Block
T (K)	120
Space Group	*P* $2_1/n$
Z	4
a (Å)	21.930(7)
b (Å)	15.889(5)
c (Å)	27.582(8)
α (°)	90
β (°)	105.622(9)
γ (°)	90
V (Å^3)	9256(5)
d_{calc} (g cm^{-3})	1.483
GOF	0.943
R_1, wR_2[a] (%)	8.37, 26.85

[a] $R_1 = \sum\big||F_o| - |F_c|\big| / \sum |F_o|$, $wR_2 = \{\sum[w(F_o^2 - F_c^2)^2] / \sum[w(F_o^2)^2]\}^{1/2}$ for $F_o > 4\sigma(F_o)$.

7.5.5 Magnetic Measurements.

Data were collected using a Quantum Design MPMS3 SQUID magnetometer. All sample preparations were performed in a dinitrogen-filled Vigor glovebox. For solid-state samples, powdered microcrystalline samples were loaded into polyethylene bags, sealed, and inserted into drinking straws for measurements. Ferromagnetic impurities were checked through a variable field measurement (0 to 10 kOe) of the magnetization at 100 K; linear fits of the *M* versus *H* data between 0 and 10 kOe (Figure A3.1) indicates the absence of ferromagnetic impurities. Magnetic

susceptibility data were collected between 2 K and 360 K. Data were corrected for the diamagnetic corrections for the sample were calculated from Pascal's constants.[26] Solution magnetic data obtained from Evans' ^{1}H NMR method was fit using the regular solution model[17,18] (Equation 7.1):

$$\chi T = \frac{\chi T_{max}}{1+e^{\left(\frac{\Delta H}{RT}-\frac{\Delta S}{R}\right)}} \tag{7.1}$$

References

(1) Brooker, S. Spin Crossover with Thermal Hysteresis: Practicalities and Lessons Learnt. *Chem. Soc. Rev.* **2015**, *44* (10), 2880–2892.

(2) Létard, J.-F.; Guionneau, P.; Goux-Capes, L. Towards Spin Crossover Applications. In *Spin Crossover in Transition Metal Compounds III*; 2006; Vol. 235, pp 221–249.

(3) Prat, I.; Company, A.; Corona, T.; Parella, T.; Ribas, X.; Costas, M. Assessing the Impact of Electronic and Steric Tuning of the Ligand in the Spin State and Catalytic Oxidation Ability of the FeII(Pytacn) Family of Complexes. *Inorg. Chem.* **2013**, *52* (16), 9229–9244.

(4) Kershaw Cook, L. J.; Kulmaczewski, R.; Mohammed, R.; Dudley, S.; Barrett, S. A.; Little, M. A.; Deeth, R. J.; Halcrow, M. A. A Unified Treatment of the Relationship Between Ligand Substituents and Spin State in a Family of Iron(II) Complexes. *Angew. Chemie* **2016**, *55* (13), 4327–4331.

(5) Lin, H.-J.; Siretanu, D.; Dickie, D. A.; Subedi, D.; Scepaniak, J. J.; Mitcov, D.; Clérac, R.; Smith, J. M. Steric and Electronic Control of the Spin State in Three-Fold Symmetric, Four-Coordinate Iron(II) Complexes. *J. Am. Chem. Soc.* **2014**, *136* (38), 13326–13332.

(6) Nakano, K.; Suemura, N.; Yoneda, K.; Kawata, S.; Kaizaki, S. Substituent Effect of the Coordinated Pyridine in a Series of Pyrazolato Bridged Dinuclear Diiron(II) Complexes on the Spin-Crossover Behavior. *Dalt. Trans.* **2005**, No. 4, 740–743.

(7) Hansch, C.; Leo, A.; Taft, R. W. *A Survey of Hammett Substituent Constants and Resonance and Field Parameters*; 1991; Vol. 91.

(8) Real, J. A.; Gaspar, A. B.; Carmen Muñoz, M. Thermal, Pressure and Light Switchable Spin-Crossover Materials. *Dalton Transactions*. The Royal Society of Chemistry June 21, 2005, pp 2062–2079.

(9) Barrett, S. A.; Kilner, C. A.; Halcrow, M. A. Spin-Crossover in [Fe(3-Bpp)2][BF4]2 in Different Solvents - A Dramatic Stabilisation of the Low-Spin State in Water. *Dalt. Trans.* **2011**, *40* (45), 12021–12024.

(10) Rodríguez-Jiménez, S.; Barltrop, A. S.; White, N. G.; Feltham, H. L. C.; Brooker, S. Solvent Polarity Predictably Tunes Spin Crossover T1/2 in Isomeric Iron(II) Pyrimidine Triazoles. *Inorg. Chem.* **2018**, *57* (11), 6266–6282.

(11) Weber, B.; Walker, F. A. Solution NMR Studies of Iron(II) Spin-Crossover Complexes. *Inorg. Chem.* **2007**, *46* (16), 6794–6803.

(12) Hagiwara, H.; Minoura, R.; Okada, S.; Sunatsuki, Y. Synthesis, Structure, and Magnetic Property of a New Mononuclear Iron(II) Spin Crossover Complex with a Tripodal Ligand Containing Three 1,2,3-Triazole Groups. *Chem. Lett.* **2014**, *43* (6), 950–952.

(13) Hagiwara, H.; Minoura, R.; Udagawa, T.; Mibu, K.; Okabayashi, J. Alternative Route Triggering Multistep Spin Crossover with Hysteresis in an Iron(II) Family Mediated by Flexible Anion Ordering. *Inorg. Chem.* **2020**, *59* (14), 9866–9880.

(14) Alvarez, S.; Alemany, P.; Casanova, D.; Cirera, J.; Llunell, M.; Avnir, D. Shape Maps and Polyhedral Interconversion Paths in Transition Metal Chemistry. *Coord. Chem. Rev.* **2005**, *249* (17–18), 1693–1708.

(15) Sorai, M.; Ensling, J.; Hasselbach, K. M.; Gütlich, P. Mössbauer Effect Study on Low-Spin 1A1 ⇌ High Spin 5T2 Transition in [Fe(2-Pic)3]Cl2. II. Influence of Non-Coordinating Solvent Molecule in [Fe(2-Pic)3] Cl2 · X1 X = C2H5OH, CH3OH, H2O and 2H2O. *Chem. Phys.* **1977**, *20* (2), 197–208.

(16) Han, W. K.; Qin, L. F.; Pang, C. Y.; Cheng, C. K.; Zhu, W.; Li, Z. H.; Li, Z.; Ren, X.; Gu, Z. G. Polymorphism of a Chiral Iron(II) Complex: Spin-Crossover and Ferroelectric Properties. *Dalt. Trans.* **2017**, *46* (25), 8004–8008.

(17) Hogue, R. W.; Feltham, H. L. C.; Miller, R. G.; Brooker, S. Spin Crossover in Dinuclear N4S2 Iron(II) Thioether-Triazole Complexes: Access to [HS-HS], [HS-LS], and [LS-LS] States. *Inorg. Chem.* **2016**, *55* (9), 4152–4165.

(18) Kahn, O. *Molecular Magnetism*; VCH: New York, NY, 1993.

(19) Rodríguez-Jiménez, S.; Yang, M.; Stewart, I.; Garden, A. L.; Brooker, S. A Simple Method of Predicting Spin State in Solution. *J. Am. Chem. Soc.* **2017**, *139* (50), 18392–18396.

(20) Shores, M. P.; Klug, C. M.; Fiedler, S. R. Spin-State Switching in Solution. In *Spin-Crossover Materials: Properties and Applications*; Halcrow, M. A., Ed.; John Wiley & Sons Ltd: Oxford, UK, 2013; pp 281–301.

(21) Toftlund, H. Spin Equilibrium in Solution. *Monatshefte Fur Chemie* **2001**, *132*, 1269–1277.

(22) Muller, T.; Bräse, S. Azides. *Kirk-Othmer Encycl. Chem. Technol.* **2012**.

(23) Tona, V.; De La Torre, A.; Padmanaban, M.; Ruider, S.; González, L.; Maulide, N. Chemo- and Stereoselective Transition-Metal-Free Amination of Amides with Azides. *J. Am. Chem. Soc.* **2016**, *138* (27), 8348–8351.

(24) APEX3. Bruker Analytical X-Ray Systems, Inc.: Madison, WI. 2016.

(25) Sheldrick, G. M. SHELXTL. *SHELXTL*. Version 6. Analytical X-Ray Systems: Madison, WI. 1999.

(26) Bain, G. A.; Berry, J. F. Diamagnetic Corrections and Pascal's Constants. *J. Chem. Educ.* **2008**, *85* (4), 532–536.

Chapter 8: Closing Remarks and Future Directions

8.1 Summary of Solvent Induced Spin State Switching

The results from Chapter 4 demonstrate the sensitivity of solution spin state switching on the dissolving solvent. The iron(II) complex, [((^{TIPS}C≡C)$_3$tren)Fe(OTf)$_2$] (**8-1**), is high spin in the solid state, however in can be high spin (HS), low spin (LS), or undergo coordination induced spin state switching (CISSS) depending on the dissolving solvent. The differences in the magnetic properties in various solvents is due to the change in the coordination of the triflate anions. Strongly coordinating solvents displace both triflate anions, resulting in a HS state when the donating atom is oxygen and a LS state when the donating atom is nitrogen. Non-coordinating solvents do not displace the triflate anion, leading to the retention of the HS state. In the moderately coordinating solvent, acetone, **8-1** undergoes CISSS. However, this event is dependent on the concentration and hydrogen isotope identity of the acetone. These results from these studies highlight the sensitivity of the of the magnetic properties on solvent choice and concentration.

8.2 Future Directions for Solvent Induced Spin State Switching

8.2.1 Deuteration Studies

During the original investigation, **8-1** showed some unique properties in acetone. In an 80 mM solution with $(CH_3)_2CO$, **8-1** undergoes CISSS, but with the same concentration in $(CD_3)_2CO$, **8-1** stays in the HS state between 2 K and 300 K. Aggregation studies using dynamic light scattering indicate temperature dependent aggregation in $(CH_3)_2CO$ but not in $(CD_3)_2CO$. These studies suggest the magnetic property differences in deuterated and non-deuterated acetone is due to differences in aggregation of **8-1**. Yet it is still unclear why the hydrogen isotope identity is causing

these magnetic property differences. Perhaps the density difference between the two solvents and/or the change in the hydrogen bonding strength is enough to perturb the spin-state switching properties for **8-1**. To understand why the spin state switching event is not operative in $(CD_3)_2CO$, further studies into the effect the hydrogen isotope identity has on the magnetic properties are needed. Additionally, studies into other solvents would be ideal to understand if these hydrogen isotope identity effects only occur when acetone is used.

8.2.2 Concentration Dependence

There have been reports that have shown concentration and aggregation can affect the magnetic properties.[2,3] The magnetic susceptibility values of a sample of **8-1** in $(CD_3)_2CO$ with a 5 mM concentration (via Evans' method) are significantly higher than what was observed for a sample with an 80 mM concentration (via magnetometry measurements). While some of the difference in the magnetic susceptibility values is likely due to the larger error in Evans' method NMR, the aggregation studies indicate smaller aggregates form in the 5 mM compared to the 80 mM sample. Similar differences in the aggregate sizes at 5 mM and 80 mM concentrations are also observed for **8-1** in $(CH_3)_2CO$, but not in CH_3OH.[1]

The change in the aggregation size at different concentration is particularly interesting for samples of **8-1** in $(CH_3)_2CO$. As indicated in Chapter 4, an 80 mM solution of **8-1** in $(CH_3)_2CO$ undergoes CISSS. At 80 mM, the aggregate size increases at the temperature is lowered, indicating that the concentration-dependent aggregation is important to the spin state switching event. Whereas, at 5 mM, the aggregate size remains consistent as the temperature is changed. Due to the concentration limitations of magnetometry measurements, the magnetic susceptibility values of **8-1** in $(CH_3)_2CO$ at a 5 mM concentration were not collected. However, based on the aggregation studies at this concentration it is unlikely a spin state switching event would be observed.

Based on these findings, it is of interest to further investigate the impact concentration has on the aggregation and magnetic properties of **8-1** in $(CH_3)_2CO$. The concentrations used for this study will be dependent on obtaining reliable data using solution magnetometry. To do this, a concentration is needed where the raw magnetic moment is significantly larger than the magnetic moment of pure $(CH_3)_2CO$. These concentrations can be calculated by following equation 8.1; where m is the mass of the sample, *g* is the *g*-factor, *S* is the total spin, *H* is the field in oersted, *T* is the temperature, MW is the molecular weight of the compound, χ_{solv} is the magnetic moment of the solvent at temperature *T*, and χ^* is the predicted magnetic moment of the sample.

$$\frac{m\, g^2\, (S(S+1))\, H}{8\, T\, (MW)} + \chi_{solv} = \chi^* \tag{8.1}$$

From this equation, using T = 25 K and assuming a S of 2, the ideal concentration range for these studies is 50 – 170 mM. The solubility of **8-1** should allow the higher concentration to be reached at room temperature, however, studies should be performed to see if any precipitate forms when these high concentration samples are cooled. Based off the data reported in Chapter 4, I believe **8-1** will remain high spin at lower concentrations and start showing a spin state switching event with $T_{1/2}$ values shifting to higher temperatures as the concentration is increased. Samples with concentrations below 50 mM may be reliably measured using magnetometry but may be challenging. If there is a desire to measure these low concentration samples, direct communication with Quantum Design will help determine if these experiments are feasible with the current MPMS3 instrument at Colorado State University.

8.2.3 Various Alkyne Protecting Groups

The formation of aggregates of **8-1** are likely due to the presence of the three triisopropylsilyl groups on the ligand. By switching the silyl groups, the formation and size of the aggregates can be changed. The results in Chapter 4 indicate the formation of larger aggregates of **8-1** at lower

temperatures help promote the spin state switching event in $(CH_3)_2CO$. This spin state switching event has a $T_{1/2}$ value at 171 K and ends when 78% of the sample is in the low spin state. It may be possible to tune the spin state switching event to occur at higher temperatures or reach a full low spin state by increasing the size of the aggregates through modification of the silyl groups on the ligand. Initial investigations should focus on silyl groups with long alkyl chains and with bulky groups. Both groups should help form large aggregates but will provide different Fe···Fe distances. Studying these two types of silyl groups will help determine if only the aggregation size affects the magnetic properties or if the distance between the molecules plays a role.

8.3 Conclusion of Post-Synthetic Modification Efforts

The work in Chapter 5 shows that a successful post-synthetic modification can be performed on the high spin iron(II) complex **8-1** to synthesize an iron(II) complex capable of spin-state switching. The reaction proceeds after the triisopropyl groups are removed using tetrabutylammonium difluorotriphenylsilicate, and in the presence of a copper(I) catalyst. The reaction proceeds with a variety of azides and produces clean triazole containing iron(II) complexes. Each of the *para*-R-phenyl triazole complexes exhibit different solid-state properties: the unsubstituted, **8-2**, is HS at all temperatures, electron donating (methoxy), **8-3**, undergoes spin state switching with a $T_{1/2}$ value of 289 K, and the electron withdrawing (trifluoromethyl), **8-4**, shows the start of a spin state switching event around room temperature. The bis(trifluoromethane)sulfonimide (NTf_2) salts of **8-2** and **8-3** have been previously synthesized following the traditional route and magnetically characterized by Hagiwara and co-workers.[5,6] Comparison of the previously reported NTf_2 salts with the triflate salts **8-2** and **8-3** suggest that the crystal packing environment has a significant impact on the magnetic properties for these

triazole complexes relative to the electronic contributions of the ligand substituents. This hypothesis is supported by the work in Chapter 7. The influence of the crystal packing environment is removed when studying the solution magnetic properties, allowing for investigation into the electronic contributions of the ligand substituents. However, the solution magnetic properties of **8-2** – **8-4** are similar, suggesting that these ligand substituents do not have a significant effect on the ligand field, but can lead to changes in the crystal packing environment that can result in differences in solid state magnetic properties.

8.4 Future Directions for Post-Synthetic Modification Triazoles

8.4.1 Traditional Triazoles

By synthesizing the iron(II) triazole complexes post-synthetically, the oxidation step that is required during the traditional synthesis is avoided, allowing oxidative sensitive groups to be included on the ligand. However, additional reagents are needed to isolate the pure iron(II) triazole complexes after the post-synthetic cycloaddition reaction. These reagents can lead to the formation of different crystal polymorphs or co-crystallize with the iron(II) triazole complexes, leading to magnetic properties that are different from the same complex synthesized traditionally. A comparison of the traditionally- and post-synthetically-made iron(II) triazole compounds should be investigated to determine if one synthetic route favors the formation of a spin state switching polymorph or if the addition of a co-crystallized reagent from the post-synthetic modification affects the magnetic properties.

8.4.2 Other Substituents

The results in Chapters 6 and 7 suggest that the crystal packing environment has a more significant impact on the solid-state magnetic properties than the electron donating and

withdrawing properties of the ligand substituent. Due to this, substituents can be chosen to help modify interactions found in the crystal structure to investigate how these interactions affect the magnetic properties. Substituents can be varied in bulkiness, flexibility, and ability to form noncovalent interactions with neighboring complexes. The bulkiness and flexibility of the substituent will impact the packing of the complex, with more bulky and less flexible substituents favoring longer Fe···Fe distances. Including substituents with groups that can hydrogen bond or pi-pi stack will help increase the number of intermolecular interactions, leading to greater communication between complexes that can ultimately lead to the observation of hysteresis for spin state switching complexes.

In Chapter 7, the solution magnetic properties of the iron(II) triazole complexes were investigated to determine if there was a relationship between the Hammett parameter of the substituent and the spin state switching temperature, $T_{1/2}$. The comparison of the solution magnetic properties of **8-2 – 8-4** indicate a very weak *para* Hammett trend, where electron-withdrawing groups stabilize the low spin state. The sample size used to establish this trend was small, however the electron donating (methoxy) and withdrawing (trifluoromethyl) groups have the largest Hammett parameter values for substituents that can be included on the phenyl ring while maintaining safe handling of related azides. Investigation of additional *para*-substituents with Hammett values between methoxy and trifluoromethyl would help determine if there is a stronger correlation between the Hammett values and $T_{1/2}$ than what is reported in Chapter 7.

The *para*-substituent effects were also investigated in Chapter 7. Compound **7-2** and the unsubstituted 1-benzyl-1,2,3-triazole iron(II) complex (**7-5**) were used to establish the Hammett trend. A strong relationship between the *para* Hammett parameter and $T_{1/2}$, indicating electron donating groups stabilize the high spin state. However, this relationship is based off two

substituents and is likely to change upon further characterization of other *para*-substituents. Ideal substituents to expand this study include 1-adamantyl (σ_{meta} = -0.12), 1-cyclohexenynl (σ_{meta} = -0.10), cyclohexyl (σ_{meta} = -0.05), CH_2SO_2R (σ_{meta} = 0.15), $COOCH(C_6H_5)_2$ (σ_{meta} = 0.36), 3-1H-naphtho[2,1-b]pyran-1-one (σ_{meta} = 0.38), and 2-(benzothiopyronyl) (σ_{meta} = 0.48).

Expanding the substituents that are included on the R-1,2,3-triazole iron(II) complexes will provide valuable insight into how ligand substituents impact the solid-state and solution magnetic properties of spin state switching complexes.

8.4.3 Other Reactions

Compound **8-1** was designed for the post-synthetic azide alkyne cycloaddition reaction; however, the alkynes offer many possibilities for other post-synthetic modification reactions. Some reactions that can be performed post-synthetically and result in unique iron(II) complexes include: addition reactions to form alkenes, cycloaddition reactions to form cyclobutene, and nucleophilic substitution reactions with the acetylide anion that is formed after removal of the triisopropylsilyl groups. The reactions suggested here will be more challenging to performed compared to the azide-alkyne cycloaddition and may take numerous failed synthetic conditions before the desired post-synthetic product is formed. For those that want to perform post-synthetic reactions, my advice is start with reaction conditions that are reported for traditional and related post-synthetic reactions. Talking with older graduate students and other groups may lead to a reagent that is not commonly used in literature but will be perfect for your reaction. Finally, celebrate little victories and when you feel down about the number of failed reactions, keep trying it will feel amazing when you find the ideal reaction conditions!

References

(1) Livesay, B. N.; Shores, M. P. Influence of Coordinated Triflate Anions on the Solution Magnetic Properties of a Neutral Iron(II) Complex. *Inorg. Chem.* **2021**, *60* (20), 15445–15455.

(2) Vicente, A. I.; Wu, X.; Ortin, Y.; Ferreira, L. P.; Carvalho, M. D. D.; Realista, S.; Barker, A.; Morgan, G. G.; Galamba, N.; Costa, P. J.; et al. Directing Self-Assembly in Solution towards Improved Cooperativity in Fe(Iii) Complexes with Amphiphilic Tridentate Ligands. *Dalt. Trans.* **2019**, *48* (13), 4239–4247.

(3) Johnson, C. J.; Morgan, G. G.; Albrecht, M. Predictable Adjustment of Spin Crossover Temperature in Solutions of Iron(III) Complexes Functionalized with Alkyl-Urea Tails. *J. Mater. Chem. C* **2015**, *3*, 7883–7889.

(4) Vicente, A. I.; Wu, X.; Ortin, Y.; Ferreira, L. P.; Carvalho, M. D. D.; Realista, S.; Barker, A.; Morgan, G. G.; Galamba, N.; Costa, P. J.; et al. Directing Self-Assembly in Solution towards Improved Cooperativity in Fe(Iii) Complexes with Amphiphilic Tridentate Ligands. *Dalt. Trans.* **2019**, *48* (13), 4239–4247.

(5) Hagiwara, H.; Tanaka, T.; Hora, S. Synthesis, Structure, and Spin Crossover above Room Temperature of a Mononuclear and Related Dinuclear Double Helicate Iron(II) Complexes. *Dalt. Trans.* **2016**, *45* (43), 17132–17140.

(6) Hagiwara, H.; Minoura, R.; Udagawa, T.; Mibu, K.; Okabayashi, J. Alternative Route Triggering Multistep Spin Crossover with Hysteresis in an Iron(II) Family Mediated by Flexible Anion Ordering. *Inorg. Chem.* **2020**, *59* (14), 9866–9880.

Appendix 1: Supporting Information for Chapter 4.

A1.1 Crystallography

Table Appendix 1.1. Compiled crystallographic information for **4-1**

	4-1
Formula	$C_{44}H_{78}F_6FeN_4O_6S_2Si_3$
Formula weight	1077.34
Color, habit	orange, block
T (K)	100
Space Group	*P* $2_1/c$
Z	4
a (Å)	13.3419(8)
b (Å)	14.0053(9)
c (Å)	30.3824(19)
α (°)	90
β (°)	92.963(3)
γ (°)	90
V (Å^3)	5669.6(6)
d_{calc} (g cm^{-3})	1.26
GOF	1.056
R_1, wR_2[a] (%)	7.00, 20.18

[a] $R_1 = \sum\big||F_o| - |F_c|\big| / \sum |F_o|$, $wR_2 = \{\sum[w(F_o^2 - F_c^2)^2] / \sum[w(F_o^2)^2]\}^{1/2}$ for $F_o > 4\sigma(F_o)$.

A1.2 Solid State Magnetic Data

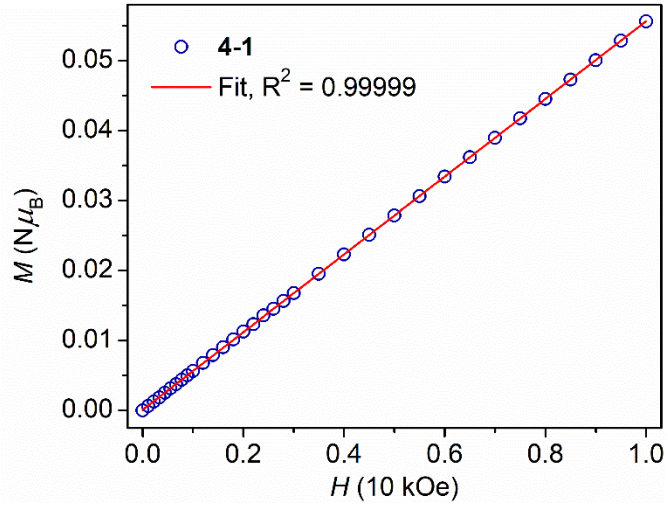

Figure Appendix 1.1. Field dependence of magnetization for **4-1** collected at 100 K. The data were fit to a linear regression ($y = 0.0556\,x + 6.82 \times 10^{-5}$), shown in red.

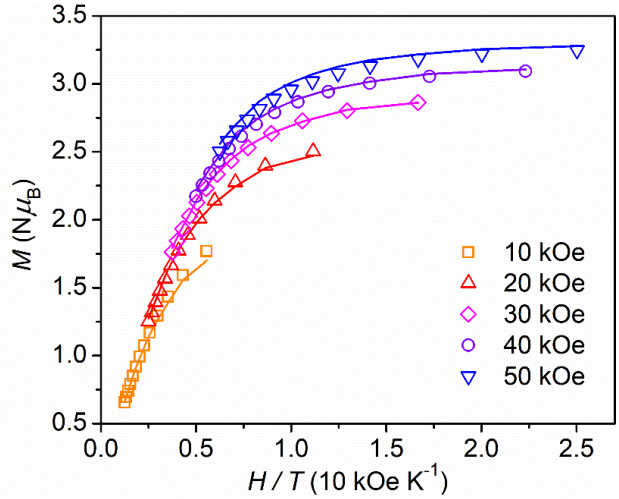

Figure Appendix 1.2. Reduced magnetization collected on **4-1**. The lines represent the fit obtained from fitting in tandem with magnetic susceptibility in PHI. The values associated with the fit are shown in Table A1.2.

Table Appendix 1.2. Magnetic parameters for **4-1** obtained *via* PHI[1]

	g	Θ (cm^{-1})	D (E) (cm^{-1})	TIP (10^{-5} cm^3 mol^{-1})	R^2
((^{TIPS}C≡C)$_3$tren)Fe(OTf)$_2$	2.08	0.0214	3.58 (0.656)	100	0.999999
(**1**)	2.08	0.0249	-2.91 (-1.51)	100	0.999997

We note that the signs of anisotropy parameters are not reliably determined from fitting magnetic susceptibility data alone. The parameters collect in Table A1.2 com from simultaneous fitting of susceptibility (χ_M vs T) and magnetization (M vs H/T) data. Results from the fit with the positive D anisotropy value are reported in the manuscript because those parameters gave a better fit for a procedure where only the reduced magnetization data were used.

A1.3 Electronic Absorption Spectra

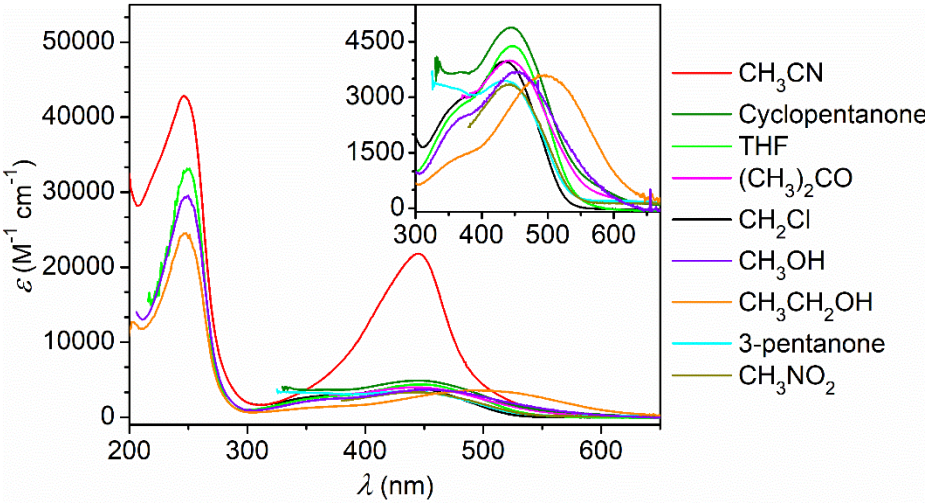

Figure Appendix 1.3. Electronic absorption spectra of **4-1** in various solvents. The insert is focused on the 300-670 nm region.

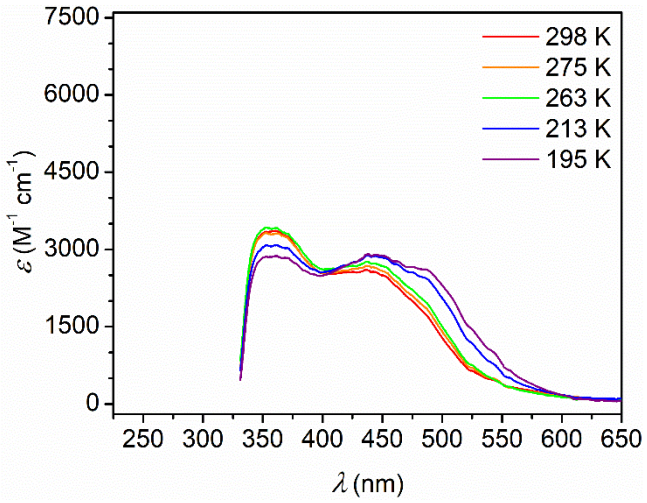

Figure Appendix 1.4. Variable temperature electronic absorption spectra of **4-1** in d_6-$(CD_3)_2CO$ between 298 K and 195 K.

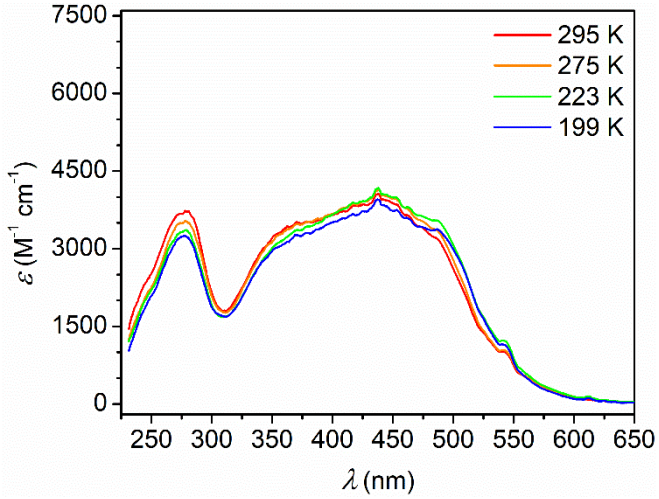

Figure Appendix 1.5. Variable temperature electronic absorption spectra of **4-1** in d_4-CD_3OD between 298 K and 199 K.

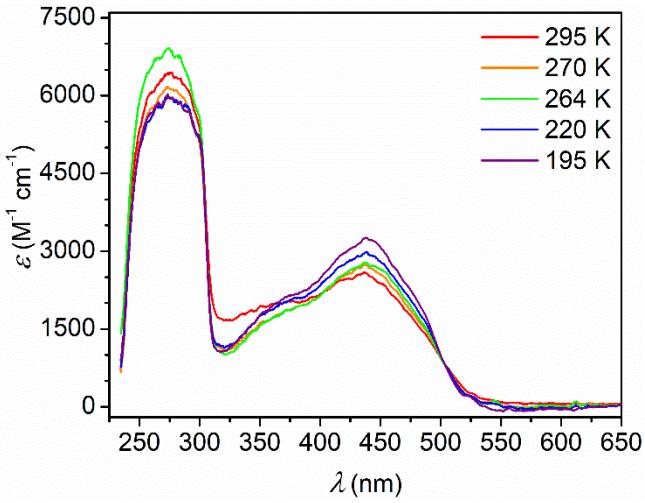

Figure Appendix 1.6. Variable temperature electronic absorption spectra of **4-1** in d_2-CD_2Cl_2 between 298 K and 195 K.

A1.4 Solution Magnetic Data

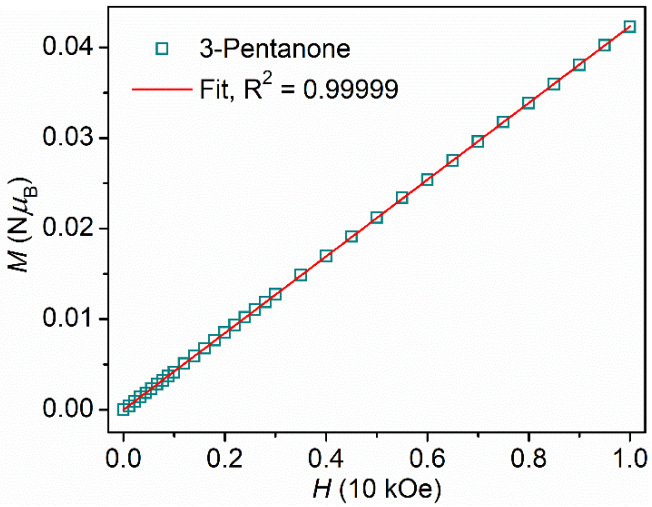

Figure Appendix 1.7. Field dependence of magnetization for 3-pentanone solution of **4-1** collected at 100 K. The data were fit to a linear regression ($y = 0.04234\,x - 1.00 \times 10^{-5}$), shown in red.

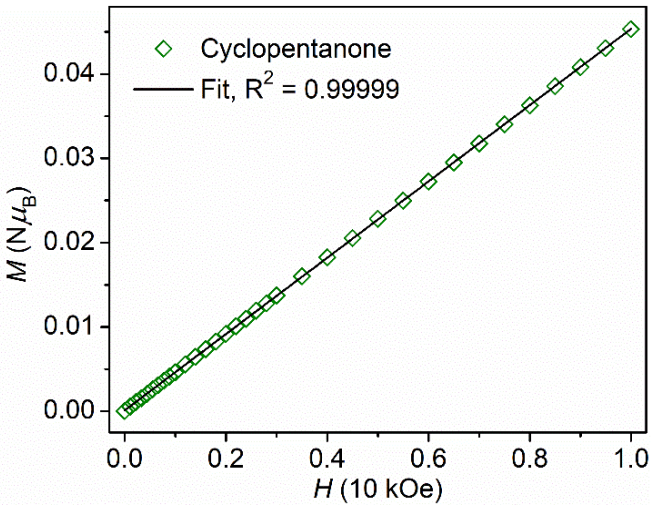

Figure Appendix 1.8. Field dependence of magnetization for cyclopentanone solution of **4-1** collected at 100 K. The data were fit to a linear regression (y = 0.04526 x + 1.09 × 10-4), shown in black.

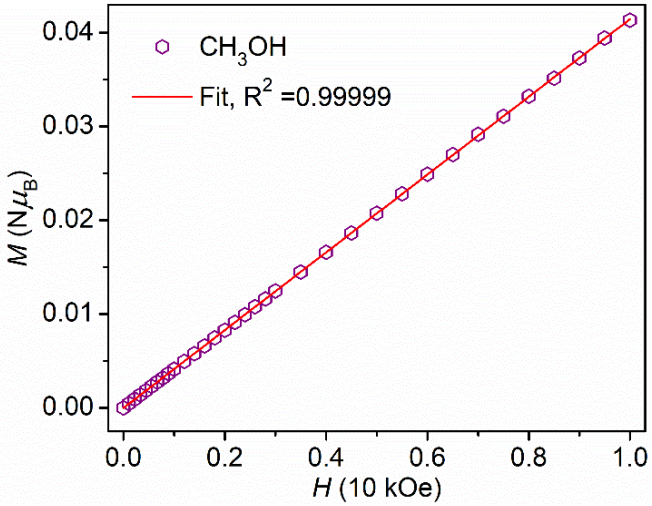

Figure Appendix 1.9. Field dependence of magnetization for CH_3OH solution of **4-1** collected at 100 K. The data were fit to a linear regression ($y = 0.04148\,x - 1.56 \times 10^{-5}$), shown in red.

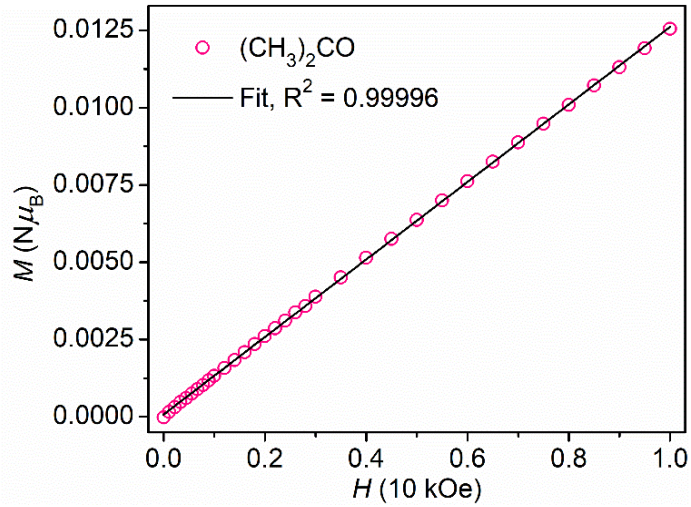

Figure Appendix 1.10. Field dependence of magnetization for $(CH_3)_2CO$ solution of **4-1** collected at 100 K. The data were fit to a linear regression ($y = 0.01254\,x + 7.22 \times 10^{-5}$), shown in black.

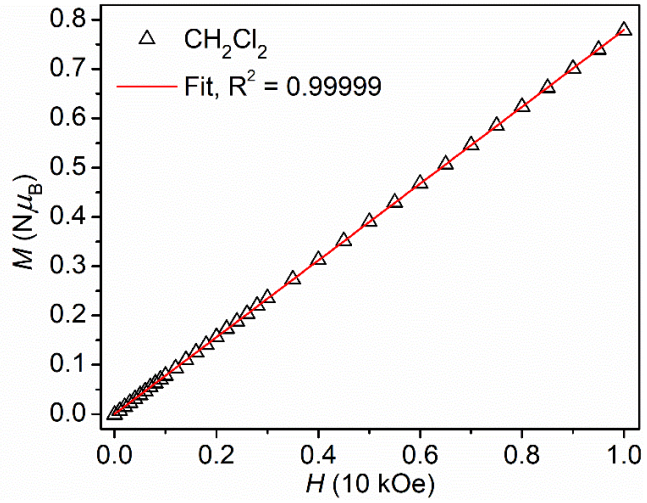

Figure Appendix 1.11. Field dependence of magnetization for CH_2Cl_2 solution of **4-1** collected at 100 K. The data were fit to a linear regression ($y = 0.77927\,x + 7.41 \times 10^{-5}$), shown in black.

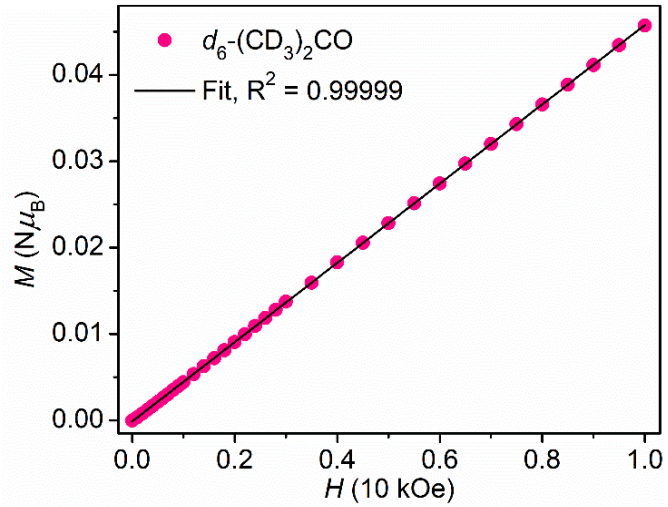

Figure Appendix 1.12. Field dependence of magnetization for d_6-$(CD_3)_2CO$ solution of **4-1** collected at 100 K. The data were fit to a linear regression ($y = 0.04587\,x - 1.26 \times 10^{-5}$), shown in black.

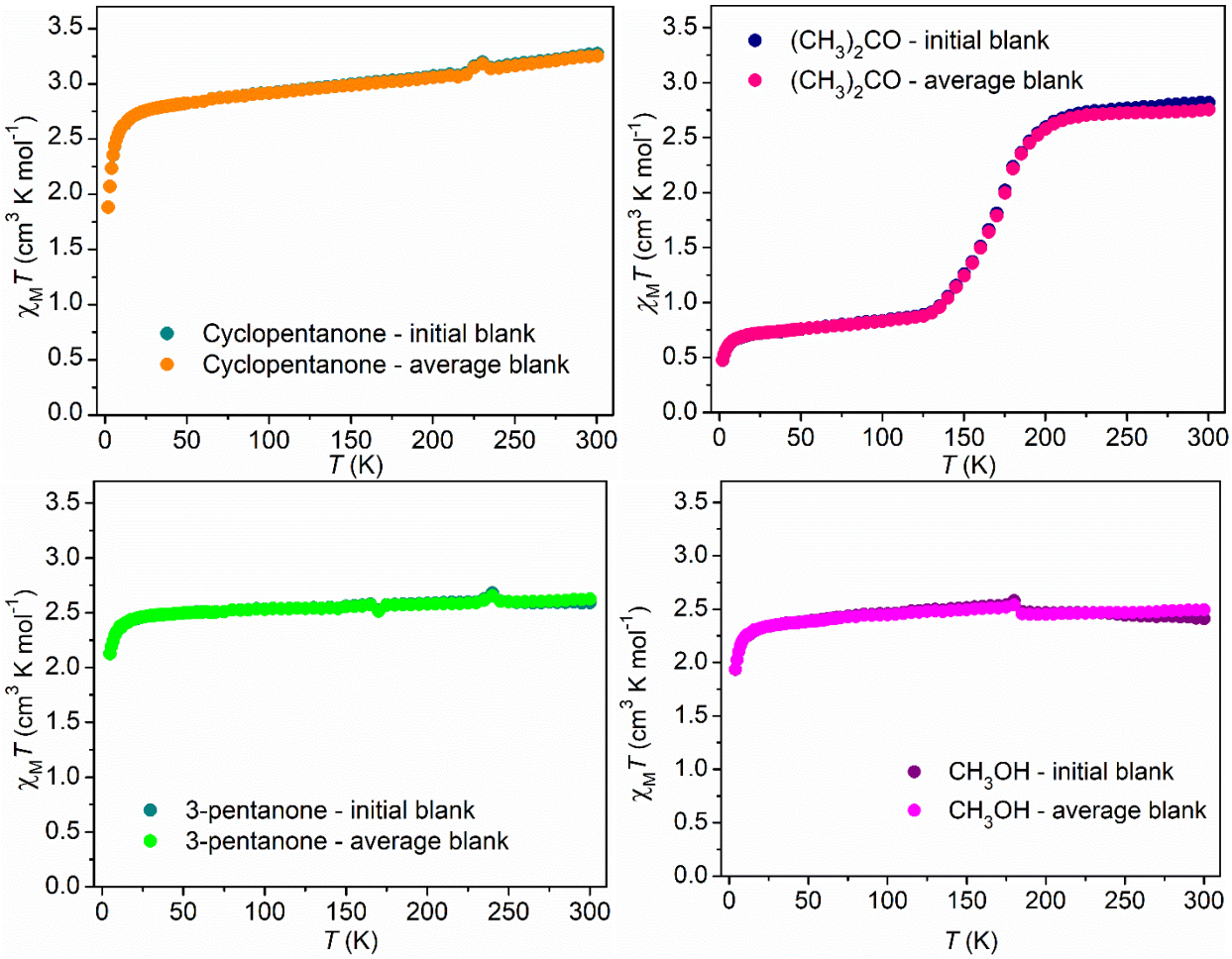

Figure Appendix 1.13. Temperature dependence of magnetic susceptibility for compound **4-1** in several solvents. Data were collected at 1000 Oe field. The initial solvent blank was collected by measuring a sample of pure solvent in the MPMS and accounting for temperature dependence in each data point. The average blank means the magnetic susceptibility of the solvent blank was averaged across all temperatures and a single susceptibility value was used in the determination of sample magnetic susceptibility.

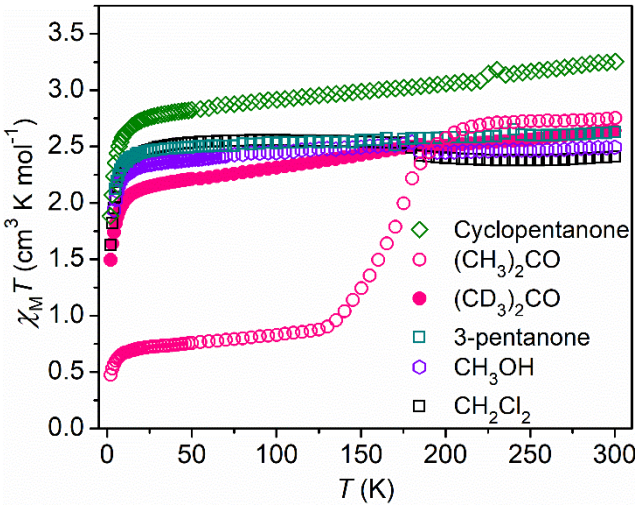

Figure Appendix 1.14. Solution magnetic data for **4-1** in cyclopentanone (green open diamonds), $(CH_3)_2CO$ (pink open circles), $(CD_3)_2CO$ (pink closed circles), 3-pentanone (teal open squares), CH_3OH (purple hexagons), and CH_2Cl_2 (black open squares), collected between 2K - 300 K at 1000 Oe.

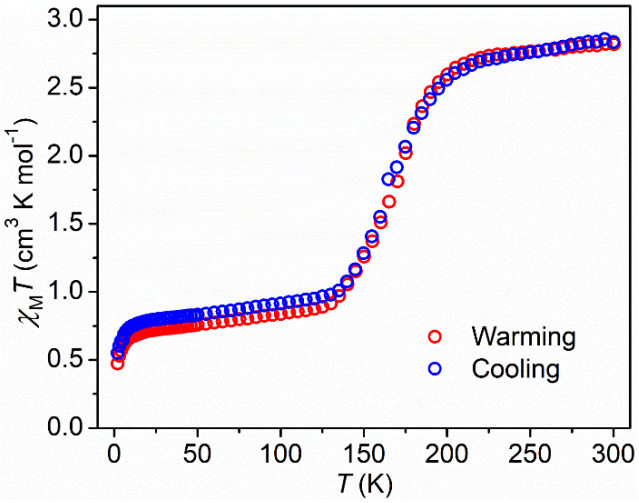

Figure Appendix 1.15. The warming (red circles) and cooling (red circles) of the temperature dependence of the magnetic susceptibility of **4-1** in $(CH_3)_2CO$.

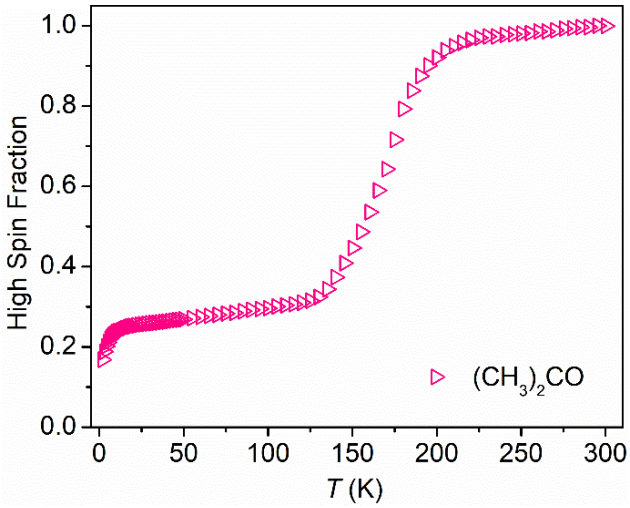

Figure Appendix 1.16. The temperature dependence of the high spin fraction for **4-1** in $(CH_3)_2CO$. A high spin fraction of 1.0 is obtained when the sample has a magnetic susceptibility of 2.82 cm^3 K mol^{-1} and a fraction of 0.0 is obtained when the sample has a magnetic susceptibility of 0.00 cm^3 K mol^{-1}.

The thermodynamic parameters of the spin switching event of **4-1** in $(CH_3)_2CO$ were approximated by fitting the variable temperature data to an equation based on the ideal solution model.[2,3] The data was best modeled when two Fe(II) centers were included, one center undergoes the spin switching event and one stays high spin at all temperatures measured, and inclusion of temperature independent magnetic susceptibility (TIP) values.

$$\chi T = \left(\%HS * \left[\frac{g_{HS}^2}{4} C_{HS} + (TIP_{HS} * T)\right]\right) + \left((1 - \%HS) * \left[\frac{\left[\frac{g_{HS}^2}{4} C_{HS} + [\![(TIP]\!]_{HS} * T)\right] - \left[\frac{g_{LS}^2}{4} C_{LS} + [\![(TIP]\!]_{LS} * T)\right]}{1 + \exp\left[\frac{\Delta H}{R} * \left(\frac{1}{T} - \frac{1}{T_{1/2}}\right)\right]}\right]\right)$$

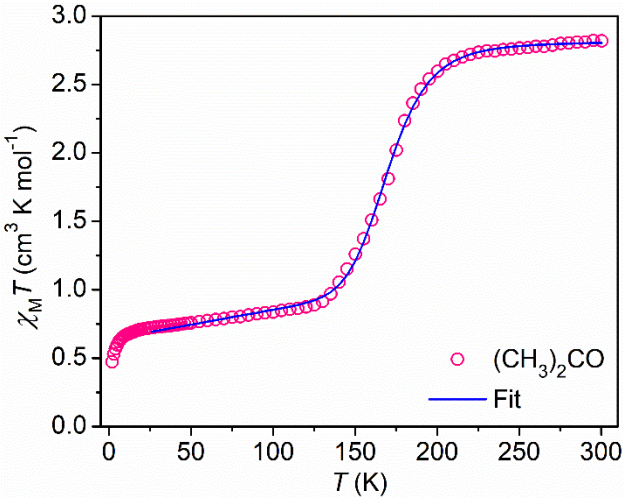

Figure Appendix 1.17. Solution magnetic data for **4-1** $(CH_3)_2CO$ (pink open circles) collected between 2 K - 300 K at 1000 Oe. The best fit from the regular solution model is shown by the blue line.

Table Appendix 1.3. Thermodynamic parameter for the spin switching event of **4-1** in $(CH_3)_2CO$ obtained using the regular solution model. The entropy term ΔS is calculated from the expression $\Delta S = \Delta H / T_{1/2}$

	4-1
g_{HS}	1.96
TIP_{HS} (cm^3 mol^{-1})	0.00948
g_{LS}	1.96
TIP_{LS} (cm^3 mol^{-1})	0.0121
$T_{1/2}$ (K)	170.8
ΔH (kJ mol^{-1})	19.0
ΔS (J mol^{-1} K^{-1})	111.4
%HS	23
R^2	0.981243

A1.5 Room Temperature ^{1}H NMR

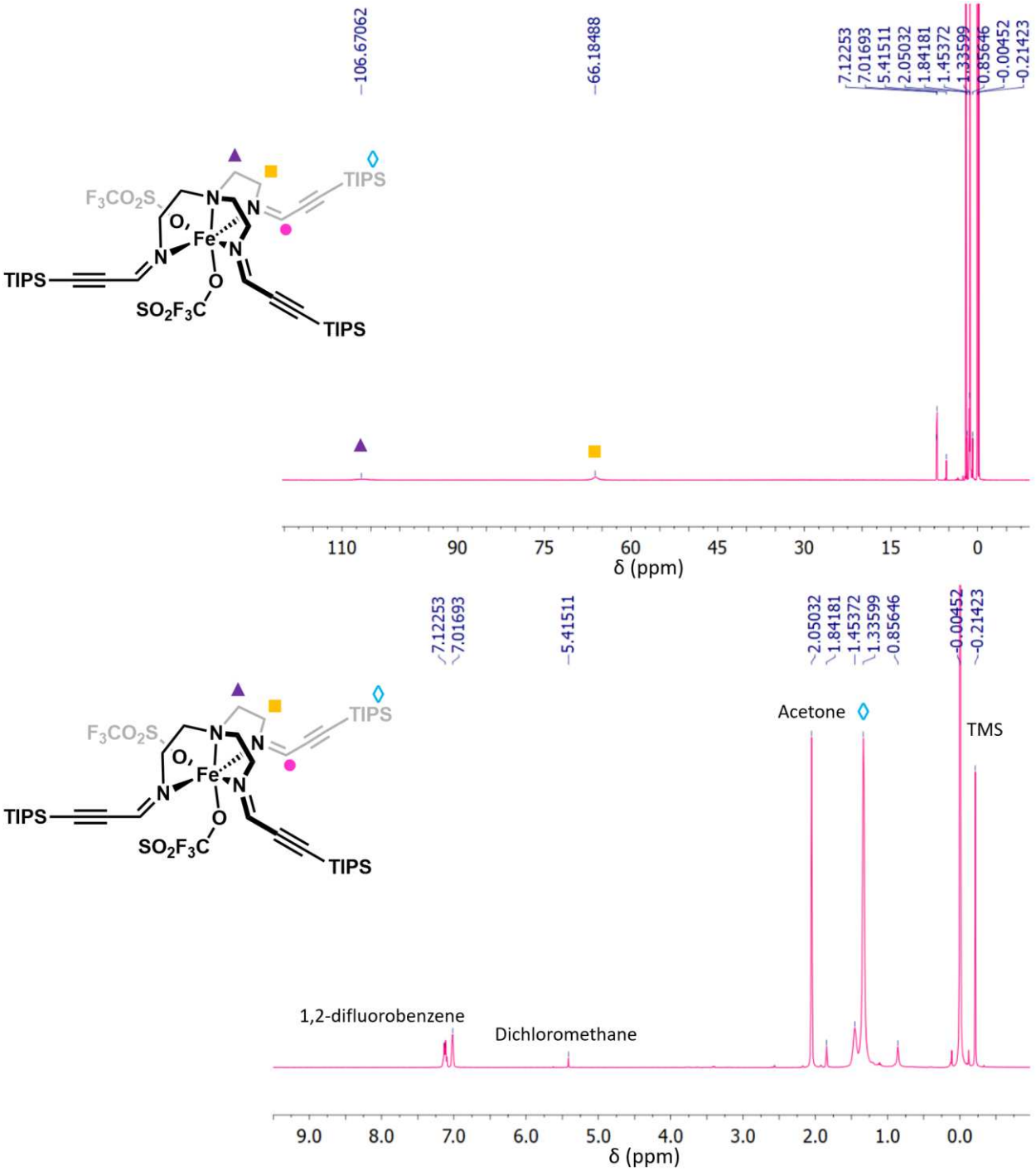

Figure Appendix 1.18. The paramagnetic ^{1}H NMR spectra (full spectra, top, and zoom in on 9.5 ppm to -1.0 ppm range, bottom) of **4-1** in d_6-$(CD_3)_2CO$ with added TMS and 1,2-difluorobenzene, collected at 298 K on a 500 MHz Varian spectrometer. The ^{1}H NMR signal for the imine protons are expected to be very broad and/or lay outside of the spectral window.

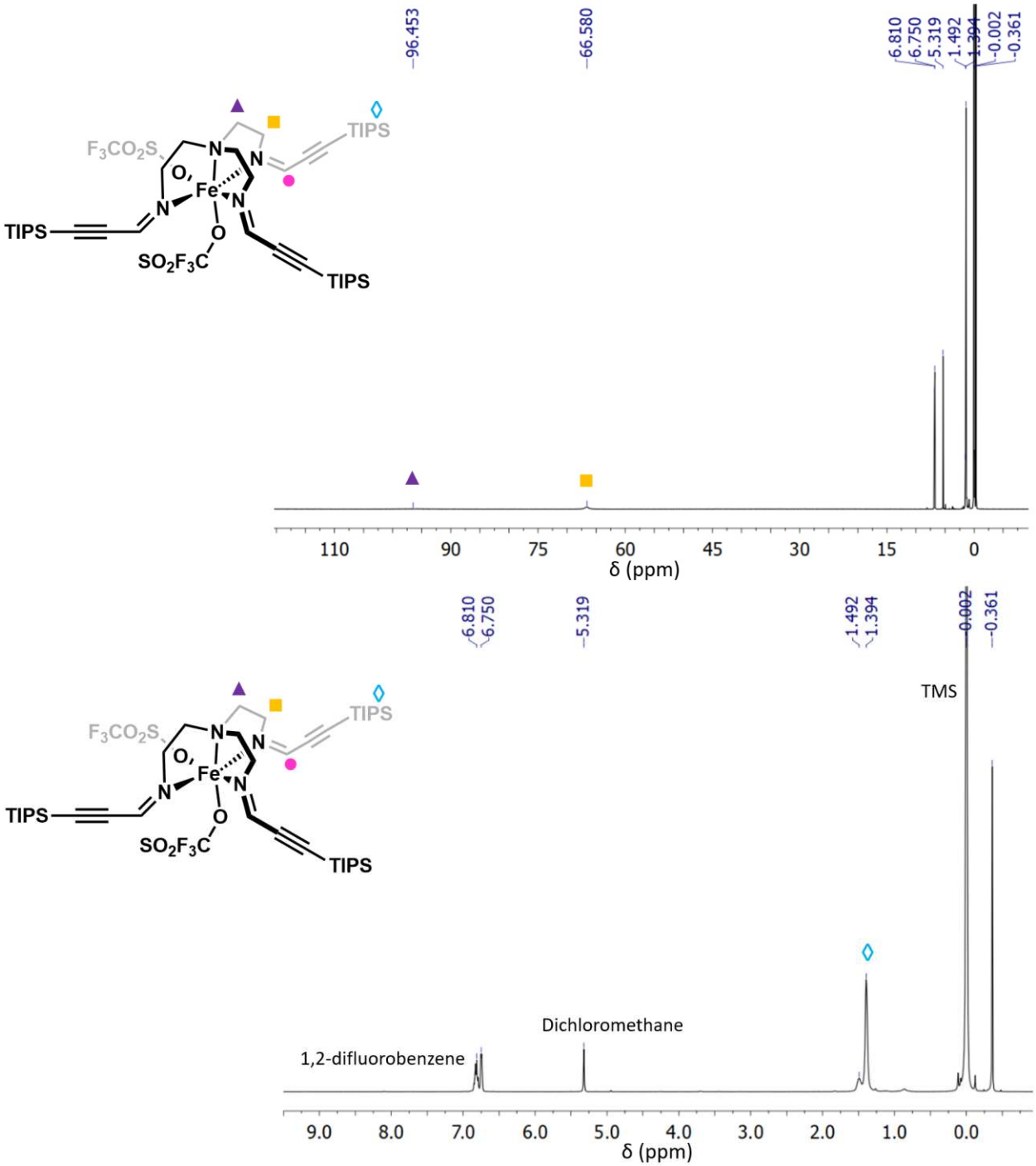

Figure Appendix 1.19. The paramagnetic ^{1}H NMR spectra (full spectra, top, and zoom in on 9.5 ppm to -1.0 ppm range, bottom) of **4-1** in d_2-CD_2Cl_2 with added TMS and 1,2-difluorobenzene, collected at 298 K on a 500 MHz Varian spectrometer. The ^{1}H NMR signal for the imine protons are expected to be very broad and/or lay outside of the spectral window.

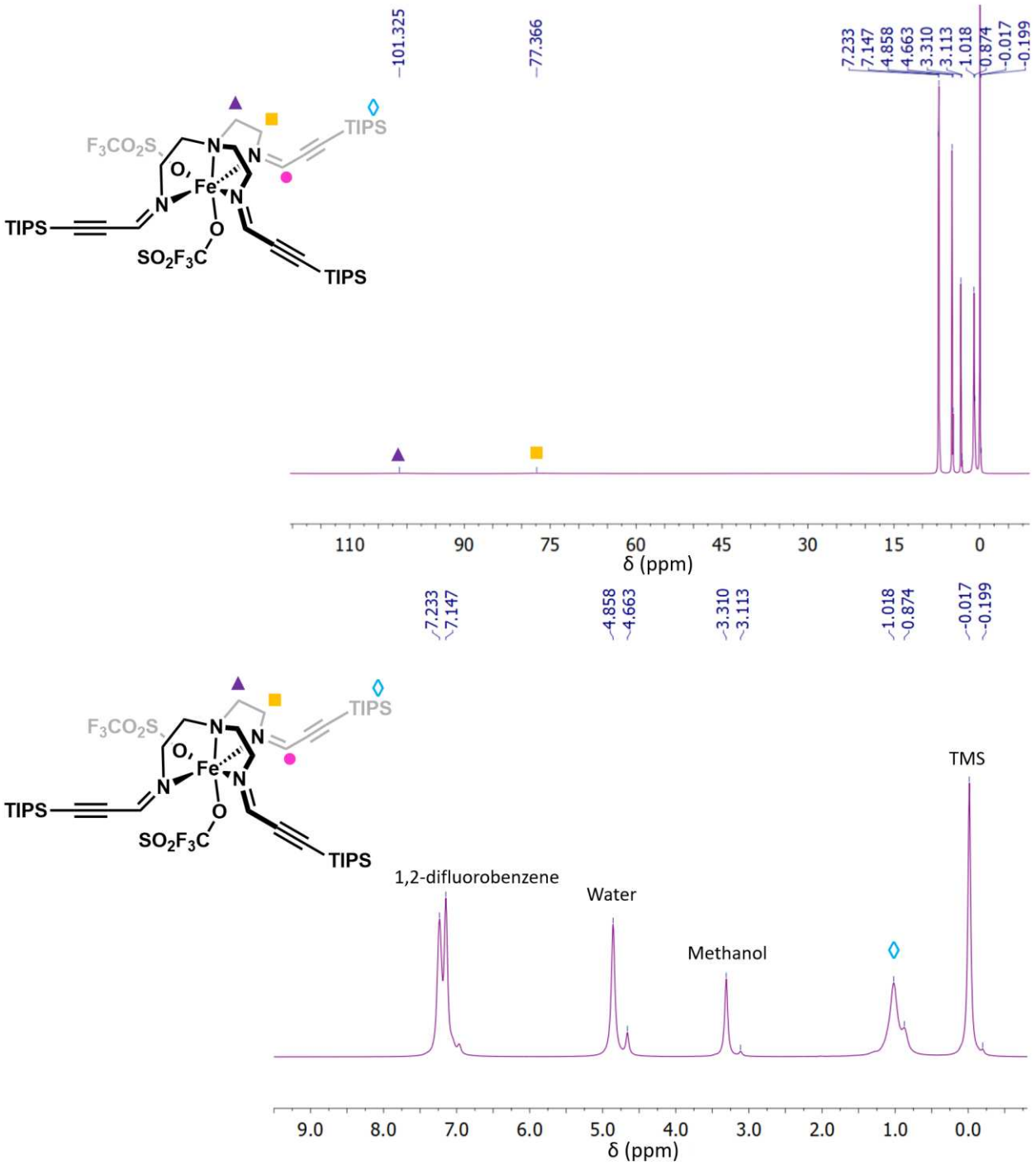

Figure Appendix 1.20. The paramagnetic ^{1}H NMR spectra (full spectra, top, and zoom in on 9.5 ppm to -1.0 ppm range, bottom) of **4-1** in d_4-CD_3OD with added TMS and 1,2-difluorobenzene, collected at 298 K on a 500 MHz Varian spectrometer. The ^{1}H NMR signal for the imine protons are expected to be very broad and/or lay outside of the spectral window.

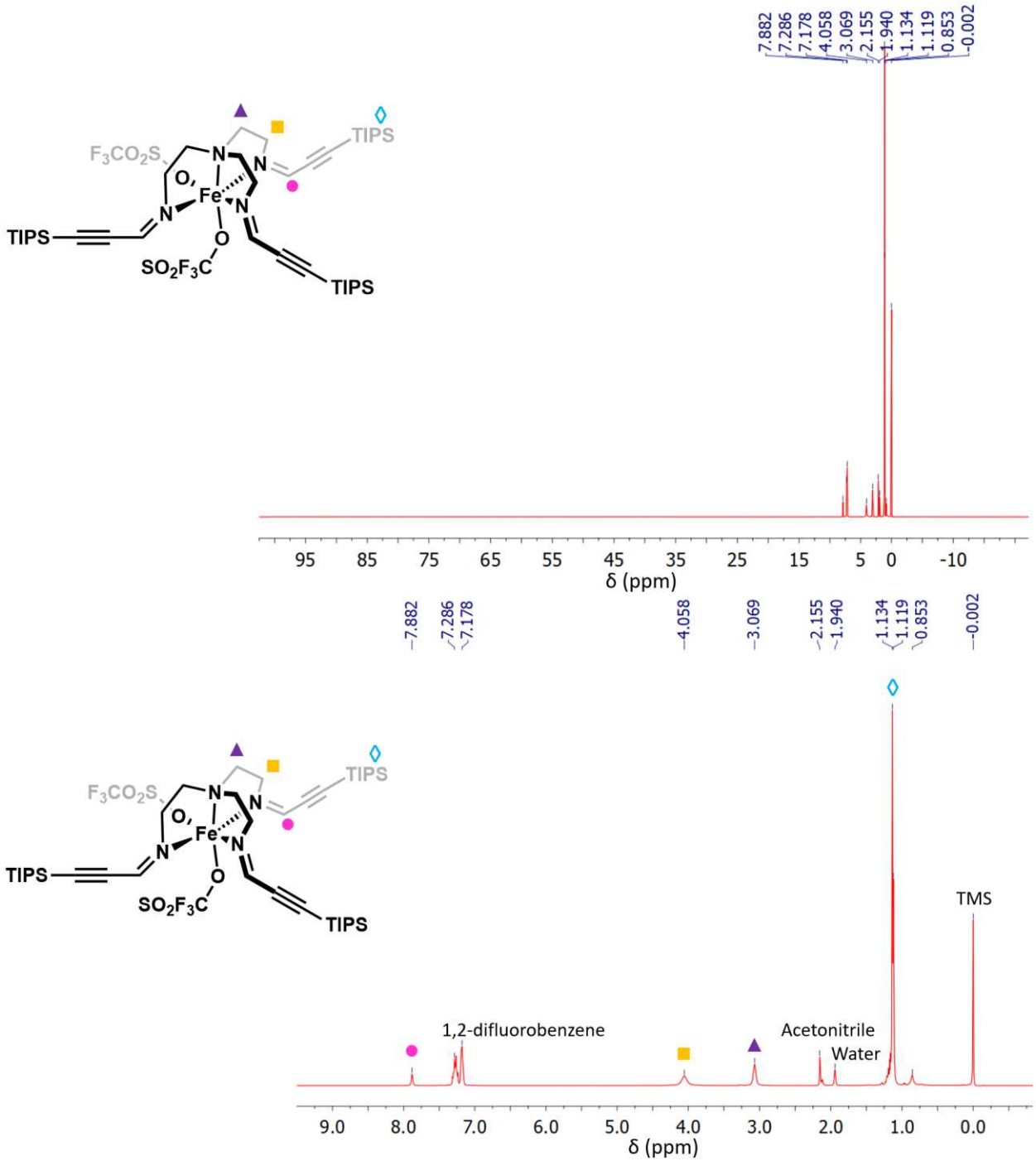

Figure Appendix 1.21. The paramagnetic ^{1}H NMR spectra (full spectra, top, and zoom in on 9.5 ppm to -1.0 ppm range, bottom) of **4-1** in d_3-CD_3CN with added TMS and 1,2-difluorobenzene, collected at 298 K on a 400 MHz Varian spectrometer.

A1.6 Room Temperature ^{19}F NMR

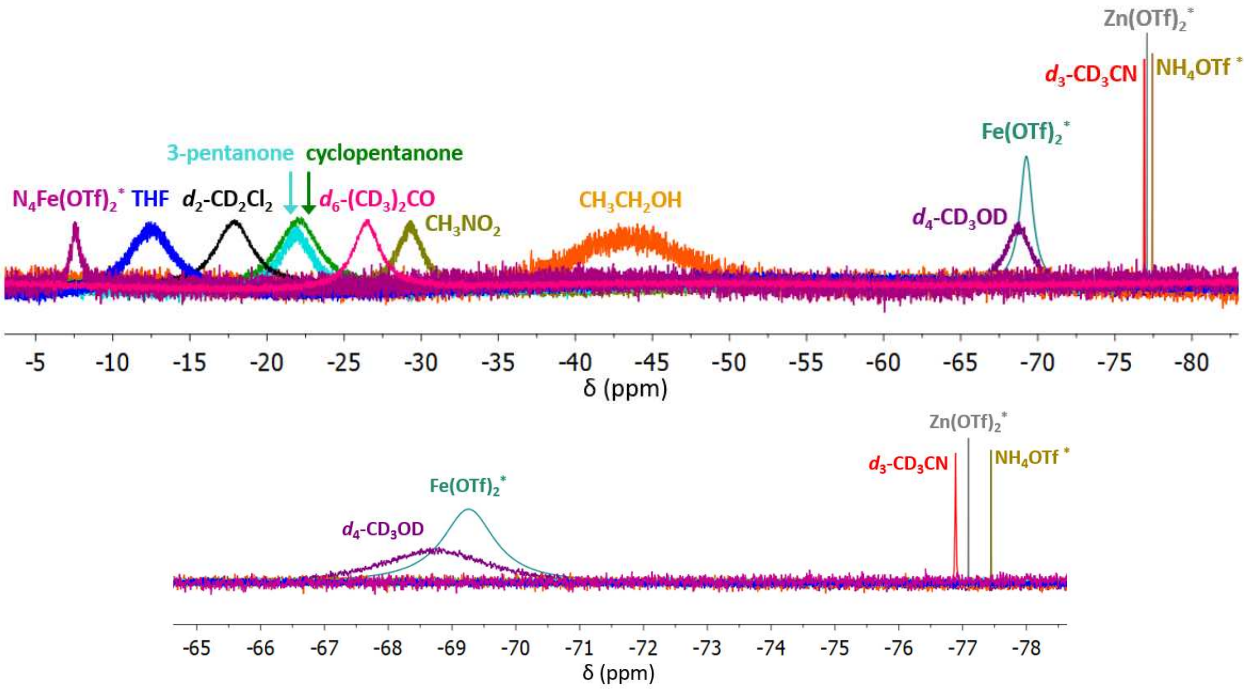

Figure Appendix 1.22. Overlay of ^{19}F NMR spectra of **4-1** in various solvents and triflate standards (top) and a zoomed in spectra of the -65 ppm to -79 ppm window (bottom). All spectra all were referenced using a capillary in appropriate solvent with 1,2-difluorobenzene. Triflate standards (*) were measured in d_1-$CDCl_3$ (bound standard) or d_3-CD_3CN (free standards).

A1.7 Variable Temperature ^{19}F NMR

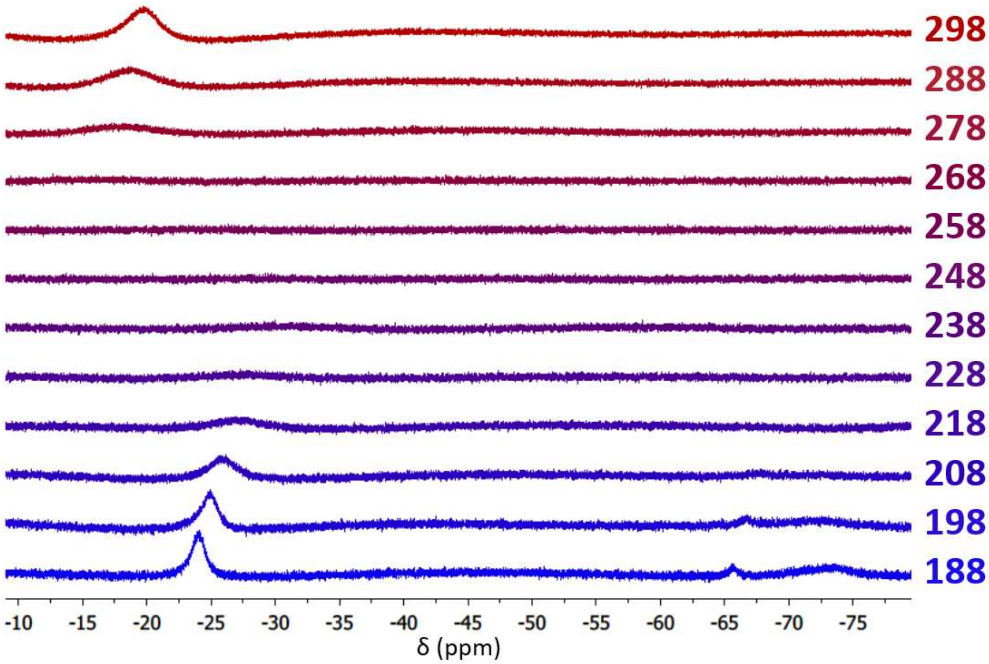

Figure Appendix 1.23. Variable temperature ^{19}F NMR of **4-1** (5 mM) in d_2-CD_2Cl_2 between 298 K and 188 K referenced to 1,2-difluorobenzene, collected on a 500 MHz instrument.

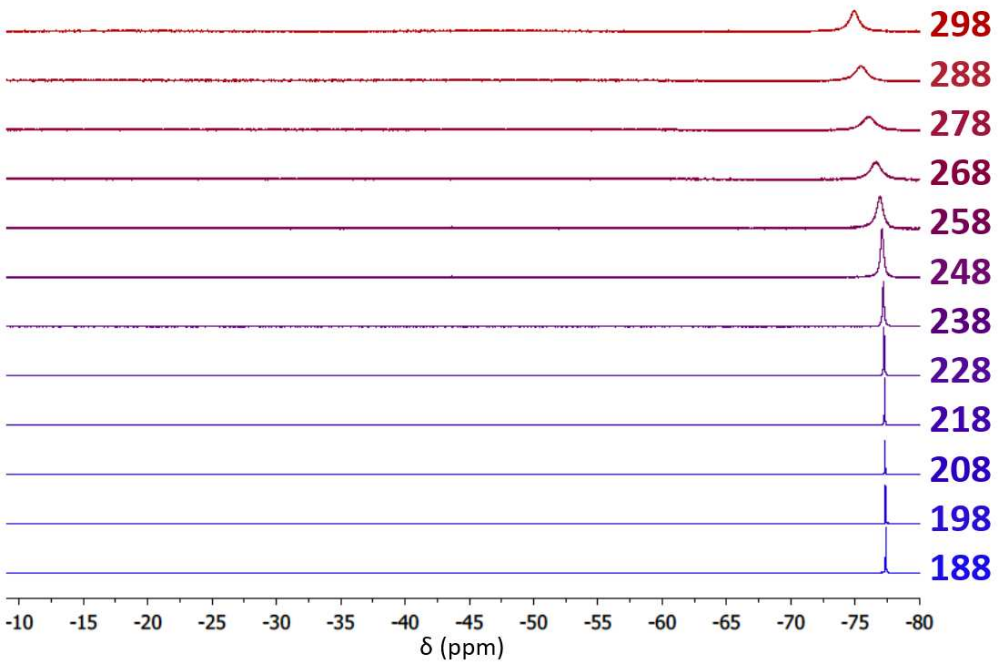

Figure Appendix 1.24. Variable temperature ^{19}F NMR of **4-1** (5 mM) in d_4-CD_3OD between 298 K and 188 K referenced to 1,2-difluorobenzene, collected on a 500 MHz instrument.

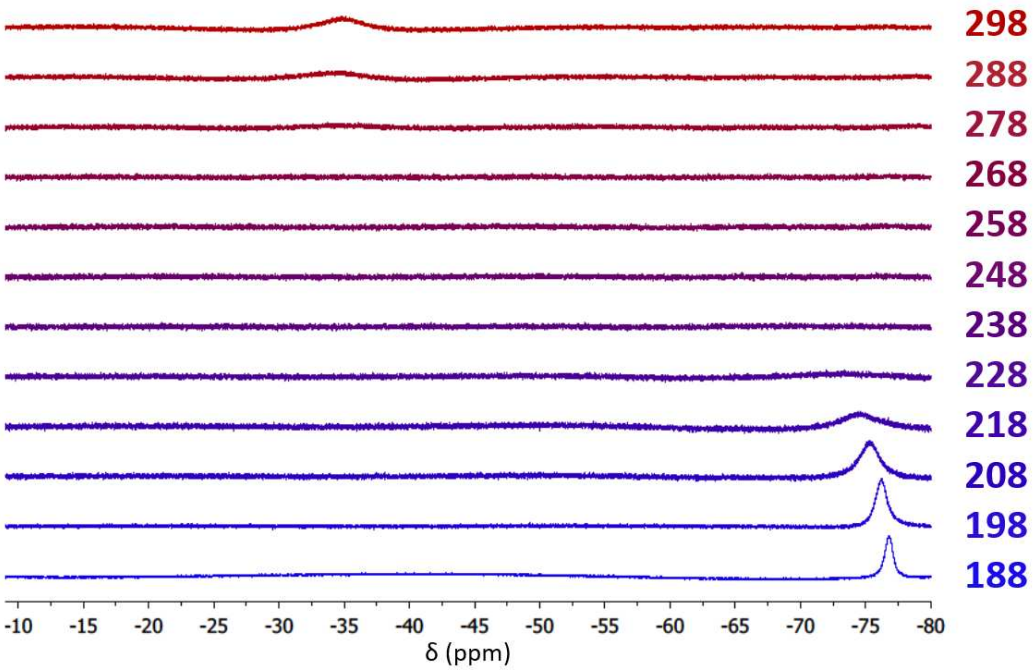

Figure Appendix 1.25. Variable temperature ^{19}F NMR of **4-1** (5 mM) in d_6-$(CD_3)_2CO$ between 298 K and 188 K referenced to 1,2-difluorobenzene, collected on a 500 MHz instrument.

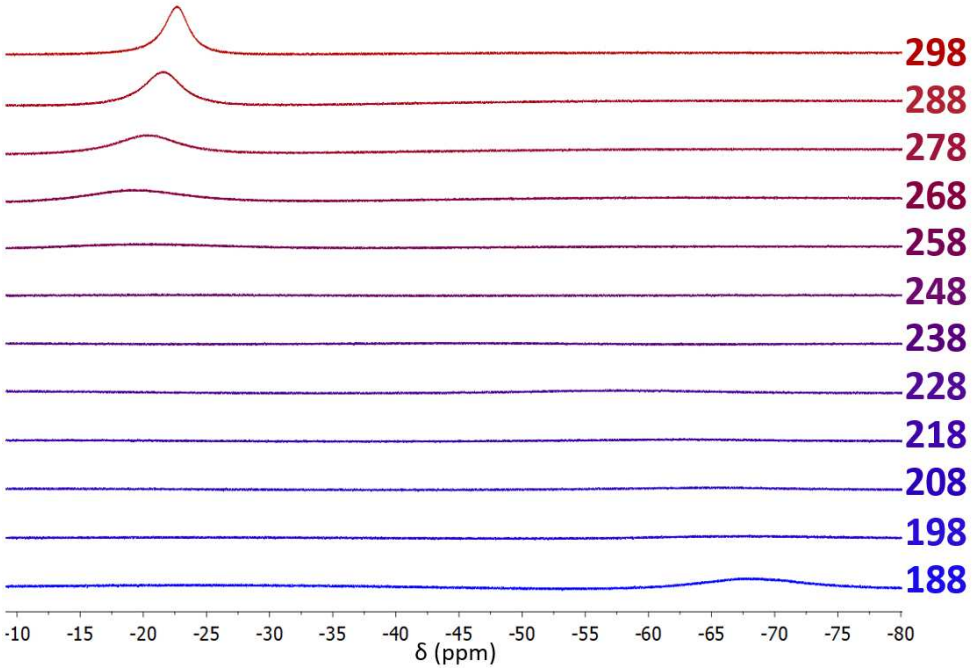

Figure Appendix 1.26. Variable temperature ^{19}F NMR of **4-1** (80 mM) in d_6-$(CD_3)_2CO$ between 298 K and 188 K referenced to 1,2-difluorobenzene, collected on a 500 MHz instrument

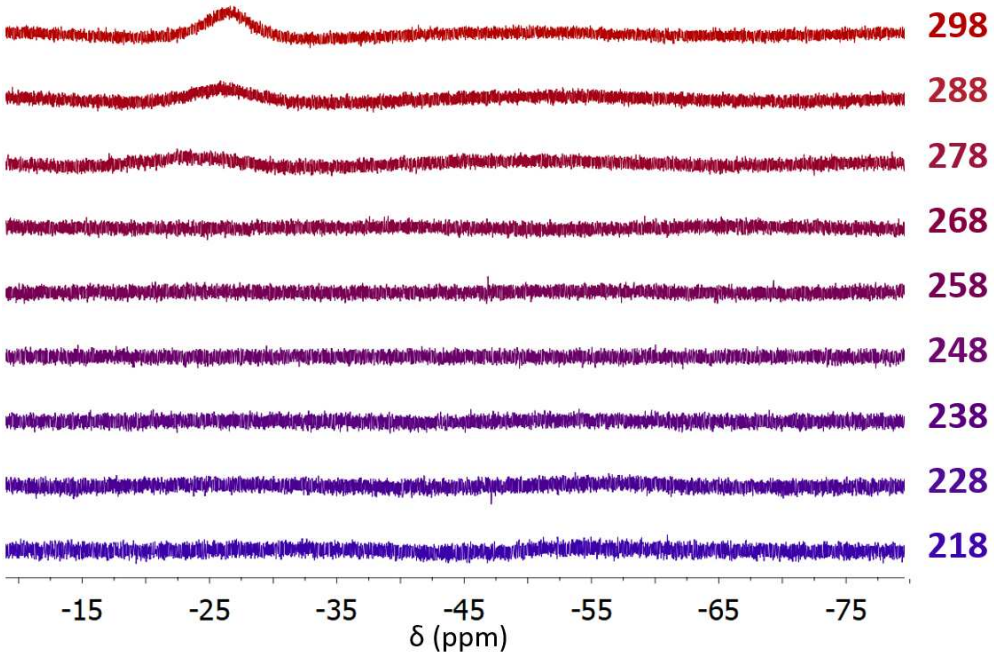

Figure Appendix 1.27. Variable temperature ^{19}F NMR of **4-1** (5 mM) in cyclopentantanone between 298 K and 218 K referenced to 1,2-difluorobenzene, collected on a 500 MHz instrument.

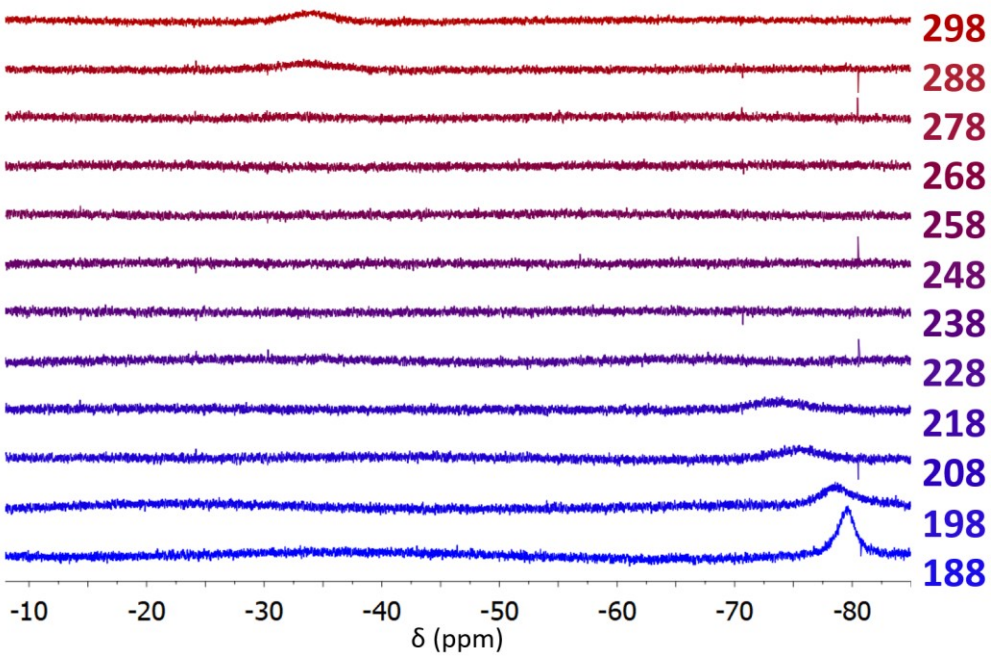

Figure Appendix 1.28. Variable temperature ^{19}F NMR of **4-1** (5 mM) in $(CH_3)_2CO$ between 298 K and 188 K referenced to 1,2-difluorobenzene, collected on a 500 MHz instrument.

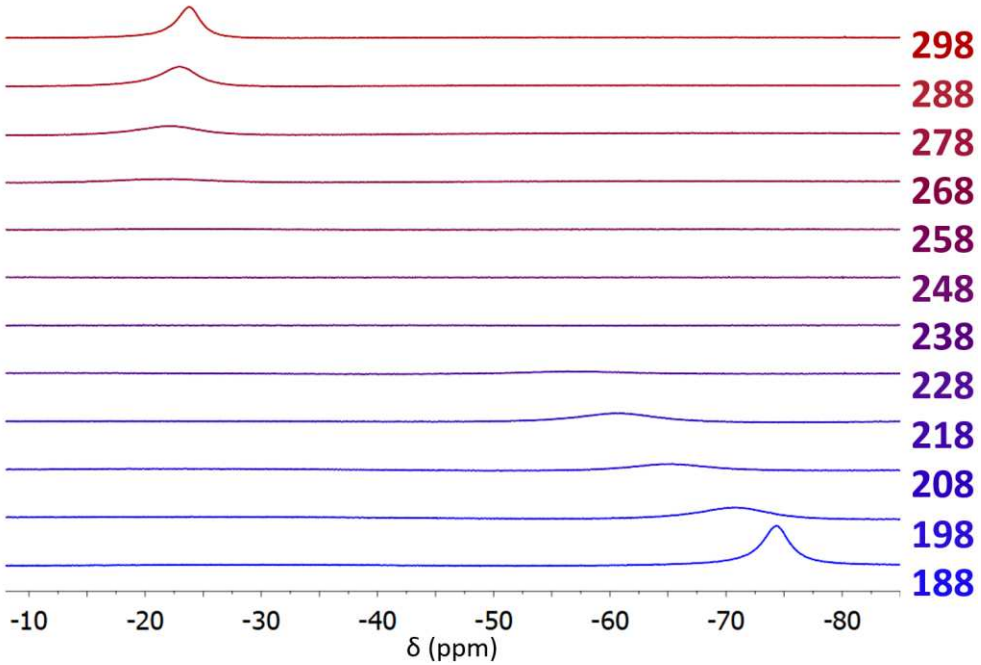

Figure Appendix 1.29. Variable temperature ^{19}F NMR of **4-1** (80 mM) in $(CH_3)_2CO$ between 298 K and 188 K referenced to 1,2-difluorobenzene, collected on a 500 MHz instrument.

A1.8 Variable Temperature ^{1}H NMR

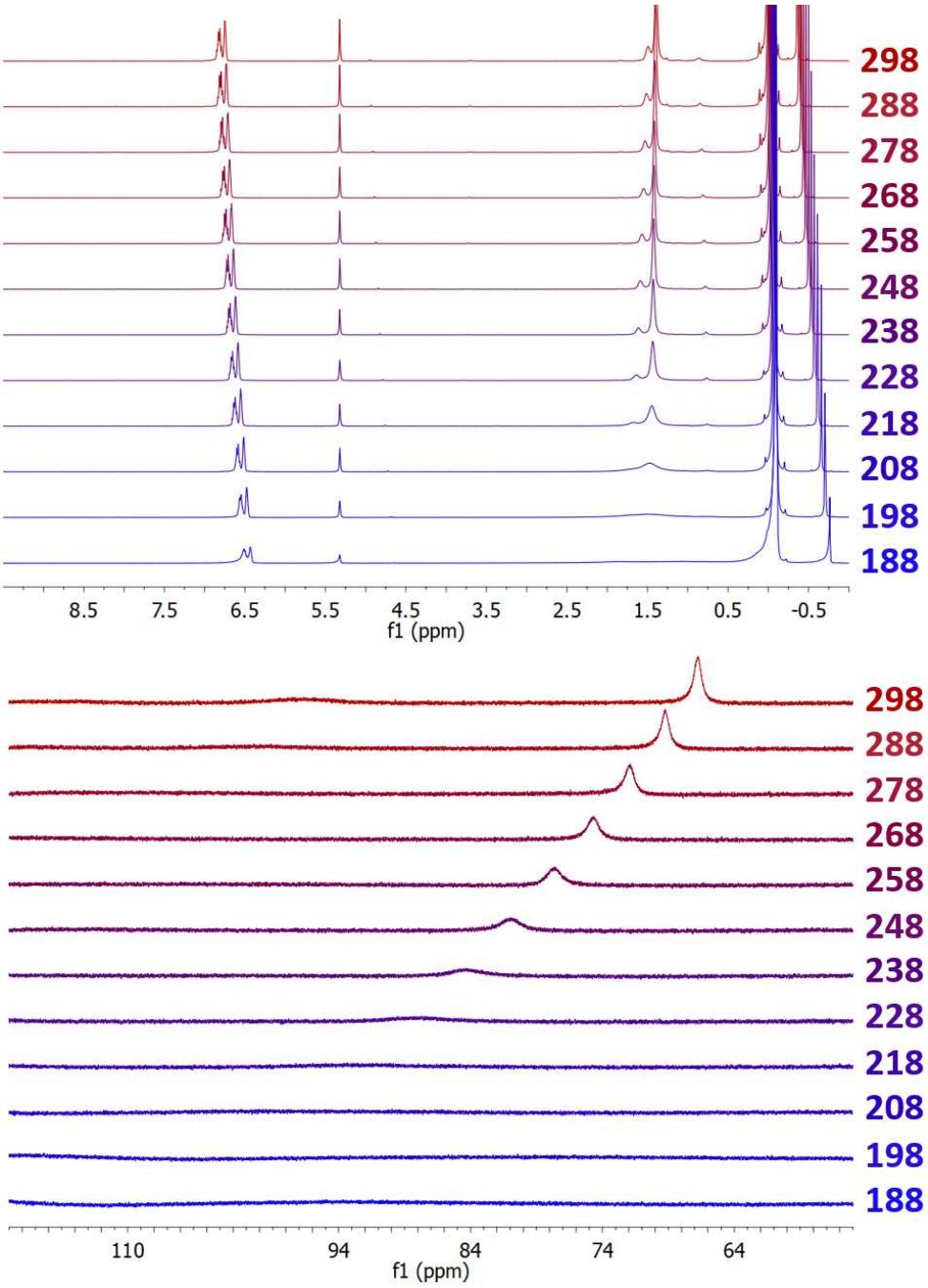

Figure Appendix 1.30. Variable temperature Evans' ^{1}H NMR method of **4-1** in d_2-CD_2Cl_2 between 298 K and 188 K with TMS in a capillary and sample solution and 1,2-difluorobenzene in a capillary, collected on a 500 MHz instrument.

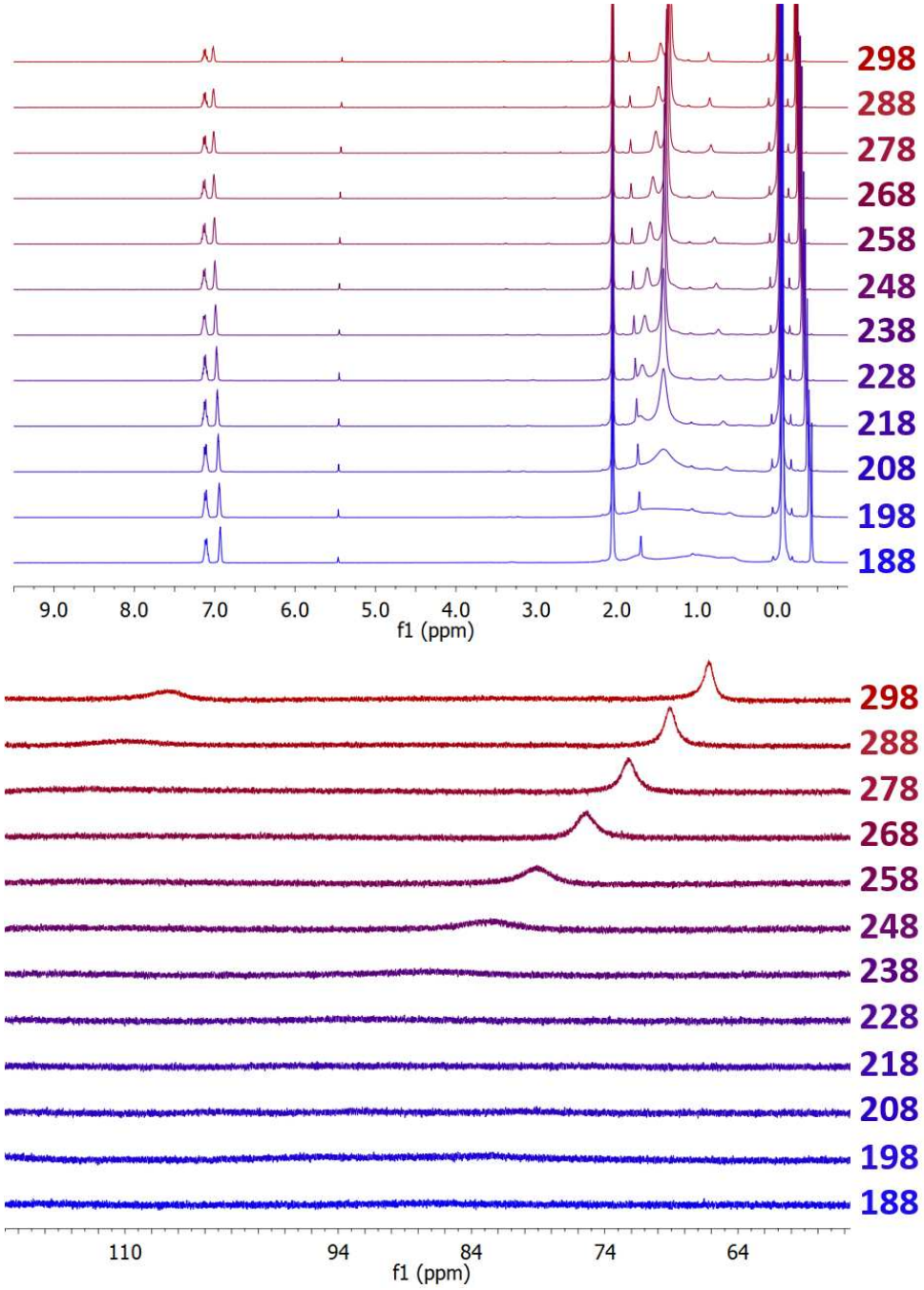

Figure Appendix 1.31. Variable temperature Evans' ^{1}H NMR method of **4-1** in d_6-$(CD_3)_2CO$ between 298 K and 188 K with TMS in a capillary and sample solution and 1,2-difluorobenzene in a capillary, collected on a 500 MHz instrument.

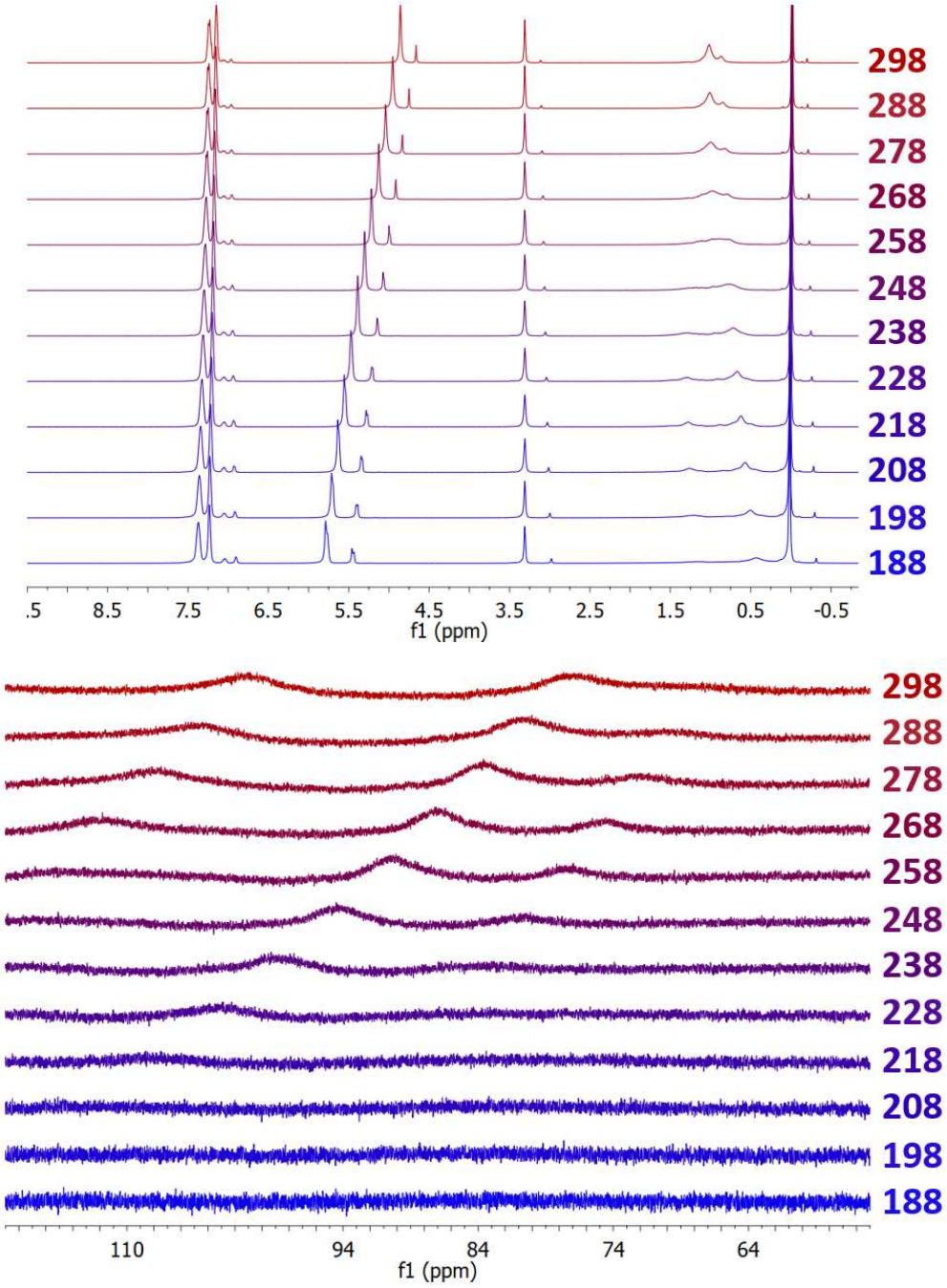

Figure Appendix 1.32. Variable temperature Evans' ^{1}H NMR method of **4-1** in d_4-CD_3OD between 298 K and 188 K with TMS in a capillary and sample solution and 1,2-diflorobenznene in a capillary, collected on a 500 MHz instrument.

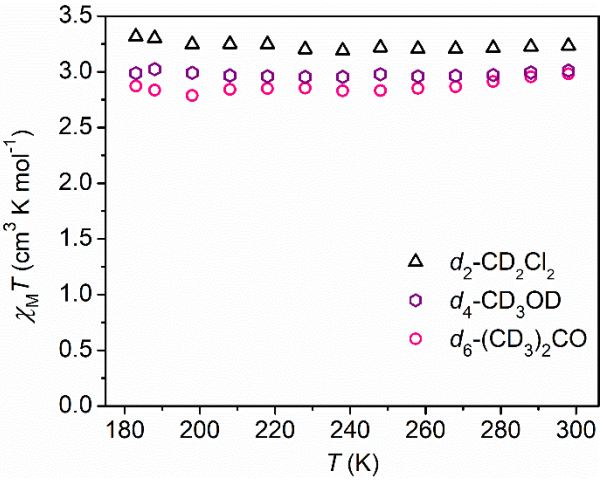

Figure Appendix 1.33. Variable temperature magnetic susceptibility data, collected via Evans' method for 5 mM solutions of **4-1** in d_2-CD_2Cl_2 (black triangles), d_4-CD_3OD (purple hexagons), and d_6-$(CH_3)_2CO$ (pink circles), in the temperature range 183 K - 248 K, using a Varian Inova 500 MHz NMR spectrometer.

A1.9 Stability Test

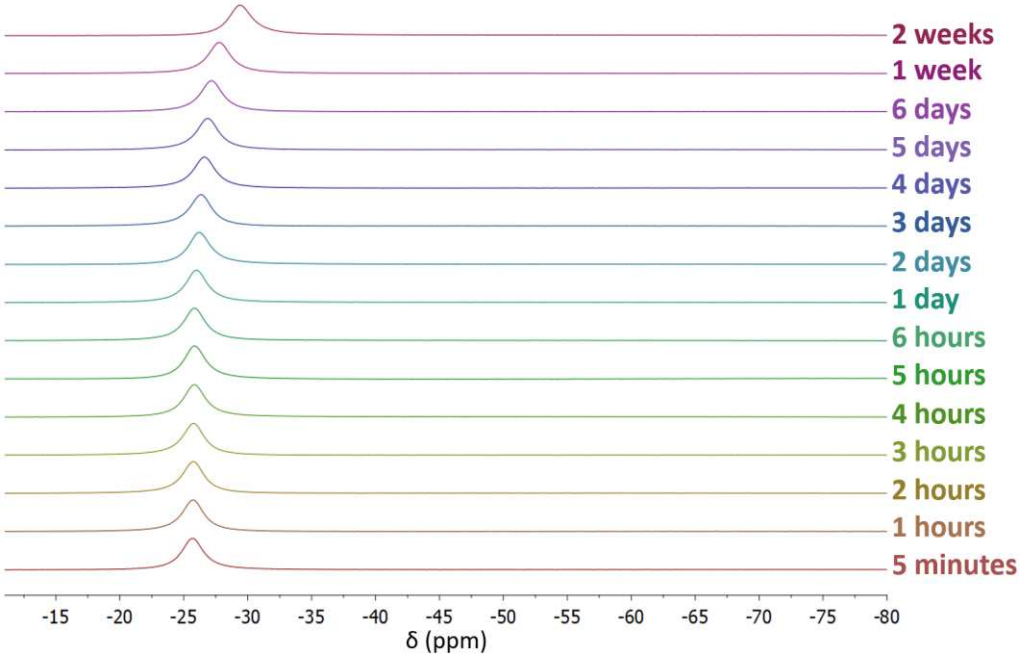

Figure Appendix 1.34. The ^{19}F NMR of **4-1** (80 mM) in d_4-$(CD_3)_2CO$ collected after 5 minutes to 2 weeks referenced to 1,2-difluorobenzene, collected on a 400 MHz instrument.

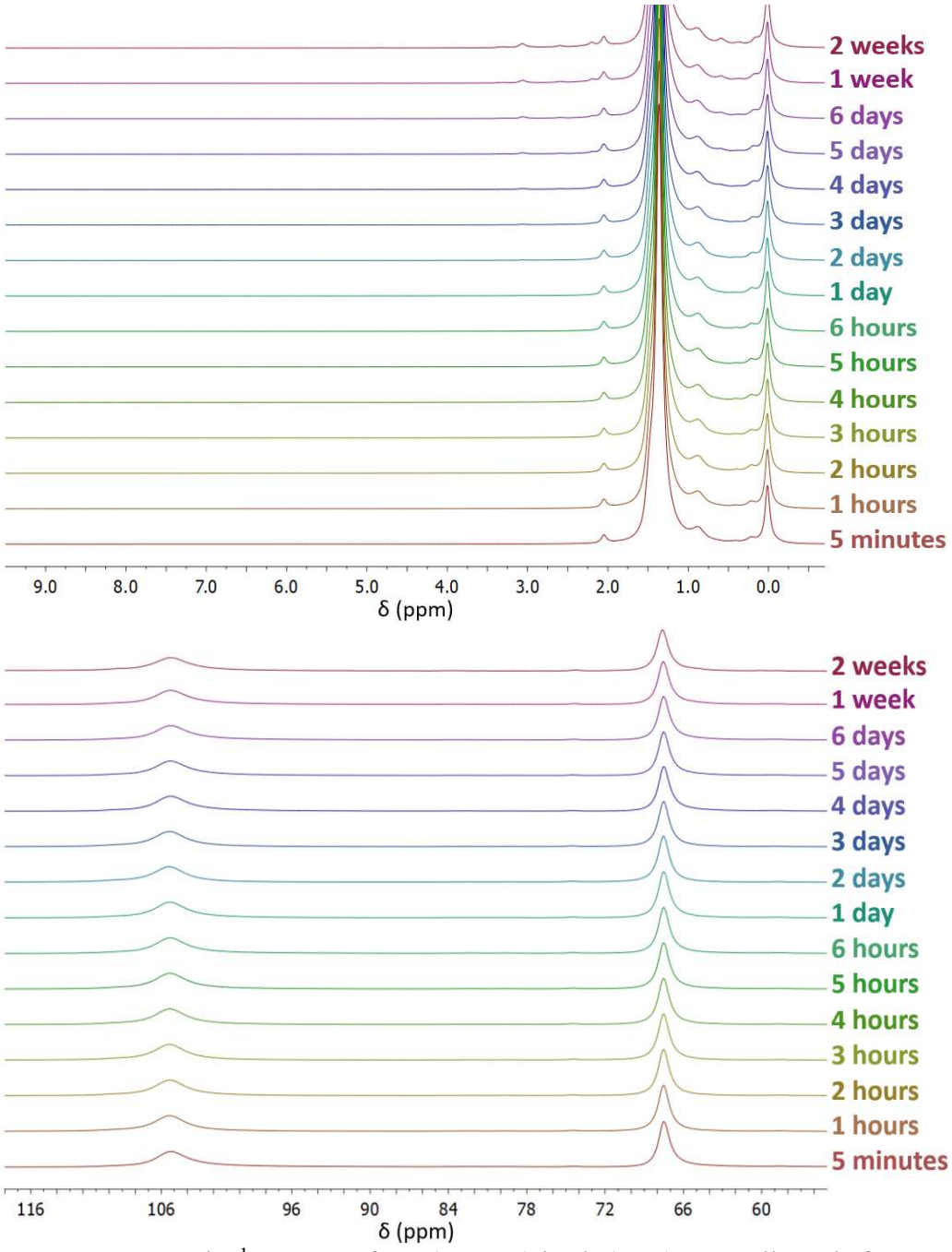

Figure Appendix 1.35. The ^{1}H NMR of **4-1** (80 mM) in d_4-$(CD_3)_2CO$ collected after 5 minutes to 2 weeks, collected on a 400 MHz instrument.

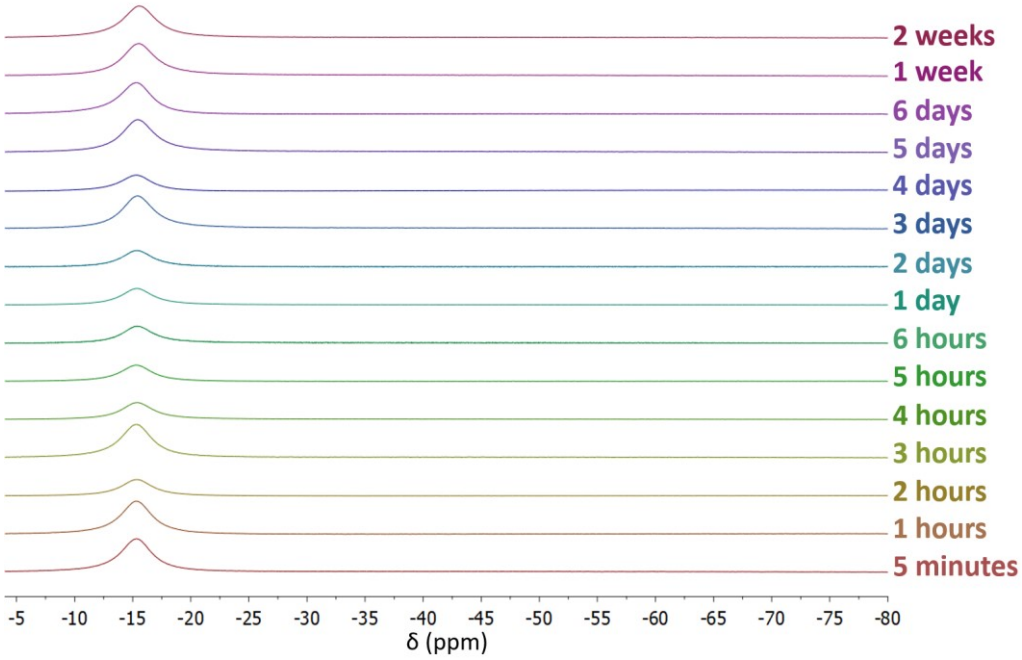

Figure Appendix 1.36. The ^{19}F NMR of **4-1** (80 mM) in d_2-CD_2Cl_2 collected after 5 minutes to 2 weeks referenced to 1,2-difluorobenzene, collected on a 400 MHz instrument.

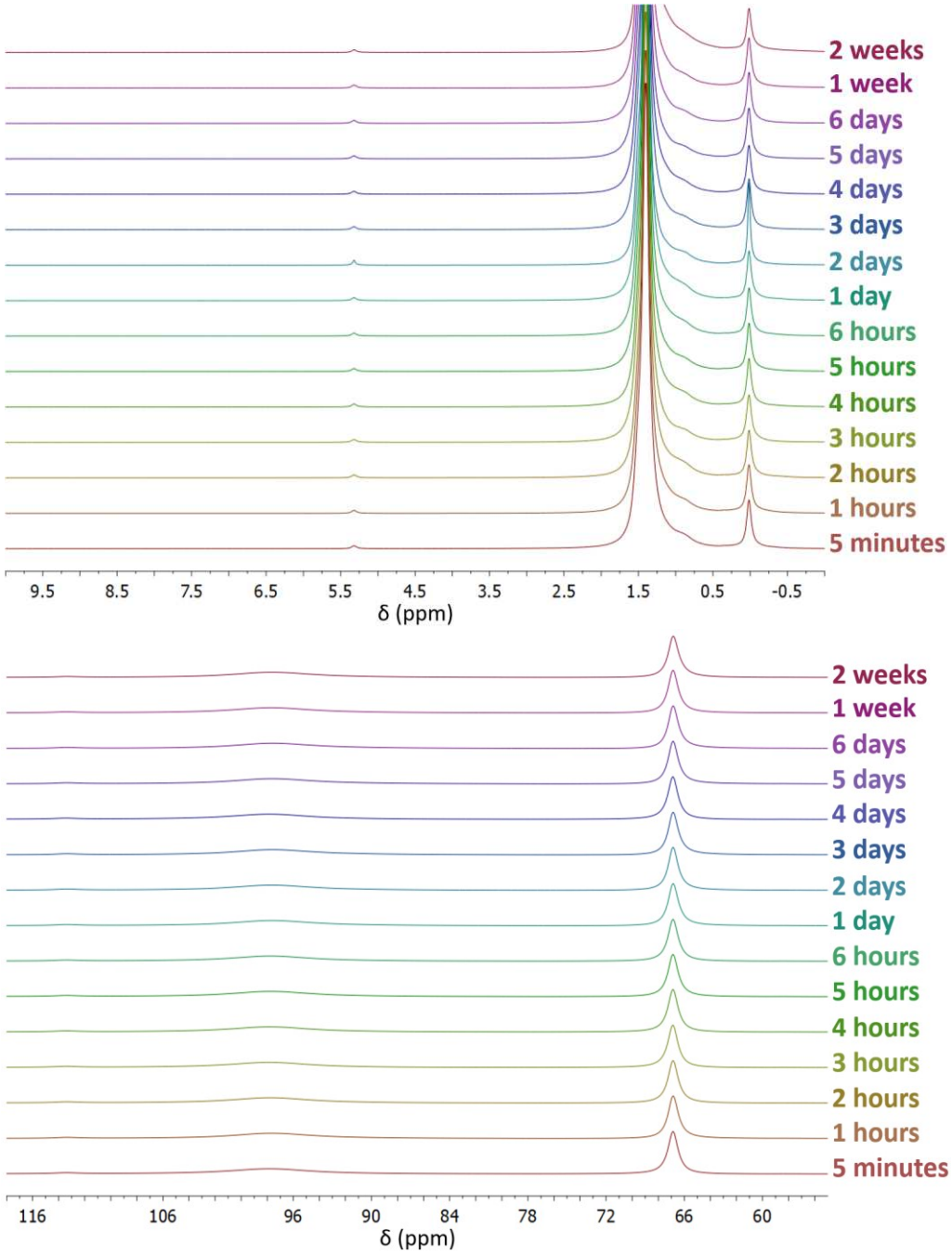

Figure Appendix 1.37. The ^{1}H NMR of **4-1** (80 mM) in d_2-CD_2Cl_2 collected after 5 minutes to 2 weeks, collected on a 400 MHz instrument

A1.10 Conductivity

Table Appendix 1.4. Room temperature conductivity values for 0.001 M solution of **4-1** in various solvents and their physical parameters.

Solvent	ε [4]	DN [5]	Basicity [5]	HBD [5]	E_T^N [6]	a^{TM} [7,8]	Conductivity (μS cm^{-1})
CH_3NO_2	37.27	2.7	92	22	0.481	-1.4	134
CH_3CN	36.64	14.1	86	19	0.460	-0.2	252.9
CH_3OH	33.0	30	50	98	0.762	-0.3	139.9
CH_3CH_2OH	25.3	19.2	45	86	0.654	-0.5	37.7
$(CH_3)_2CO$	21.01	17	81	8	0.355	-1.0	117.8
3-pentanone	17.0	15		0	0.265		51.5
Cyclopentanone	13.58	18		0	0.269		22.1
CH_2Cl_2	8.93	1	80	13	0.309	-1.8	4.8
THF	7.52	20	67	0	0.207	-0.3	1.9

ε is the dielectric constant or relative permittivity of the solvent.
DN is the donor number of the solvent.
Basicity is the cation solvating tendency of the solvent.
HBD is the ability of the solvent to donate a hydrogen atom to form a hydrogen bond.
E_T^N is a normalized value of solvent polarity using water and tetramethylsilane as extreme polar and nonpolar references.
a^{TM} is the coordination ability of a solvent towards transition metal ions.

A1.11 Dynamic Light Scattering (DLS)

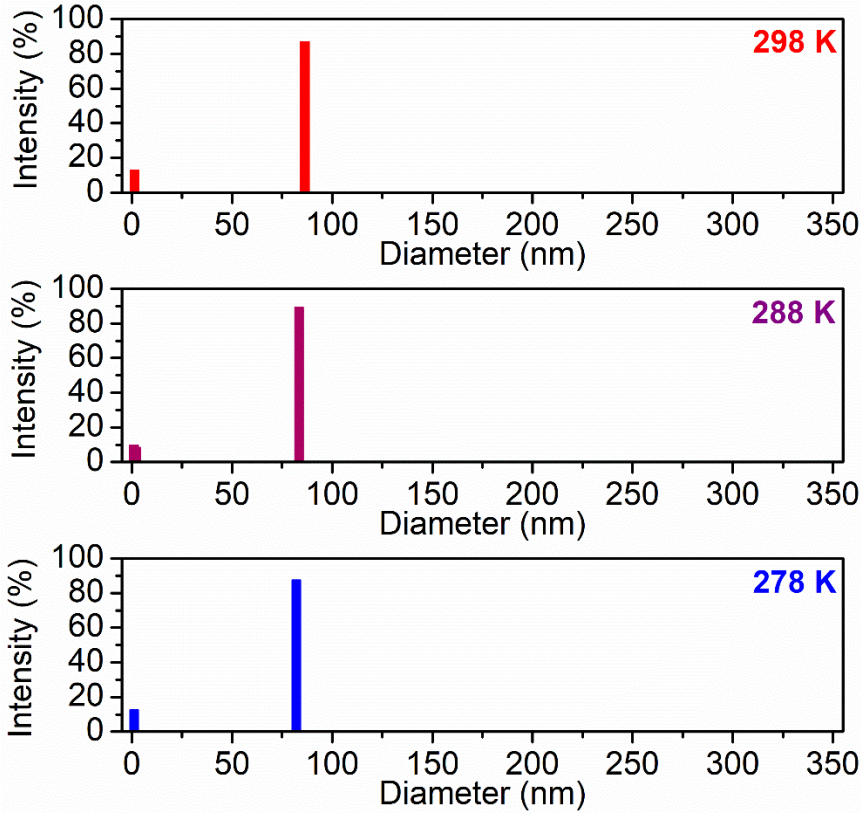

Figure Appendix 1.38. DLS analysis of a 5 mM solution of **4-1** in $(CH_3)_2CO$ collected at 298 K (red), 288 K (purple), and 278 K (blue).

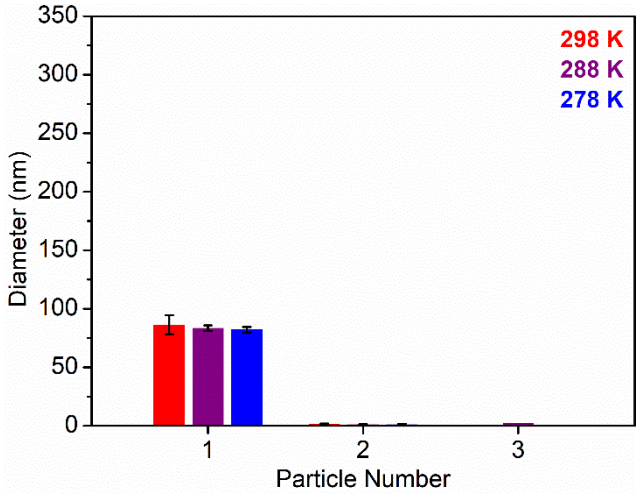

Figure Appendix 1.39. The solvodynamic diameter of 5 mM solution of **4-1** in $(CH_3)_2CO$ collected 298 K (red), 288 K (purple), and 278 K (blue).

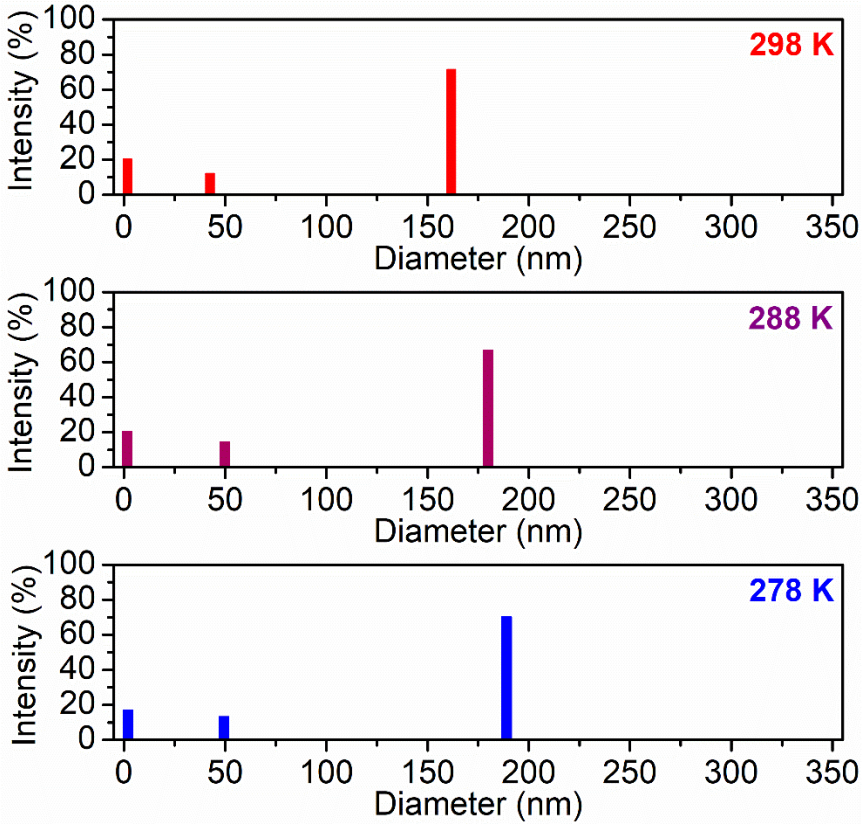

Figure Appendix 1.40. DLS analysis of an 80 mM solution of **4-1** in $(CH_3)_2CO$ collected at 298 K (red), 288 K (purple), and 278 K (blue).

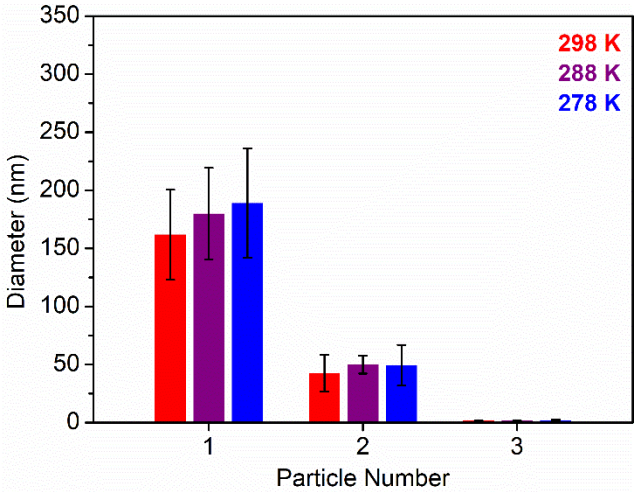

Figure Appendix 1.41. The solvodynamic diameter of 80 mM solution of **4-1** in $(CH_3)_2CO$ collected 298 K (red), 288 K (purple), and 278 K (blue).

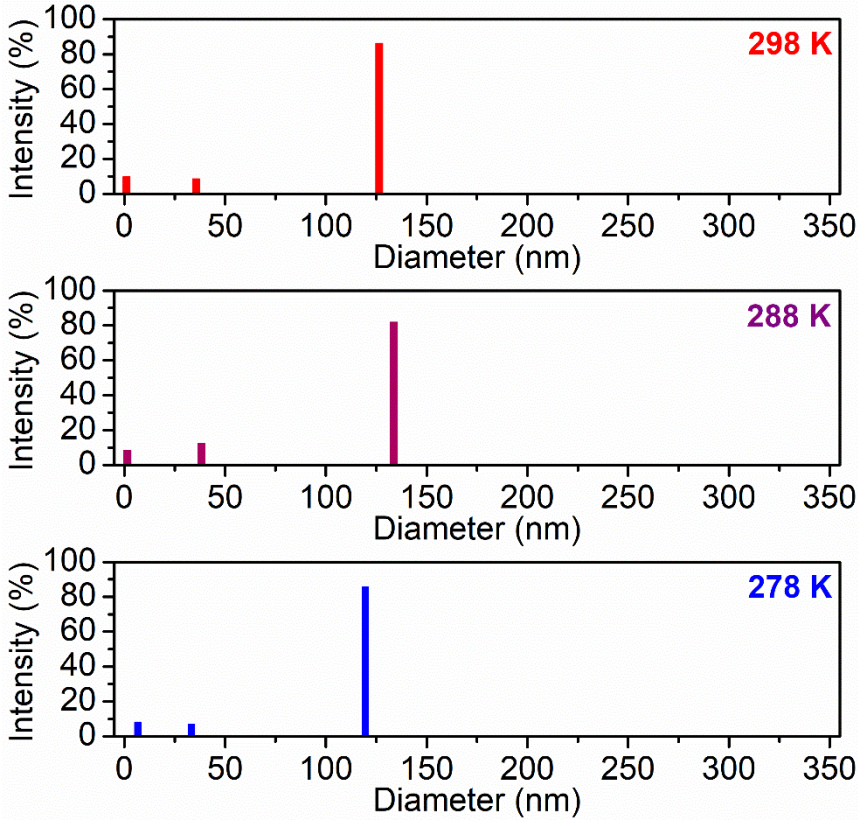

Figure Appendix 1.42. DLS analysis of a 5 mM solution of **4-1** in d_6-$(CD_3)_2CO$ collected at 298 K (red), 288 K (purple), and 278 K (blue).

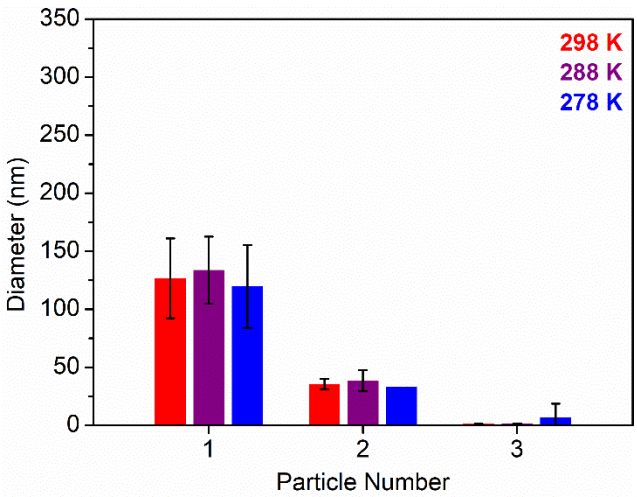

Figure Appendix 1.43. The solvodynamic diameter of 5 mM solution of **4-1** in d_6-$(CD_3)_2CO$ collected 298 K (red), 288 K (purple), and 278 K (blue).

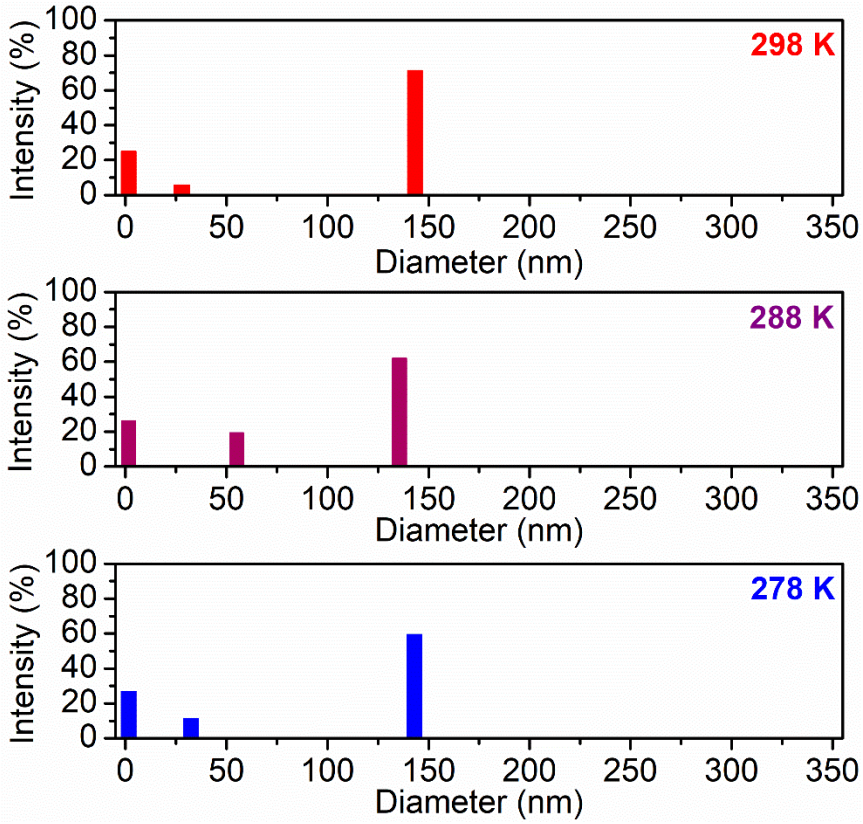

Figure Appendix 1.44. DLS analysis of an 80 mM solution of **4-1** in d_6-$(CD_3)_2CO$ collected at 298 K (red), 288 K (purple), and 278 K (blue).

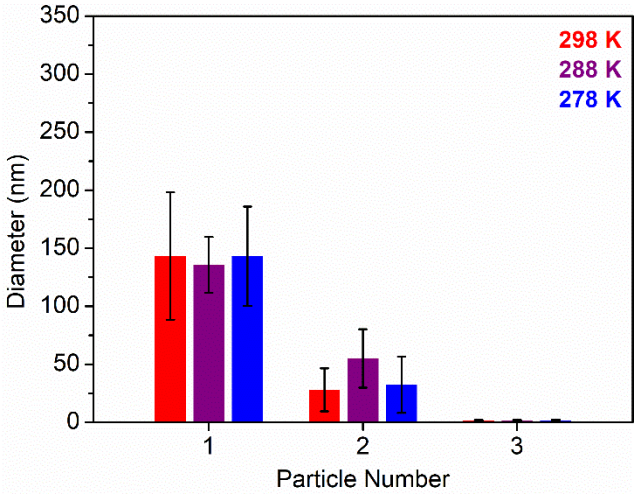

Figure Appendix 1.45. The solvodynamic diameter of 80 mM solution of **4-1** in d_6-$(CD_3)_2CO$ collected 298 K (red), 288 K (purple), and 278 K (blue).

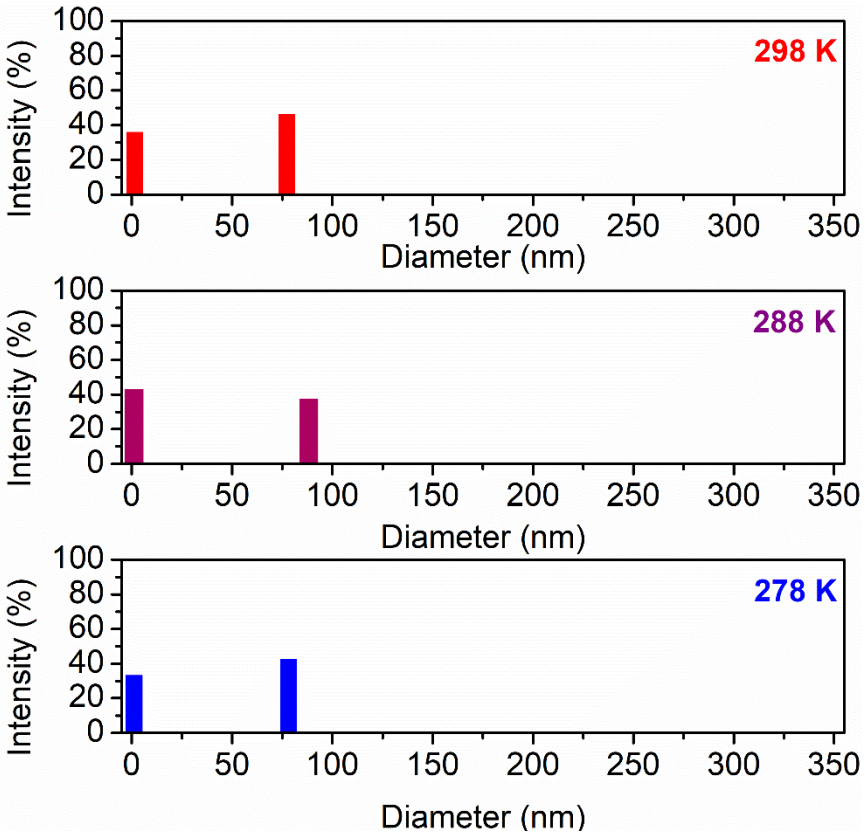

Figure Appendix 1.46. DLS analysis of a 5 mM solution of **4-1** in CH_3OH collected at 298 K (red), 288 K (purple), and 278 K (blue).

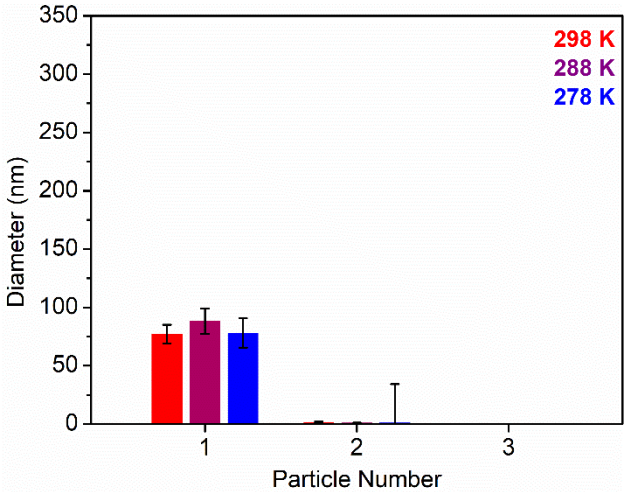

Figure Appendix 1.47. The solvodynamic diameter of 5 mM solution of **4-1** in CH_3OH collected 298 K (red), 288 K (purple), and 278 K (blue).

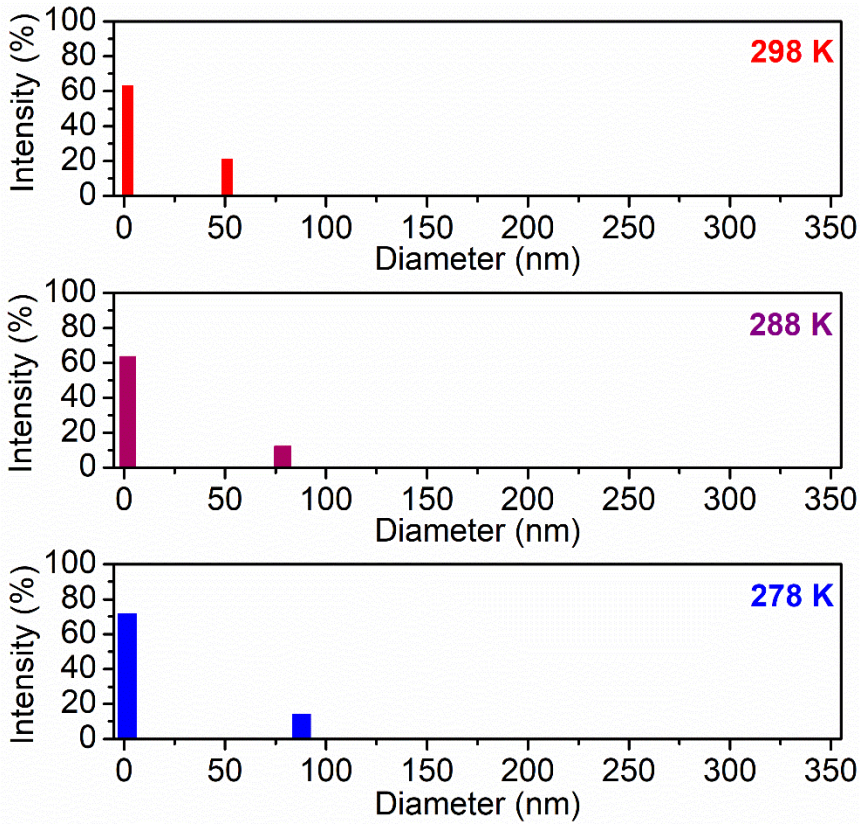

Figure Appendix 1.48. DLS analysis of an 80 mM solution of **4-1** in CH_3OH collected at 298 K (red), 288 K (purple), and 278 K (blue).

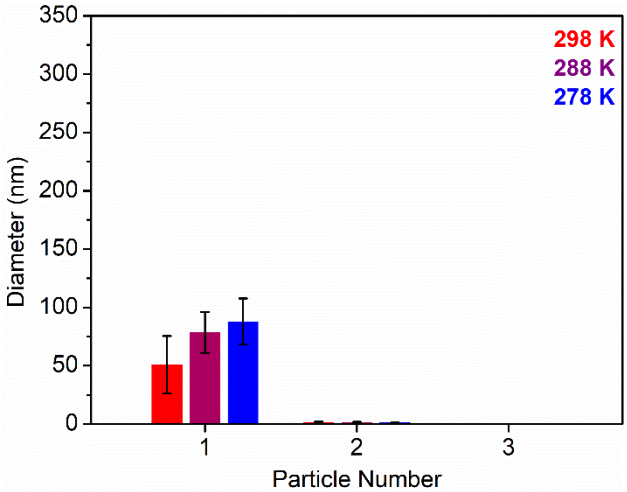

Figure Appendix 1.49. The solvodynamic diameter of 80 mM solution of **4-1** in CH_3OH collected 298 K (red), 288 K (purple), and 278 K (blue).

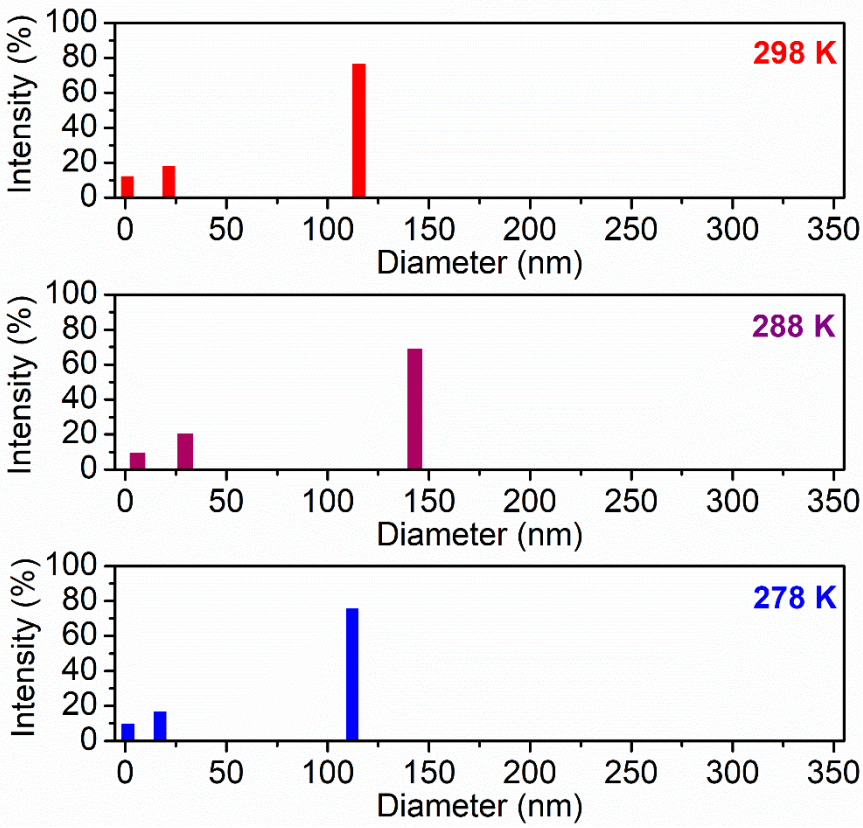

Figure Appendix 1.50. DLS analysis of a 5 mM solution of **4-1** in CH_2Cl_2 collected at 298 K (red), 288 K (purple), and 278 K (blue).

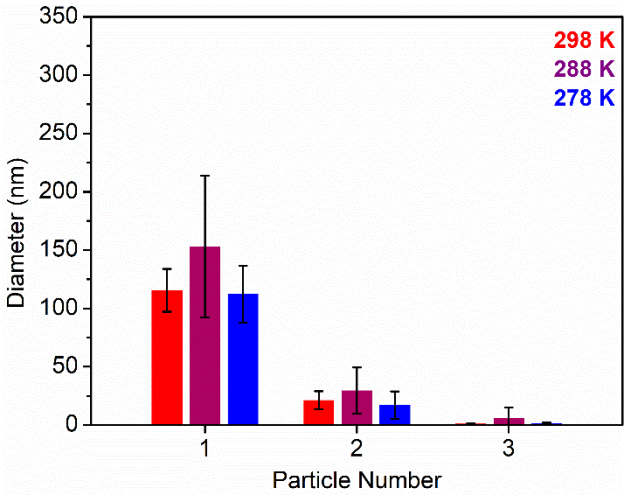

Figure Appendix 1.51. The solvodynamic diameter of 5 mM solution of **4-1** in CH_2Cl_2 collected 298 K (red), 288 K (purple), and 278 K (blue).

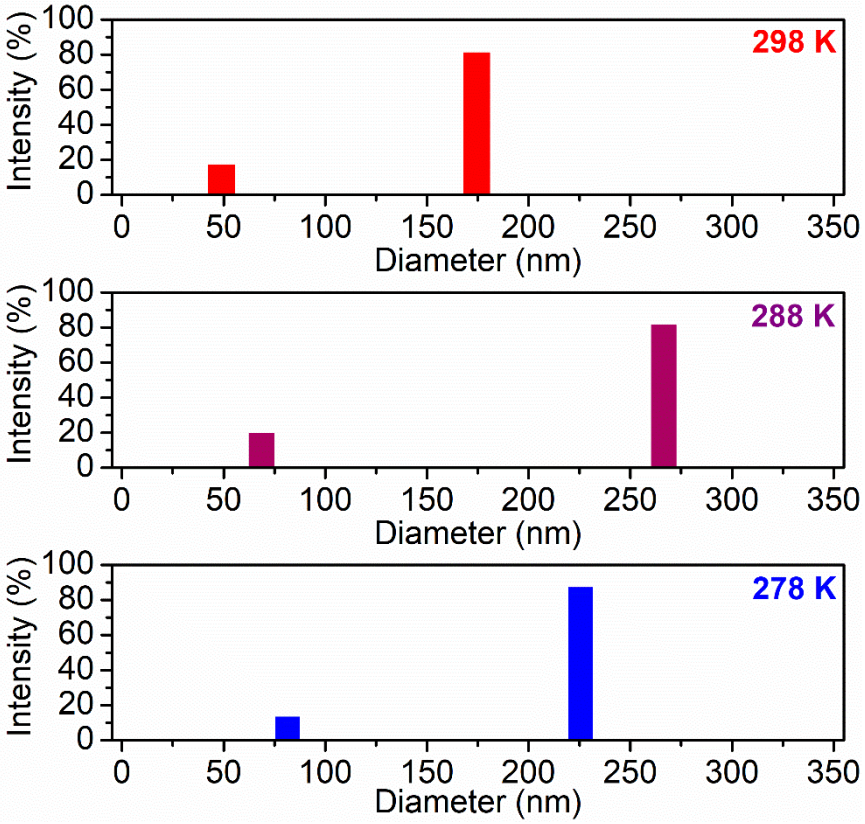

Figure Appendix 1.52. DLS analysis of an 80 mM solution of **4-1** in CH_2Cl_2 collected at 298 K (red), 288 K (purple), and 278 K (blue).

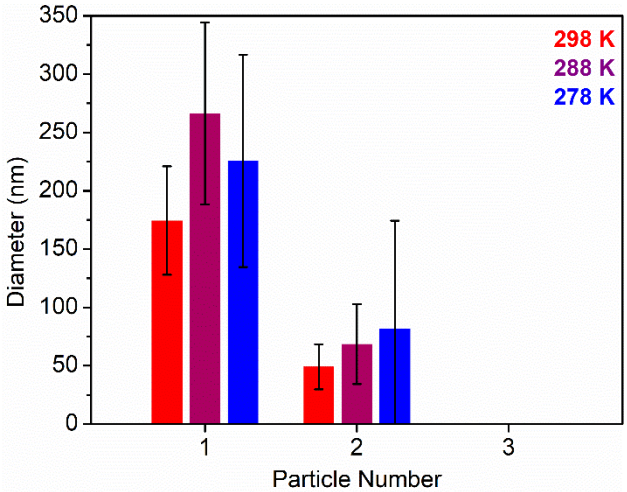

Figure Appendix 1.53. The solvodynamic diameter of 80 mM solution of **4-1** in CH_2Cl_2 collected 298 K (red), 288 K (purple), and 278 K (blue).

References

(1) Chilton, N. F.; Anderson, R. P.; Turner, L. D.; Soncini, A.; Murray, K. S. PHI: A Powerful New Program for the Analysis of Anisotropic Monomeric and Exchange-Coupled Polynuclear d- and f-Block Complexes. *J. Comput. Chem.* **2013**, *34* (13), 1164–1175.

(2) Kahn, O. *Molecular Magnetism*; VCH: New York, NY, 1993.

(3) Ni, Z.; Shores, M. P. Supramolecular Effects on Anion-Dependent Spin-State Switching Properties in Heteroleptic Iron(II) Complexes. *Inorg. Chem.* **2010**, *49* (22), 10727–10735.

(4) Spingler, B.; Schnidrig, S.; Todorova, T.; Wild, F. Some Thoughts about the Single Crystal Growth of Small Molecules. *CrystEngComm* **2012**, *14*, 751–757.

(5) Marcus, Y. The Properties of Organic Liquids That Are Relevant to Their Use as Solvating Solvents. *Chemical Society Reviews*. The Royal Society of Chemistry January 1, 1993, pp 409–416.

(6) Reichardt, C. Solvatochromic Dyes as Solvent Polarity Indicators. *Chem. Rev.* **1994**, *94* (8), 2319–2358.

(7) Alvarez, S. Coordinating Ability of Anions, Solvents, Amino Acids, and Gases towards Alkaline and Alkaline-Earth Elements, Transition Metals, and Lanthanides. *Chem. – A Eur. J.* **2020**, *26* (19), 4350–4377.

(8) Díaz-Torres, R.; Alvarez, S. Coordinating Ability of Anions and Solvents towards Transition Metals and Lanthanides. *Dalt. Trans.* **2011**, *40* (40), 10742–10750.

Appendix 2: Supporting Information for Chapter 6

A2.1 ^{1}H NMR Spectra

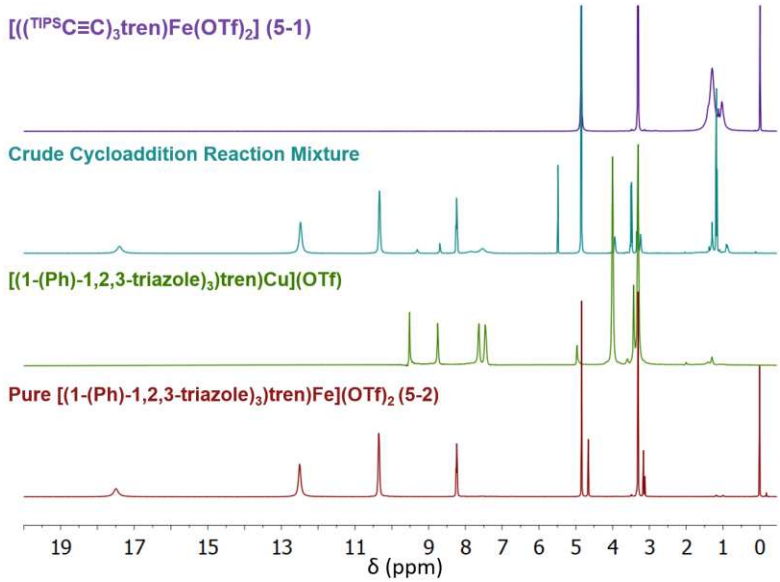

Figure Appendix 2.1. The ^{1}H NMR spectra between 20 ppm and 0 ppm in d_4-CD_3OD of the crude cycloaddition reaction mixture with phenyl azide (teal) compared to [((^{TIPS}C≡C)$_3$tren)Fe(OTf)$_2$] (**6-1**, purple), [(1-Ph-1,2,3-triazole)$_3$)tren)Cu(OTf) (green), and pure [(1-Ph-1,2,3-triazole)$_3$)tren)Fe(OTf)$_2$ (**6-2**, red).

A2.2 Crystal Packing Diagrams

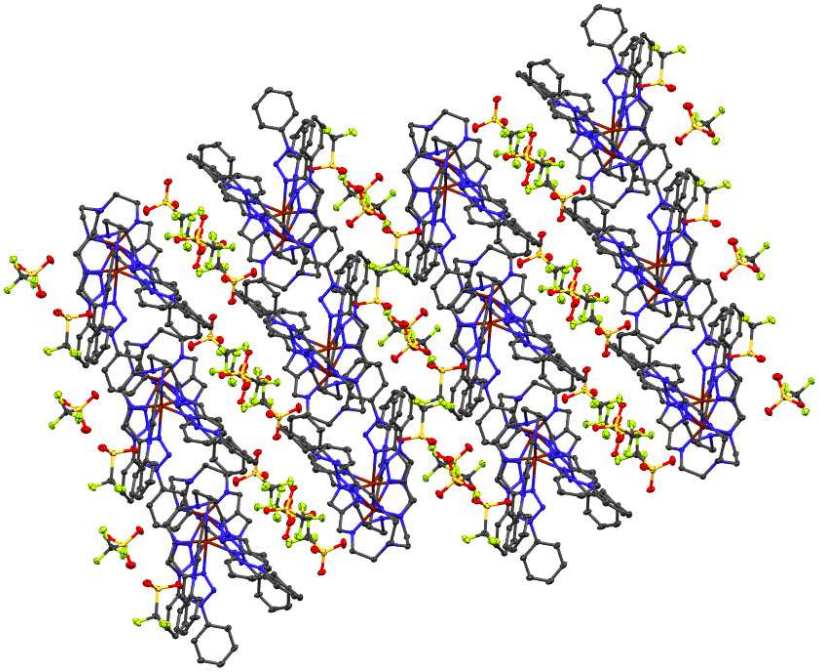

Figure Appendix 2.2. Crystal packing diagram of [(1-Ph-1,2,3-triazole)$_3$)tren)Fe](OTf)$_2$ (**6-2**) showing the cation stacking channels. Dark red, blue, gray, red, yellow, and green ellipsoids represent Fe, N, C, O, S, and F respectively. Hydrogen atoms were omitted for clarity.

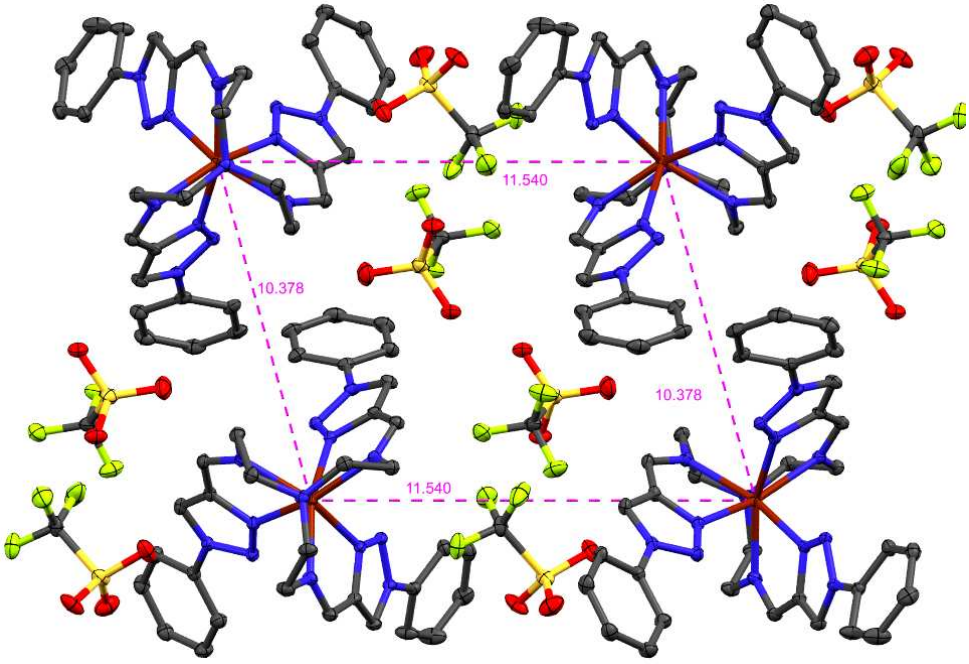

Figure Appendix 2.3. The intermolecular Fe···Fe distances of [(1-Ph-1,2,3-triazole)$_3$)tren)Fe](OTf)$_2$ (**6-2**). Dark red, blue, gray, red, yellow, and green ellipsoids represent Fe, N, C, O, S, and F respectively. Hydrogen atoms were omitted for clarity.

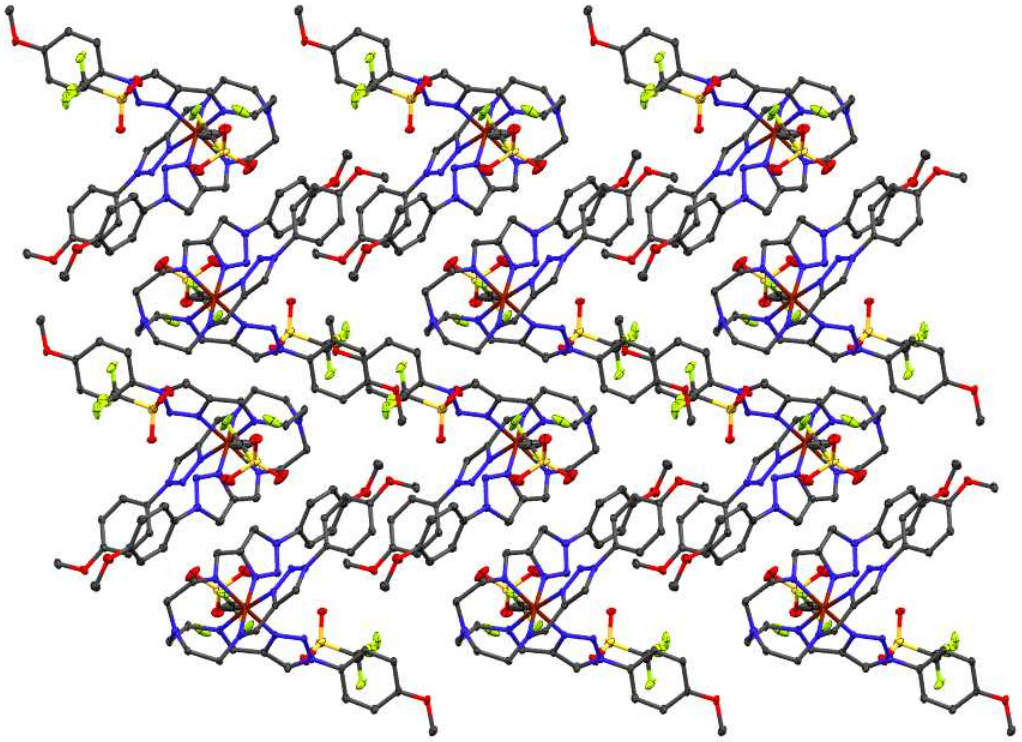

Figure Appendix 2.4. The crystal packing diagram of [(1-(4-MeO-Ph)-1,2,3-triazole)$_3$)tren)Fe](OTf)$_2$ (**6-3**). Dark red, blue, gray, red, yellow, and green ellipsoids represent Fe, N, C, O, S, and F respectively. Hydrogen atoms were omitted for clarity.

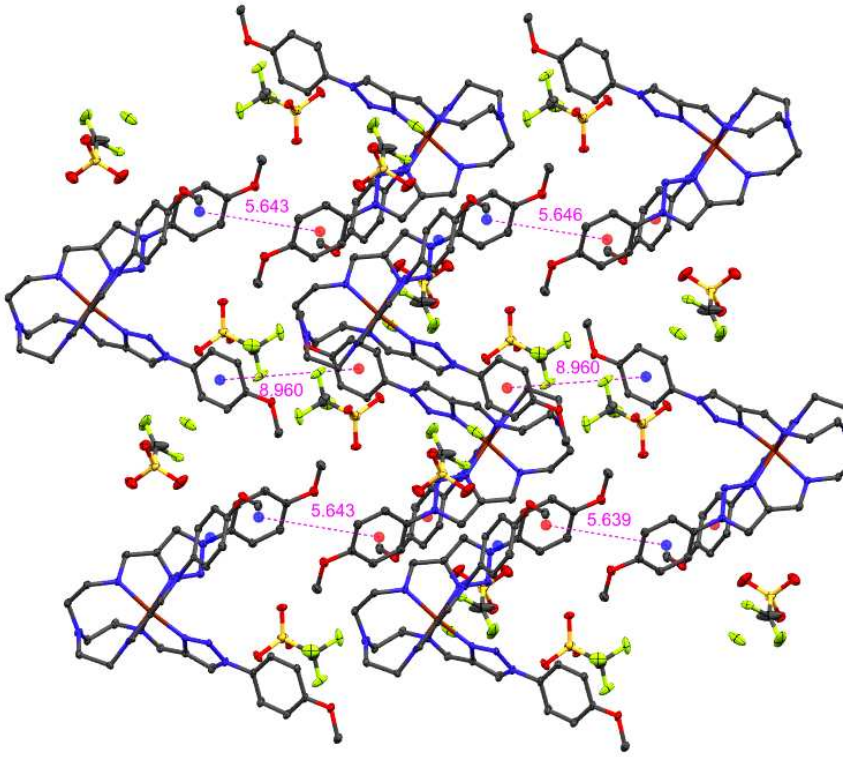

Figure Appendix 2.5. The π-π interactions between 4-MeO-Phenyl rings of adjacent [(1-(4-MeO-Ph)-1,2,3-triazole)$_3$)tren)Fe](OTf)$_2$ (**6-3**) complexes. Dark red, blue, gray, red, yellow, and green ellipsoids represent Fe, N, C, O, S, and F respectively. Hydrogen atoms were omitted for clarity.

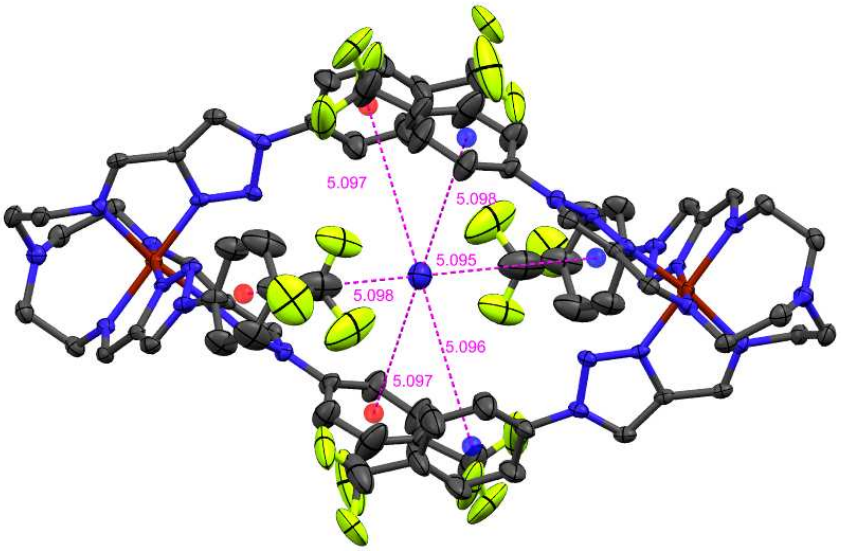

Figure Appendix 2.6. The cation cation-π interactions between the ammonium cation and two [(1-(4-CF$_3$-Ph)-1,2,3-triazole)$_3$)tren)Fe](OTf)$_2$ (**6-4**) complexes. The red and blue centroids were calculated to find the distance between the ammonium ion and the phenyl groups of **6-4**. Dark red, blue, gray, red, yellow, and green ellipsoids represent Fe, N, C, O, S, and F respectively. Hydrogen atoms were omitted for clarity.

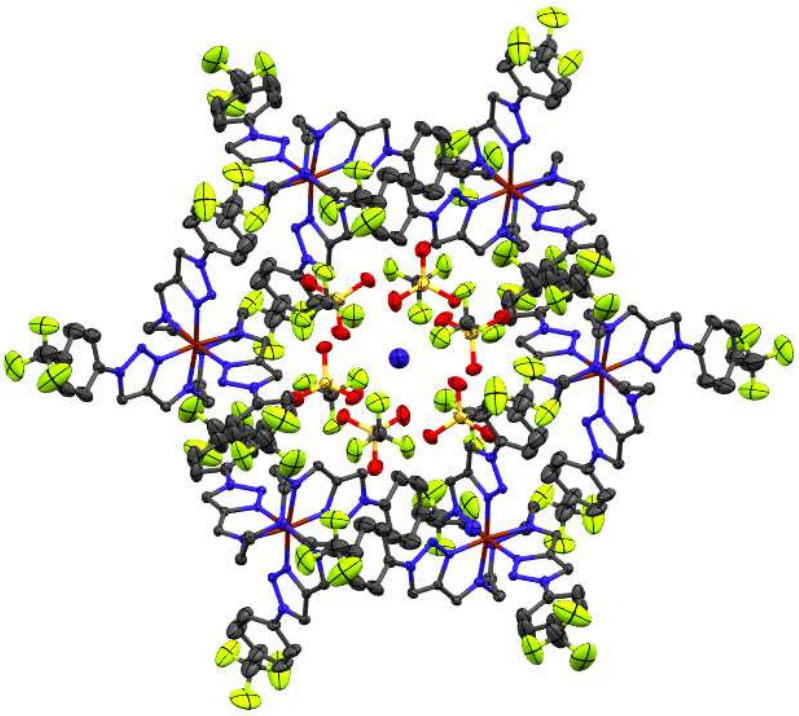

Figure Appendix 2.7. The crystal packing diagram of [(1-(4-CF_3-Ph)-1,2,3-triazole)$_3$)tren)Fe](OTf)$_2$ (**6-4**). Dark red, blue, gray, red, yellow, and green ellipsoids represent Fe, N, C, O, S, and F respectively. Hydrogen atoms were omitted for clarity.

A2.3 Solid State Magnetic Data

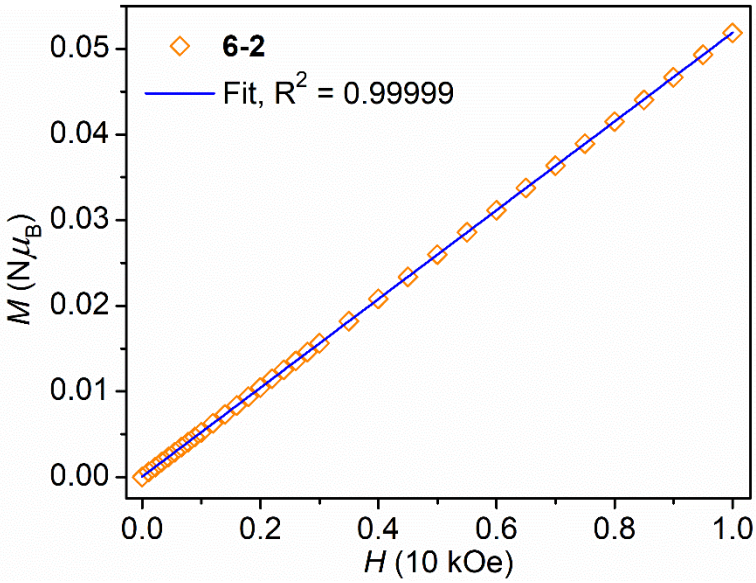

Figure Appendix 2.8. Field dependence of magnetization for **6-2** collected at 100 K. The data were fit to a linear regression ($y = 0.05183\ x + 4.65 \times 10^{-5}$), shown in blue.

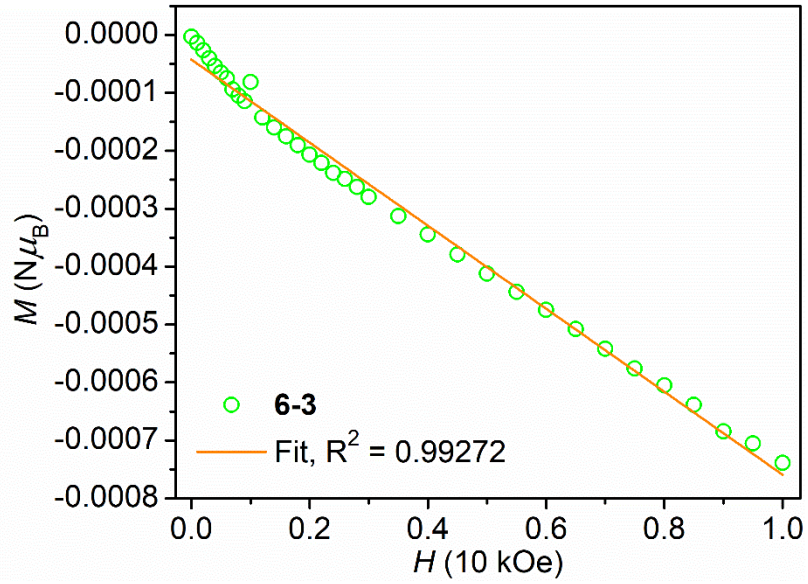

Figure Appendix 2.9. Field dependence of magnetization for **6-3** collected at 100 K. The data were fit to a linear regression ($y = -7.17 \times 10^{-4}\ x - 4.26 \times 10^{-5}$), shown in orange.

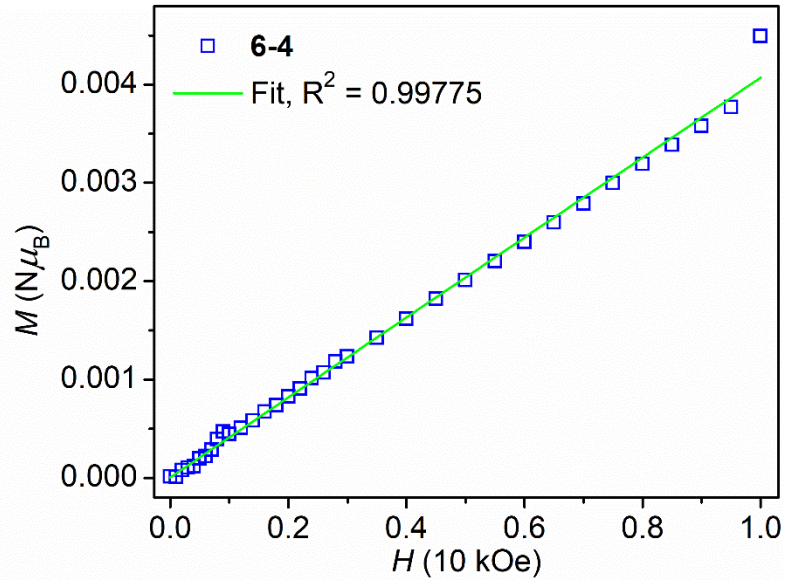

Figure Appendix 2.10. Field dependence of magnetization for **6-4** collected at 100 K. The data were fit to a linear regression ($y = 0.00355\ x + 8.32 \times 10^{-5}$), shown in green.

Table Appendix 2.1. Magnetic Parameters for **6-2** obtained *via* PHI[1]

	g	Θ (cm^{-1})	D (E) (cm^{-1})	TIP (10^{-5} cm^3 mol^{-1})	R^2
[((1-Ph-1,2,3-triazole)$_3$tren)Fe](OTf)$_2$ **6-2**	2.07	0.130	11.5 (0.374)	170	0.995547

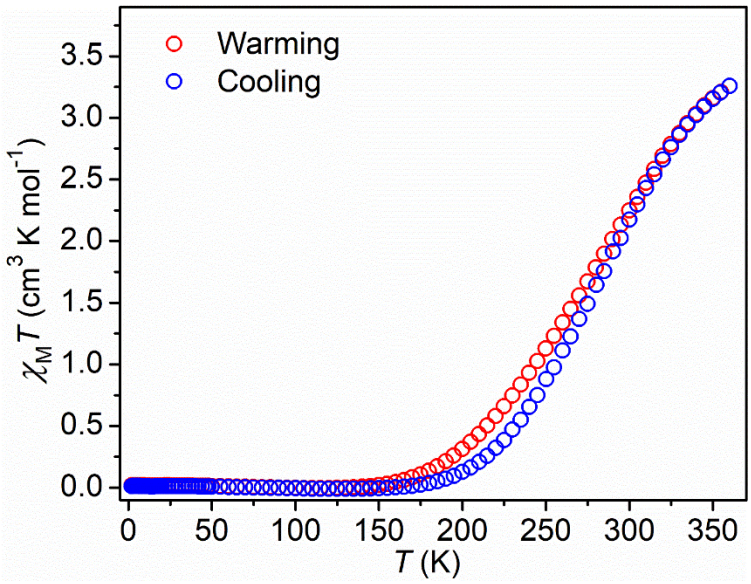

Figure Appendix 2.11. The warming (red circles) and cooling (red circles) of the temperature dependence of the magnetic susceptibility of **6-3** collected with a 2 K scan rate.

Table Appendix 2.2. Thermodynamic Parameters for **6-3** and **6-4** obtained from fitting the solid state magnetic data to the regular solution model.[2,3]

	ΔH (kJ mol^{-1})	ΔS (J mol^{-1} K^{-1})	$\chi_M T$ max (cm^3 K mol^{-1})	$T_{1/2}$ (K)	R^2
[((1-(4-MeO-Ph)-1,2,3-triazole)$_3$)tren)Fe](OTf)$_2$ **6-3**	14.52	52.31	3.5	277.5	0.967454
[((1-(4-F$_3$C-Ph)-1,2,3-triazole)$_3$)tren)Fe](OTf)$_2$ **6-4**	11.75	22.0	3.5	534.2	0.983857

A2.4 Electronic Absorption Spectra

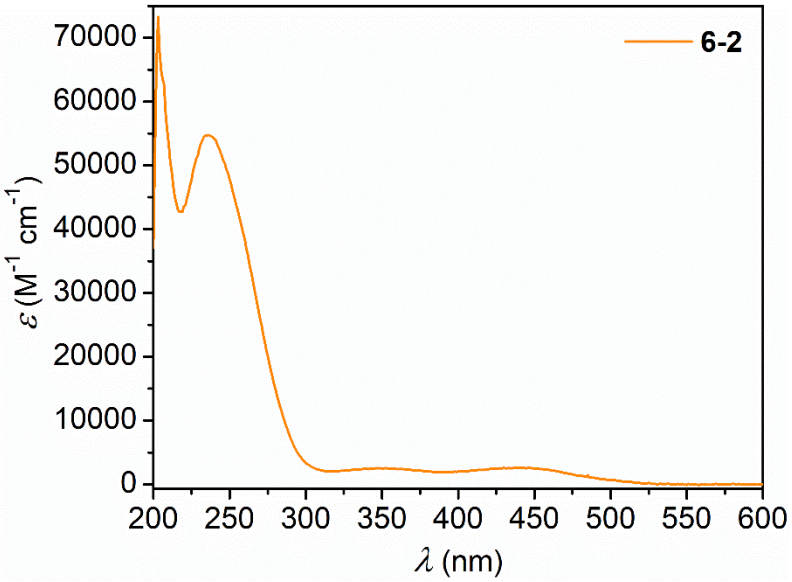

Figure Appendix 2.12. Electronic absorption spectrum of **6-2** in CH_3OH.

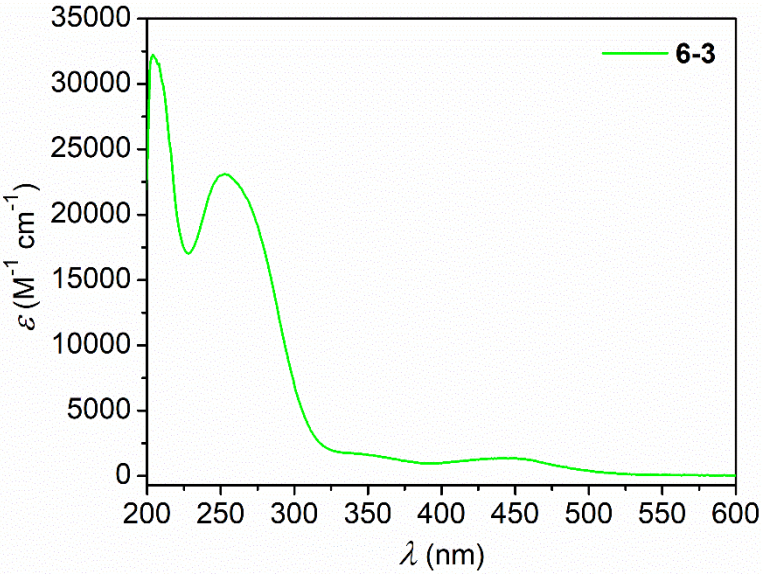

Figure Appendix 2.13. Electronic absorption spectrum of **6-3** in CH_3OH.

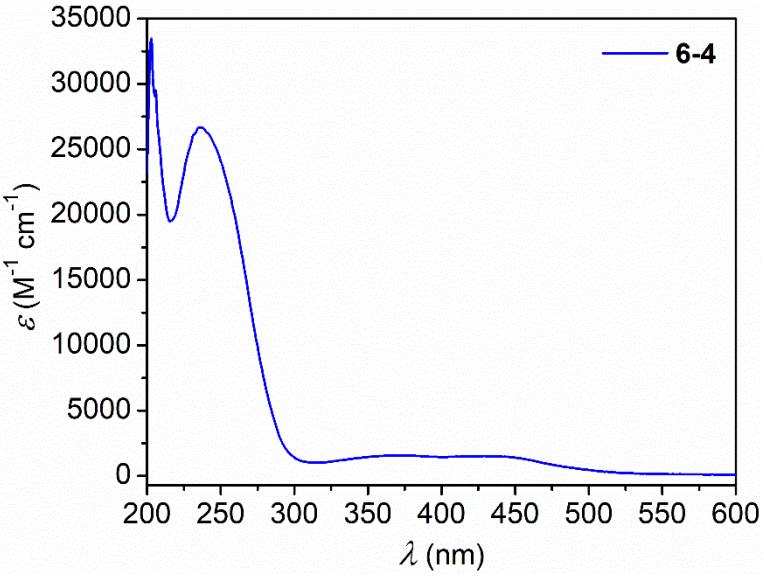

Figure Appendix 2.14. Electronic absorption spectrum of **6-4** in CH_3OH.

A2.5 Infrared Spectroscopic Data

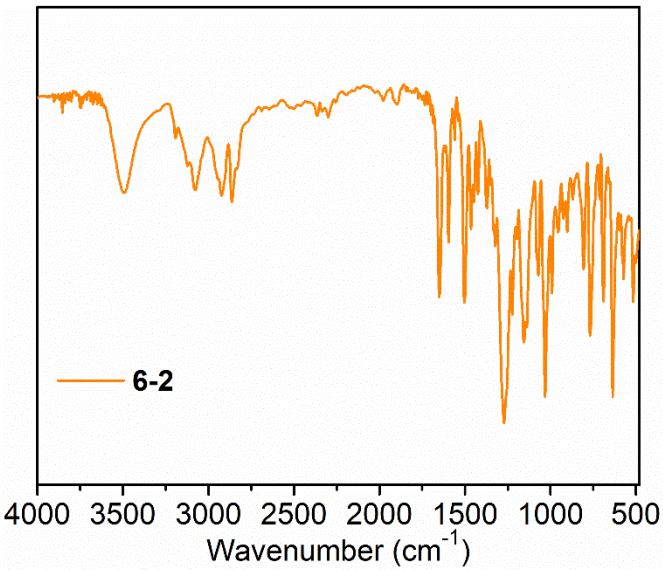

Figure Appendix 2.15. IR spectrum of **6-2**

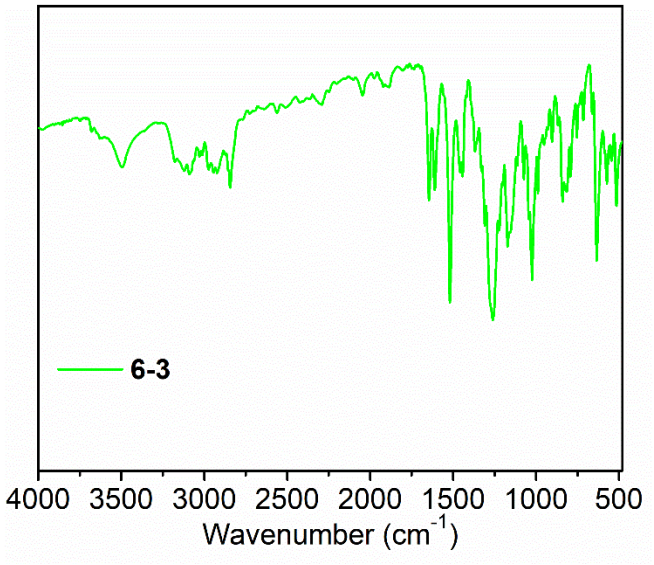

Figure Appendix 2.16. IR spectrum of **6-3.**

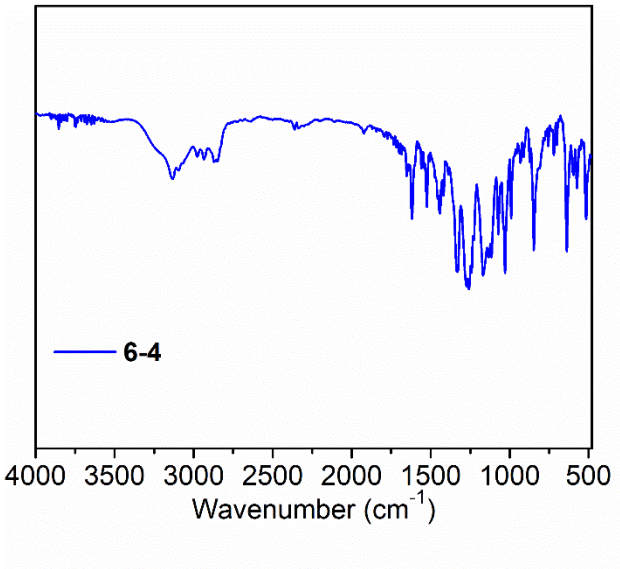

Figure Appendix 2.17. IR spectrum of **6-4.**

References

(1) Chilton, N. F.; Anderson, R. P.; Turner, L. D.; Soncini, A.; Murray, K. S. PHI: A Powerful New Program for the Analysis of Anisotropic Monomeric and Exchange-Coupled Polynuclear d- and f-Block Complexes. *J. Comput. Chem.* **2013**, *34* (13), 1164–1175.

(2) Kahn, O. *Molecular Magnetism*; VCH: New York, NY, 1993.

(3) Hogue, R. W.; Feltham, H. L. C.; Miller, R. G.; Brooker, S. Spin Crossover in Dinuclear N4S2 Iron(II) Thioether-Triazole Complexes: Access to [HS-HS], [HS-LS], and [LS-LS] States. *Inorg. Chem.* **2016**, *55* (9), 4152–4165.

Appendix 3: Supporting Information for Chapter 7

A3.1 Solid State Magnetic Data

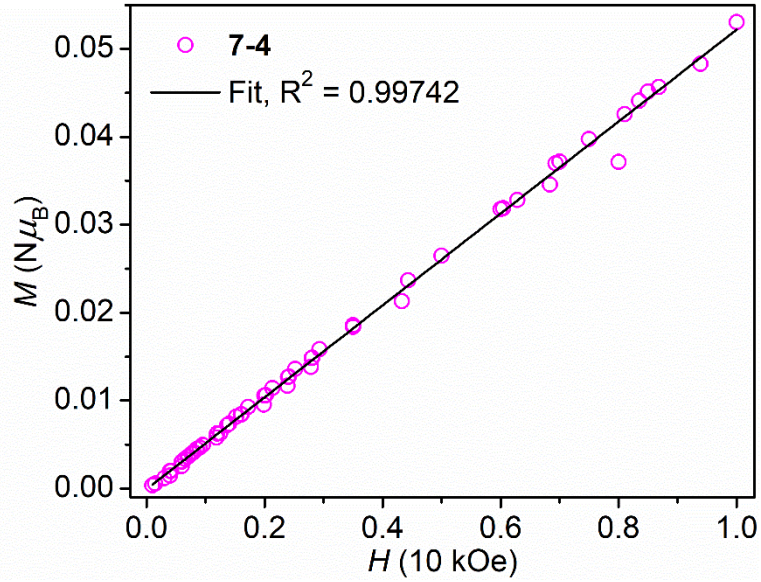

Figure Appendix 3.1. Field dependence of magnetization for **7-4** collected at 100 K. The data were fit to a linear regression ($y = 0.05226\ x - 7.18 \times 10^{-5}$), shown in black.

A3.2 Solution Magnetic Data

Table Appendix 3.1. Selected $\chi_M T$ values for **7-1** – **7-4** and the calculated $T_{1/2}$ values obtained from fitting the solution magnetic data with the regular solution model.

Compound	$\chi_M T$ value (cm^3 K mol^{-1})		$T_{1/2}$ (K)
	298 K	198 K	
7-1 H-Ph	2.71	0	253.8
7-2 MeO-Ph	2.52	0	261.2
7-3 CF_3-Ph	2.37	0	264.6
7-4 $PhCH_2$	3.08	0.30	247.7

A3.3 Electronic Absorption Spectra

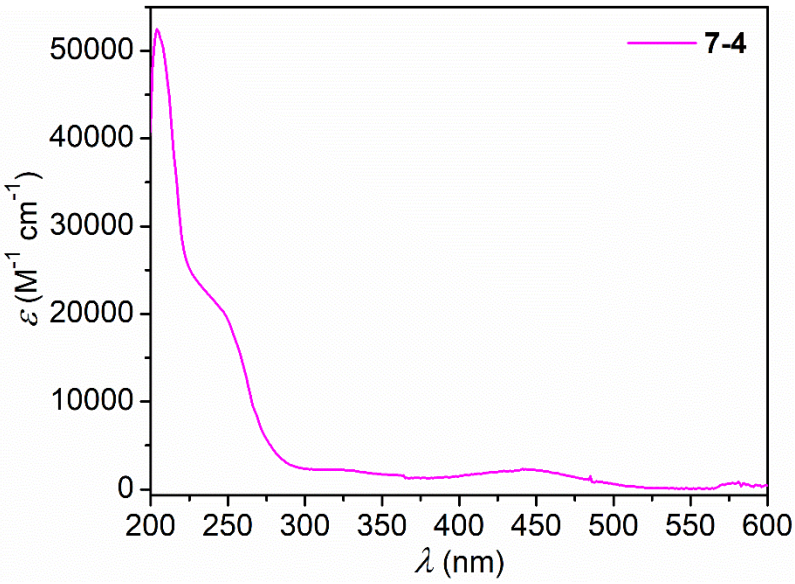

Figure Appendix 3.2. Electronic absorption spectrum of 7-4 in CH_3OH

A3.4 Infrared Spectroscopic Data

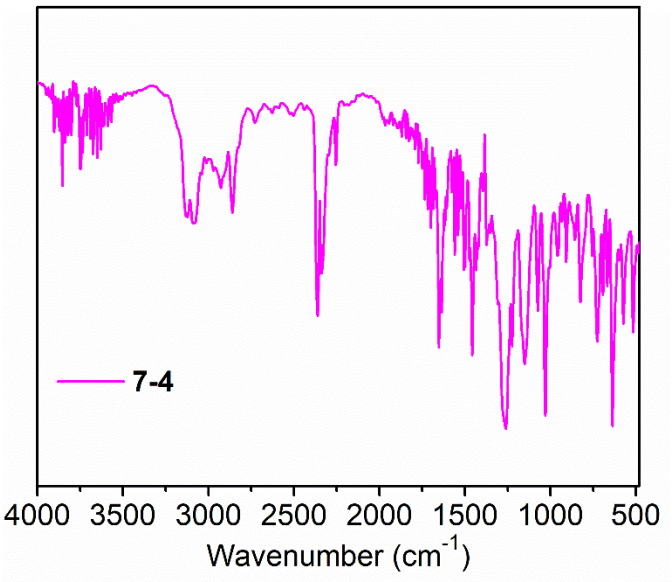

Figure Appendix 3.3. IR spectrum of 7-4